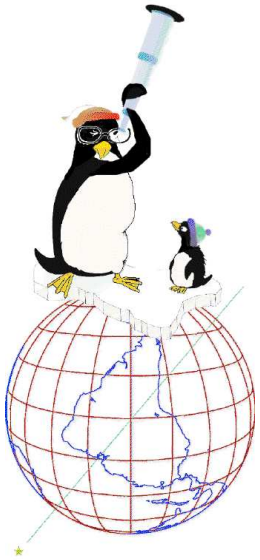

Measuring the Composition of Cosmic Rays with the SPASE and AMANDA detectors

by

Katherine Rawlins

A dissertation submitted in partial fulfillment of the

requirements for the degree of

Doctor of Philosophy

(Physics)

at the

University of Wisconsin – Madison

2001

Abstract

Cosmic rays arriving at Earth are the most energetic particles ever measured, and the mystery of their origin and acceleration has perplexed physicists since their discovery. Above 10^{15} eV, we can only study them indirectly from the extensive air showers they produce in the atmosphere, using large ground-based detectors. Reconstructing the original cosmic ray's energy and mass from ground observations alone is very difficult, but possible from measuring different components of an air shower with a coincidence experiment.

SPASE/AMANDA is a unique such coincidence experiment, a surface scintillator array and buried ice Cherenkov detector working together at the South Pole. SPASE-2 detects the electrons in the air shower, while AMANDA-B10 detects the penetrating high-energy muons from their Cherenkov light. Together, the two detectors pin down a very accurate shower position and direction.

A technique is developed in this work for characterizing and quantifying the amount of light released into the ice by the high-energy muons. The photon field is sampled by the AMANDA detector's optical modules, and fit to an expected form. The amount of light is parametrized by the average measured amplitude at a fixed distance from the muons' track (a parameter called $K50$), which is proportional to the muon energy loss in the ice.

Combining the information from the two detectors (muons from AMANDA, and electrons from SPASE), the energy and mass of the cosmic ray primary can be measured. Experimental data from 1998 have been reconstructed in this way, and by comparing the data to simulations of proton and iron cosmic ray primaries, the average log mass $\langle \ln A \rangle$ of cosmic rays as a function of energy has been measured between 4×10^{14} eV and 6×10^{15} eV. The mass is unchanging at $\langle \ln A \rangle = 2.0$ up to 1.2×10^{15} eV, where the mass begins to rise to $\langle \ln A \rangle = 2.8$ at 6×10^{15} eV.

Acknowledgments

A list of all the people who deserve acknowledgment would be too much of a burden on this document's already-bursting page count. The author list of the AMANDA Collaboration alone is over 100 names long, and this experiment would not exist without their hard work. But I must thank in particular all those in AMANDA who have taken an interest in my project and given me useful suggestions and encouragement, particularly Ped Miočinović, Marek Kowalski, Paolo Desiati, and Till Neunhöffer.

This project in particular would not exist, of course, without the SPASE Collaboration as well. The "SPASE cases" at the Bartol Research Institute and the University of Leeds (Katie Rochester, Tom Gaisser, Xinhua Bai, Glenn Spiczak, Todor Stanev, and Ralph Engel) have all shared their data, expertise, and CPU with me a great deal over the past three years. I also owe them for their hospitality in Delaware and that charming little lab area on the third floor of Sharp Lab.

Meanwhile, back in Madison, the "wamanda" group has always given me family-like support. I must thank especially Francis Halzen for realigning my perspective on things every once in a while, Gary Hill for keeping me vigilant in times of *ennui*, Rellen Hardtke for always providing the voice of reason when it is most desperately needed, and Ty DeYoung for being my model of everything an AMANDA grad student should be and convincing me that joining this group would not be a horrible idea.

I would still be waiting for the final results of this thesis, were it not for the "VAX Extraction Team" of Dan McCammon, Darryn Schneider, Kyle Mandli, and Kevin Rhodes, who worked swiftly and diligently in my hour of need to rescue the SPASE data from its prison of VAX tapes. My last chapter would have been speculation without them.

With all my heart I thank my parents Jody Ames and Eric Rawlins for their encouragement

since the age of zero, and all the mentors and teachers who have fanned the fire over the years, such as Tucker Hiatt, Frank Firk, Peter Parker, and Julianne Moses.

I would like to thank some of the good friends who have kept me stable through difficult times: Steve Deiker for all his advice on how to survive graduate school, Rob Atkins "the only other person in Wisconsin who cares about cosmic ray composition," Brian Schwartz for motivating me to win our bet, and my greatest friend D.J. Pisano for taking that first Tech A lesson with me and for having shared in just about everything that I find meaningful for nine years.

And most of all I must thank my advisor Albrecht Karle for taking a chance, believing in me, guiding me through my struggles with patience, tolerating my attitude with good humor, and setting my life on a very interesting course.

Contents

List of Tables

List of Figures

Chapter 1

Introduction to Cosmic Rays

1.1 Why cosmic rays?

In the early 1910's, Victor Hess studied the mysterious discharging of electroscopes on balloons as a function of altitude, discovering an unforeseen source of radiation coming from the sky. These cosmic rays have perplexed physicists ever since. Now known to include protons, atomic nuclei, electrons, positrons, and photons, cosmic rays rain down upon Earth's atmosphere from all directions. They are a radiation hazard to astronauts and Concorde flight attendants. Detectors both in space and on the ground have tried to determine their nature and origin.

Astroparticle physics in general and cosmic ray physics in particular offer a unique astronomical window on this curious high-energy corner of the universe. In addition, it is becoming an important tool for high-energy physics. While human-built accelerators are reaching a point of diminishing returns in size and energy, cosmic rays arriving at Earth are the most energetic particles ever measured, with energies of up to 3×10^{20} eV [31].

However, as in neutrino astronomy, what makes the study exciting is often the same thing that makes it difficult. As cosmic ray energies rise through the realm of supernova blast waves and into strange new phenomena, our knowledge and understanding of cross-sections and energy loss physics begins to dwindle. Finding a mechanism which can generate these energies poses a challenge to both astronomy and particle physics. Measuring them at all (or at all well) poses an equally daunting challenge to designers of experiments. Without direct accelerator data to compare to, cosmic ray

physics depends heavily on extrapolations, modeling, and assumptions.

1.2 The energy spectrum

The most striking feature of cosmic rays is their falling power-law energy spectrum, measured by many experiments using both direct and indirect techniques (see Figure 1.1). The spectrum is well-described by the power-law equation

$$dN/dE \propto E^{-\alpha}$$

where the spectral power index α is a subject of much discussion and excitement. This spectral index stays remarkably constant at $\alpha = 2.7$ across a huge range of energies, from a GeV up to a PeV. At around 3 PeV (a point known as the "knee"), the power-law slope steepens to $\alpha = 3.0$. Beyond the knee, at even higher energies, are still more puzzling features; in particular, the spectrum flattens again at energies of around 10^{19} eV, in a feature known as the "ankle."

1.3 Composition

At low energies where fluxes of cosmic ways are high, experiments can be flown in space or high in the atmosphere on balloons to identify the different particles in the cosmic ray zoo with precision. In this regime there are plenty of clues to the mystery. The ratio of different elements known to be secondary and primary (for instance, B/C or sub-Fe/Fe) can be used to estimate the amount of matter that cosmic rays have traversed on their way here [10]. Proportions of radioactive isotopes present in cosmic rays is an indication of how long ago they were produced [10]. Some experiments can identify electrons and positrons in the cosmic rays, others search for "ultraheavy" nuclei. Such techniques have provided a wealth of valuable information for solving the puzzle, but only up to energies of GeV per nucleon (see [13] for a review of some of these measurements).

The highest-energy direct measurements of cosmic rays are balloon-borne experiments such as SOKOL, JACEE, and RUNJOB. At hundreds of TeV, cosmic rays are dominated by protons and nuclei (electrons and positrons having disappeared due to inverse-Compton scattering off of the 2.7° microwave background). These instruments can distinguish between nuclei (protons, helium, CNO, Mg-group, and iron) up to about 10^{14} eV. At 10^{15} eV, however, the flux of particles has

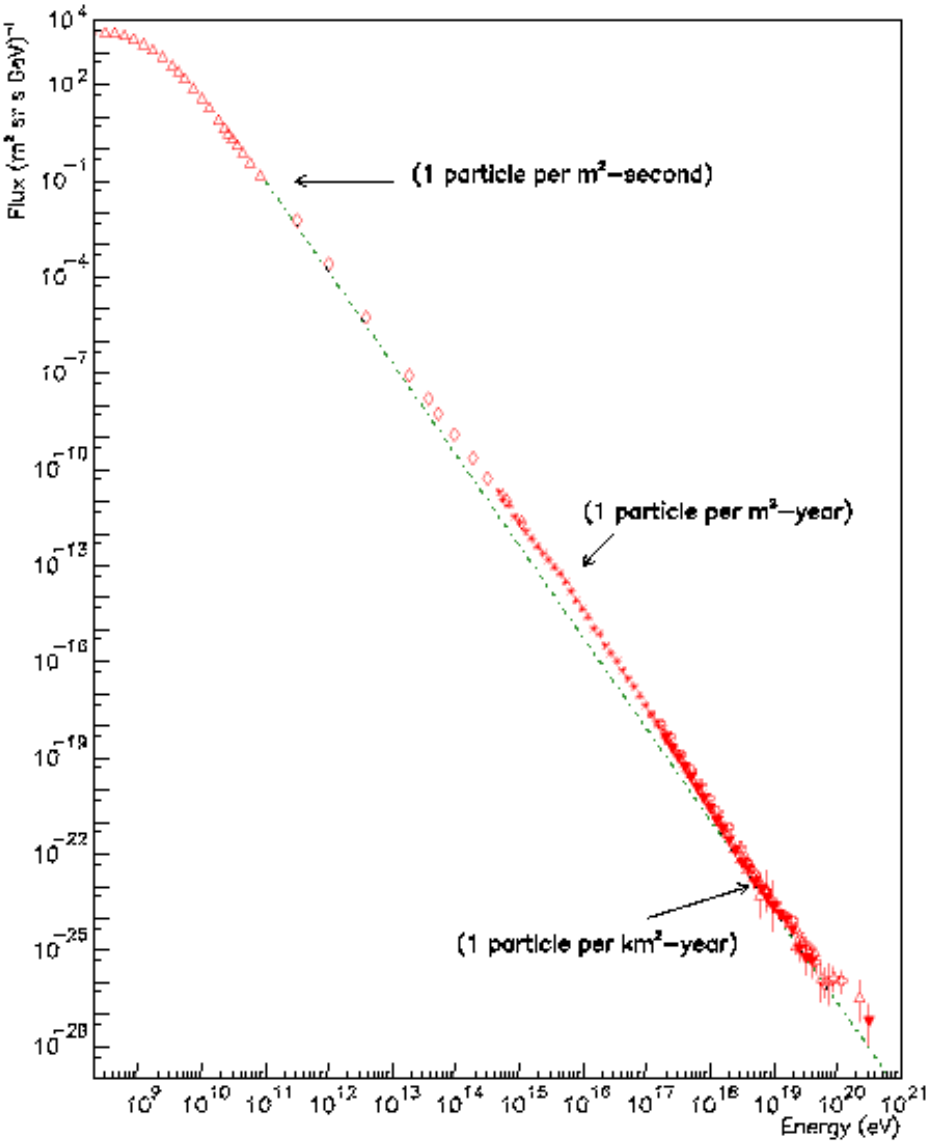

Figure 1.1: Energy spectrum of cosmic rays, from [7].

fallen to one particle per m^2 per year, far too low for even a satellite-borne instrument to collect significant statistics. We must turn instead to large ground-based detectors, which can indirectly measure properties of the cosmic rays by observing the extensive air showers that they produce in our atmosphere. To understand data from these experiments, we rely heavily on theoretical modeling of these air showers.

1.4 Extensive air showers

When a cosmic ray primary particle enters Earth's atmosphere, it interacts with a nucleus (most likely nitrogen) and produces a cascade of particles known as an air shower. This first interaction of the primary occurs at a depth in the atmosphere characterized by its interaction length $\lambda \propto 1/\sigma$ where σ is the cross section for the interaction.

The products of the first interaction include secondary hadrons (smaller nuclei) and charged and neutral pions (and also kaons if the primary energy is high enough). The neutral pions decay to two gamma rays, which then produce e^+, e^- pairs in an electromagnetic cascade:

$$\begin{aligned} \pi^0 &\rightarrow \gamma + \gamma \\ &\qquad \hookrightarrow e^+ + e^-. \end{aligned}$$

Meanwhile, hadrons interact with other particles and disintegrate into smaller nuclei. The charged pions and kaons decay to muons and neutrinos:

$$\pi^{\pm} \rightarrow \mu^{\pm} + \nu_{\mu} \quad (\text{or } \overline{\nu}_{\mu})$$

The neutrinos escape detectors' further notice, while the muons reach the surface only if they do not decay *en route*.

Throughout the shower, the balance of particles is determined by the changing probabilities for interaction or decay. At the beginning of the shower, secondary nucleons and electrons have high energies, particle interaction rates are high, and the total number of particles is increasing. As the particles lose energy, however, they drop below thresholds for further particle production, and the shower begins to thin out. In between these two phases of the shower is "shower max," the point at which the particle count reaches its maximum.

There are three components, then, that can be measured at the ground: the electromagnetic

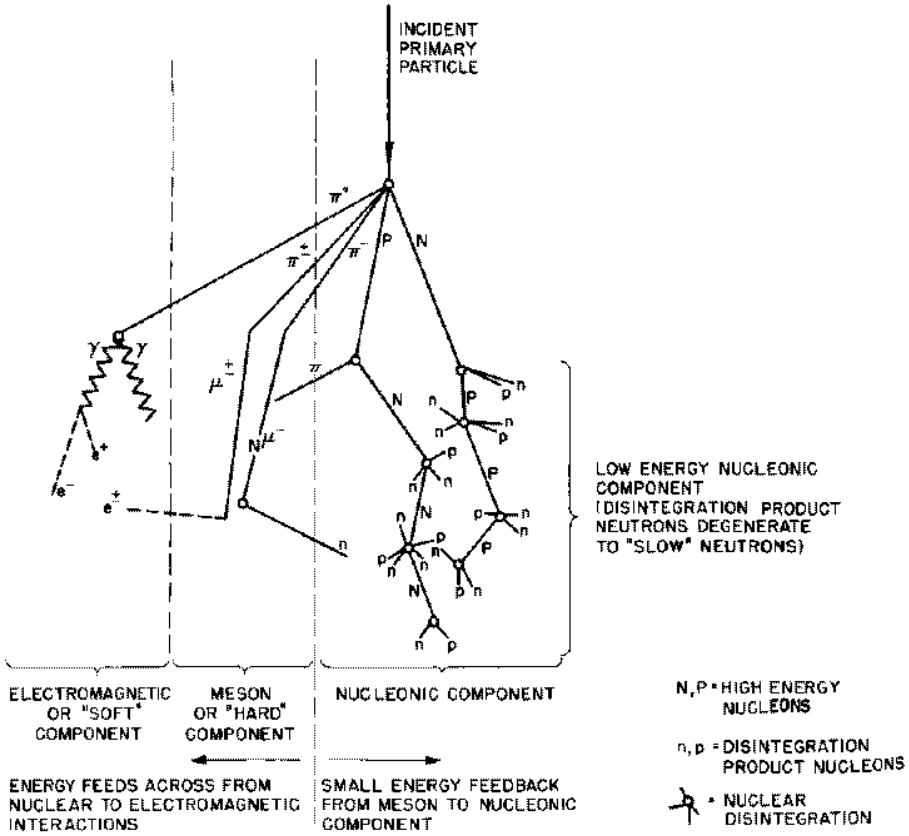

Schematic Diagram of Cosmic Ray Shower

Figure 1.2: An extensive air shower and its different components, from [9].

component (photons and electrons), the hadronic component, and the muonic component[1]. Figure 1.2 summarizes these components. A 1 PeV proton primary will produce on average 80% photons, 18% electrons, 1.7% muons, and 0.3% hadrons at sea level [10].

1.5 Air shower detectors

Ground (or underground) detectors for air showers come in as many varieties as there are particles to detect, if not more. Some of the common techniques include:

- Scintillators, which detect the passage of charged particles through a scintillating medium. They are primarily used to detect the electromagnetic component, but if shielded with lead (or buried deep underground, as in MACRO and Soudan-2) they can also be used to detect muons.
- Air Cherenkov telescopes, which detect Cherenkov light from relativistic charged particles in the medium of the atmosphere.
- Ionization chambers, which detect hadrons.
- Atmospheric fluorescence detectors, which detect the fluorescence emission from N_2 molecules excited by the air shower particles.
- Water/ice Cherenkov telescopes, which detect Cherenkov light from relativistic muons passing through ice or water.

Having such a variety of detection methods is very important. Since any one experiment can fall victim to unknown systematic effects or incorrect modeling, cross-checking between fundamentally different measurement techniques can help reassure us that we are on the right track. Furthermore, employing multiparticle measurements within one detector (or operating multiple detectors in coincidence) is a powerful tool for disentangling all the interdependences which can confuse an analysis.

1.6 Observations and data at the knee

Many experiments, based on the different detection techniques described above, have explored cosmic rays in the knee region. The knee itself (the change in power spectrum index) has been

[1]Technically speaking, of course, one can also measure the neutrino component with a detector on the other side of the Earth, as is done with AMANDA [77] and other underground detectors.

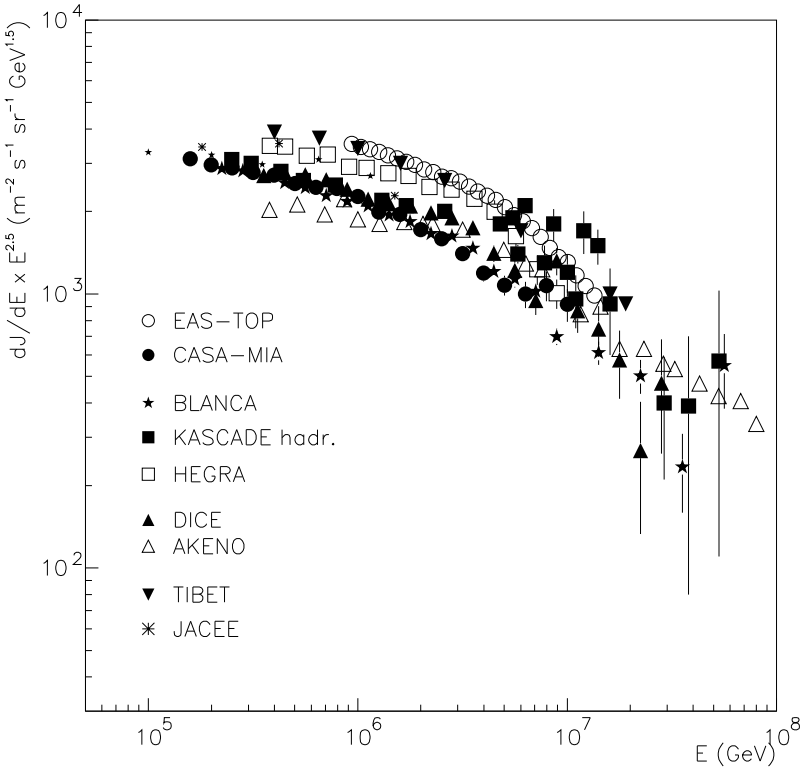

Figure 1.3: All-particle energy spectrum, in the region of the knee, from [1].

observed by all experiments with sensitivity in this region, whether they detect the electromagnetic component, muon component, or hadron component of the showers, as shown in Figure 1.3.

Figure 1.4 sets the stage for our discussion of cosmic ray mass composition. At 100 TeV to 1 PeV, direct measurements are still possible but statistics are scarce and error bars are large. At these same energies, air shower experiments become sensitive. Lacking the ability to directly measure cosmic ray mass on an event-by-event basis, air shower detectors must use indirect techniques to measure the composition of the cosmic rays, which will be discussed in more detail in Chapter 3. These methods are highly model-dependent, making the absolute proportions of the various nuclei very difficult to measure reliably.

Many experiments therefore choose rather to emphasize *changes* in composition (the upward

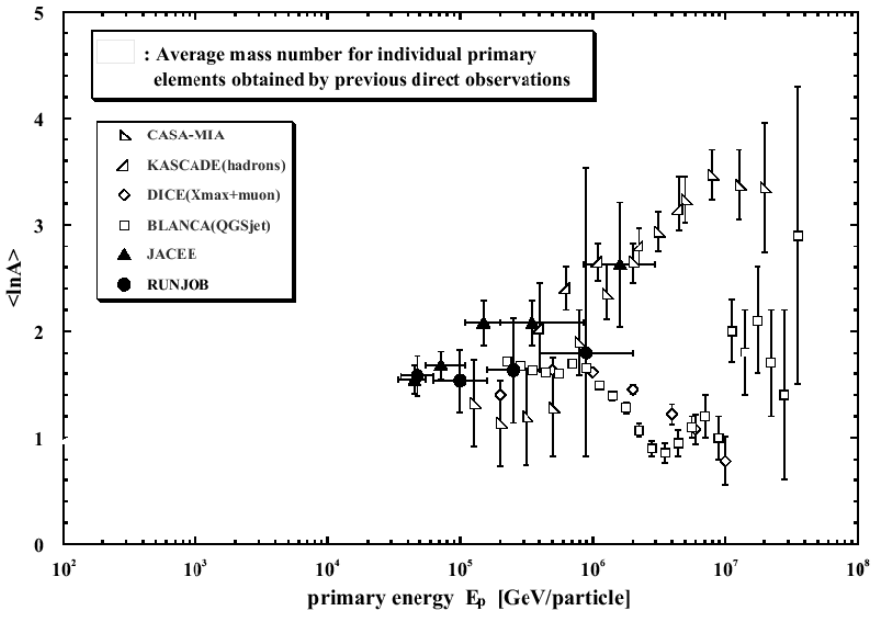

Figure 1.4: Mean log mass ($\ln A$) as a function of energy, in the region of the knee, from [30].

or downward trend of some mass estimator), which is a more robust measurement. But even then, as one can see in Figure 1.4, past 1 PeV the results of different experiments begin to diverge and disagree. Although many experiments favor *heavier* nuclei with increasing energy, a handful of them (most notably DICE) find the nuclei getting *lighter*[2]. CASA/BLANCA data shows the composition getting first lighter and then heavier through the knee region. So do cosmic rays get lighter (more "proton-like") or heavier (more "iron-like") with energy? The question must still be considered open; in this work, the SPASE and AMANDA detectors will weigh in.

[2]The DICE experiment recently announced updated composition results, in which certain systematic effects in their detector were taken into account. After the systematics correction, the lightward-sloping result shown here is now flatter (more consistent with zero composition change) [59].

Chapter 2

Cosmic Ray Acceleration and Propagation

2.1 A likely mechanism: Fermi Acceleration

"Fermi Acceleration," first proposed in 1949 [15], is a model of particle acceleration in a diffusive medium containing shock fronts.[1] Fermi's original paper proposed what is now called "second-order Fermi acceleration," in which a particle is afloat in a sea of shocks or disturbances moving in random directions off which it can scatter (in particular, Fermi imagined "magnetized clouds"). The particle encounters a shock head-on (which boosts its energy) more often than a shock from behind (which drains its energy). After many successive shocks from randomized directions, the particle will have gained more energy than it will have lost, leaving it with a net acceleration. Although a promising candidate for an acceleration mechanism for cosmic rays, this theory was found to be too "slow" to explain them.

However, under different conditions a similar idea (involving shocks and diffusion) offers a compelling solution to the cosmic ray acceleration problem, and is now the most favored model. Called "first-order Fermi acceleration" or "diffusive shock acceleration," this model has been approached from several different angles [17, 18] which all give the same basic answer. The principle is best visualized as single shock front with a particle crossing back and forth across it.

The shock wave itself can be thought of as a discontinuity in velocity between two plasmas, one upstream with a velocity U_1, and the other downstream with slower velocity U_2 (see Figure 2.1). In this description, the discontinuity itself is at rest. Alternatively, one can consider the upstream

[1] Good reviews of cosmic ray acceleration theory include Drury [11], Gaisser [2] and Chapter 21 of Longair [3].

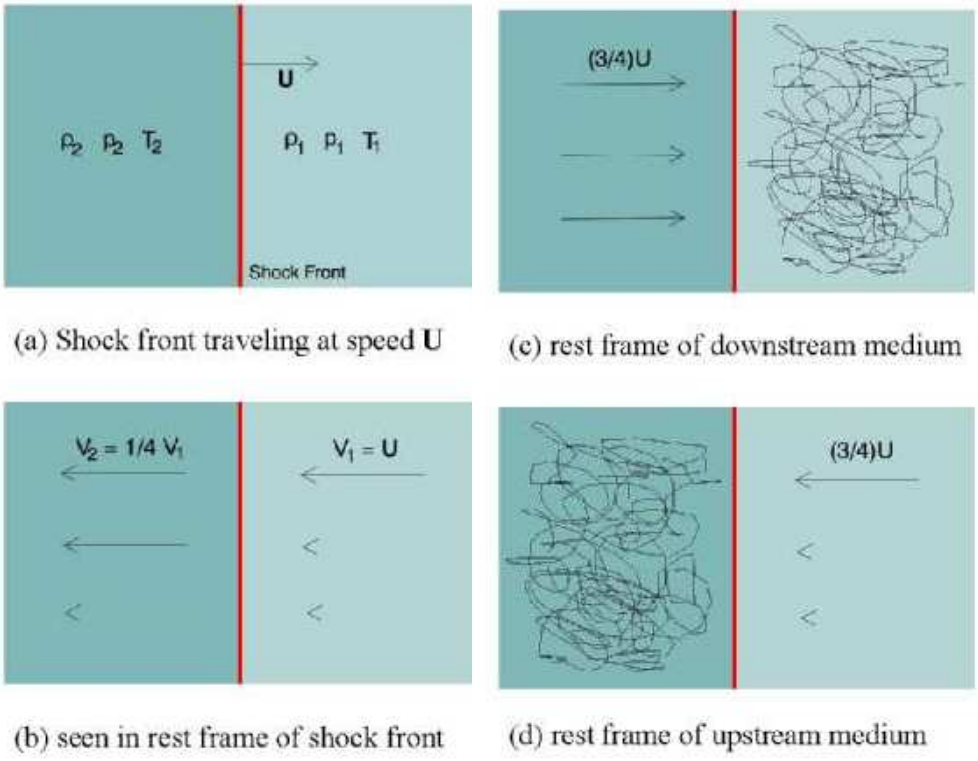

Figure 2.1: First-order Fermi mechanism diagrams, from [3].

material to be at rest. In this picture, the shock and the material downstream of it (the interstellar medium into which the shock is spreading), have a velocity $U_1 - U_2 = U$.

A particle in either of these plasmas scatters off of the magnetic structures and disturbances in the plasma. It diffuses through the plasma (with a characteristic diffusion constant κ) and is eventually isotropized in direction. If the particle's motion does not itself influence the magnetohydrodynamics of the plasma, then it is called a "test particle" and many simplifications can be made. For one thing, the ratio of the velocities U_2/U_1 (also called the "compression ratio" r) is determined by the ratio of specific heats γ of the two plasmas (for an ideal ionized gas, $\gamma = 5/3$):

$$r = U_2/U_1 = (\gamma + 1)/(\gamma - 1) = 4$$

If a particle with speed v crosses the shock front at an incident angle θ (either upstream $\rightarrow$ downstream or downstream $\rightarrow$ upstream), it will appear in the rest frame of its destination region

to have gained momentum, equal to [11]:

$$\frac{\Delta p}{p} = \frac{U_1 - U_2}{v}\cos\theta = \frac{U}{v}\cos\theta$$

Averaging over angles θ, this yields

$$\frac{\langle \Delta p \rangle}{p} = \frac{4}{3}\left(\frac{U_1 - U_2}{v}\right) = \frac{4}{3}\frac{U}{v} = \xi$$

for each *pair* of crossings (back and forth across the shock). Since particle directions are isotropized on either side of the shock, a particle is likely to make repeated shock front crossings and thus gain energy repeatedly. Unlike the second-order Fermi process with its randomized shock directions, this process is first-order in U and is often likened to the acceleration of a ball bouncing between two walls moving toward each other. The process continues until the particle escapes from the shock environment. Thus the distribution of energies of the particles depends on the balance between the acceleration timescale and the escape timescale.

A particle in the upstream region cannot escape, but during the time it spends in the downstream region, the probability of escape is given by [11]:

$$P_{esc} = 4U_2/v$$

If the process is left to continue for a long time, *and* if we assume that the system is in a steady state, then we can compute the momentum (or energy) spectrum of the particles. After n cycles back and forth across the shock, a particle of initial energy E_0 now has $E = E_0(1+\xi)^n$, while the probability of not escaping during those n crossings is $(1 - P_{esc})^n$. The number of particles which are successfully accelerated to energy E can be solved for[2]:

$$N(>E) \propto (E/E_0)^{-\gamma} \quad \text{where} \quad \gamma \approx P_{esc}/\xi = \frac{3U_2}{U_1 - U_2}$$

Turning this into a differential distribution yields:

$$dN/dE \propto E^{-(1+\gamma)}$$

The resulting accelerated particles follow a power-law energy spectrum. This makes the theory an appealing explanation for many astrophysical phenomena. Non-thermal particles obeying power-law spectra abound in the universe, especially in locations where one might expect shock fronts; the

[2]See [2], [3] for details of the derivation.

bow shock of the Earth (or of other planets) as it passes through the solar wind is a well-known example within our own Solar System where non-thermal particles are observed. Further out in the universe, non-thermal particles are seen in stellar wind termination shocks, supernova remnants, and other shocked environments.

This formulation (with $r = 4$) predicts $\gamma = 1$, leading to a cosmic ray spectral index of -2. This is the spectrum of the particles at the site of their acceleration; the particles must then be propagated through the Galaxy to the Earth. Since the rate at which cosmic rays escape from the Galaxy increases with cosmic ray energy, the underlying energy spectrum at the *source* (the "injected" spectrum) must be flatter than the spectrum observed at Earth:

$$I(E)_{Earth} = I(E)_{source}\lambda(E)$$

The mean escape column density, λ, goes as $E^{-0.6}$ [16] (this is observed from the primary to secondary ratio as a function of energy). So the theory predicts a cosmic ray spectrum *at the Earth* with an index of -2.6, which is very close to the measured index of -2.7.

Modifications of the basic theory can change the index; γ is generally parametrized as $1 + \epsilon$, where ϵ is a small correction. For instance, adding confinement of particles near the shock by Alfvén waves steepens the spectrum. Weakening the shock (reducing the compression ratio to $r < 4$) [12], or adding synchrotron losses during the acceleration also steepen the spectrum. Lifting the "test particle" condition and allowing the accelerated particles themselves to exert pressure on the system flattens the spectrum. More accurate magnetohydrodynamics (including non-linear effects, sphericity of shock waves, etc.) have been studied in detail by a variety of theorists, but the simple picture allows us to make order-of-magnitude estimates of many of the expected properties of cosmic rays.

2.2 A likely origin: within the Galaxy

Cosmic rays arrive isotropically at Earth (aside from a small dipole anisotropy which is consistent with the effect of the Solar System's motion through the interstellar medium [11]) to within a few parts in 10^4 at 100 GeV [16]. But this is expected, as the trajectory of any charged particle traveling through the Galaxy's magnetic field B will be bent with a gyroradius equal to $r_g = p/ZeB \approx E(10^{15}eV)/ZB(\mu G)$ (for a radius in parsecs). For protons of energy 10^{15} eV, mov-

ing through a galactic magnetic field of 2 μG, this radius is half a parsec, much smaller than the Galaxy itself. Thus the galactic magnetic field contains the cosmic ray particles and isotropizes their directions.

At low energies, the relative abundances of different nuclei provide important clues to cosmic ray origin. Lithium, beryllium, boron, sub-Fe nuclei, and ^{3}He, are all more abundant in cosmic rays than in the Solar System. These elements can be produced by the fragmentation of a heavier nucleus when it collides with interstellar matter, a process called spallation. Common source elements produce rarer secondaries: Li, Be, and B are produced from spallation of C, sub-Fe elements from Fe, and ^{3}He from ^{4}He. The abundance of secondary nuclei relative to primary nuclei measures the amount of material along the cosmic ray's journey from source to Earth; the more material along its path, the more spallation and the greater the ratio between secondary and primary abundances. From measuring and modeling these relative abundances, we know that the path length of light cosmic ray particles through the medium they travel through is $\approx$ 80 kg m^{-2} at a few GeV [11] (depending on energy, as discussed above).

Meanwhile, radioactive isotopes provide a measure of cosmic ray age, how long they have been traveling. ^{10}Be makes a good clock, with a half-life of about 3×10^6 years. Its abundance relative to more stable nuclei indicates an age for cosmic rays of about 20×10^6 years [16]. Putting the two pieces of information together and using the relation $\lambda = \rho v t_{age}$, we can compute the average density ρ of the medium through which cosmic rays travel: about 0.3 atoms/cm^3 [34], and conclude that these cosmic rays are confined to the Galactic disk (where $\rho \approx 1$ atom/cm^3) and halo (which is less dense) for their entire lifetime.

2.3 A likely source at the knee: supernova shocks

A supernova produces a total of $10^{50} - 10^{52}$ ergs. 90% of this energy is released in the form of neutrinos, so at most 10% can be considered available to accelerate cosmic rays. The rate of supernovae is something on the order of 1-10 per galaxy per century (or about 10^{-9} supernovae/sec). So the total power available for the acceleration of cosmic rays in our own galaxy is $E_{sn}R_{sn} \approx 10^{40} - 10^{42}$ ergs/s. Meanwhile, from the spectrum and intensity of cosmic rays we can compute the total power required to sustain the cosmic ray population in a steady state: it equals the energy

density of the particles (1 eV/cm^3) times the volume of the Galaxy (about 10^{11} pc^3) divided by the lifetime of the particles (2×10^7 years), which equals about 10^{40} ergs/s. The coincidence in numbers suggests that supernova shock waves make a good candidate for the accelerators of cosmic rays.

The model is far from confirmed, and plenty of details are still left to explain. A shock moving through the normal interstellar medium cannot reach energies beyond the knee, but a shock expanding into an already energetic environment (such as the hot stellar wind of the progenitor star or a Wolf-Rayet star [20, 21, 22]) could bridge the gap in energy between the knee and the ankle. An alternative theory proposes that the Galactic cosmic rays disappear at the knee and an extragalactic source takes over: for instance accelerated protons from accretion disks of active galactic nuclei (AGN) [23].

2.4 Maximum energy of the Fermi mechanism

Since the Fermi mechanism for acceleration is gradual over many cycles across the shock, acceleration must be able to compete with energy loss. Furthermore, a shock environment (such as a supernova) has a finite age and therefore a finite time in which particles that we observe could be accelerated. These considerations lead to a natural cutoff energy for Fermi-accelerated particles. Acceleration will stop when the acceleration timescale t_{accel} exceeds the age of the shock.

The acceleration timescale is determined by the diffusion constant of the plasma, κ and the speed of the shock U and is roughly $t_{accel} \propto \kappa/U^2$ [11]. But the length scale on which a particle diffuses in a magnetic environment ($= \kappa/v$) is on the order of its gyroradius. For maximum efficiency, $\kappa = (1/3) r_g v$. In other words, for particles with a given energy, heavier nuclei have smaller gyroradii and are easier to accelerate quickly. But the acceleration timescale increases with energy as particles become harder to deflect or scatter.

Thus, if the acceleration is limited by the age of the shock (equal to R/U where R is the radius of the acceleration region and U is the shock velocity[3]), then:

$$t_{age} = t_{accel}$$

[3]Supernova shocks have a more complicated relation between age and size, but to keep the theory general we will make this estimate.

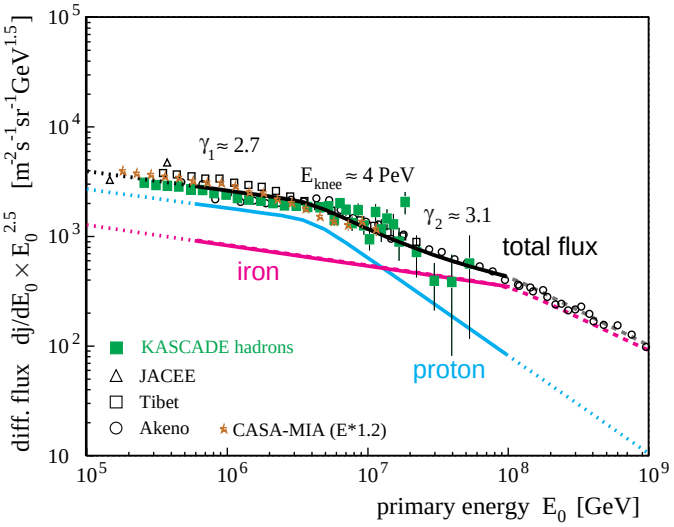

Figure 2.2: Simulation of the knee in protons and iron separately (with some data too),from [10].

$$R/U = \kappa/U^2$$

$$R = \kappa/U \propto r_g v/U = \left(\frac{p}{ZeB}\right)\frac{v}{U} = \frac{E}{ZeB}\frac{1}{U}$$

$$E_{max} \propto RZeBU$$

One can arrive at the same answer by requiring that the diffusion length scale be smaller than the acceleration region, or (as is true of accelerators in general) that the gyroradius of the particles be less than the size of the accelerator. In this sense the energy cutoff is a general feature of accelerators.

For a typical β of a supernova shock $= 0.01$ [11] and a typical radius R of a supernova shock region $= 3 \times 10^{17}$ meters, a proton's E_{max} comes to 10^{14} eV, just below the knee. But the acceleration limit for different elements should occur at a constant rigidity pc/Ze. In other words, there should be a knee in the proton spectrum first, and in the iron spectrum later. Composition-sensitive experiments should therefore observe an increase in the proportion of heavy elements in the cosmic ray spectrum as we pass the knee and protons are being drained from the spectrum (see Figure 2.2).

2.5 The leaky box model

The observed knee could reflect a spectrum change at the source, as discussed above, or alternatively it could be due to a change in propagation behavior of cosmic rays. The confinement and escape of cosmic ray particles can be primitively described by a "leaky box" model. In this model, particles diffuse freely within some volume, and are reflected at its boundaries but with some probability of escape from the volume at each reflection. As a result, the degree of confinement of cosmic rays depends on the rigidity pc/Ze. Iron, with its smaller gyroradius, is more confined by magnetic fields; therefore it leaks out of the Galaxy less easily. Like the Fermi maximum energy model discussed above, the leaky box model predicts a spectral cutoff for each particle at a fixed rigidity. Protons would disappear first and iron last, with the composition getting heavier through the knee.

2.6 Physics at the ankle

If the physics of the knee is a mystery, then the physics in the "ankle" region of the cosmic ray spectrum ($10^{19} - 10^{21}$ eV) is an even deeper mystery. The highest energy particle measured to date has an energy of around 3×10^{20} eV [31]. This is equal to about 50 Joules, or the energy of a tennis ball moving at 100 km/hr [5]. At the energies of the ankle, detectors must be kilometers in size to catch even a handful of events. The ankle structure raises questions: what are the cosmic rays composed of, and why does the energy spectrum change again? But the most difficult question is, how is it possible that these particles are here at all?

As cosmic rays reach an energy of about 6×10^{19} eV, they are likely to interact with the ambient low-energy photons of the Cosmic Microwave Background. These interactions produce pions[4] via:

$$p + \gamma \rightarrow n + \pi^+$$

$$p + \gamma \rightarrow p + \pi^0$$

and the cosmic ray has been sapped of its energy. This effect (called the Greisen-Zatsepin-Kuzmin or GZK cutoff [14]) is expected to drain the cosmic ray energy spectrum of events above about

[4]Pair production is another possible result of this interaction, with a lower energy threshold and smaller path length. However, the energy loss is not as catastrophic as for pion production and so it is not as important for energy cutoff considerations [5].

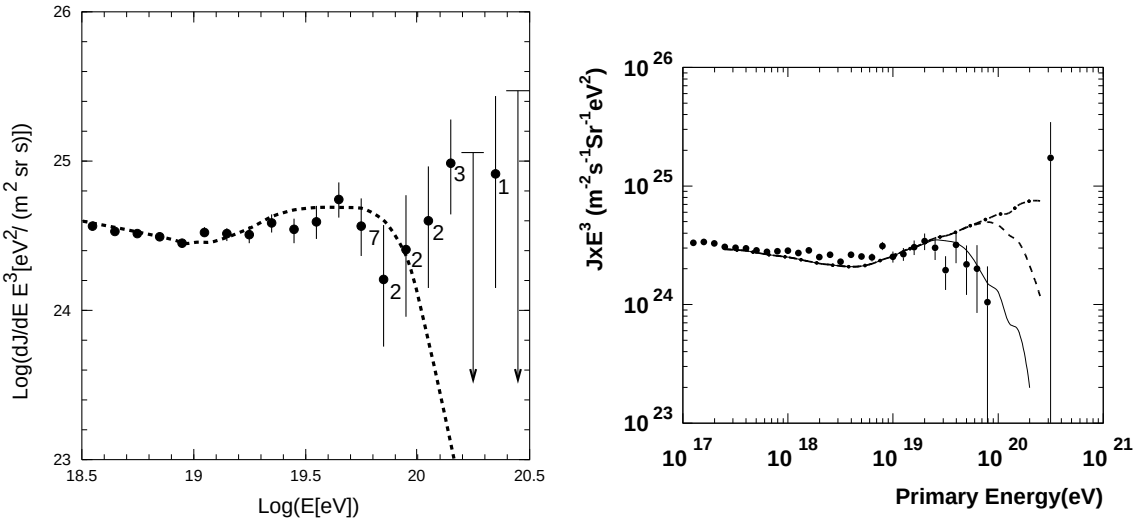

(a) AGASA energy spectrum

(b) HiRes (monocular) energy spectrum

Figure 2.3: Energy spectra in the region of the ankle, according to two detectors, both figures taken from [7].

6×10^{19} eV if they are uniformly distributed in the Universe (see Figure 2.3). Their detection at Earth constrains their distance to be within 100 Mpc [7].

Collectively from the Volcano Ranch, Haverah Park, Yakutsk, AGASA, and Fly's Eye experiments, there are about 20 events recorded beyond this cutoff [55], however new results from HiRes [52, 54] suggest that the spectrum does in fact show a cutoff at the expected energy. The contradictory results (from detectors with completely different detection principles) demonstrate the vulnerability of these experiments to systematics, and motivate the construction of hybrid detectors capable of detailed cross-checking.

The gyroradius of a 10^{19} eV proton (rather than a 10^{15} eV one) in the galactic magnetic field is about 5 kpc, larger than the disk of the Galaxy. The intergalactic magnetic field is two orders of magnitude weaker than the galactic field, so cosmic rays are not deflected there. Therefore they have not been isotropized, and an experiment should be able to trace them back to their source or at least detect anisotropies in their arrival directions. Searches for anisotropy have been made using the handful of events that have been detected, and results are again mixed; AGASA, which claims

17 events above 10^{20} eV, also claims to see significant anisotropy in the directions of the Galactic center and anticenter [56, 57]. HiRes, which has fewer events but claims a larger aperture to high energies, sees no anisotropy [53].

2.7 Proposed mechanisms at the ankle

Coming up with an acceleration mechanism for 10^{20} eV particles is difficult. The maximum energy that a particle can attain via the Fermi acceleration mechanism is $E = kZeBRU$ as shown earlier, where B is the magnetic field in the shock region, R is the size of the shock region, U is the velocity of the shocks themselves, and k is an efficiency factor which is always less than one. Even under optimal conditions ($k = 1$ and $\beta = 1$) it takes either a formidable magnetic field *or* a huge volume to accelerate a proton up to 10^{20} eV. Supernova shocks, although powerful accelerators, simply cannot do the job.

There are many proposals for alternative accelerators for ultra-high-energy cosmic rays. Hot spots in the lobes of radio galaxies such as M87 (termination shocks of relativistic jets) are candidates for pushing the Fermi mechanism to its limits (see Figure 2.4). But since they are extragalactic objects, the GZK problem is left unexplained unless the bulk of cosmic rays that we observe are coming from a handful of powerful sources in our local neighborhood. The termination shock of the Galactic wind is another candidate [25].

Another possibility is "direct" acceleration rather than statistical (that is, a one-shot acceleration by a colossal EMF rather than the gradual acceleration of the Fermi mechanism). The surface of a rapidly rotating neutron star could provide such an acceleration [24]. In this model, acceleration need not compete with energy loss mechanisms which plague the slower Fermi process. In addition, the sources can be Galactic and avoid the GZK dilemma. However, this acceleration mechanism also has a maximum energy cutoff; for an EMF generated by a magnetic field B moving at a velocity U, the maximum potential is RUB, and the maximum energy then is $RUBZe$, coincidentally the same as for slow acceleration [11].

As an alternative, some suggest that the highest energy cosmic rays are produced more locally, by the decay or interaction of some other particle which can traverse the Universe uninhibited by the Cosmic Microwave Background. Ultra high energy neutrinos, for instance, colliding with relic

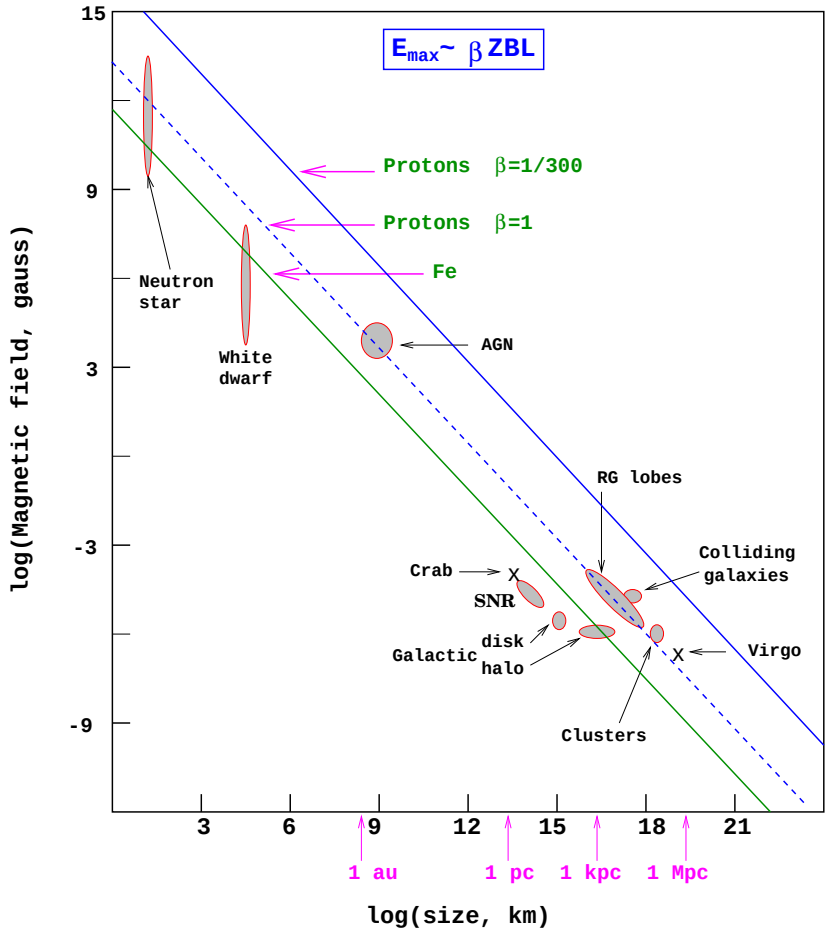

Figure 2.4: Maximum energies reached by various objects, and what is necessary to produce cosmic rays, from [7] (but based on [4]).

neutrinos at the Z resonance could produce high-energy protons [26]. Others suggest instead that the decay of some very massive and as-yet undiscovered particle beyond the Standard Model is responsible for events beyond the ankle. Candidates include topological defects, strings, monopoles, and other strange objects [27, 7], all of which are beyond the scope of this thesis.

2.8 The relevance of composition

Different theories lead to different predictions for the mass composition of the cosmic rays at the knee. Constant-rigidity cutoff models predict an increase in average mass in the knee region as protons first disappear. Accretion onto the black hole of an AGN, on the other hand, predicts that protons should begin to dominate in the knee region, because heavier nuclei cannot survive the photon fields of the dense central region without being broken up by pion photoproduction [23]. Measuring the composition of these particles will be crucial for deciding between the competing theories.

Chapter 3

Separation of protons and iron

3.1 Air shower observables

Past 10^{14} eV, we cannot directly measure the primary nucleus and must rely on extensive air showers. Therefore, to distinguish between different primary compositions, one must find an *observable* of the air shower which depends on the primary mass.

The difference between proton and iron showers can be qualitatively understood by considering a nucleus of mass A to be approximately a superposition of A proton primaries all arriving at once. For a given total energy E, each nucleon has an energy E/A. In other words, a proton has all of its energy wrapped up in one particle, while the energy of an iron nucleus has its energy distributed to 56 nucleons and into 56 smaller proton-like air showers. This phenomenon underlies many of the observable differences between proton and iron showers.

3.1.1 Depth of shower max

An important shower parameter is the "depth of shower maximum" or X_{max}. This is the depth in the atmosphere (measured in g/cm^2) at which the density of particles in the shower is the greatest.

Qualitatively, an iron primary can be approximated as 56 proton primaries all arriving at once and each with 1/56th of the total energy. So an iron primary is more likely to have its first interaction *higher* in the atmosphere. In addition, each nucleon has a fraction $1/A$ of the total energy; each of the small showers in the superposition loses energy for further particle production sooner in

its development. As a result of both these effects, heavier primaries have a smaller X_{max} than light primaries.

Quantitatively, the relation between X_{max} and the primary particle's properties is approximately [2]:

$$X_{max} = (1 - B)X_0 \left(\ln \left(\frac{E}{\epsilon} \right) - \ln A \right)$$

where ϵ is the critical energy[1] in air, X_0 is the radiation length[2] in air (37.1 g/cm^2), and B is a model-dependent fudge factor. Simulations of shower development for protons and iron are shown in Figure 3.1. Since some of the fluctuations of many superimposed proton-like showers cancel each other out and are averaged away, fluctuations in X_{max} from shower to shower also become smaller with increasing primary mass.

3.1.2 Cherenkov light

Cherenkov light is emitted by the charged particles in the air shower, overwhelmingly the electrons. There is a great deal of useful information in the lateral distribution function (LDF) of this light. In particular, one can measure X_{max} from the slope of the function (either by taking a fitted slope parameter, as is done in HEGRA [49] or the ratio of the intensity at two different distances, as is done in SPASE/VULCAN [106]. Meanwhile, the Cherenkov light intensity at a far enough distance away (around 100 meters) provides a composition-independent measure of the shower energy. Thus an array which is sensitive to both the near (X_{max}-sensitive) and far (energy-sensitive) regimes of Cherenkov light is a powerful tool for measuring composition.

Imaging Cherenkov telescopes (such as DICE [51]) can furthermore measure the light intensity as a function of altitude, a more direct measurement of X_{max} and of the evolving structure of the shower's longitudinal development.

3.1.3 Number and distribution of electrons

The electron component of air showers has been studied extensively for many years and is relatively well-understood. The lateral distribution function of the electrons has a form known as the

[1] The energy at which bremsstrahlung losses dominate over ionization.

[2] Thickness over which an electron loses $1 - 1/e$ of its energy by bremsstrahlung.

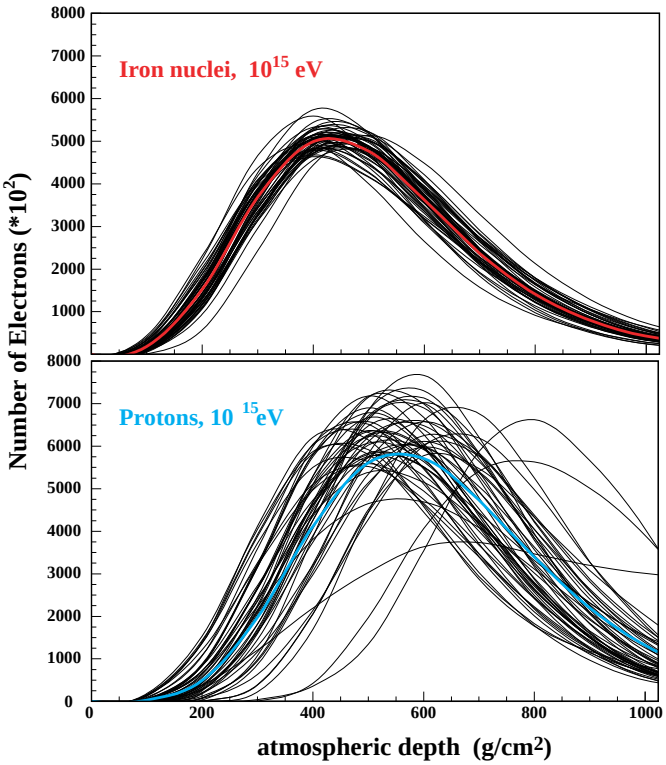

Figure 3.1: Shower development (number of electrons) as a function of atmospheric depth for many sample iron showers (upper), and proton showers (lower), according to CORSIKA/QGSJET simulations. The mean depth of shower max (X_{max}) is smaller for iron than for protons; the fluctuations between individual showers are also smaller for the heavier primary. From [10].

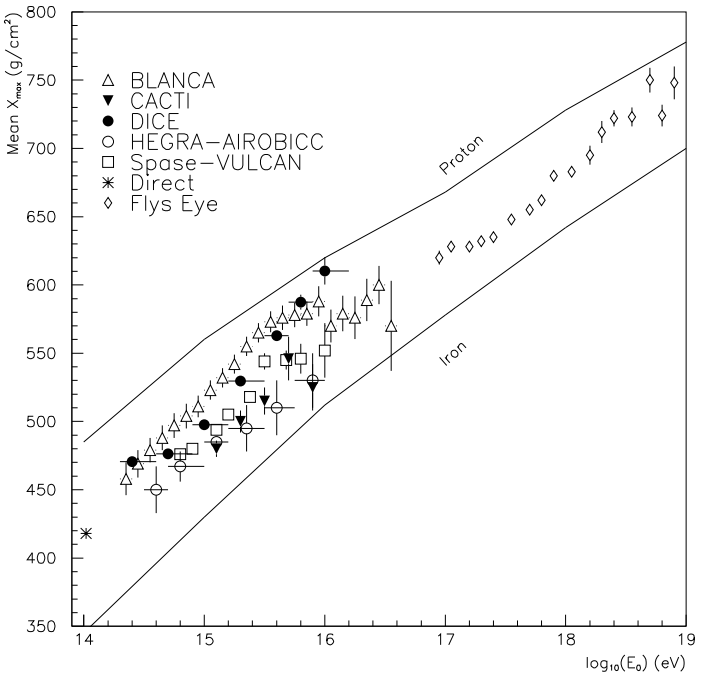

Figure 3.2: Measured X_{max} as a function of energy, in the region of the knee. Proton and iron lines represent CORSIKA/QGSJET simulations. From [1].

$S(30)$	Mean Energy (p)	Mean Energy (Fe)
5	200 TeV	400 TeV
10	350 TeV	650 TeV
20	650 TeV	1.2 PeV
30	950 TeV	1.6 PeV
50	1.4 PeV	2.4 PeV
100	2.9 PeV	4.3 PeV

Table 3.1: Mean energies of protons and iron at $S(30)$ values commonly referred to in this work.

Nishimura-Kamata-Greisen (NKG) function [19]:

$$S(r) = CN_e \left(\frac{r}{r_0}\right)^{-\alpha} \left(1 + \frac{r}{r_0}\right)^{-(\eta-\alpha)}$$

Here, $S(r)$ is the density of particles as a function of radius, N_e is the total electron count, C is a detector-dependent normalization constant, r_0 is a characteristic Moliere unit[3], and α and η are also empirically measured for each detector.

Because the behavior of the electrons is dominated by QED/electromagnetic cascade physics, this functional shape of the LDF is largely independent of energy and composition. The total number of electrons in the shower scales very nearly[4] with the energy of the primary. However the number of electrons at a ground detector N_e (or "shower size") depends not only on the energy but also on the height of interaction X_{max} and thus on the composition.

The SPASE detector, for example, measures a parameter called $S(30)$, the particle density at 30 meters from the shower core. This can be used as an energy estimator, but it is *not* a composition-independent one. The relationship between $S(30)$ and energy is plotted in Figure 3.3 for SPASE Monte Carlo simulations; protons and iron follow parallel but distinct trends.

3.1.4 Number and distribution of muons at the surface

Like the electron distribution, the muon lateral distribution function at surface level has been extensively studied and mapped out with simulations. Unlike the electron number, the muon number does strongly depend on both energy and composition. To understand this, consider again a heavy nucleus to be a superposition of A separate nucleons. For each nucleon, the smaller energy fraction

[3]Mean perpendicular distance an electron is scattered after passing through one radiation length.

[4]With a power index close to one.

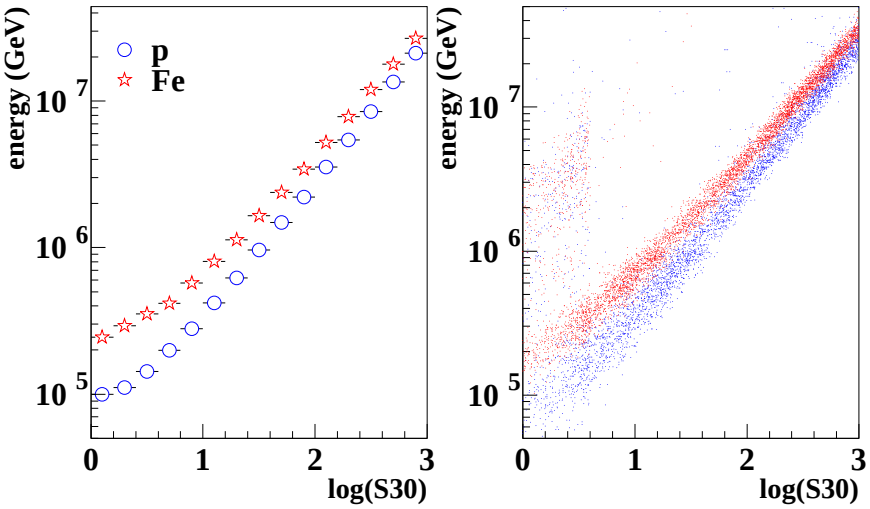

Figure 3.3: Relationship between true primary energy and SPASE's observable $S(30)$.

that it carries results in lower energies of secondary pions. Pions with lower energy are more likely to decay into muons before they interact again in the shower.

The number of muons as a function of muon energy E_μ is parametrized by the equation [2]:

$$N_\mu(> E_\mu) = A\frac{14.5 \text{ GeV}}{E_\mu \cos\theta}\left(\frac{E}{AE_\mu}\right)^{0.757}\left(1 - \frac{AE_\mu}{E}\right)^{5.25}$$

where A is the primary mass number, E is the primary energy, and θ is the zenith angle of the shower. The last term (to the 5.25 power) is usually a small correction except at very high muon energies, reflecting changes in the cross section of pion production. Simulations of this muon energy spectrum is shown in Figure 3.4. Simplifying the formula, the number of muons behaves as [5]:

$$N_\mu = kA\left(\frac{E}{A}\right)^{\alpha}$$

where α is 0.757. Iron showers produce more muons for equivalent primary energy by about a factor of two.

At extremely high energies, showers develop deep enough in the atmosphere that the path length available for the pions to decay becomes shortened. As a result, the distinction in muon

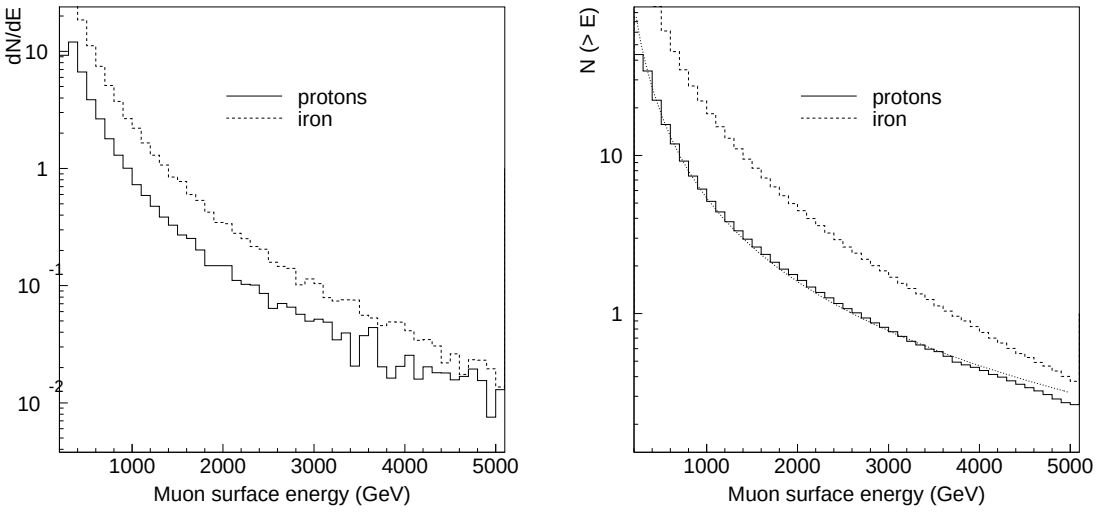

(a) Differential

(b) Integrated ($N_\mu(> E_\mu)$), with theoretical curve (dotted) for protons.

Figure 3.4: Number of muons at the surface as a function of muon energy, for primaries of $E \approx 3$ PeV.

number between protons and iron begins to blur. However, this occurs at energies higher than will be addressed in this work.

The lateral distribution function of muons at the surface looks like [43]:

$$\rho_\mu(r) = N_\mu \left(\frac{C}{R_0^2}\right) (r/R_0)^{-0.75}(1 + r/R_0)^{-2.52}$$

where R_0 is a characteristic distance. In general, the muon distribution depends sensitively on a combination of complex factors: hadronic interaction models, interaction depth, zenith angle, and atmosphere. Therefore, it is difficult to draw conclusions from this measurement alone.

3.1.5 Number and distribution of muons underground/underwater/underice

High-energy muons (that is, muons capable of reaching a detector at depth) are created by the decay of pions and kaons whose energies are still high. Thus, high-energy muons come from high in the atmosphere and can be used to probe the properties of the shower while it is still early in its development. But like the surface muons, the properties of these penetrating muons depend on hadronic processes which are not fully understood or have not been directly measured. The propagation of the muons through the rock or ice at high energies adds additional uncertainties. To make matters more difficult, deeply buried muon detectors are often built for some other primary purpose, such as detection of neutrinos or proton decay. Thus they are in some ways poorly suited for studying cosmic rays. AMANDA, for instance, is too sparse an array to sample the muon lateral distribution function in detail, while other detectors such as Soudan-2 and MACRO are too small to sample anything but a small piece of the function. The inventive physicist, however, must not be discouraged; these detectors can still yield results [44, 45, 46]. To use this observable, we must first understand the number and shape of muons as a function of energy and composition.

The number of muons at depth can be computed by combining our knowledge of the muon energy spectrum at the surface with a simple model of muon energy loss in matter, described by the equation:

$$-\frac{dE_\mu}{dx} = a_{eff} + b_{eff} E_\mu$$

This subject will be discussed in further detail in Chapter 5, but a short discussion here will allow us to derive how many muons survive to depth. A muon at the surface must have a minimum energy

E_{min} in order to reach a slant depth in the ice X before losing all of its energy. E_{min} can be computed by solving the above differential equation, yielding:

$$E_{min} = \left(\frac{a_{eff}}{b_{eff}}\right)(e^{b_{eff}X} - 1)$$

The number of muons reaching a depth X therefore is equal to the number of muons at the surface with energy equal or greater to E_{min}. In other words, if the surface muons have an energy distribution given by:

$$N_{\mu_{surf}}(> E) = KE^{-\gamma_\mu}$$

then the number of muons at depth is:

$$N_{\mu_{depth}} = N_{\mu_{surf}}(> E_{min}) = KE_{min}^{-\gamma_\mu} = K\left[\left(\frac{a_{eff}}{b_{eff}}\right)(e^{b_{eff}X} - 1)\right]^{-\gamma_\mu}$$

Many underground detectors perform counting experiments with muons, and are interested in the total number of muons which will be observed at the particular depth of the detector. This total intensity curve as a function of depth (called the "depth-intensity relation") can be computed by setting the muon spectral index (γ_μ, above) equal to the cosmic ray index, and this curve has been mapped by underground detectors [67].

In this work, however, we do not perform a counting experiment but rather study the structure and properties of the muon events themselves. The volume of AMANDA spans a large range of depths from 1500 to 2000 meters, and so the number of muons in a given *event* will be different between the top of the detector and the bottom. We need to understand not how many total muons reach a certain fixed depth, but rather how the muon intensity within a single event changes as it propagates through the detector's range of depths. Put another way, we want to know the *relative* rather than *absolute* muon intensity as a function of depth.

Fortunately, this can be computed just as easily using the same equation but a different γ_μ. As discussed in the previous section, $N_{\mu_{surf}}(> E_\mu)$ scales as $E_\mu^{-1.757}$. Each single event (of a given energy and composition) therefore contains muons which follow a power spectrum with an index of $\gamma_\mu = 1.757$. By using this muon spectral index in the depth equation above, we compute the shape of the muon intensity as a function of depth, for an event. Figure 3.5 shows the fraction of muons

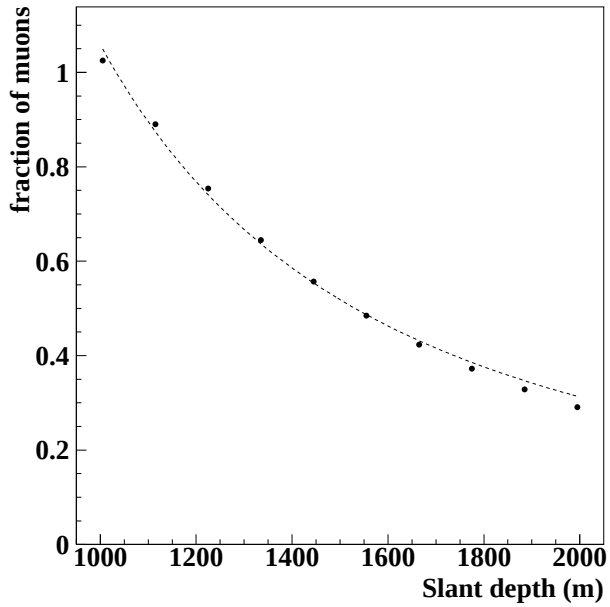

Figure 3.5: Fraction of muons reaching slant depth X, as a function of X, from air shower and muon propagation simulations. The fraction is defined to be one at the arbitrary reference depth of 1000 meters. Dashed line: theoretical expectation.

which reach a slant depth X as a function of X, according to simulations. The curve is normalized to be equal to one at at the reference slant depth of $X = 1000$ m. The theoretical expectation derived from the equation above is superimposed for comparison (arbitrarily normalized).

The shape of the lateral distribution reflects the distribution of transverse momenta imparted to the muons when they are created in the atmosphere, which has the general form [2]:

$$\rho_\mu(r) = N_\mu C \frac{1}{(r + r_0)^\alpha}$$

where α is around five and r_0 is a characteristic length which depends on composition *only* and is energy-*independent*. Transverse momentum is distributed to pions and kaons in invariant proportions at the top of the shower. So muons from iron showers are more widely-distributed, only because their transverse momentum is imparted higher in the atmosphere and they have more room to spread out before hitting the detector. This can be seen in Figure 3.6, in which the muon lateral distributions of simulated proton and iron showers of comparable muon number are compared to each other and to the theoretical expectation.

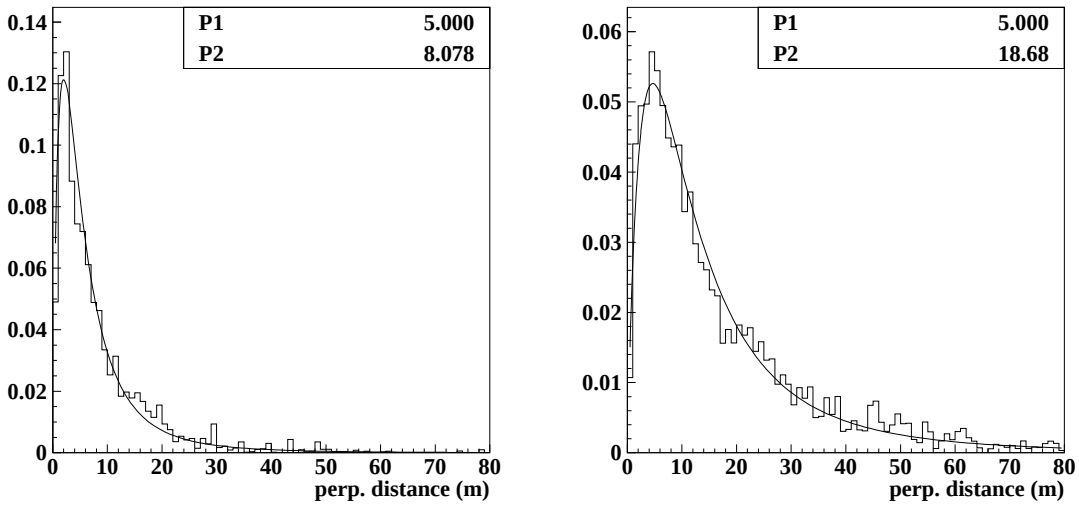

(a) Proton events

(b) Iron events

Figure 3.6: Lateral distribution of muons at a slant depth of 1700 meters, for all events with $N_\mu(X = 1000 \text{ m}) = 100$, fit to the theoretical form described in the text with α fixed at 5.0 and r_0 as a free parameter.

The plots above illustrate averaged properties of air showers. Figure 3.7 shows the muonic properties of four *individual* Monte Carlo events: the number of muons as a function of depth, the spectrum of muon energies at the surface, and the lateral distribution function at the depth of AMANDA.

3.2 Separation techniques: coincidence experiments

Extensive air showers contain different particle components: the electronic component (which can be measured at the surface), the Cherenkov-light component (which images the charged particles in the air), the muon component (which can be measured at the surface or underground), and the neutrino component (which can only be measured on the other side of the Earth). Unfortunately, all of them are tangled functions of both mass and energy. No component individually can make a uniquely-determined measurement of mass; only by measuring two or more components simultaneously can mass composition be pulled out of data.

3.2.1 N_e and Cherenkov light

There are several cosmic ray experiments made of a scintillator array operated in coincidence with Cherenkov telescopes either surrounding the array or embedded inside it. Some examples include:

- CASA/BLANCA [33]
- HEGRA/AIROBICC [48]
- SPASE/VULCAN [106]
- EAS-TOP

The specific techniques for using combined information vary amongst experiments. Some plot a Cherenkov light parameter against an electronic parameter to separate nuclei or to measure energy. Others use the scintillator array with its accurate shower direction and core reconstruction to form a subset of quality events and then reconstruct X_{max} and energy from the Cherenkov properties alone.

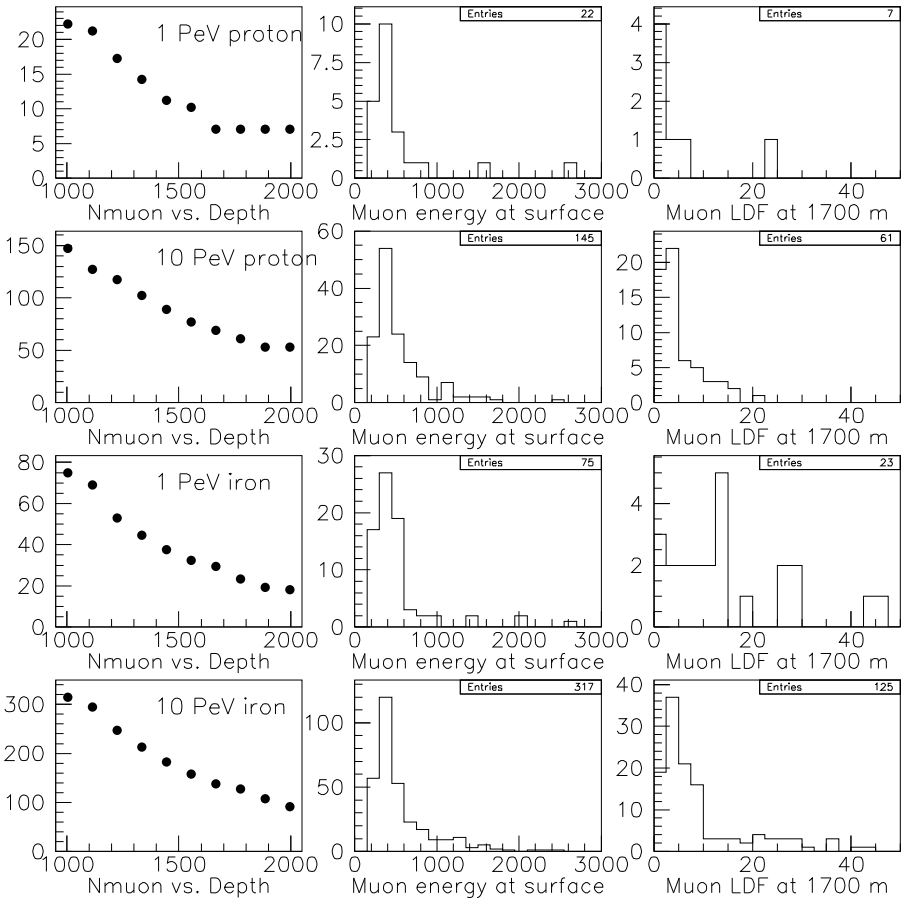

Figure 3.7: Muon distributions for four sample Monte Carlo events.

3.2.2 N_e and surface N_μ

If one can measure both the electronic component and the muonic component of an air shower, then one has an extra tool in the arsenal. These two variables together can give a composition-independent determination of the energy. For this reason, many scintillator arrays are built with muon detectors integrated within them, for instance:

- KASCADE [32, 63]
- EAS-TOP [36, 60]
- CASA/MIA [35]

Generally the muon distributions are not sampled as well as the electrons in these experiments, so muon detection is not the focus of the experiment. However by plotting the electron count N_e and muon count N_μ against each other, protons and iron can be separated.

3.2.3 Other combinations

The HiRes fluorescence detector has been used in coincidence with the MIA muon array to study cosmic ray composition past the knee [42]. HiRes on its own, with its technique of directly measuring the longitudinal development of the shower, does not really need MIA in the same way that electromagnetic or Cherenkov light detectors need muonic backup. However, MIA coincidences provide a restricted data set which is very tightly constrained in shower direction, allowing better energy resolution and reduced systematic errors.

Other hybrid detectors are planned for the near future. The Pierre Auger Observatory for instance will employ a combination of water Cherenkov detectors and fluorescence detectors [64]. The underground Soudan-2 detector has also proposed building a surface air Cherenkov telescope above its site [47].

3.2.4 N_e and deep underground muons

Measuring the electron component at the surface together with the muon component at depth is a relatively new approach, employed by separated detectors built in proximity to each other:

- EAS-TOP/MACRO [40]
- EAS-TOP/LVD [37, 38]
- SPASE/AMANDA (this work)

The Gran Sasso laboratories (housing the LVD and MACRO experiments) have begun to explore the potential of these coincidences, but it is difficult. The basic technique is to measure the muon multiplicity as a function of electron shower size (similarly to the $N_\mu - N_e$ analysis that is done by surface muon detectors such as KASCADE). But specific approaches can vary. One can also measure muon energy loss rather than multiplicity (since protons and iron of the same energy have different kinematic limits for muon energy, they are separable by their energy behavior) [38]. Or, if one has an energy-sensitive Cherenkov array at the surface, one can also compare muon multiplicity to shower energy rather than N_e [39].

The site of the Gran Sasso detectors, at the depth of over 3000 m.w.e., implies a threshold muon surface energy of 1.4 TeV to reach the detector. As a result, the detector reaches full efficiency at the energy range of the knee, and must contend with detector turn-on and threshold effects. The AMANDA site at the South Pole, at a depth of only 1700 m.w.e., can explore lower energies.

3.2.5 Three components

Some sites have the capability to observe three components simultaneously:

- KASCADE: electrons, muons, hadrons [63]
- CASA/MIA/DICE: electrons, muons, Cherenkov light[50]
- SPASE/VULCAN/AMANDA: electrons, muons, Cherenkov light[113]

With three observables, the properties of the shower are overconstrained. However, there are enough sources of uncertainty in both models and measurements that these triple-coincidence experiments are invaluable for consistency checking.

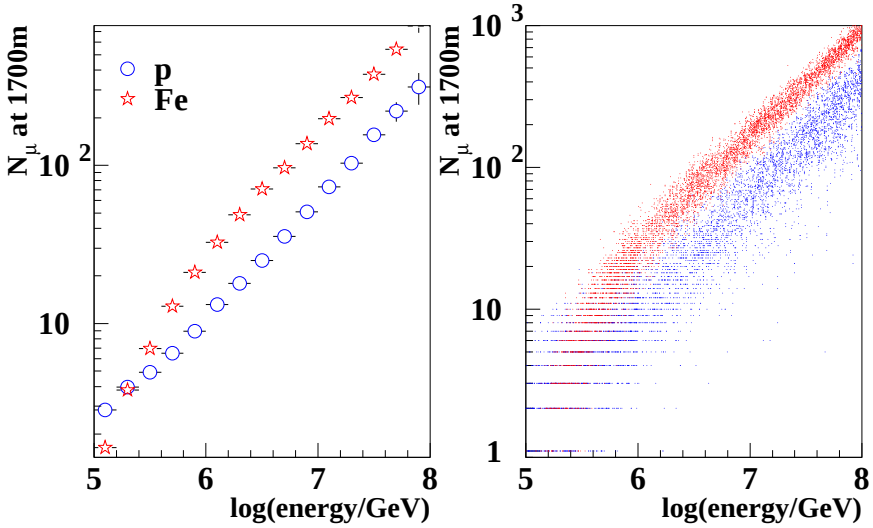

Figure 3.8: Relationship between N_μ and cosmic ray primary energy

3.3 Composition with SPASE/AMANDA

As with other coincidence experiments, SPASE and AMANDA can measure different observables which are all energy- and composition-dependent, but which *together* can isolate energy or composition. SPASE measures the shower size $S(30)$; this is a measure of N_e. AMANDA, a muon detector, receives information only about the high-energy muons in the air shower. The muons are described by a lateral distribution function as discussed above; their total number N_μ and the shape of the function (described by a characteristic width r_0) are therefore the two potential observables for AMANDA. The width r_0 is in principle a powerful separation parameter, and an attempt to exploit it was attempted (see Appendix B), however, AMANDA is ill-designed to measure it. The number of muons N_μ, however, is directly related to the amount of energy loss in the form of light which is released into the ice. AMANDA, a large and fully active calorimeter, is well-suited to this observable, as we will see later. Thus, N_μ will be the focus of this work, and its dependence on primary energy is shown in Figure 3.8.

Before proceeding further, we must explore our ability to measure composition using the ob-

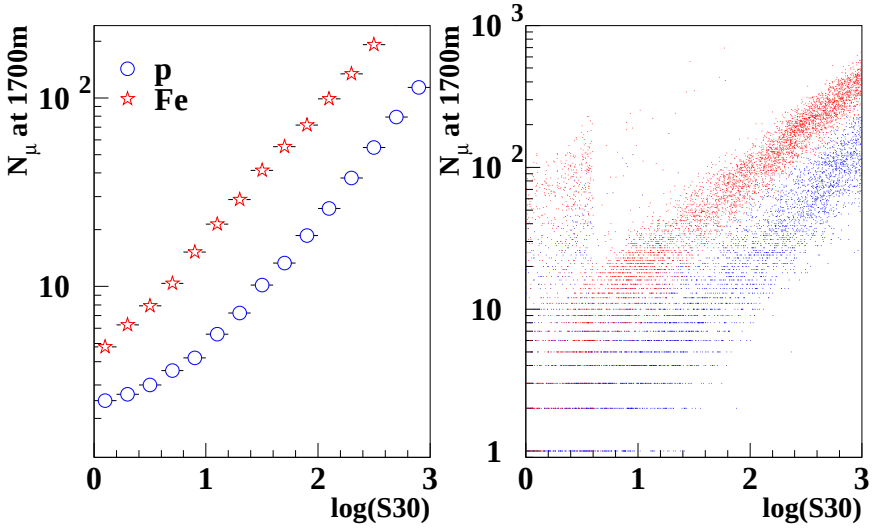

Figure 3.9: Relationship between N_μ and SPASE parameter $S(30)$

servables at hand. Assuming we find a way to perfectly measure the number of muons at AMANDA's depth, can this observable (combined with $S(30)$ from SPASE) distinguish between protons and iron? The answer, as one can see from Figure 3.9, is yes. When the two variables are plotted against one another, the two nuclei separate nicely.

So our mission would seem simple enough: to find a *composition-independent* measure of the number of muons in AMANDA. A technique for doing this will be discussed in Chapter 8. However, if the muon number is not simulated correctly or if our measurement of it suffers from systematic errors, we must be very careful that our techniques are robust. Systematic errors will be discussed in Chapter 9.

Chapter 4

AMANDA and SPASE

4.1 The AMANDA detector

AMANDA (the Antarctic Muon And Neutrino Detector Array) is an ice Cherenkov telescope constructed within the Antarctic ice cap near the South Pole. AMANDA's primary mission is the detection of high-energy neutrinos, from the Cherenkov light emitted by its interaction products. A ν_μ interaction near the detector in rock or ice produces a high-energy muon[1] which travels faster than the speed of light in ice. The detector, an array of photomultiplier tubes buried in the ice, measures the resulting pattern of Cherenkov light, and from this pattern reconstructs the muon's trajectory. At this time, neutrino-induced muons are seen by AMANDA, which are consistent in spectrum and zenith angle distribution with cosmic ray-induced (or "atmospheric") neutrinos from the northern hemisphere [77]. Thus, AMANDA can place upper limits on the fluxes of extragalactic neutrinos [94], neutrinos from WIMPS [99], magnetic monopoles [97], gamma ray bursts [96], and point sources [81].

Cosmic ray muons (produced in the atmosphere above the South Pole) constitute the dominant background for neutrino-induced muons, and so great pains are taken to remove them from neutrino analyses [79]. Ultimately, the two are distinguished by their direction; an upgoing event must be neutrino-induced, while a downgoing event is almost assuredly cosmic ray muon-induced. In searching for neutrinos, cosmic ray muons which have been mistakenly reconstructed as upgoing are a formative background.

[1] Similarly, a ν_e interaction produces a high-energy electron and a ν_τ interaction a tau lepton. It is the muon tracks, however, which are best understood in AMANDA and relevant here for cosmic ray studies.

In this work, however, cosmic ray muons are the *signal*, rather than the background. Together with the SPASE array on the surface of the ice, AMANDA can be calibrated using cosmic ray events, and can even measure properties of cosmic rays themselves. Placing such a cosmic ray study in the context of AMANDA's neutrino mission can be confusing. Some techniques and terminology will be borrowed, others specially developed for this work. Some difficult challenges of a neutrino analysis can be avoided here, while cosmic rays present new and different challenges of their own.

4.1.1 The hardware

The building block of AMANDA is the optical module (OM): a glass pressure housing containing a photomultiplier tube (PMT), silicon gel for optical coupling between the glass and the PMT, and electronics of varying sophistication for distributing high voltage and transmitting output pulses.

The array is structured as long strings of these optical modules deployed down holes over two kilometers deep. The holes are drilled using hot water, the strings then lowered into the hole while it is still liquid. When the water-filled hole is allowed to refreeze, the OM's are locked in place, each one connected to the surface by a coax or twisted pair cable which provides both high voltage to the module and signal transmission to the surface.

The configuration of the detector has changed over the years as more holes have been drilled and more OM's deployed to enlarge the array. In 1996, the detector consisted of 86 modules on four strings (the AMANDA-B4 detector). In 1997, it had grown to 302 modules on ten strings (the AMANDA-B10 detector). In 1998 and 1999, it had 428 modules on thirteen strings (the AMANDA-B13 detector). And in 2000 up to the present day there are 677 modules on nineteen strings, a configuration called AMANDA-II, seen in Figure 4.1. The modules on a string are separated by 10-20 meters (depending on the string), and the strings themselves are separated by 30-60 meters. A range of depth between 1500 meters and 2000 meters is the most densely instrumented.

This work focuses on data from the AMANDA-B10 array. More detailed descriptions of this configuration and the data it collected in 1997 can be found in [82]. Although 13 strings were present in 1998 and 1999, SPASE/AMANDA coincidence data from just the 10-string subarray can be analyzed identically to the 1997 array, to increase data statistics (this will be discussed in greater detail later in Appendix C).

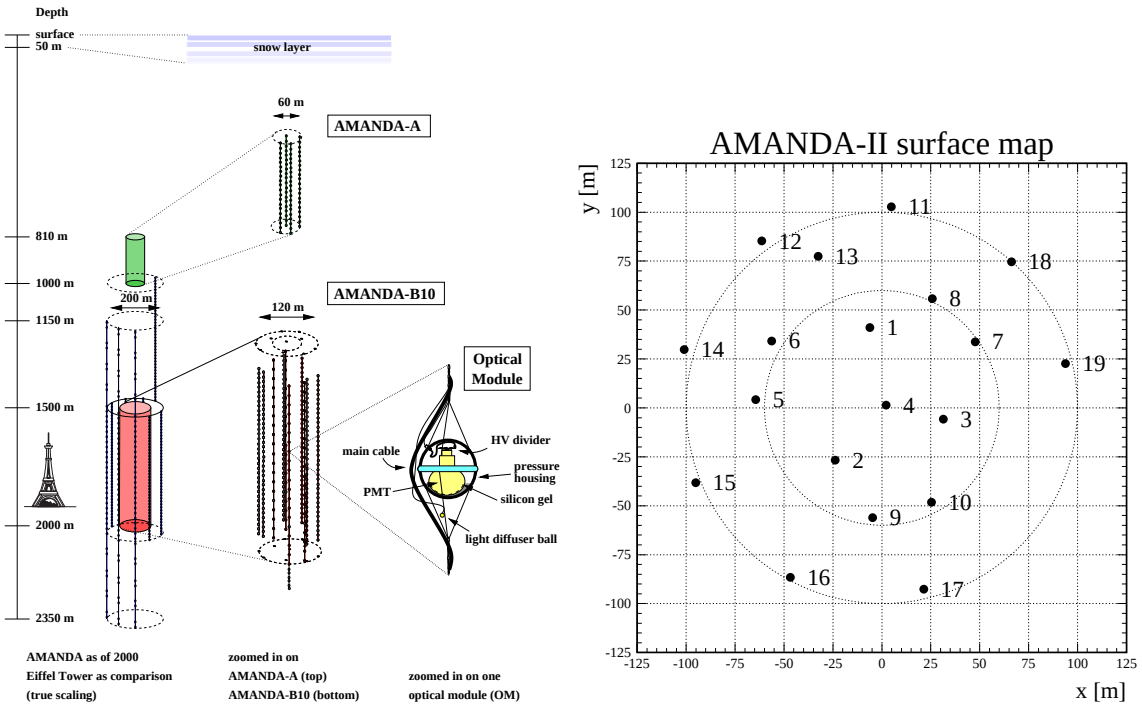

(a) Schematic of the 19-string AMANDA-II detector.

(b) Top view of AMANDA-II. The inner 10 strings form AMANDA-B10, and are roughly contained in a circle of radius 60 meters from the center of the array.

Figure 4.1: The AMANDA detector.

4.1.2 The DAQ

The Data Acquisition (DAQ) system at the surface records the amplitude (ADC) and time (TDC) of pulses arriving from the OM's. The detector's trigger can come from a variety of sources. In normal mode, a hit multiplicity trigger logic determines when a required number of hits have arrived within a required time window, and initiates a trigger. Or, the trigger can come from an external source. SPASE-AMANDA coincidence events are of the second type; the SPASE detector provides an external trigger and AMANDA operates in "slave mode." This type of trigger offers many advantages for calibrating AMANDA and reducing systematics or uncertainties related to AMANDA trigger efficiency.

Amplitude and time information are recorded for all triggers, which occur at a rate of approximately 100 Hz. When a trigger is received, a common stop signal is sent to the TDC's, and all TDC times (which are stored in a rotating buffer) are read out. The peak amplitude within a smaller time window (which is measured by a peak-sensing ADC) is also read out. Hit information for an OM is stored as a series of up to 16 leading and trailing edges, and one amplitude[2].

This data is calibrated, cleaned, and analyzed later, as the bulk of the data (which is taken during the Antarctic winter) can only reach the northern hemisphere once the South Pole Station opens for the summer. The first analysis task is to quickly reconstruct the track of the muon through the detector from its pattern of Cherenkov light, and to filter a subset of quality events which qualify for the next stage of a more refined analysis. Special triggers (such as SPASE triggers) are separated from the data at this early stage and set aside.

Figure 4.2 shows two sample SPASE/AMANDA coincidence events. One can see from these event displays several phenomena: the progression of the timing of hits (displayed from early to late through the colors of the rainbow) from the top of the detector to the bottom, the larger ADC values (displayed as larger circles) located near the track and getting smaller with distance, and the superior placement of the track by a combined fit (the green track) as opposed to the SPASE track alone (the

[2]The fact that many hits but only one amplitude can be recorded for an OM is problematic. A simple way to adapt is to cut away all hits but the first one. Although this sacrifices information, it increases the probability that the amplitude is associated with the correct hit.

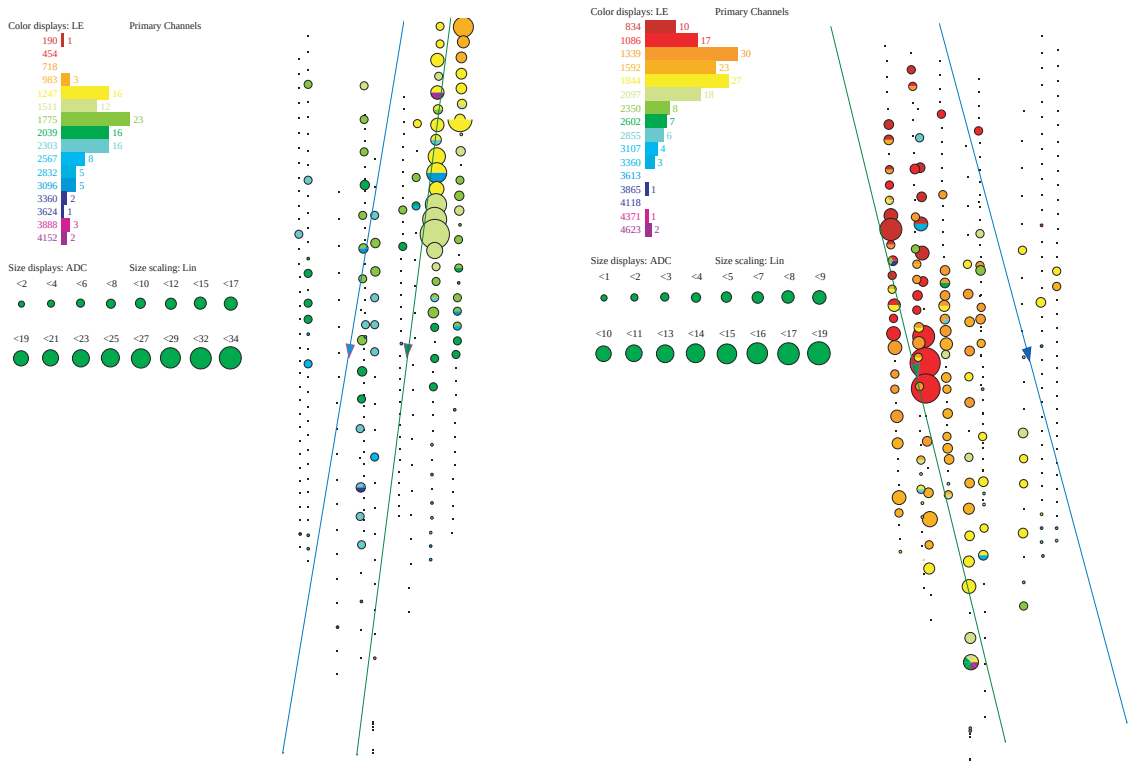

(a) Event 210449

(b) Event 015480

Figure 4.2: Two example coincidence events in AMANDA. (They have been rotated for the best view.)

blue track), which can be off by tens of meters.

4.2 The SPASE detectors

There have actually been two SPASE (South Pole Air Shower Experiment) arrays at the South Pole. The first, SPASE-1 [107, 108, 109] operated between 1987 and 1997. It was a triangular grid of 16 scintillator detectors, 1 m^2 each, with a 30 meter grid spacing. The second, SPASE-2 [110], was completed in 1996 and has been operating ever since. It consists of 30 "stations" on a 30 meter triangular grid (the same spacing as SPASE-1) where each station contains four scintillators of area 0.2 m^2 each. One of these modules is run at a low gain in order to extend the station's dynamic range. The angular acceptance of SPASE-2 and AMANDA-B10 operating in coincidence is about

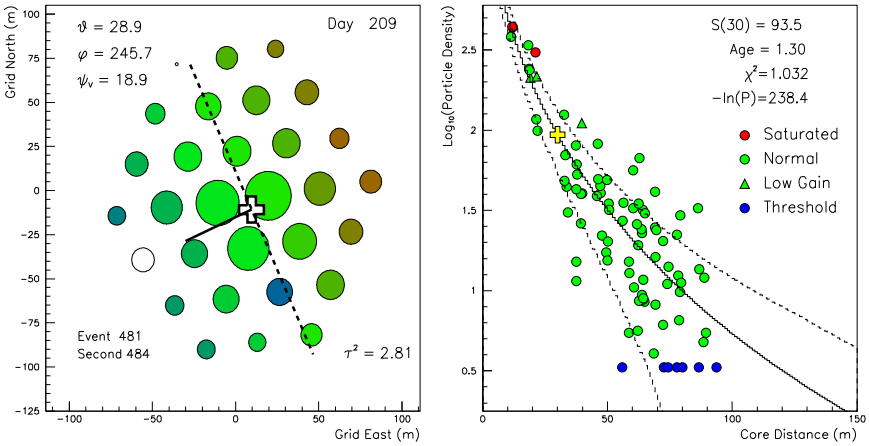

Figure 4.3: Sample SPASE event display and lateral distribution fit to determine $S(30)$, from [114].

100 m^2sr, about twice the acceptance of EAS-TOP/MACRO [110]. SPASE-2 triggers with a station multiplicity condition: 5-fold within one microsecond when VULCAN is also operating, and 4-fold when it is not. The energy threshold is about 50 TeV for primary protons. [106].

SPASE, similarly to AMANDA, reconstructs the shower direction from the arrival times of charged particles in its scintillators. The accuracy of this reconstruction depends on the size of the shower; a small shower with few hits has a larger error on the fitted direction.

Like other ground arrays, SPASE reconstructs the shower size and properties by fitting the lateral distribution of amplitudes to the NKG function. Since the shape of this function is invariant, the shower size is expressed by the particle intensity at a constant distance. For SPASE events, shower size is characterized by the parameter $S(30)$, which is the measured particle density at 30 meters from the core of the shower, in units of particles/m^2. The core location and the shower size are fitted simultaneously. Figure 4.3 shows a sample event, its lateral distribution function, and how $S(30)$ is fit to the data. Figure 4.2 shows how the resolution of SPASE's reconstruction of direction, core location, and shower size all improve with larger showers. Figure 4.5 shows the relationship between $S(30)$ and the electron number N_e, and how it is independent of primary composition.

The scintillators saturate at the level of about 100 particles per module, the low-gain scintillators at roughly five times this amount. This means that a 10^{17} eV primary energy shower will saturate even the low-gain module of a station 30 meters from the shower core [110]. Scintillator

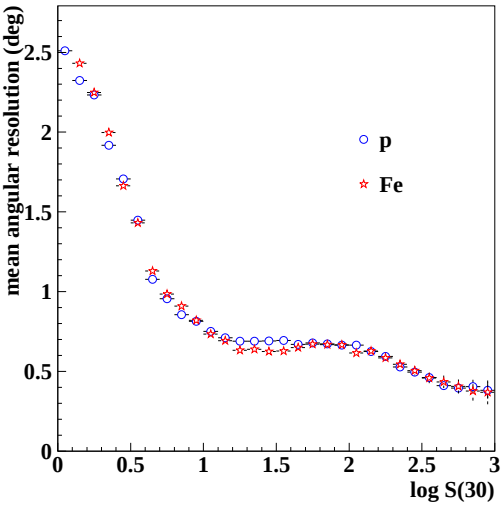

(a) Track angular resolution, for protons (blue) and iron (red).

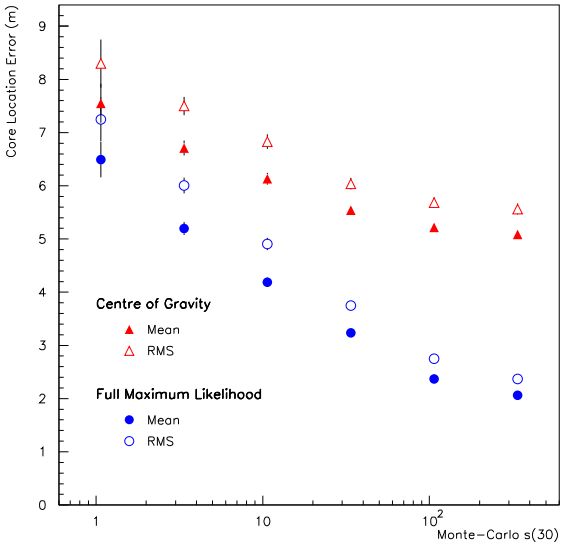

(b) Core position resolution, from [114]

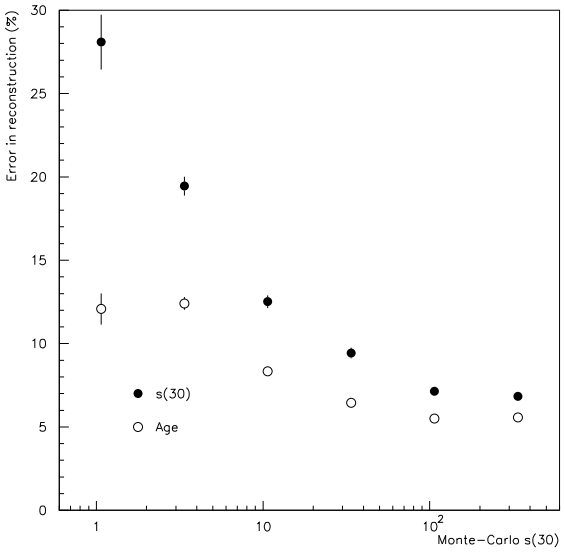

(c) $S(30)$ resolution, from [114]

Figure 4.4: The performance of SPASE-2, according to Monte Carlo, as a function of $S(30)$.

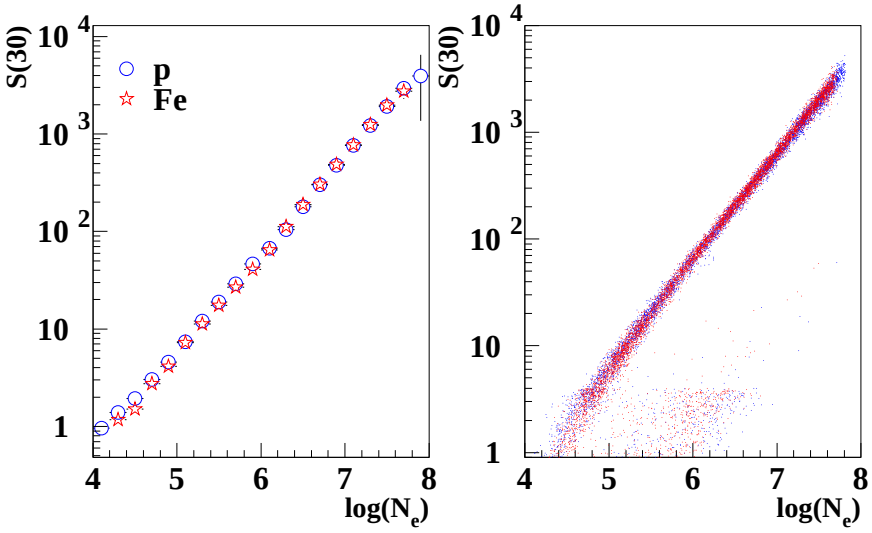

Figure 4.5: Relationship between the true number of electrons at ground level and the shower size estimator $S(30)$.

saturation will be discussed in more detail in Chapter 9.

4.3 The VULCAN detector

VULCAN [111] is an array of air Cherenkov telescopes, 9 detectors in all, which is embedded within SPASE-2 (see Figure 4.6). In 1997, all the telescopes were aimed toward the sky in a direction which, when traced backwards, aims at the center of the AMANDA-A detector (four prototype strings which were deployed at about 900 meters depth). In 1998, the telescopes were re-aimed at the center of AMANDA-B10. As a result, SPASE/VULCAN coincidences with AMANDA-B10 from 1997 are rare mis-aimed events, and of unknown reliability and systematics. Coincidences from 1998, when the telescopes were properly aimed, are of greater value. SPASE/VULCAN/AMANDA coincidences from 1998 were analyzed for composition in [113] and will not be discussed further in this work.

4.4 The GASP detector

GASP [112] was an air Cherenkov telescope embedded in SPASE-1, consisting of ten mirrors and two PMT's for each mirror. The viewing angle of each PMT in GASP is 1.5 degrees, and with

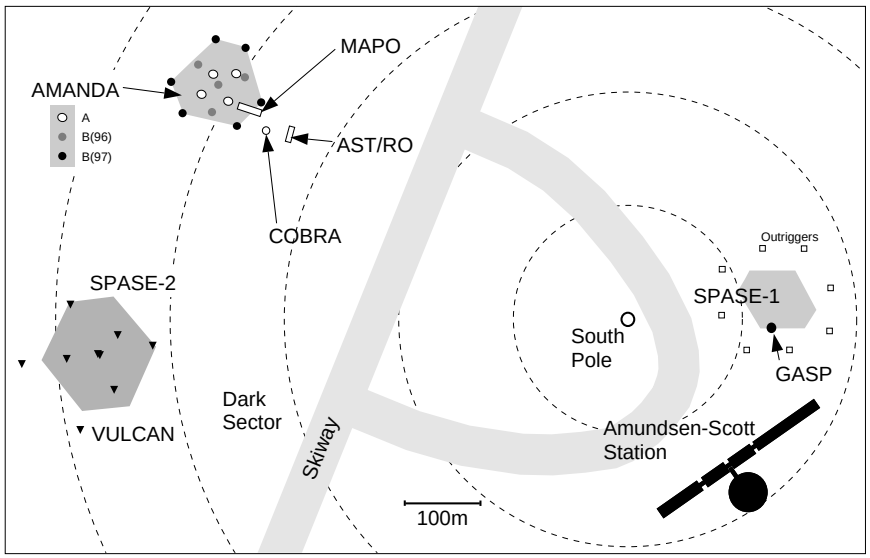

Figure 4.6: Layout of AMANDA, SPASE-1, SPASE-2, and VULCAN, from [114].

all the mirrors aligned the angular acceptance of GASP is approximately 0.5 degrees. The telescopes were aimed at the sky in alignment with AMANDA-B10. The detector triggers at a proton primary energy of approximately 1 TeV. Because of its narrow field of view, this telescope provides a precise beam for pointing calibration of AMANDA (see Chapter 7).

4.5 SPASE/AMANDA data

SPASE/AMANDA coincidences are a special subclass of AMANDA events. Every SPASE trigger (regardless of direction or energy) sends a trigger to AMANDA. TDC and ADC gates are opened at fixed times relative to the trigger to collect any hits. The event is given a tag so that it can be identified as a SPASE trigger and separated from the rest of the AMANDA data offline. These coincidences occur at a rate of about 5 Hz (for the 5-fold trigger) or 8 Hz (for the 4-fold trigger) [110].

Meanwhile, SPASE records its own data for the same events and reconstructs their direction and shower size using a program called SPV. Offline, the SPASE events and AMANDA events must be matched up with each other. Each detector records the time of each event according to its own GPS clock. Events within one millisecond of each other are considered a match; the flight time of

the particles from one detector to the other is approximately 6 microseconds.

The exact positioning of the TDC and ADC gates changes from year to year. In 1997, the TDC gate was 32 microseconds wide and centered on the trigger time, and the ADC gate was 4 microseconds wide and was opened about 1 microsecond before the arrival of the first pulses from the event. In 1998, the ADC gate was widened to 9 microseconds. This change turns out to be crucial for data quality, and is discussed later (see Appendix C).

4.6 SPASE/AMANDA Monte Carlo Simulations

A simulation of an air shower passing through not one but two experiments (which happen to be separated from each other by over a kilometer of ice) involves several distinct stages. At each stage, there are uncertainties and systematics (some better understood than others). For this work, we will employ one "baseline" simulation chain, but will vary some of the links in the chain one at a time to investigate systematic effects. These effects will be discussed in Chapter 9.

Events were generated with an E^{-1} energy spectrum, to ensure plenty of statistics in the interesting high-energy regime. To mimic the actual cosmic ray energy spectrum, Monte Carlo events are all re-weighted to an $E^{-2.7}$ spectrum below $\log E(\mathrm{GeV}) = 6.5$ (the knee), and to an $E^{-3.2}$ spectrum above it[3]. Figure 4.7 shows the resulting energy spectrum of the simulated and re-weighted events.

4.6.1 Air shower simulation and hadronic interaction model

There are several different air shower simulation packages available for experimenters. Much of the physics of air showers is well understood; the electromagnetic interactions for instance can be simulated exactly with QED. The common weak point to all air shower simulations, however, is the details of the *hadronic* interactions. Accelerator data (on which simulations are based) do not reach the very high energies of cosmic ray showers, and do not collect data well in the forward direction which is relevant for most air shower interactions. So an air shower simulation must employ extrapolations and assumptions. There have been several independent attempts to simulate these

[3]In our simulations, protons and iron are given a knee at the same *energy*, even though some cosmic ray theories and experimental evidence suggests that the knee occurs at the same *rigidity* for different nuclei. This was done because we want to measure this phenomenon rather than assume it.

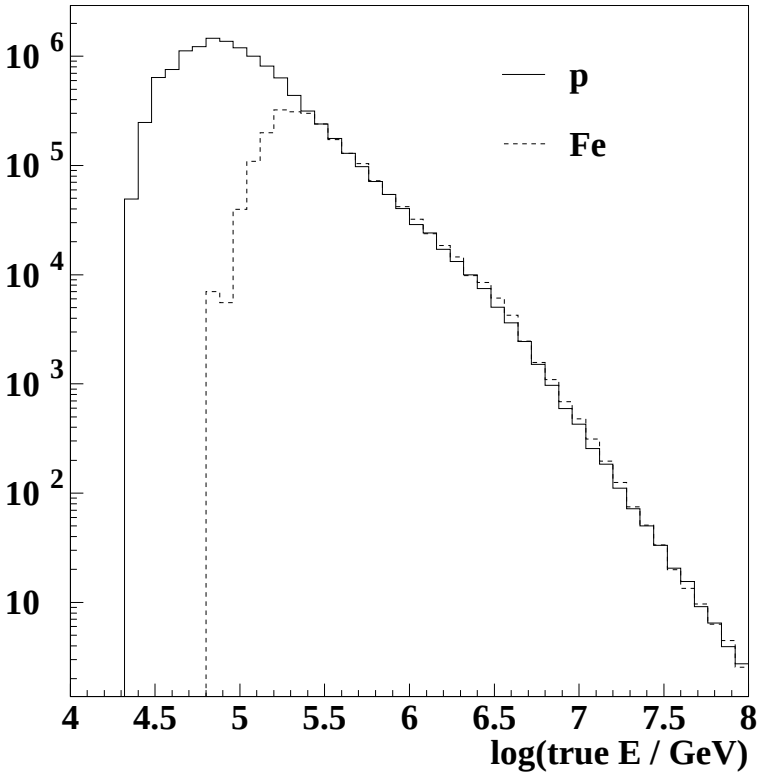

Figure 4.7: Distribution of true primary energy for simulated protons (solid) and iron (dashed). The "knee" occurs at $\log E(\mathrm{GeV}) = 6.5$ for both nuclei. This is the number of simulated events *after* they have passed through the SPASE trigger simulation, so the SPASE threshold is seen to occur at different energies for protons and iron.

hadronic details, resulting in a small collection of different models (the most commonly used being QGSJET, VENUS, SIBYLL, HPDM, and DPMJET[4]). Similarities and differences between these hadronic interaction models comprise a body of literature on their own[5], and some software packages which model the entire air shower (such as MOCCA and CORSIKA) have modularized their code so that the different hadronic interaction models can be directly compared to each other. Meanwhile, experiments test their data against the different models to measure whether one is favored over the others. The final verdict, of course, is still out.

For this work, the baseline hadronic interaction model used will be MOCCA/QGSJET. The MOCCA code has been customized for the South Pole (in atmosphere, overburden, and magnetic field, for instance) [114]. A similar simulation generated with the SIBYLL interaction model will be used later to demonstrate the systematic uncertainty in the results due to hadronic interaction model.

4.6.2 SPASE detector simulation

The response of the SPASE and VULCAN detectors together are simulated by the program MONTE [114]. It is only at this stage that the shower is given an orientation relative to the Earth: it is assigned axis coordinates $(x_{core}, y_{core}, \theta, \phi)$ relative to SPASE, in a local SPASE coordinate system. To make the best use of each of the showers (which have been time-consuming to simulate), they can be "reused" at this stage of the process. That is, each shower is duplicated many times but its core position is scattered all over the SPASE array.

The arrival times and densities of the shower particles are then computed for each scintillator module. Noise hits are added, and the information is converted to a "raw data" format mimicking real data. The simulated values are smeared to reflect Poissonian fluctuations, uncertainties in detector pedestal values, and so forth. The simulated data is then ready to be processed through the SPASE/VULCAN reconstruction program SPV, identically to real data.

---

[4] A new hadronic interaction model called neXus has also been introduced recently [75]. It has not been subject to as many tests yet (except by the Karlsruhe group) and is extremely slow.

[5] For a thorough review of the five interaction models, their similarities and differences, systematic effects on N_e and N_μ, and ensuing experimental confusion, see anything by the CORSIKA authors, for instance [29]. A shorter and more accessible review is [28].

4.6.3 Muon propagation

After hitting SPASE, the air shower penetrates the South Pole snow and ice, only the high-energy muons reaching the depth of AMANDA. Unfortunately, the propagation of high-energy muons through matter is another source of uncertainty, as the physics of muon energy loss is not well-known at high energies.

For this work, the baseline muon propagator is the PROPMU code developed by Lipari and Stanev [74]. An alternative propagator MMC [98] has been recently written by members of the AMANDA collaboration, intending to bridge the gap between treatment of energy losses at low and high energies; this will also be used to study systematics.

4.6.4 AMANDA detector simulation

The program `amasim` simulates the response of the AMANDA detector to an event. The simulation includes at its heart the propagation of light through the ice from source to OM. To correctly simulate the scattering and absorption of photons is a time-intensive computation, so rather than perform the simulation for each photon, tables of results are compiled separately by the software package PTD (Photon Transport and Detection) [87]. `amasim` interfaces to these photon tables to look up the photon intensity and arrival time probability distribution for any module from any muon or shower.

`amasim` then builds a PMT waveform which would result from the photon hits, and sends this waveform through a simulation of AMANDA's hardware and DAQ: cables, thresholds, peak-ADC's, TDC's, multiplicity logic and triggering, and data output [89].

The output of `amasim` has the same format as experimental data, and can be put through the identical chain of processing (calibration, hit cleaning, reconstruction, etc.).

4.7 Calibration

"Raw" data (or Monte Carlo) contains the times at which signals arrived at the DAQ on the surface, and the amplitudes in millivolts of the pulses when they arrive. However, the quantities of real interest are the arrival times of photons *in the ice* and the amplitudes of pulses measured in units of *photoelectrons*.

The amplitude calibration is very straightforward: an ADC spectrum is taken for each OM, and the position of the pedestal single photoelectron peak is measured in units of millivolts. To correct the timing, we need two calibration constants: the signal transit time t_0 between photocathode and TDC, and an additional correction to account for "amplitude slewing." The rise time of pulses ($\sim$ 5 ns at the PMT) is smeared over 200 ns from the long journey up the electrical cable. The exact time at which the waveform crosses the TDC discriminator threshold depends on the amplitude of the pulse. In particular, the threshold-crossing time varies as:

$$t_{le} = t_0 + \alpha \frac{1}{\sqrt{ADC}}$$

and the second calibration constant α parametrizes the additional correction which is computed from the ADC on an event-by-event basis. The calibration constants for each individual OM are measured each year during the austral summer season.

SPASE/AMANDA triggers are calibrated identically to normal AMANDA triggers. Distinct sets of calibration constants are used for 1997 and 1998 data, as many things change (including, sometimes unintentionally, the cable lengths and t_0's) between seasons. Monte Carlo, which is generated to look identical to raw 1997 data, is identically calibrated using 1997 calibration constants.

4.8 OM cleaning and hit cleaning

The OM's in the AMANDA-B10 detector exhibit dark noise, at a rate of around 300 Hz for the inner four strings and around 1100 Hz for the outer six. Some is inherent photomultiplier noise, and the rest is due to decays of radioactive ^{40}K in the glass housing (see Appendix E for more detail on this phenomenon).

Although maximum-likelihood reconstructions are written to take into account the probability of a hit originating from noise, stray noise hits can still fool the algorithms and some are more vulnerable than others. In any case, cleaning out noise hits is a crucial aspect of muon reconstruction. This is done in two stages: removing bad OM's completely from the array, and removing hits on an event-by-event basis which are likely to be noise.

Lists of "bad" OM's are available for both 1997 and 1998 (see Appendix C). These OM's are permanently removed in software by setting their sensitivity to zero. Then, within each event, hits

are deemed likely to be noise and temporarily removed if they:

- Arrive outside a time window of 4500 ns in which all of the "real" (that is, muon-induced) pulses are expected to arrive,
- Are "isolated" hits (that is, there are no other hits within 70 meters and 500 ns),
- Have an unphysical time over threshold (less than 125 ns or more than 2000 ns),
- Have no ADC, a very low ADC, or an unphysically high ADC (less than 0.3 photoelectrons or more than 1000 photoelectrons),
- Are likely to be due to crosstalk,
- Are not the first hit (which is likely to be the one correctly associated with the recorded ADC).

The difference between *permanent* cleaning of OM's and *temporary* or event-by-event cleaning of hits is important enough to warrant a short discussion here. Many reconstruction techniques implemented in AMANDA do not use information from OM's which are not hit. If this is the case, then it doesn't matter whether an OM is removed permanently from the array, or if only its hit is removed. If, however, the reconstruction makes use of the information that a particular OM did *not* receive a hit, then it is important to know whether that OM *should have* received a hit at all. If an OM is noisy and is removed from the analysis entirely, then its probability of not being hit is always exactly one, and the reconstruction must recognize this. If, on the other hand, the OM is operating normally but had its only hit removed because it fell outside the time window or had a bad ADC, then its probability of not being hit is still a relevant part of the overall likelihood, and should still be considered by the reconstruction. In this work, modules *not* hit are included in the reconstruction (in fact they are a crucial part of the likelihood), and so the two types of cleaning are performed separately. Permanent OM cleaning is done after calibration but before any reconstruction is done; event-based hit cleaning is done together with reconstruction.

Chapter 5

Light in ice, and event reconstruction

More than the photomultiplier tubes, glass, cables, amplifiers, pulse-shapers, readout electronics, triggering, and other details, the most fundamental part of the detector is the ice itself. "Ice properties" is an umbrella term encompassing scattering and absorption by dust, scattering and absorption by bubbles, index of refraction, vertical structure, and special properties of the column of re-frozen water immediately surrounding the OM's ("hole ice"). By exploring the underlying physics of light propagation in ice, we will arrive in this chapter at a new reconstruction technique well-suited for muon bundles (and with great potential for muon energy reconstruction in general).

5.1 Muon energy loss in matter

Consider a single muon of energy E. As it passes through the ice, it loses energy from a variety of different energy loss mechanisms. Muon energy loss mechanisms can be divided into two categories: continuous and stochastic. In general, the energy loss of the muon is described by the equation

$$-\frac{dE_\mu}{dx} = a(E_\mu) + b(E_\mu)E_\mu$$

where the first piece (a) is the continuous loss, and the second piece (bE_μ) describes the stochastic losses.

Muons lose energy continuously along their path by ionizing the electrons from nearby atoms. The coefficient $a(E_\mu)$ depends only weakly on E_μ, especially above $E_\mu > 10$ GeV, where its value flattens at approximately 0.002 GeV/(g cm^2) [2, 66], or about 2 MeV/cm in ice. A 10 GeV muon

travels 50 meters in ice, which is reconstructible with minimum quality by AMANDA. Thus, this approximation is valid for muons in AMANDA.

Stochastic (or "discrete") losses can come from a variety of mechanisms. The dominant ones for muons are bremsstrahlung, e^+e^- pair production, and photonuclear (also called hadroproduction). The loss rates from all these processes are energy-dependent. To first order, they are linear with energy (hence the term bE_μ in the equation above), where the b coefficient can be expressed as $b = b_{brem} + b_{epair} + b_{hadr}$ and each term contains some energy-dependence. Some of the components of b flatten at high muon energies, allowing us to approximate $b \approx 8 \times 10^{-6}$ g^{-1}/cm^2 for pure iron [66], $b \approx 4 \times 10^{-6}$ g^{-1}/cm^2 for standard rock [2], or $b \approx 3.4 \times 10^{-6}$ g^{-1}/cm^2 for ice [79]. At a "critical energy" $E_c = a/b$, stochastic losses begin to dominate over ionization (continuous) losses. This transition occurs at $E_\mu > \approx 600$ GeV for muons in ice.

The muons in a muon bundle have a spectrum of energies (see Figure 3.4). However, since the energy spectrum is steep, the bulk of the muons are below the critical energy and can be thought of as approximately monoenergetic. This approximation is not important for the analysis to be described later in this work; it merely provides a convenient framework for describing the general concept and its context.

5.2 Cherenkov and shower light

Of the energy released in ionization, discussed above, a small percentage of it (around 0.05%) goes into Cherenkov light [73]. This phenomenon is caused by the disruption of the local electromagnetic field in matter (such as air, water, or ice) by the passage of a relativistic charged particle. It is easily visualized and treated as an electromagnetic shock wave from a charged particle traveling through a medium at a velocity greater than the speed of light in that medium. The light is emitted at a fixed[1] Cherenkov angle of $\approx 41^\circ$ for ice and has a spectrum described by $dn/d\lambda \propto \lambda^{-2}$.

The stochastic processes discussed above produce small shower-like bursts of light at the points on the muon's track where the interactions occur. The importance and treatment of these showers depends on the type of event being analyzed. In ν_e events, the energetic electron produces one large

[1]Technically, the angle depends on the index of refraction in the medium which, although a constant for all practical purposes here, does change with the density of the ice.

shower which is not quite spherical. A muon track, on the other hand, will produce a linear light pattern with stochastic bursts of light at various points along its trajectory. These mini-showers along a muon track are simulated in detail for the muons in AMANDA, but reconstructing each of them is nearly impossible with the poor spatial resolution of the AMANDA phototubes. Instead, we often instead treat the stochastic showers as an averaged phenomenon.

5.3 Scattering and absorption

Understanding scattering and absorption processes is crucial for operating a water or ice Cherenkov detector. These properties determine the detector's mode of operation, optimal design, and strengths and weaknesses. Deep Antarctic ice, for instance, has a long absorption length ($\approx$ 100 m) compared to ocean water ($\approx$ 20 m), making AMANDA a more efficient light collector than oceanic competitors over large volumes. On the flipside, ice has a short effective scattering length ($\approx$ 20 m) compared to ocean water ($\approx$ 100 m), making the exact timing of photons and the precise direction reconstruction of tracks more difficult. Either way, to fully understand and exploit a detector, one must describe these phenomena in greater detail, the aim of this section.

Dust is the most important contributor to absorption and scattering in deep Antarctic ice. Air bubbles, formidable scatterers if present, at depths beyond 1400 meters have been squeezed into air hydrate crystals which match the refractive index of ice almost perfectly and are essentially invisible. Dust grains, about 0.04 microns in size [71], instead are the dominant cause of both absorption and scattering effects at AMANDA depths.

Both effects can be described by a propagation length (λ_e for effective scattering length[2] and λ_a for the absorption length) or a coefficient defined as one over the wavelength ($b_e \equiv 1/\lambda_e$ and $a \equiv 1/\lambda_a$, respectively). These scattering and absorption coefficients as a function of frequency are shown in Figure 5.1(a).

Which wavelengths are important for AMANDA depends also on the transmission properties of the glass, the quantum efficiency of the glass, and the Cherenkov light spectrum, some of which

[2]The geometric scattering length λ_s, the distance that a photon travels before being scattered, is actually very small, but one must also consider the mean angle of scattering at each event, $\langle \cos\theta \rangle$, which is about 0.8-0.9 for dust [71]. The effective scattering length λ_e is equal to the distance at which $1/e$ of photons have been isotropized in direction, and is equal to $\lambda_s/(1 - \langle \cos\theta \rangle)$ [70], about five times larger.

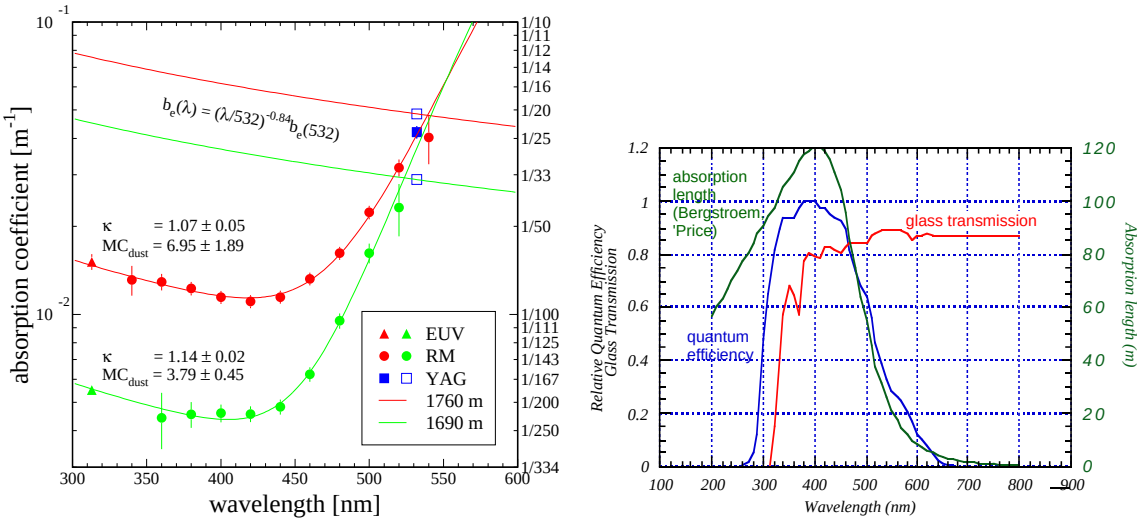

(a) Scattering and absorption coefficients as function of wavelength, from [84]

(b) Wavelength dependence of PMT quantum efficiency, glass transmission, and absorption length, from [102]

Figure 5.1: Wavelength dependence of optical properties

are shown in Figure 5.1(b). Cherenkov light peaks in blue and UV wavelengths, but the glass of the optical modules' pressure housings is transparent only up to about 350 nm. Thus, the wavelength region of importance to AMANDA is from 350-500 nm.

5.4 Vertical structure (dust layers)

A YAG laser[3] at a frequency of 532 nm was first used to map the scattering and absorption coefficients in detail as a function of depth [83], revealing fluctuations and structures due to dusty layers of ice. Figure 5.2 shows the scattering coefficient b_e (at 532 nm) as a function of depth in the instrumented region of AMANDA-B10. There are dusty layers in the ice: peaks in b_e at depths of 1600 meters (z = +130 in the AMANDA coordinate system), 1750 meters (z = −20), and 1880 meters (z = −150). Shallower of AMANDA-B10 depths (< 1400 meters), the ice contains air bubbles which dramatically increase the scattering. Deeper (> 2000 meters) is another large scattering peak

[3]The physical laser is at the surface, and light is piped into fiberoptic cables which lead to isotropizers buried with each module in the ice. Therefore each OM can be used as an emitter. This technique cannot be used at shorter wavelengths because attenuation in the fiberoptic cables becomes too great [86]; instead we must depend on *in situ* emitters such as LED's and laser modules.

Depth from...	...to	Dust
$-\inf$	-240	dusty
-240	-180	clear
-180	-140	dusty
-140	-60	clear
-60	0	dusty
0	70	clear
70	180	dusty
180	inf	clear

Table 5.1: Summary of dusty and clear depth ranges

due to another dusty layer. The peaks in scattering are correlated with known ice age epochs in the Earth's geological history.

Absorption at 532 nm is nearly flat as a function of depth, but this is because at this wavelength absorption is dominated by the ice itself rather than dust. At shorter wavelengths, nearer the peak of AMANDA sensitivity and the minimum of the absorption curve in Figure 5.1(a), the ice contribution has dropped and the dust contribution becomes dominant in absorption as well as scattering. Thus, the same peaks and valleys as a function of depth appear in the absorption coefficient a. Recently, emitters at a variety of other frequencies (470 nm with blue LED's, 370 nm with UV LED's, and 337 nm with a Nitrogen laser) have been used to more comprehensively map out the scattering and absorption properties as a function of both depth and wavelength [85]. The results confirm both the predicted wavelength dependence of b_e and a, and the presence of correlated dust peaks in both b_e and a.

5.5 Effect of ice properties on AMANDA observables

A great deal of effort has gone into understanding how the timing of hits is affected by scattering. Without this understanding, reconstruction of muon tracks in AMANDA is impossible. Since the scattering length of photons is 20-30 meters, and the spacing between OM's is 10-20 meters, all but the closest hits in AMANDA arrive delayed relative to the arrival time of the Cherenkov cone. The greater the distance between the OM and the muon track, the more twisted a path the photon follows to get to the OM after multiple scatterings. As a result, both the absolute delay and the width of the distribution of arrival times increase with distance.

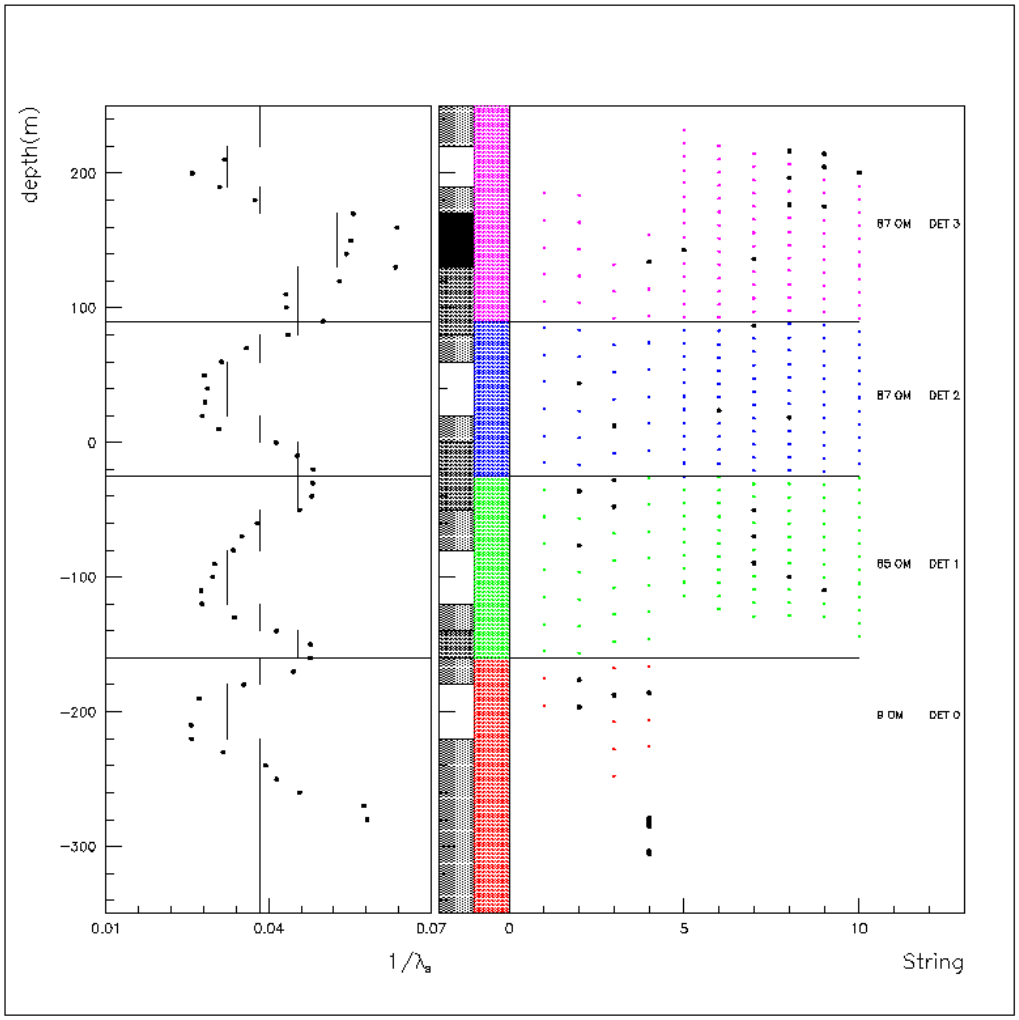

Figure 5.2: Scattering coefficient as a function of depth, indicating the presence of horizontal dust layers, from [79].

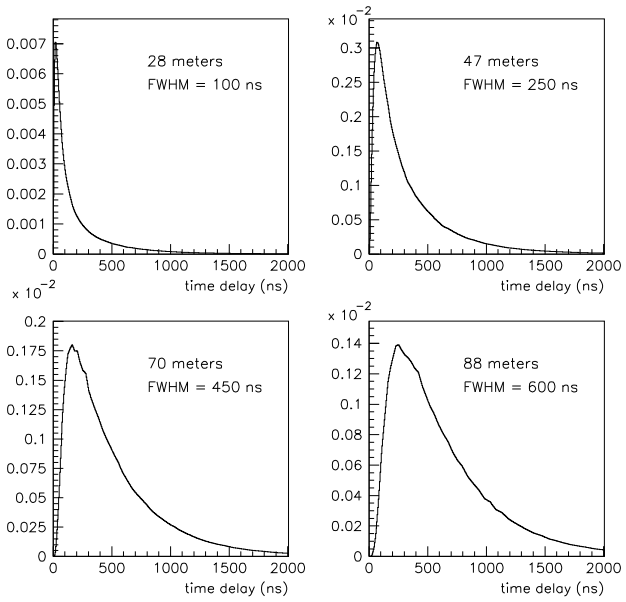

Figure 5.3: Simulated photon arrival time delay distributions for an infinite muon, at four different distances, according to PTD simulations.

In a medium where both scattering and absorption are present, the resulting arrival time distributions cannot be expressed in an analytical form. Instead, they must be either tabulated, parametrized, or simulated photon by photon. The last option is too time-consuming, so AMANDA employs both tables and parametrizations. For simulations, many photons are simulated offline and the results tabulated by a package called PTD (Photon Transport and Detection) [87]. These tables (often called simply the "photon tables") allow the AMANDA detector simulation software to look up for each OM at each distance the probability distributions of arrival times from which it then samples hits. Figure 5.3 shows examples of such distributions simulated by PTD, for four different distances from the track. For *reconstructing* events, a different approach is taken. The timing distributions are parametrized with an analytic function (the "Pandel function"). This function and its application are well documented, for instance in [72], [88], and [76], so I will not discuss it in detail here. Furthermore, it is not timing but rather amplitudes that will take center stage in this work.

Understanding amplitudes is still in its infancy. To date, amplitude information from PMT's is only used to make corrections to the timing information to improve leading edge measurement accu-

racy or compute a more accurate timing likelihood function. In this work, however, the distribution of photons in the detector and the *quantity* of light measured by OM's will be the key observable, to be discussed at great enough length later that the subject deserves a detailed foundation here.

The lateral distribution of photons is controlled both by scattering and absorption. For a point source, the shape of this lateral distribution function has the form:

$$I_{photons} \propto \frac{1}{\lambda_e d} e^{-d/\lambda_{eff}}$$

where d is the perpendicular distance from the OM to the muon track, and λ_{eff} is an effective propagation length due to the combined effects of absorption and scattering, given by:

$$\lambda_{eff} = \sqrt{\lambda_e \lambda_a / 3} = 1/\sqrt{3 a b_e}$$

For a *line* source of light, however, the flux of light at each distance is an integral over all small track elements, and the result is a more complicated function [69]:

$$I_{photons} \propto \frac{1}{\lambda_e} K_0(d/\lambda_{eff})$$

Here, K_0 is a modified Bessel function of the second kind which, for large enough values of its argument z, can be approximated as $\sqrt{2/(\pi z)} e^{-z}$. So, the flux of photons at a distance d is approximately:

$$I_{photons} \propto \frac{1}{\lambda_e \sqrt{d/\lambda_{eff}}} e^{-d/\lambda_{eff}}$$

5.5.1 Relationship between b_e, a, and λ_{eff}

The scattering and absorption coefficients b_e and a are related differently at different wavelengths; we are most interested in the wavelength region between 350 and 450 nm. b_e has been well mapped out as a function of depth at 532 nm, but enough has been measured at other wavelengths to make some simple generalizations. First of all, b_e at 532 nm can be extrapolated to shorter wavelengths using the relation:

$$b_e(\lambda) = \left(\frac{\lambda}{532 \text{ nm}} \right)^{0.84} b_e(532 \text{ nm})$$

For the wavelengths of interest, $b_e(400 \text{ nm}) \approx 1.3 b_e(532 \text{ nm})$. Once at these shorter wavelengths, the two coefficients b_e and a are correlated with each other; the equation for the absorption coefficient:

$$a(\lambda) = A e^{-0.48\lambda} + B e^{-6700/\lambda} + C M_{dust} \lambda^{-\kappa}$$

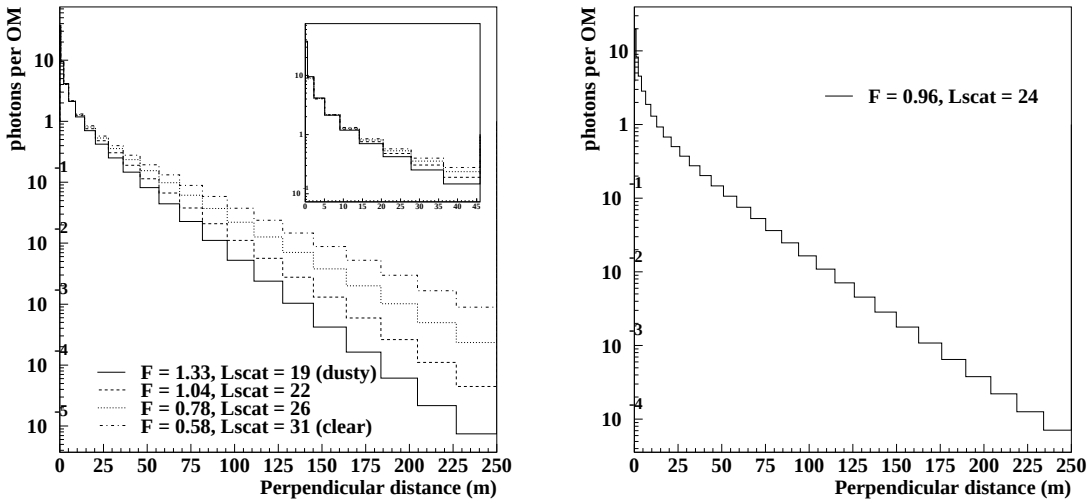

(a) The four "groups" of ice implemented in Monte Carlo (see Figure 5.2).

(b) The "bulk" ice model.

Figure 5.4: Lateral distribution of photon intensity, according to PTD simulations.

in the wavelength region of interest becomes dominated by the third term which depends linearly on the concentration of dust. Thus if the scattering coefficient rises, the absorption coefficient rises with it roughly linearly [90]. The ratio between them is approximately 1/6 [85]. So, using the relations $b_e(400\text{ nm}) \approx 1.3 b_e(532\text{ nm})$ and $a(400\text{ nm}) \approx 1/6 b_e(400\text{ nm})$, we can approximate:

$$\lambda_{eff} \approx \sqrt{\lambda_e(400\text{ nm})\lambda_a(400\text{ nm})/3} \approx 1.1\lambda_e(532\text{ nm}) = 1.1/b_e$$

λ_{eff} is proportional to λ_e of scattering only; we will use this fact to simplify the calculations. Within one ice layer, the photon amplitude should follow this distribution:

$$I_{photons} \propto \frac{1}{\sqrt{\lambda_{eff} d}} e^{-d/\lambda_{eff}}$$

This form agrees quite well with simulations of photons propagated with PTD. Figure 5.4 shows the lateral distribution of photoelectrons per OM for four different ice "groups" of different dust concentration, as well as the average or "bulk" ice.

At small distances d, the Bessel function approximation breaks down, and PMT saturation

effects will kick in for large events. But fortunately, a typical event will not sample this distance region with very many modules, so the error is kept minimal.

5.5.2 A complete model of ADC behavior at all depths and distances

The "raw ADC" of an optical module is the amplitude (in millivolts) of the electrical pulse arriving at the Analog-to-Digital Converter in the surface electronics of AMANDA. In the calibration stage of analysis, this number is converted to an amplitude in photoelectrons (PE's). This number of photoelectrons seen by an OM is also referred to as the "calibrated ADC," or simply "ADC." I will be using this term in the remainder of this work to refer to OM amplitudes in units of PE's.

A single muon traveling through a uniform layer of ice with a propagation length λ_{eff} will produce ADC's in AMANDA with the simple shape described above. However, we are faced with a more complicated situation. Firstly, some fraction of the multiple muons in a muon bundle range out as they traverse the detector. So the overall amount of light will drop between the top of the detector and the bottom. Secondly, the ice is not uniform but structured in layers. An OM in a dusty ice layer will receive less light than an OM in a clear layer. Figure 5.5 demonstrates the basic idea.

The first issue has been addressed already, in Chapter 3; The number of muons in an event as a function of slant depth X is easily expressed as:

$$N_{\mu_{depth}} = K[(\frac{a_{eff}}{b_{eff}})(e^{b_{eff}X} - 1)]^{-\gamma_\mu}$$

Therefore the ADC at each OM should be proportional to the muon intensity:

$$ADC_{expect} \propto N_{\mu_{depth}}(X)$$

where X is the slant depth of the track element nearest to the OM.

Since the SPASE/AMANDA coincidence events we will study in this work have a zenith angle of only 12°, an OM is likely to receive its photons in the same ice layer as it was emitted, if the distance traveled is small enough. Ice layers are about 50 meters thick, so a photon traveling 100 meters away from a 12° track will travel 20 meters if it travels directly perpendicular. But of course at these distances photons are sure to have scattered several times *en route* and in reality photons begin to cross across different ice layers at distances more like 80 meters. Past this distance, the

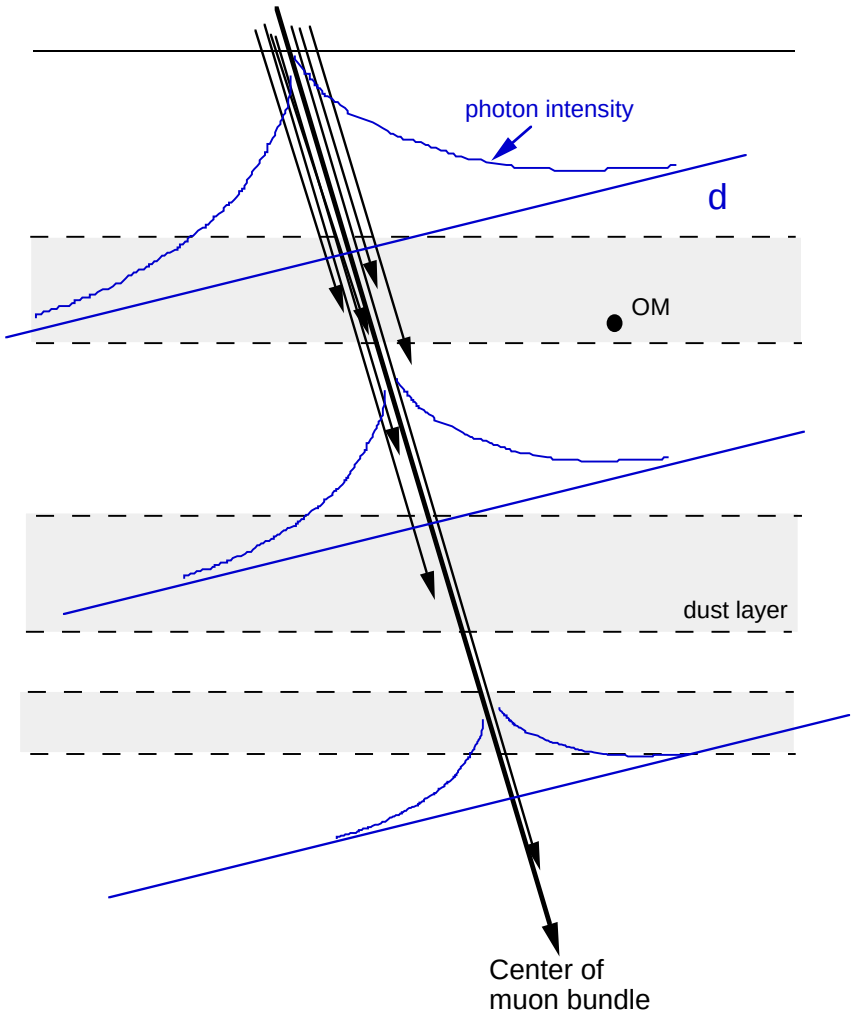

Figure 5.5: Schematic of the light intensity field surrounding a muon bundle. The observed average ADC will be higher for OM's at shallow depths (range-out correction) and lower for OM's in dust layers (dust layer correction).

propagation behavior observed by the OM more resembles bulk ice properties rather than that of the OM's resident ice layer; the "bulk" ice has its own propagation length $\lambda_{eff}(bulk)$. So here the exponential shape of the ADC changes slope from $\lambda_{eff}(z)$ to $\lambda_{eff}(bulk)$. The lateral distribution function is best described, therefore, by a split function with $\lambda_{eff}(z)$ below a transition point D and $\lambda_{eff}(bulk)$ above it:

$$ADC_{expect} = \begin{cases} NN_{\mu_{depth}}(X)\frac{1}{\sqrt{\lambda_{eff}\, d}}e^{d/\lambda_{eff}(z_{OM})} & , d < D \\ N'N_{\mu_{depth}}(X)\frac{1}{\sqrt{\lambda_{eff}\, d}}e^{d/\lambda_{eff}(bulk)} & , d > D \end{cases}$$

The normalization of the two curves must match at the transition point:

$$N' = Ne^{-(D/\lambda_{eff}(z) - D/\lambda_{eff}(bulk))}$$

5.5.3 Testing the theory with data

The distribution of light relative to a track is difficult to measure experimentally in AMANDA, because the track itself must be reconstructed using only information from the same light. However, SPASE coincidences can be used as a sample of reliable tracks or a calibration beam. A very accurate track can be reconstructed by anchoring the track at shower core on the surface and varying only the zenith and azimuth in AMANDA using the timing of OM hits (this will be discussed in more detail in the next sections). Once the ADC *average* behavior has been tested using *timing only*, we will use ADC's for more specialized reconstruction on an event-by-event basis.

Figure 5.6 shows the average ADC as a function of OM depth, for several different regions of distance. The expectation from the theory matches the data particularly well in the range of 50-80 meters, but matches reasonably well at all distances. Figure 5.8 shows the ADC as a function of distance, for several different regions of depth. Here we can see the shape of the lateral distribution function within each icelayer.

At small distances (such as 25 meters), the measured ADC's appear to follow the bumps and wiggles of the icelayers with a "phase shift" in depth of about 20-30 meters, which disappears for farther distances. The explanation for this effect is: photons at short distances arrive unscattered from muons which are traveling downward. Therefore the OM is sampling light primarily from the ice directly *above* it. At farther distances, photons have been scattered and isotropized by the time they reach the OM, so the OM samples more equally from the ice both above and below it.

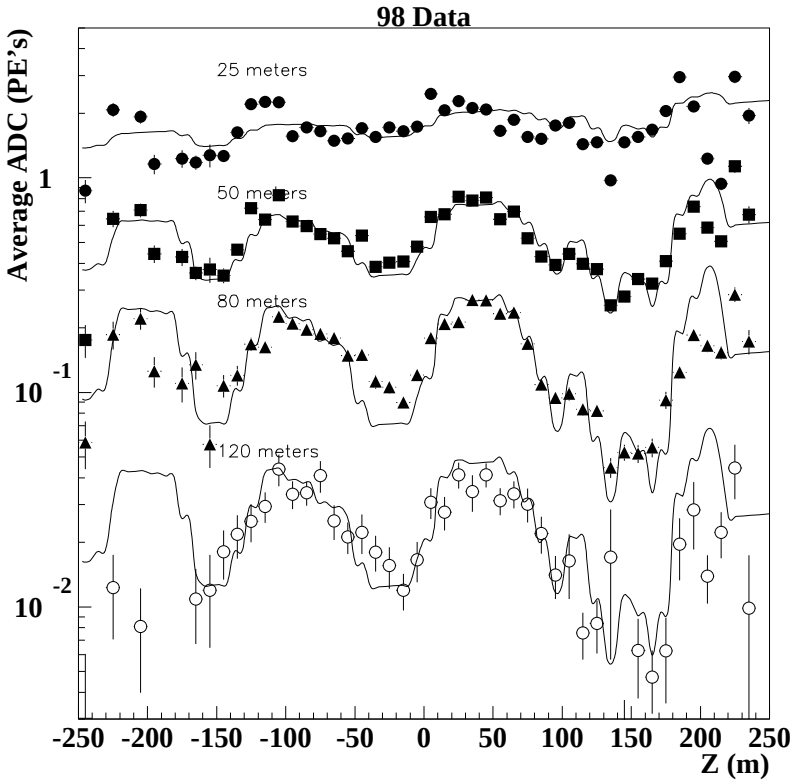

Figure 5.6: ADC as a function of OM depth, for four slices of perpendicular distance. The dotted curve is the theoretical expectation presented in this chapter (with an arbitrary absolute normalization).

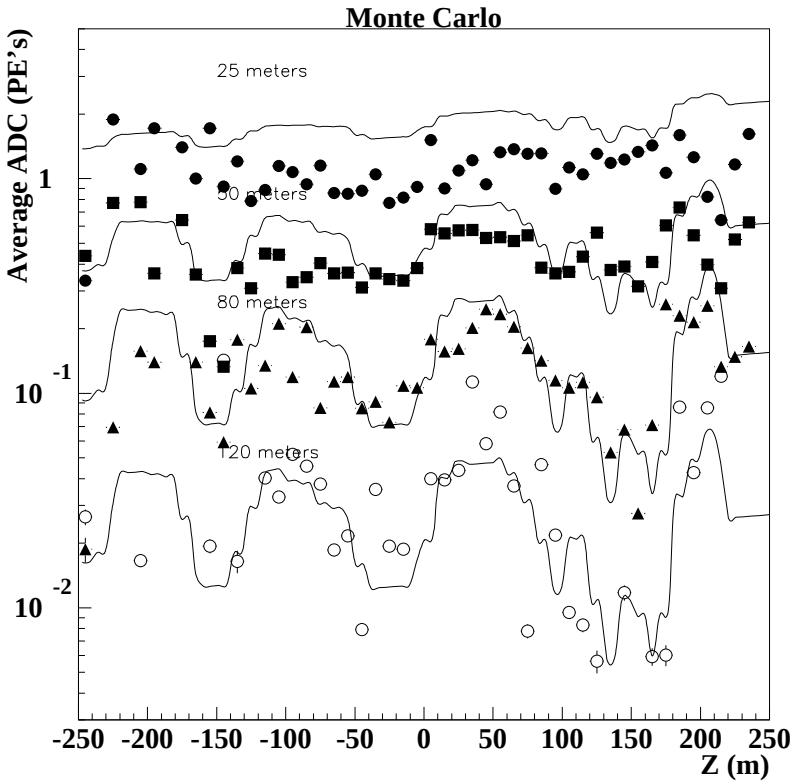

Figure 5.7: Same as Figure 5.6, but for Monte Carlo.

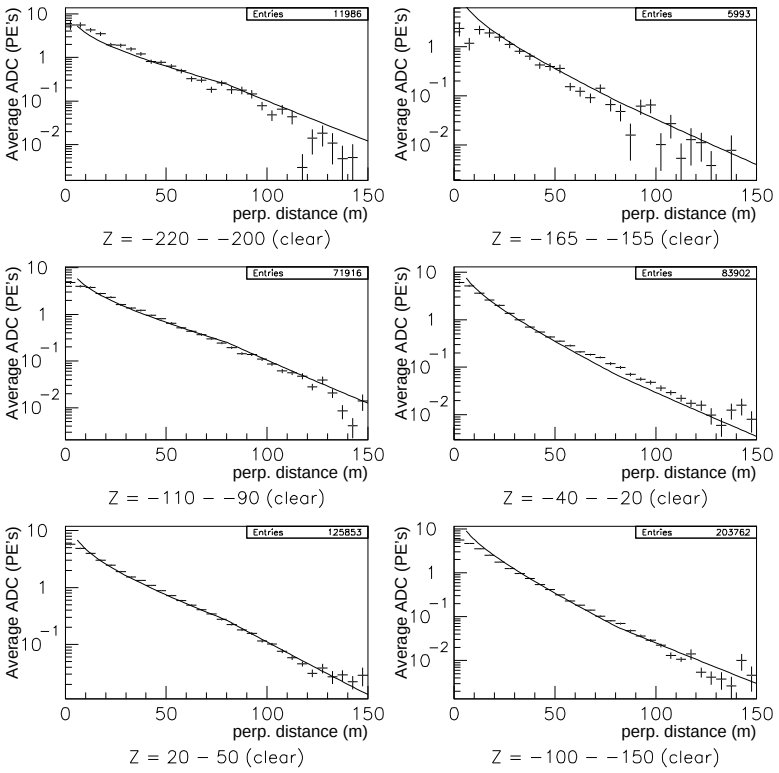

Figure 5.8: ADC as a function of perpendicular distance, for six slices of OM depth. The dotted curve is the theoretical expectation (as in Figure 5.6)

5.6 Reconstructions

5.6.1 General AMANDA reconstruction philosophy: maximum-likelihood

Hits in AMANDA are not only few in number and sparse in their geometry, but also often resulting from light which has been scattered *en route*. Thus, a geometric fit of a perfect Cherenkov cone to the timing of hits (similarly to what is done in SPASE for instance) does not work very well in AMANDA. Scattering being a probabilistic process, AMANDA's reconstruction technique must also be probabilistic.

AMANDA's reconstruction software package, `recoos`, has a likelihood maximizer at its core. The user inputs an event (with its pattern of hits, amplitudes, and times) and a hypothesis track with some number of free parameters (for instance, vertex position (x_0, y_0, z_0) and track direction (θ, ϕ)). `recoos` then iterates through different values of the free parameters, for each one computing the total likelihood $\mathcal{L}$ of the event having arisen from the test hypothesis:

$$\mathcal{L} = P(obs.event|hypothesis) = \prod_{OM's} \mathcal{L}_{OM}$$

$$-\log(\mathcal{L}) = \sum_{OM's} -\log(\mathcal{L}_{OM})$$

The minimizer adjusts the free parameters until $\mathcal{L}$ is maximized. (In practice, the "negative log likelihood" $-\log(\mathcal{L})$ is more easily manipulated, and it is this quantity which is *minimized* by `recoos`, hence the confusing nomenclature.)

The heart of the question, of course, is how to compute $\mathcal{L}_{OM}$? This quantity is the probability of observing a certain hit (or hit pattern) given a hypothesis (most simply, an infinite muon track). But $\mathcal{L}_{OM}$ is difficult to compute; one must incorporate the physics of scattering and absorption into non-trivial probability distributions.

Standard muon reconstructions in AMANDA use only the arrival time information from the first hit in OM's. Given a track hypothesis, the probability distribution function of arrival times for a hit are expressed by the "Pandel function" [72]. The distribution function depends on the perpendicular distance of the OM from the track d, and its orientation angle to the Cherenkov light

from the track. A parametrization of this function, including some extra features and corrections such as PMT jitter time, has been implemented in AMANDA as a likelihood function called "Upandel." Its use and accuracy in reconstructing muon tracks has been well documented elsewhere [88, 76].

5.6.2 SPASE, AMANDA, and Combined fits

Between the two detectors, each event can be reconstructed in a plethora of different ways. SPASE fits the event using only SPASE hit information, independently of AMANDA (this will be called the "SPASE fit" in this work, described already in Chapters 3 and 4). Similarly, AMANDA reconstructs the same events using only AMANDA hit information, independently of SPASE (the "AMANDA fit"). There is a great diversity of techniques for doing this as well; the one used here is a "Upandel" fit with inverted Bayesian weighting[4]. Thirdly, information from the two detectors can be used together. Techniques for doing this have not been adequately explored, however there is one straightforward method that I call "core-anchoring." The location of the shower core is very well-measured by SPASE, and the center of AMANDA is 1750 meters away. If the track is "anchored" or fixed at the point of the core at the surface, then the hit information from AMANDA can fine-tune the track's direction with a long lever arm. The combined fit is implemented by assigning the track vertex (x_0, y_0, z_0) to the SPASE core at the surface, and allowing AMANDA's reconstruction program `recoos` to fit the track using its standard Upandel maximum-likelihood method but with only θ, ϕ, and time t_0 as free parameters.

5.6.3 An ADC-based maximum-likelihood reconstruction

The focus of this work is the calorimetry of muon-produced light. The amount of light can be measured primitively with the number of hit channels, but a better estimate can be measured using amplitude information from hit modules, and also the "no-hit" information (effectively, amplitude=0) from modules which are not hit.

As with any maximum-likelihood method, we must input a hypothesis track. Here, the hypothesis is a tight muon bundle surrounded by an exponentially-falling intensity of photons. As

[4]This is a likelihood-weighting technique used in AMANDA to pick out neutrino-induced muons out of the overwhelming background of cosmic ray muons. Since the technique discriminates between upward and downward tracks, the weighting must be inverted if one wants to study downgoing muons of the same quality as upgoing neutrino candidates. More details on the technique itself can be found in [93].

shown earlier in this chapter, the photon intensity as a function of distance d is parametrized as split exponential, with terms representing the intensity of muons as a function of slant depth X, and the effective attenuation length of both scattering and absorption as a function of OM depth z_{OM}. We will now use this to reconstruct muon bundles, by finding the hypothesis which best matches the ADC data.

For each OM, we must compute ADC_{expect} from the position of the OM relative to the track, the surface, and the layered ice properties. First of all, the slant depth X of the OM is defined as the distance between the track vertex at the surface and the point on the track where the OM's perpendicular intersects, shown in Figure 5.9. From X we compute $N_{\mu_{depth}}$ as described in previous sections. The normalization constant is redefined such that this quantity is equal to one at a reference depth of 1750 meters (which, for a zenith angle of 12°, is approximately the center of AMANDA). Next, $\lambda_{eff}(Z_{OM})$ is reexpressed as the bulk λ times a correction factor accounting for scattering:

$$\lambda_{eff}(z_{OM}) = \lambda_{eff}(bulk)\left(\frac{b_e(z_{OM})}{b_e(bulk)}\right)^{-1} = d_0\frac{b_e(bulk)}{b_e(z_{OM})}$$

For each OM's depth z, the scattering coefficient b_e is looked up from the table of data measured using a YAG laser in [83] (plotted in Figure 5.2), and compared to the bulk b_e at this wavelength (which is 0.042), to obtain a the correction factor $c_{ice} = \frac{b_e(bulk)}{b_e(z_{OM})}$. Meanwhile, all the normalizations (including the total number of muons) are lumped together into a single overall normalization A.

Putting it all together then, the expected ADC is then computed as:

$$ADC_{expect} = \begin{cases} AN_{\mu_{depth}}(X)\frac{1}{\sqrt{d_0 c_{ice} d}}e^{d/(d_0 c_{ice})} & , d < D \\ AN_{\mu_{depth}}(X)e^{-(D/(d_0 c_{ice}) - D/d_0)}\frac{1}{\sqrt{d_0 c_{ice} d}}e^{d/d_0} & , d > D \end{cases}$$

where A and d_0 are left as free parameters; one measuring the shape of the light's lateral distribution function (in the absence of dust), and the other measuring the total intensity of muons in the bundle. The complete track is parametrized, therefore, by eight parameters: $(x_0, y_0, z_0, t_0, \theta, \phi, A, d_0)$, where A and d_0 are the intercept and inverse-negative-slope of the underlying photon distribution.

The likelihood of an event under this scheme is computed in the following way for each OM:

$$\mathcal{L}_{OM} = P(ADC_{measured}|ADC_{expect})$$

where P is a Poisson probability. Then, the total $-\log\mathcal{L}$ for the event is simply the sum of the $-\log\mathcal{L}_{OM}$'s for all OM's, both hit and not hit.

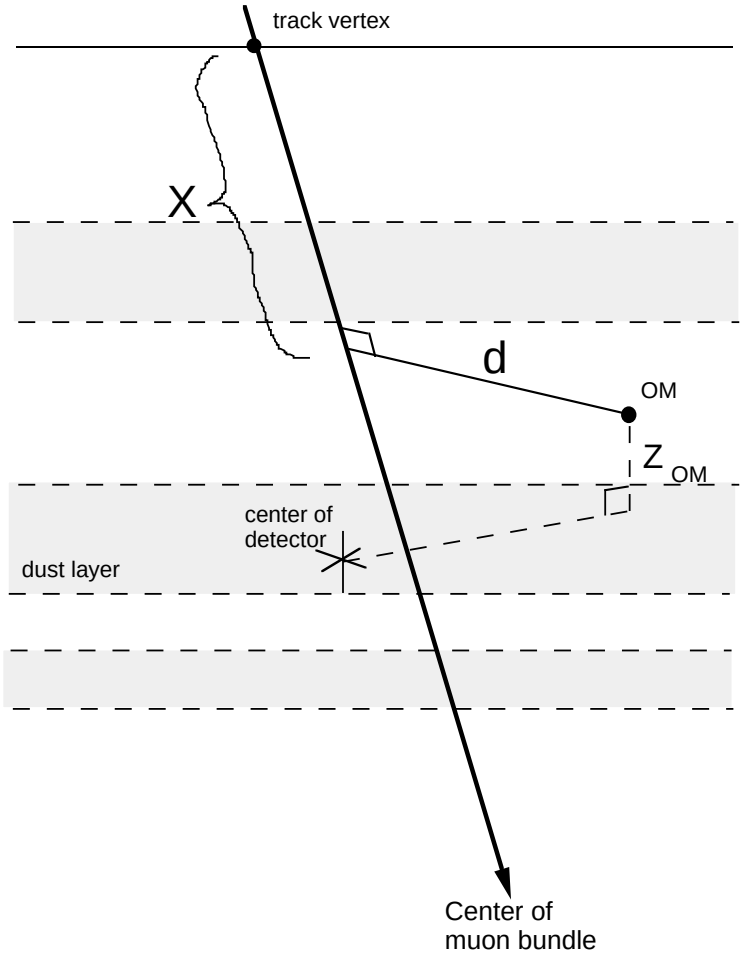

Figure 5.9: Coordinates used by ADC reconstruction.

Fit number	Fit	Type
1-3	SPASE fit (all identical)	SPASE
4	Line fit	AMANDA
5	Full fit (inv. Bayes)	AMANDA
6	Full fit (std. Bayes)	AMANDA
7	Tensor fit	AMANDA
8	Iterative full fit	AMANDA
9	Core anchoring + Full fit	Combined
10-12	(First iteration of new fits)	(Not used)
13	Core anchoring + Full fit + ADC	Combined
14	SPASE + ADC	Combined
15	Core anchoring + ADC (track free)	Combined

Table 5.2: Summary of fits performed on SPASE/AMANDA coincidences.

Figure 5.10 demonstrates the fit for a single event; large enough that one can see the lateral distribution function of ADC's by eye. The curve is the theoretical function (for bulk ice, at 1750 meters slant depth) according to the fit results for A and d_0. The fit is well-constrained by the data.

Three different fits using this likelihood formulation were performed:

- Combined fit (SPASE core + AMANDA timing) track fixed, A and d_0 fit as free parameters.
- SPASE track fixed, A and d_0 fit as free parameters.
- SPASE *core position* fixed, A, d_0, and track direction (θ, ϕ) fit as free parameters.

These are the last three fits in Table 5.2, which contains a summary of all the fits used in this work.

5.7 Performance of the fits

Which is the most accurate track? This question can only be answered in Monte Carlo, where the true primary track is known.

The three contenders are: the original SPASE track, and the two core-anchored combined fits (one based on timing and the other on ADC's). The combined fits would logically have an advantage; with the 1750-meter lever arm between the two detectors, using information from both can pin down the track very accurately. The core position in SPASE is a very well-measured quantity and a reliable "anchor" for the combined fit; all that remains is to reconstruct the direction angles (θ, ϕ) for which there is already a good first guess. However, AMANDA tends to reconstruct events

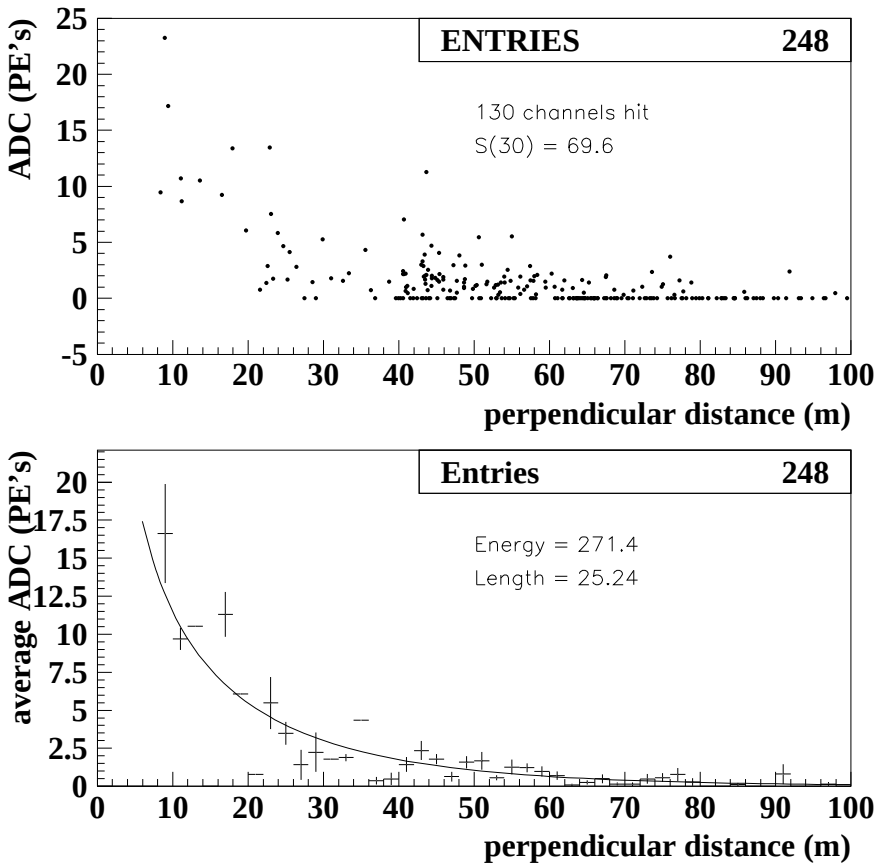

Figure 5.10: OM amplitudes as a function of perpendicular distance, for one example event (upper), its average lateral distribution (lower), and the result of this ADC-based fit: the energy and length parameters A and d_0 and the ice-averaged ADC lateral distribution derived from the fit parameters.

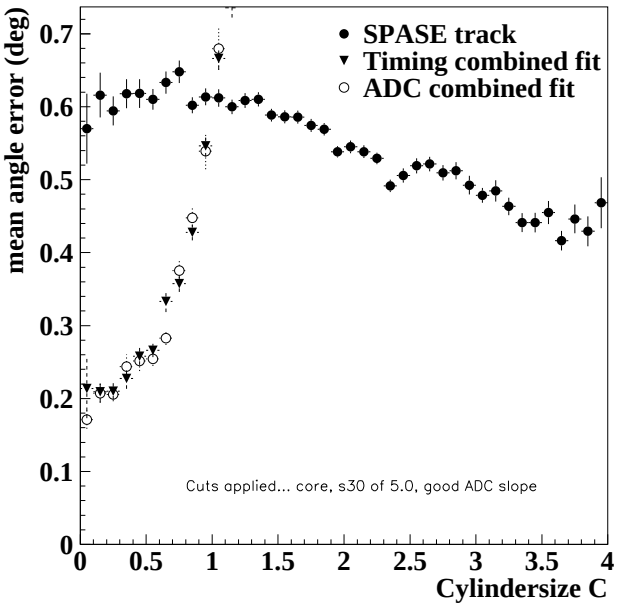

Figure 5.11: Mean angular resolution (in Monte Carlo) as a function of cylindrical proximity, for the SPASE track and combined fits.

better if the track is within its physical volume. Thus, SPASE tracks which pass *outside* AMANDA tend to get inadvertently pulled *in* by both the combined fits, distorting their accuracy. The original SPASE track itself, of course, suffers from no such bias, but is less precise of a fit. This can be seen in Figure 5.11, which plots the angular resolution vs. cylindrical proximity[5] to AMANDA for the three candidate tracks. For tracks that penetrate the physical volume of AMANDA ($C < 1.0$), the combined tracks excel. But for tracks passing outside this volume, the resolution of combined tracks suffer.

As the shower energy rises, the SPASE detector alone can fit the event more and more accurately. With higher particle counts in the scintillators, both the core location and the direction are better known. This can be seen in Figure 5.12, which shows the angular resolution of our fits vs. $S(30)$. At very high energies, the SPASE track's accuracy becomes comparable or better than the combined fits. However, in this work many more events inhabit the low-$S(30)$ ranges where the combined fits are preferred.

[5]This quantity, a measure of how close a track comes to the physical volume of AMANDA, will be defined and discussed in more detail in Chapter 6 and Appendix A.

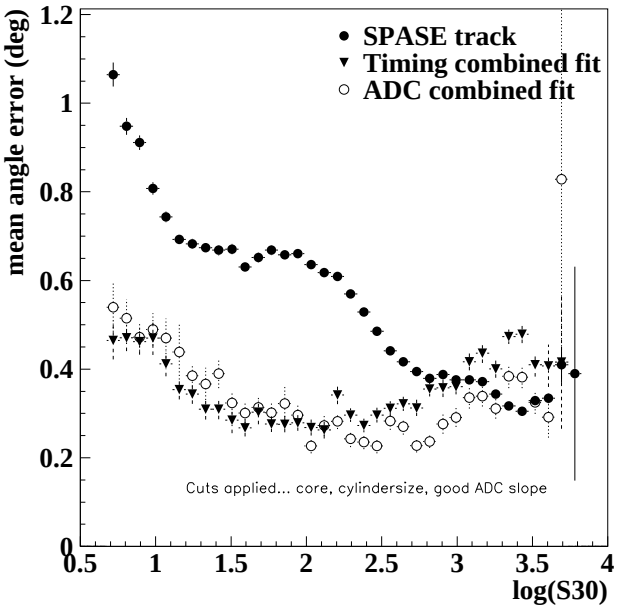

Figure 5.12: Mean angular resolution (in Monte Carlo) as a function of $S(30)$, for the SPASE track and combined fits cut to $C < 1.0$.

Thus, to use the combined fit tracks, we restrict the data set to those events passing inside AMANDA's physical volume ($C < 1.0$). This greatly reduces the number of events at our disposal, but provides a high-resolution sample.

Chapter 6

Cuts

6.1 SPASE cuts

If we are to fully take advantage of the SPASE detector as a "calibration beam" of muons or use SPASE's measurements of them in a composition analysis, then we must ensure that this beam is of the highest precision possible. SPASE reconstructions vary in both direction and energy accuracy. To choose a "starting set" of SPASE events for which these measurements from SPASE can be considered reliable, we will impose some quality cuts on the SPASE events which comprise our data and Monte Carlo sets, following similar methods as are used by other experiments.

6.1.1 Angle of SPASE direction toward AMANDA

The SPASE-AMANDA data set contains *all* SPASE triggers and the AMANDA events associated with them, even if the shower goes nowhere near AMANDA. Tracks which miss AMANDA completely will have no real hits and will not make it to later stages of analysis; eliminating these events early on reduces the data set, reduces contamination by accidental triggers (from, for instance, a coincident muon in AMANDA from another direction), and allows us to better directly compare data and Monte Carlo (which is generated only in a fixed zenith angle region of 0° to 32° and an azimuth angle region of 205° to 290°).

Thus, a simple initial cut requires that the space angle difference Ψ between the SPASE track and a line connecting the center of SPASE to the center of AMANDA ($\theta = 12^\circ, \phi = 247^\circ$) must be less than 20°. Reducing the solid angle acceptance from 2π to roughly 6% of that (in a particular

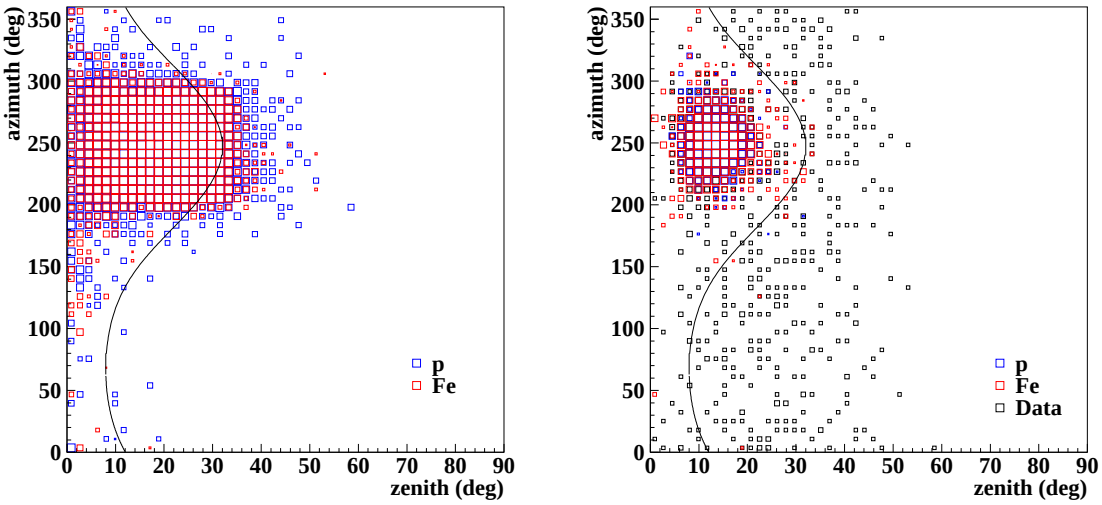

(a) SPASE direction of Monte Carlo events, before `recoos`.

(b) SPASE direction of events that remain after `recoos` (Monte Carlo in color, data in black)

Figure 6.1: Scatterplot of event zenith and azimuth directions for this data set, and proton and iron Monte Carlo (blue and red, respectively), and data (black, which is uniform over all directions in 6.1(b) and so is not shown there). The curve represents the cut $\Psi < 20°$.

nearly-vertical and high-efficiency direction) results in a reduction of raw data events by a factor of three. This cut is designed to be loose enough to pass any event that might be useful later in the analysis; it covers a wide enough swath of zenith and azimuth angles that we are in no danger of losing good events (see Figure 6.1). The cut is done by hand for 1997 data, but is performed in a "pre-analysis" stage for 1998 data.

6.1.2 SPASE core position

Although in theory an air shower detector can fit a lateral distribution function to find the core position even if it is outside the array, these fits are less reliable than if the core is inside the physical array. So we will include only events whose core is within the physical area of the SPASE detector *at the surface*. Almost all air shower experiments make a cut like this to ensure event quality.

A "surface map" of core locations for data events is shown in Figure 6.2, and the equivalent

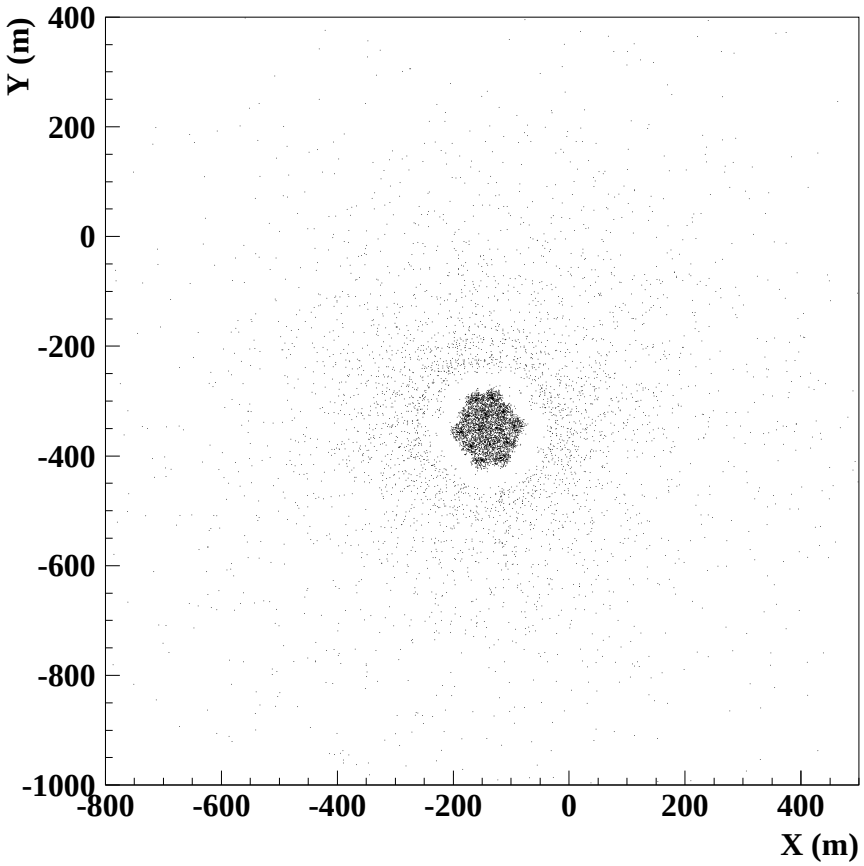

Figure 6.2: Surface core position coordinates of coincidence data events (no other processing or cuts). The same behavior is also found in Monte Carlo.

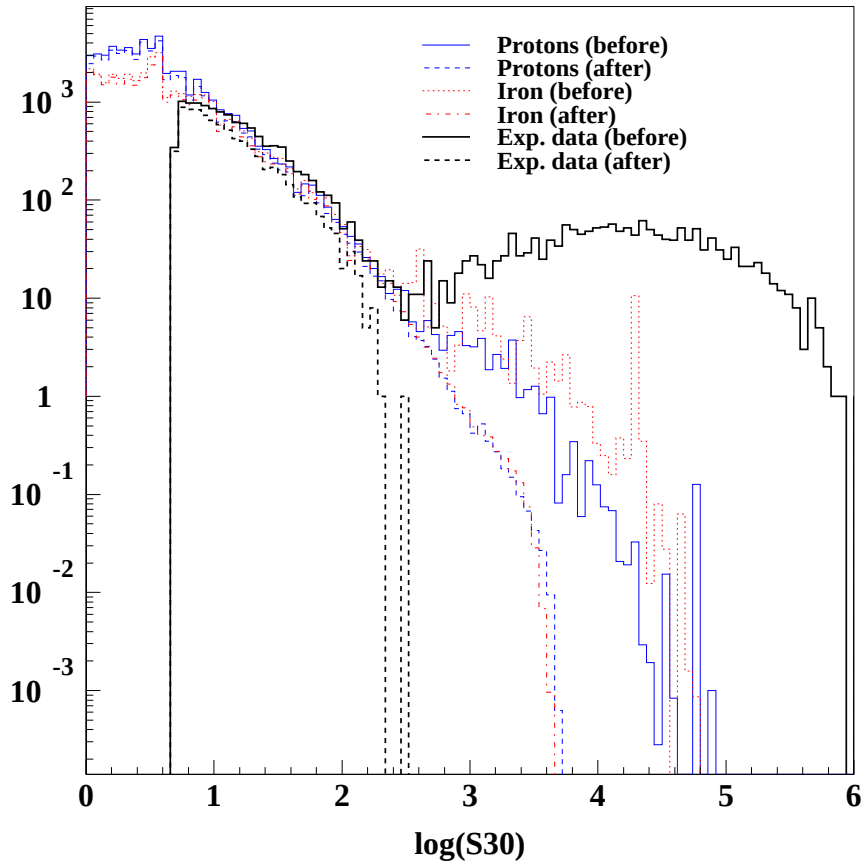

Figure 6.3: Effect of the SPASE core cut (must land within a radius of 60 meters from the center of SPASE) on the distribution of $S(30)$. Solid curves: before the cut. Dashed curves: after the cut.

map for Monte Carlo looks similar. In both data and Monte Carlo, the bulk of events land within the SPASE detector itself, but there is a "haze" of events outside the detector. The events in this haze are responsible for the long tail of very high $S(30)$ values, a result which is clearly unphysical and due to lateral distribution fits gone wrong. We can make a simple circular cut on the core position (defined as x_0 and y_0), as follows:

$$\sqrt{(x_0 - x_{center})^2 + (y_0 - y_{center})^2} < 60 \text{ m}$$

Cutting these events away leaves a much more sensible distribution of $S(30)$. The effect of the cut on the $S(30)$ distributions of data and Monte Carlo is shown in Figure 6.3. The cut removes about 10% of the data, almost all of it from the unusual high-$S(30)$ tail. After the cut, there is still a discrepancy between data and Monte Carlo at high values of $S(30)$. This will be addressed later, in Chapter 9.

6.1.3 Cuts on $S(30)$

The attentive reader has probably noticed the discontinuity in Figure 6.3 at $S(30) = 4$, and the strange behavior of both Monte Carlo and data below this size in other figures thusfar. The reason for the change in behavior is a break in the analysis technique. A primitive estimate of $S(30)$ is always made first, extrapolated from the 3rd and 4th highest-intensity stations. If this estimated $S(30)$ is less than four, the software concludes that the event is too small for a full-likelihood $S(30)$ fit to be effective and it records the estimate as-is. If the estimated $S(30)$ is larger than four, the software proceeds to the full-likelihood (and more accurate) reconstruction of $S(30)$. When this is performed, some events will now reconstruct with a small $S(30)$, and will supplement the bins less than four. To avoid this strange mix of events all with likely-misestimated shower parameters, all events with $S(30)$ less than five are discarded in this analysis.

Above $S(30) = 5$, the angular resolution of SPASE (Figure 4.4(a)) and also of combined SPASE/AMANDA fits (Figure 5.12) improves steadily with increasing shower size. Above $S(30)$ values of about 10, the resolution is stable and better than a degree. However, low-$S(30)$ events (in the range $5 \leq S(30) < 10$) will be important for this work; they comprise over half of the events above $S(30) = 5$, and we will not throw them away just yet. Instead, we will address angular resolution

"quality control" is a more efficient way a little later in this chapter.

6.2 AMANDA cuts

AMANDA is a sparse array, deployed in a natural medium, under uncontrolled conditions. For many events, there is simply not enough information contained in the hits (and their times and amplitudes) to uniquely characterize the event. If the hit pattern is an ambiguous splash of light and is not sampled adequately by the array (such as for instance stray light from a large bremsstrahlung outside of the array) reconstruction algorithms are easily confused. Therefore AMANDA analyses depend more heavily on quality cuts than other experiments. To do neutrino physics, they are essential for the separation of signal and background. To do cosmic ray physics, they are essential to evaluate the reliability of a reconstruction.

Many different manifestations of quality cuts are used in AMANDA and will be referred to in this work; they require a brief overview. Some were designed for neutrino signal separation, used commonly by the entire collaboration. Others are unique to this work and designed for composition studies.

6.2.1 Convergence in `recoos`

To constrain five free parameters (which define a track direction), an event needs a minimum of five hits[1]. To successfully converge on a maximum likelihood in a multidimensional likelihood space requires quite a bit more; the hits must be consistent with some preferential track. To put it simply, the event must have five or more hits that make some kind of sense. This condition preserves only about 4% of events from the data set, removing all the very low energy events and events which pass so far outside of AMANDA that AMANDA does not respond. The efficiency of this process will be discussed in further detail in Chapter 7.

6.2.2 The Inverted LBL Filter

To processes a complete year's data set in detail searching for a few neutrinos out of the overwhelming downgoing background is CPU-impractical; instead, a fast filter for upgoing events is

[1] After hit cleaning

applied to bring the data to a more manageable size first. A linefit (a simple χ^2 fit to the time flow of hits in the detector) is performed, and only events which pass the following cut:

$$\theta_{linefit} > 50^\circ$$

are kept in the data set. Then, a slower maximum-likelihood fit or "full fit" is performed on the remaining events. Only events which pass the next cut:

$$\theta_{fullfit} > 80^\circ \quad \text{AND} \quad NdirB_{fullfit} > 2$$

are kept. Here "$NdirB$" is the number of unscattered (or "direct" hits).

These cuts are designed to initially determine the track's direction (is it upgoing?) and quality (does it have a few nice hits?). Since the fits and cuts are performed at Lawrence Berkeley Laboratory, it is known as the "LBL Filter." All further neutrino analyses are done downstream of this procedure.

To apply this filter to SPASE events, we must invert the zenith angle requirements of the cut. So, requiring an upgoing hypothesis to have $\theta > 50^\circ$ is equivalent to requiring a downgoing hypothesis to have $\theta < 130^\circ$. Thus, the "Inverted LBL Filter" which will will use on downgoing events consists of the following cuts:

$$\theta_{linefit} < 130^\circ \quad \text{AND} \quad \theta_{fullfit} < 100^\circ \quad \text{AND} \quad NdirB_{fullfit} > 2$$

6.2.3 UW Neutrino Cuts for 1997 neutrino analysis

After the LBL Filter, the data set is still overwhelmed by cosmic ray background compared to neutrino-induced signal. Further reconstructions and quality cuts are necessary to separate the two. Exact techniques for this vary from analysis to analysis (there are too many to describe), but we will choose one as an example: the atmospheric neutrino analysis performed at UW-Madison on 1997 data [79]. Six quality cut parameters were used in this analysis: the likelihood of the fit, the number of unscattered hits, the sphericity of the hits, the track length, the difference between line fit and full fit, and the uniformity in time (or "smoothness") of the hits along the track length.

The important thing to remember here is that these cuts were developed to separate upgoing muon events of high enough quality to be confident of their upgoing direction. In this work, all the muons of interest are already downgoing; we do not need to separate them from anything. Thus the

only reason to apply cuts such as these are to create a high-statistics event sample of downgoing muons which *resemble* the neutrino-induced upgoing sample. Thus these cuts are used *only* for calibrating AMANDA's response to upgoing muons; they will not be used for composition analysis.

6.3 Specialized cuts for combined SPASE/AMANDA analyses

6.3.1 Cylindrical proximity

Unlike underground detectors, AMANDA can be sensitive to tracks that pass outside its physical volume. The efficiency is higher for a particle traveling through the center of the detector than past the edges, of course, but even particles that travel completely outside the detector can trigger AMANDA if they produce enough light.

We would like to parametrize the proximity of a track to the detector, but since AMANDA is cylindrical in shape, a simple impact parameter to the center of AMANDA is not a good measure of this. Instead we define a cylinder of radius R and height $\pm H$ which is proportional by a constant to the physical size of AMANDA-B10; the cylinder's proportionality constant is its "size." In other words, a cylinder of the exact same size, shape, and position of AMANDA-B10, is defined as "size 1.0." A cylinder of "size 1.5" has the same center position, but has 1.5 times the radius, and is 1.5 times taller both up and down. The "cylindrical proximity" C of a track is defined as the size of the cylinder of closest approach, shown in Figure 6.4. A detailed derivation of how C is computed is given in Appendix A.

The distribution of C for data and Monte Carlo (after `recoos`) is shown in Figure 6.5. Although the statistics available drops fast when one cuts strictly on this parameter, requiring the track to pass through the physical volume of AMANDA (in other words, requiring $C < 1.0$) results in a very pure, reliable, and robust set of events. Relaxing this cut out to 1.5 doubles the number of events in the sample, but sacrifices quality.

6.3.2 2-D cut on cylindrical proximity and $S(30)$

As discussed earlier in this chapter, angular resolution of reconstructed tracks declines with increasing cylindrical proximity and with decreasing $S(30)$. Unfortunately, the number of event

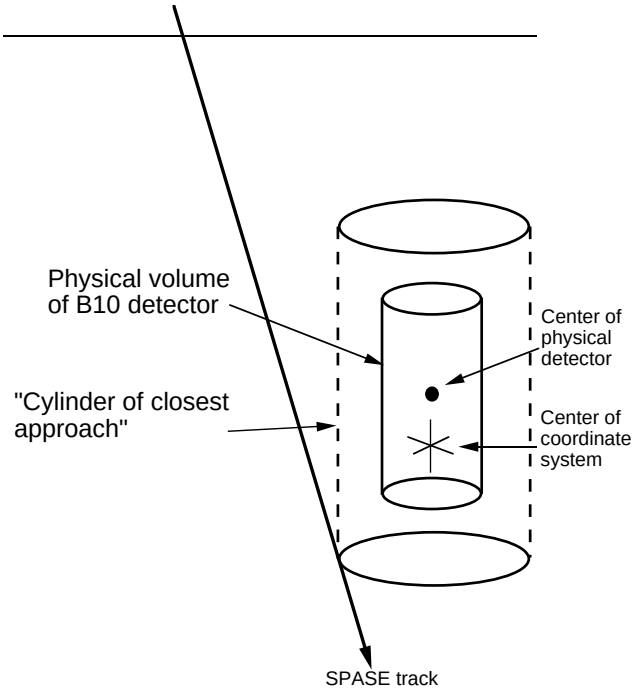

Figure 6.4: Schematic of the concept of "cylinder of closest approach."

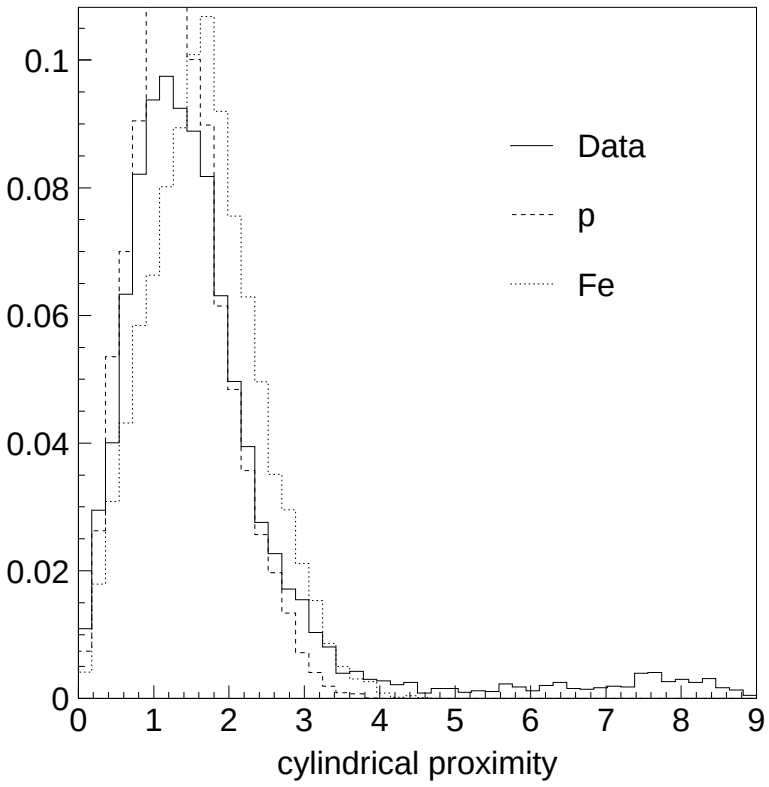

Figure 6.5: Distribution of cylindrical proximities C for data and Monte Carlo (after `recoos`). A tail of misreconstructed events is seen in the data; this is reduced with further quality cuts.

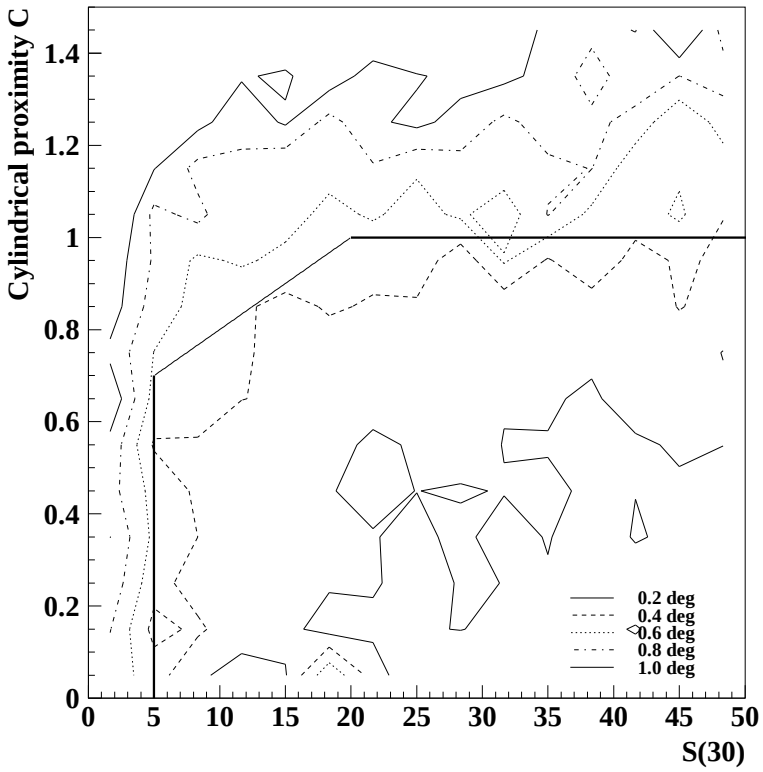

Figure 6.6: Contours of angular resolution, in the two-dimensional parameter space of $S(30)$ and C. The two-dimensional cut is also shown.

statistics also declines rapidly as these two cuts are tightened.

However, angular resolution can be preserved while still retaining events by making a two-dimensional cut in these two parameters. At small $S(30)$, the worse events are those which skim the edges of the detector ($C \approx 1.0$), while those that go through the center are still reconstructed well. Contours of constant angular resolution as a function of $S(30)$ and C are shown in Figure 6.6, together with a two-dimensional cut which preserves events with an average angular resolution of a half a degree or less.

6.3.3 Quality of N_μ fit slope

The negative-inverse-slope of the lateral distribution function (d_0) is determined by the ice properties; it should be equal to the effective attenuation length of blue light, about 26 meters.

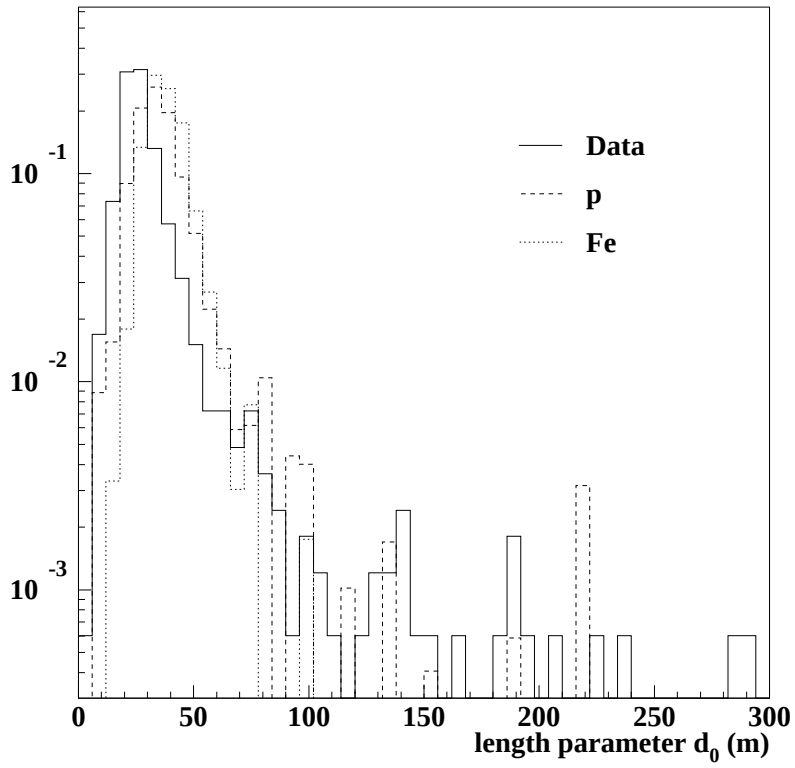

Figure 6.7: Distribution of reconstructed "length" parameter d_0.

However, we *reconstruct* this attenuation length rather than assume it. If d_0 is reconstructed as a negative or very large number, this means that the lateral distribution function did not reconstruct well (for instance, if the minimizer couldn't find a reasonable minimum), and the resulting calorimetric measurement is unreliable. We therefore use d_0 as a cut parameter for the composition analysis, throwing out any event for which d_0 is not between zero and 100 (see Figure 6.7 for distributions of this parameter). This cut does not have a large impact on the event statistics, it merely removes the most egregious outliers.

6.4 Event set for AMANDA calibration

To calibrate AMANDA for neutrino work, we duplicate the standard neutrino analysis chain on this data set, and also duplicate their cuts.

Cut	N_{events} total	$S(30) < 5$	$5 \rightarrow 10$	$10 \rightarrow 25$	$25 \rightarrow 50$	$50 \rightarrow 100$	≥ 100
none	4,119,206	3,316,767	324,124	226,552	73,083	31,201	147,479
Ψ	1,318,475	1,071,940	103,496	72,502	22,450	9,367	38,720
Ψ+core	1,181,105	1,032,709	86,337	46,747	10,752	3,663	897
core+`recoos`	43,082	34,422	4,403	2,957	871	348	81
core+`recoos`+C1.5	18,627	14,016	2,320	1,639	445	173	34
core+`recoos`+C1.0	9,609	7,236	1,192	848	223	96	14

Table 6.1: Efficiencies (event numbers) for some cuts.

- `recoos` convergence
- SPASE core cut
- LBL filter
- Loose cylindrical proximity cut (such as $C < 2.0$) *or* simple directional cut (such as $\Psi < 20^{\circ}$) (varied)
- Neutrino cuts (varied)

Other cuts can be applied later to these events for particular studies of calibration (see Chapters 7).

6.5 Event set for composition studies

Neutrino cuts must be very tight, because the signal is peeking out under a large background which much be rejected. For studying composition, however, we do not need the same standards of quality. Our only major requirement is a reliable track. Thus, the "composition event set" consists of all events which pass these cuts:

- `recoos` convergence
- SPASE core cut
- 2-dimensional cut on $S(30)$ and cylindrical proximity C
- ADC lateral distribution quality cut ($0 < d_0 < 100$)

These cuts were developed using approximately 55 days' worth from 1997; the event rates for the various cuts on this data sample are given in Table 6.1.

Chapter 7

Calibrating AMANDA with SPASE

Most telescopes can be calibrated either by pointing them at bright, well-understood objects in the sky (such as Vega in visible light or the Crab Nebula in x-rays), or by shining a calibration beam into the detector. AMANDA has neither kind of calibration source for high-energy neutrinos. But SPASE coincidences can provide such a calibration beam of downgoing muons. And although SPASE events have their limitations (they are muon bundles rather than single muons, downgoing rather than upgoing, and available only from one zenith angle), we can use them to measure some of the basic response properties of AMANDA.

7.1 Efficiency

The efficiency of the AMANDA detector is a complex function of zenith angle, particle energy, location in the detector, and a host of other factors. Characterizing the efficiency depends on accurate Monte Carlo which predicts the number of events with the potential to trigger, and the percentage of them that do.

However, the SPASE detector gives us an opportunity to measure and characterize certain efficiencies without depending on Monte Carlo. AMANDA data is taken whenever SPASE triggers, regardless of whether AMANDA triggers itself. Many of the coincidence events have few hits in AMANDA (and some have none). The efficiency (or "survival rate") of events can be plotted as the ratio between number of events which fulfill a condition and the total number of SPASE events.

To study the dependence of efficiency on energy and proximity, we have divided the parameter space into two coordinates: $S(30)$ and cylindrical proximity, C, and will examine AMANDA's

efficiency as a function of these two quantities. The data set is all 1997 SPASE coincidences which pass the SPASE "core cut" (described in the previous chapter).

7.1.1 Trigger efficiency

In normal operation, AMANDA reads out an event if more than 16 hits arrive within two microseconds. Understanding the properties of this multiplicity trigger is difficult, because it precedes any hit cleaning. Hits due to noise, crosstalk, afterpulsing, or other instrumental effects which are difficult to simulate can all participate in the trigger and effect the "turn-on" curve of AMANDA.

For SPASE coincidences, however, the trigger mechanism is completely different; the event is read out for *every* SPASE trigger at the surface. Within each SPASE coincidence event, we can count the number of hits which were read out, and estimate whether AMANDA would have triggered on its own[1]. The efficiency of SPASE events which have 16 hits or more in the event (before cleaning) is shown in Figure 7.1.

It should be warned that the actual operation of the 16-hit multiplicity trigger is not equivalent to this method (which merely counts up all hits within 32 microseconds). By including both true and accidental triggers, this method will *overestimate* the trigger efficiency.

7.1.2 `recoos` efficiency

All events are put through AMANDA hit cleaning and reconstruction (a process which requires a minimum of five good hits and convergence to a minimum). After this process, only 4% of events survive, most of which passed through or very near AMANDA. The efficiency as a function of $S(30)$ and C is shown in Figure 7.2; it reaches 100% at high energies and near proximities.

7.1.3 Cut efficiency for some typical AMANDA cuts

AMANDA analyses use a variety of quality cuts, some of which were described in the previous chapter. One can play a similar game with these cuts, testing the efficiency of the cut as a function of proximity and energy. Here we show as an example AMANDA's efficiency for the two cuts described

[1] All events are tagged, often with multiple triggers (such as "SPASE-2 and AMANDA-B10"). Ordinarily, this information is kept in the data stream, and events which *also* triggered AMANDA could be easily separated. However, in this sample of matched-up 1997 coincidence data, this information was somehow lost. It could be recovered by reprocessing all the data.

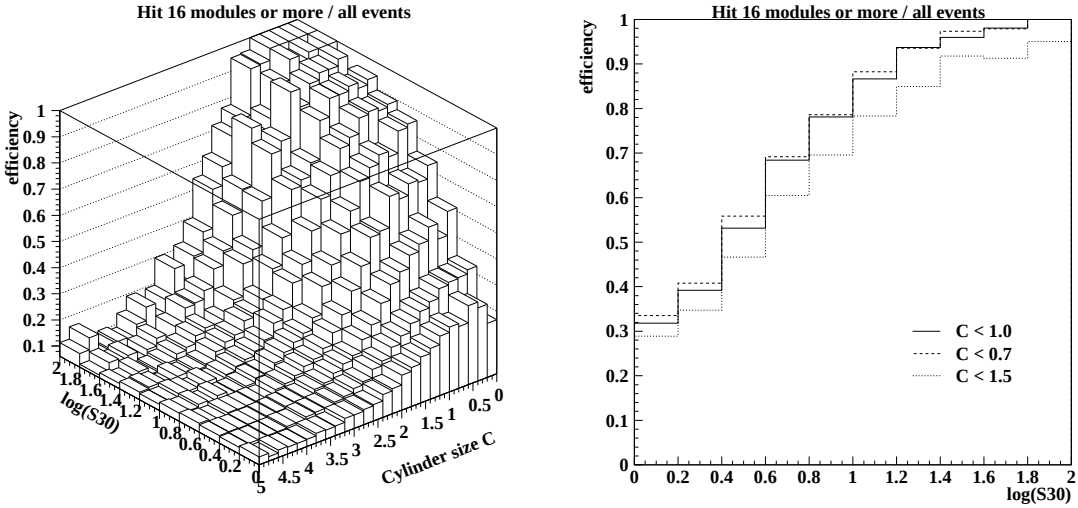

(a) Efficiency as a function of $S(30)$ and C

(b) Projection onto $S(30)$, for different C cuts.

Figure 7.1: Efficiency to have 16 (uncleaned) hits in AMANDA as a function of $S(30)$ and C.

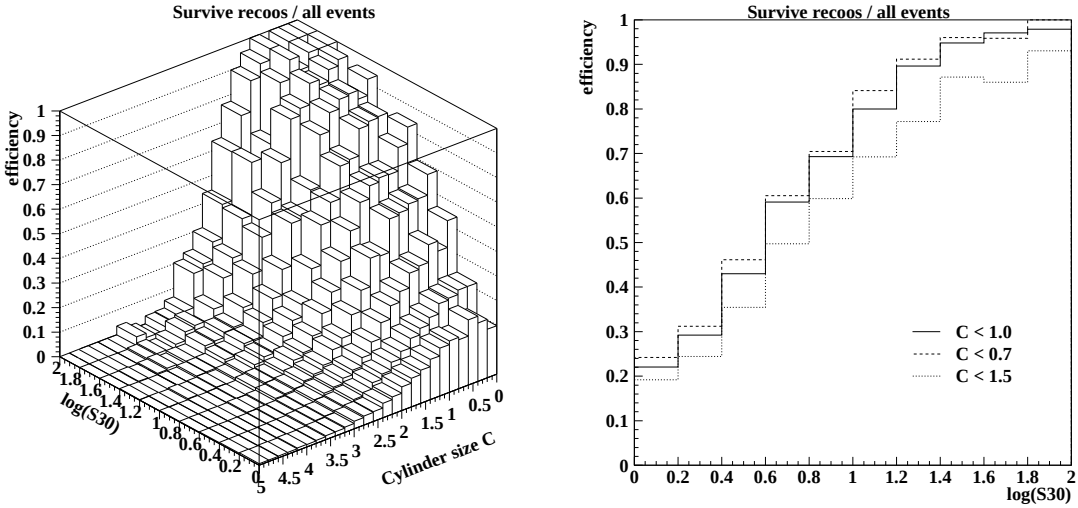

(a) Efficiency as a function of $S(30)$ and C

(b) Projection onto $S(30)$, for different C cuts.

Figure 7.2: Efficiency to reconstruct in AMANDA as a function of $S(30)$ and C.

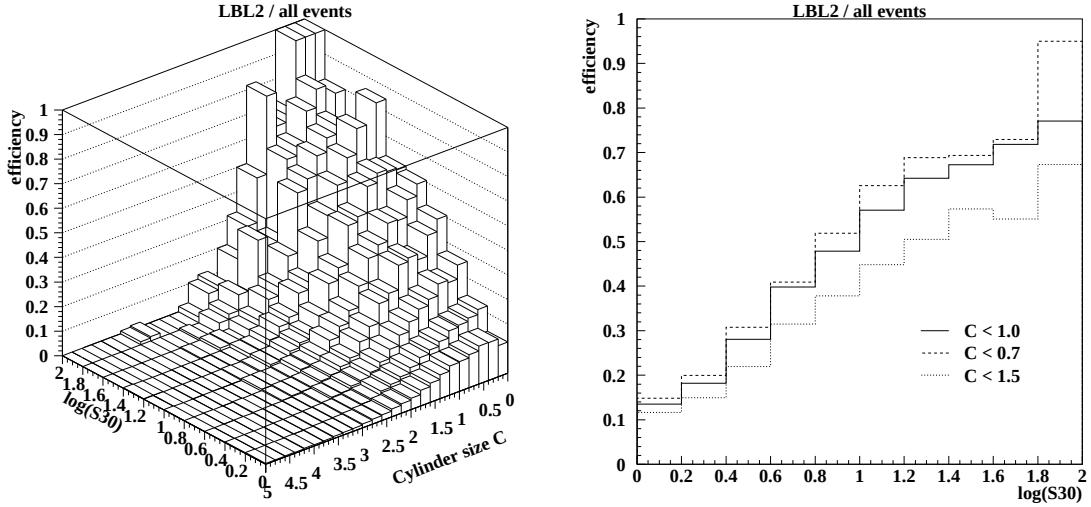

(a) Efficiency as a function of $S(30)$ and C

(b) Projection onto $S(30)$, for different C cuts.

Figure 7.3: LBL Level 2 efficiency as a function of $S(30)$ and C.

previously: the Inverted LBL Filter (Figure 7.3) and the UW neutrino quality cuts (Figure 7.4).

There are no "standard" AMANDA quality cuts; they vary from analysis to analysis. Cuts are different for specialized searches (i.e. for point sources or gamma ray bursts), and are always subject to improvement and change. This measurement is meant as a guideline; it gives us an indication of the sensitivity of our instrument to tracks outside the physical volume.

7.2 Pointing and angular resolution

Without any calibration sources of high-energy neutrinos in the sky, AMANDA is forced to measure its pointing accuracy and angular resolution with Monte Carlo simulations. However, the presence of SPASE on the surface allows for an independent measurement of these quantities. In fact, in 1997 there were not one but three surface detectors operating in coincidence with AMANDA: SPASE-2, SPASE-1, and GASP. The three detectors, operated completely independently and visible by AMANDA at two different zenith angles, increase our confidence that the result is not due to any surface-detector systematics.

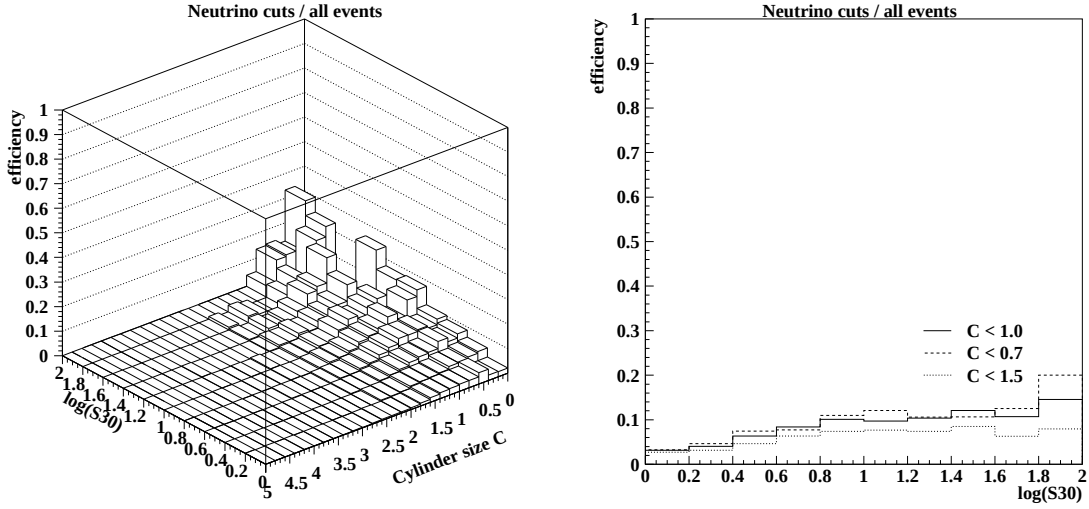

(a) Efficiency as a function of $S(30)$ and C

(b) Projection onto $S(30)$, for different C cuts.

Figure 7.4: Neutrino cut efficiency as a function of $S(30)$ and C.

For each coincidence event, SPASE-2[2] reconstructs the shower direction and core location on the surface from the arrival times of the scintillator hits; the resulting track is described by both the core location coordinates and the direction: $(x_S, y_S, z_S, \theta_S, \phi_S)$. Completely independently, AMANDA reconstructs the same event from the arrival times of the hits in the ice using the Upandel maximum-likelihood method (described in Chapter 5), and provides its own hypothesized track, described similarly by a vertex location and direction: $(x_A, y_A, z_A, \theta_A, \phi_A)$. We then compare the AMANDA direction (θ_A, ϕ_A) to the SPASE direction (θ_S, ϕ_S). By comparing directions only, and by comparing two completely independent measurements, we avoid seeing offsets that could be artificially introduced by an uncertainty in the absolute relative *positioning*[3] of the two detectors.

Since the angular resolution of the surface detectors (a degree or less for all three detectors SPASE-1, SPASE-2, and GASP) is much better than AMANDA's (about 3-4 degrees), the surface direction can be used as an estimate of the *true* shower direction. We then examine AMANDA's

[2] I will describe the technique for SPASE-2 coincidences, but of course the same procedure is followed for SPASE-1 and GASP.

[3] The relative positioning of SPASE and AMANDA has been calibrated independently, in [95] and [78].

Cut	color code
$\Psi < 20^\circ$, tight ν, all energies	black
$\Psi < 20^\circ$, tight ν, $S(30) \geq 10$	red
$\Psi < 20^\circ$, loose ν, all energies	green
$C < 1.0$, loose ν, all energies	blue
$C < 1.0$, tight ν, all energies	magenta
$C < 0.7$, tight ν, all energies	cyan

Table 7.1: Variety of cuts used to measure pointing offset in AMANDA

angular deviation from this estimate in zenith: $\Delta\theta = \theta_A - \theta_S$ and in azimuth: $\Delta\phi = (\phi_A - \phi_S)/\sin\theta_S$. Distributions of these variables are plotted for all events which pass certain quality cuts, and the resulting curve is fit to a Gaussian. Figure 7.5 shows some examples of the $\Delta\theta$ distributions (which show some interesting features). Six different cut combinations of varying stringency were tried, summarized in Table 7.1.

Looking at Figure 7.5, we see that the zenith pointing is offset from zero by about 2 degrees on average. This means that AMANDA systematically reconstructs tracks about 2 degrees *steeper* than the SPASE track. The shape of the distribution is not a perfectly symmetrical Gaussian; there is a tail at negative values (steeper AMANDA angles). The greater the asymmetry, the more the mean of the Gaussian is pulled to the negative. The magnitude of the effect varies with cut level; more constrained tracks exhibit more asymmetry, and SPASE-1 data is less asymmetric than SPASE-2. The causes of the asymmetry and of the overall shift are unknown.

The mean of the $\Delta\theta$ distribution is the "pointing offset" in zenith, and the mean of $\Delta\phi$ is the "pointing offset" in azimuth. Measurements of the pointing offsets (in both zenith and azimuth) for the three detectors are summarized in Figure 7.6. The center of the "crosshairs" in this plot represents a pointing error of zero (in other words, a reconstruction which on average points in the exact direction of the source). However, measurements from all three detectors lie at negative zenith offset of 1-2 degrees. This means that AMANDA reconstructs events on average 1-2 degrees steeper zenith than the direction of the source. There is a small negative offset in azimuth pointing, but is is negligible.

This is not the first discovery of a pointing offset in AMANDA; it has been noticed in AMANDA Monte Carlo for some time that reconstructed zeniths are 1-2 degrees steeper than the true track [81].

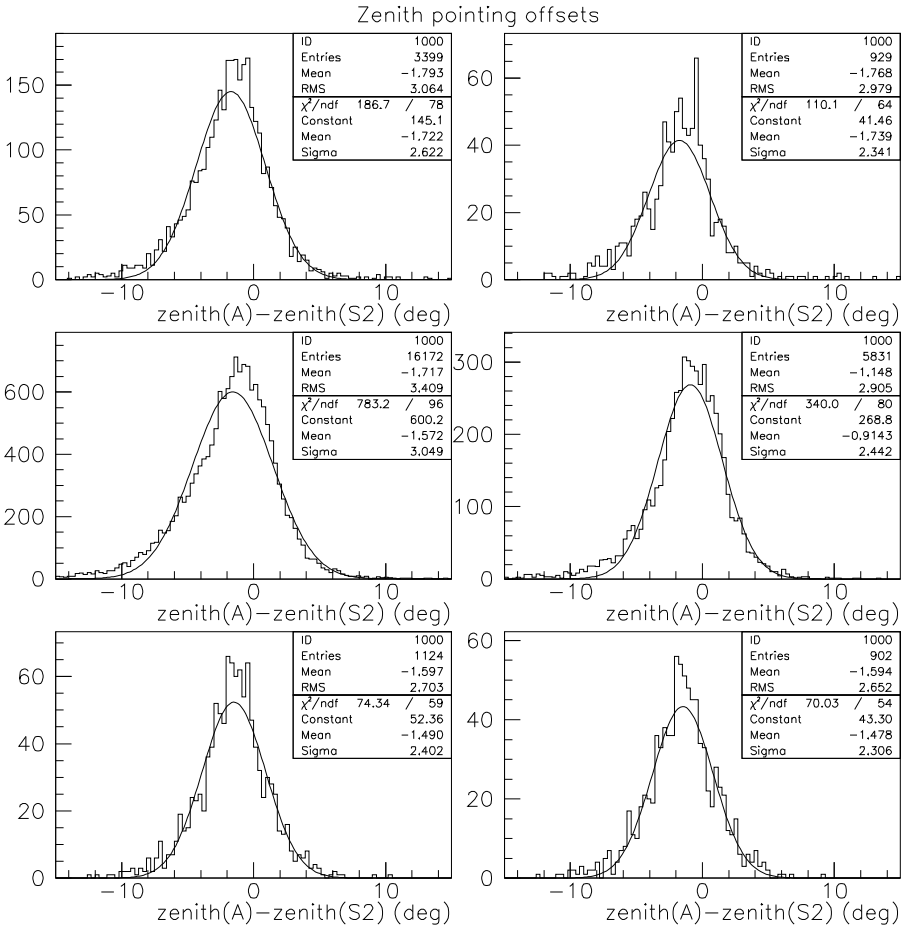

Figure 7.5: Pointing offset in zenith ($\Delta\theta$) relative to SPASE-2, for the six different sets of cuts listed in Table 7.1.

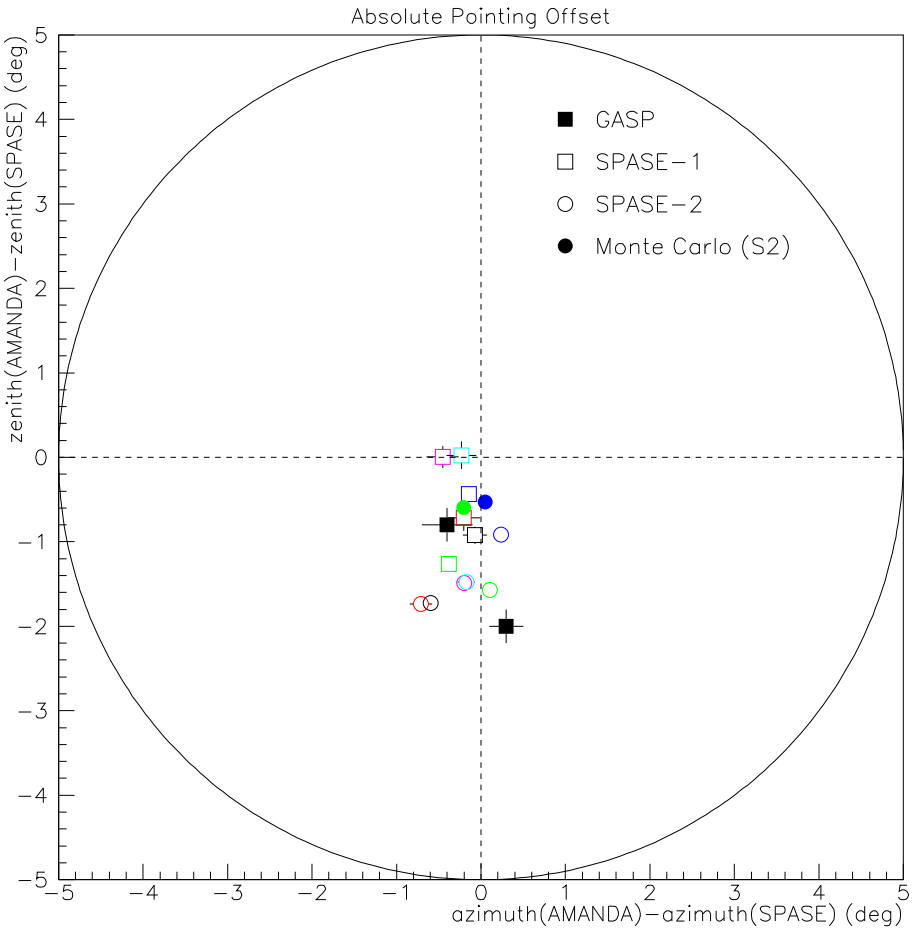

Figure 7.6: Pointing offset of AMANDA ($\Delta\theta$ vs. $\Delta\phi$), as measured relative to SPASE-2 (open circles), GASP (closed circles), and SPASE-1 (open squares). The two GASP points represent the two cameras in the detector. The six SPASE-2 and SPASE-1 points represent six different sets of cuts, listed in Table 7.1.

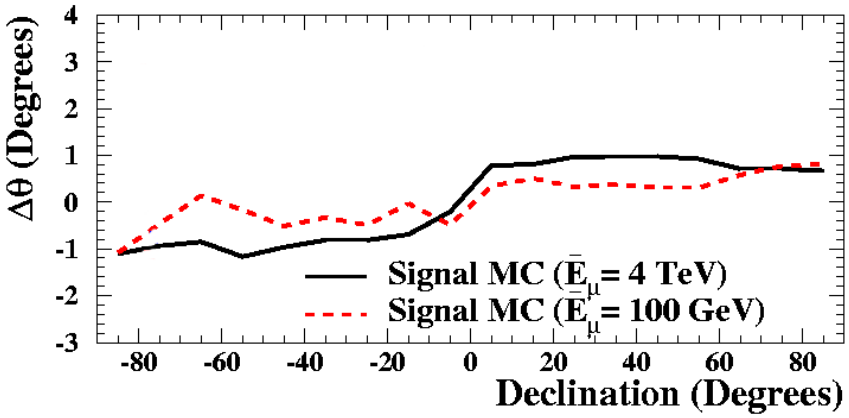

Figure 7.7: Pointing offset as a function of zenith angle for neutrino Monte Carlo, from [81].

Although the exact magnitude of the effect depends on what cuts you employ and the zenith angle of the track, the existence of an effect is agreed upon by three independent surface detectors (SPASE-1, SPASE-2, and GASP), and AMANDA's own Monte Carlo. Thus it is not a strange systematic of one particular analysis; it is a real effect.

7.2.1 Dependence on zenith angle

We expect the magnitude of the zenith pointing offset to depend on zenith angle. At $\theta = 12°$, reconstructed tracks are 1-2 degrees steeper downgoing. But at $\theta = 0°$, this cannot still be true (a track cannot get any steeper than 0°!). Likewise, at $\theta = 90°$, there is symmetry between up and down (both directions are "steeper"), and so the offset should be zero. At $\theta = 168°$ (12 ° from straight up), we expect an offset of *positive* 1-2 degrees if tracks are now pulled steeper upgoing. The expectation is confirmed by high-energy neutrino signal Monte Carlo, which is generated at all zenith angles (see Figure 7.7).

7.2.2 Impact on point source searches

Having a pointing offset is equivalent to having a misaligned telescope. Hence it is only important when looking at point sources in the sky. However, several point source searches have been conducted [81, 79], and this misalignment will result in some loss of signal.

The 5-degree radius circle in Figure 7.6 represents a typical point source search bin of size ≈ 1.6

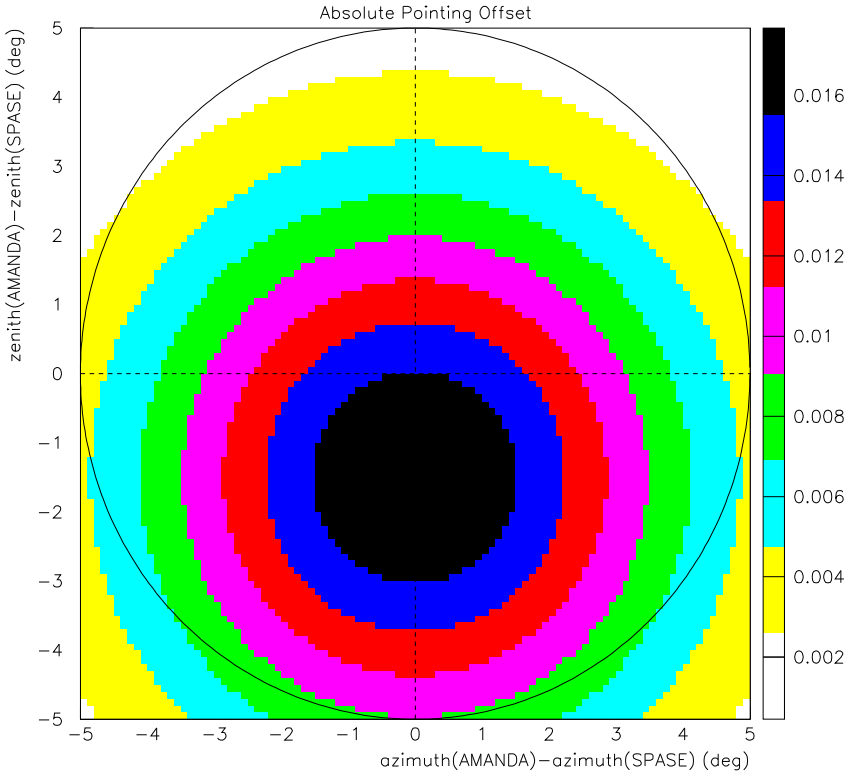

Figure 7.8: Events from a hypothetical point source which is offset with $\Delta\theta = 1.5°$.

times the angular resolution of the detector of about 3 degrees. Different specific searches employ different binsizes; this example is meant merely to guide the eye. If a point source is located at the center of the "crosshairs" in the sky, signal events in AMANDA will be measured at zenith angles 1.5 degrees steeper. The distribution of signal events from such a point source is shown in Figure 7.8

The number of events which fall off the edge of the search bin due to the offset is easily computable (see Table 7.2). At $\Delta\theta = 1.5°$, 6% of the source events are lost. At $\Delta\theta = 2.0°$, 10% of the source events are lost.

The missing events can be recovered by re-aligning the telescope when searching for point sources. Instead of centering the search bin on the crosshairs, the bin should be aimed off-center in zenith for better signal gathering. Figure 7.7 can guide our choice of this correction.

Offset	Fraction of signal events within bin	Fraction of events lost due to offset
0.0	0.7511	0
0.5	0.7463	1%
1.0	0.7321	3%
1.5	0.7087	6%
2.0	0.6768	10%
2.5	0.6374	15%
3.0	0.5915	21%

Table 7.2: Events lost due to a zenith offset, for a 2-D Gaussian distributed source of events with 3° resolution and a 5° binsize.

Chapter 8

Light calorimetry with ADC lateral distributions

8.1 Why calorimetry?

The concept of light calorimetry is used already in AMANDA analyses. For instance, the number of channels which are hit in an event (a parameter called *nch*) is used as an estimator of muon (and therefore neutrino) energy in diffuse limit analyses [94], and despite its simplicity is one of the most robust and powerful energy estimators in use in AMANDA. AMANDA is a fully active calorimeter; its entire volume is radiative. The amount of light in the detector is proportional to the energy loss of the muons passing through it, and our task is to reconstruct the muons using only the information in this light.

The *nch* estimator works especially well for events which are low-energy and pass through the physical volume of the detector. However, the principle does not work efficiently for large events or for tracks which pass outside the physical array. In this class of events, an unknown fraction of the total light is sampled by the phototubes, while the rest is lost into uninstrumented ice.

However, with our understanding of how light is emitted and propagates in ice, we can do better than just counting channels. Rather, we need only to sample the shape and structure of the photon field in the ice to reconstruct the properties of the emitter, even if most of the light ends up undetected.

8.2 $K50$

An air shower is symmetric about its own axis, and the light or particles observed in a detector will also follow a cylindrically-symmetric pattern around the primary track axis. Thus, many air shower experiments explore the shower's properties by fitting the *lateral distribution* of something (for instance an exponentially-falling Cherenkov light amplitude, or a scintillator particle density). Furthermore, since the lateral distribution is theorized to have a particular shape, the measured distribution is often parametrized by one number representing the value of the distribution at a particular constant distance from the primary track axis. Even the naming conventions for these parameters follow a kind of industry standard. For instance,

- L_{90}: AIROBICC Cherenkov light density at 90 meters from the core [48]
- $S(30)$: SPASE particle density at 30 meters from the core [110]
- $C(100)$: VULCAN Cherenkov light density at 100 meters from the core [111]
- $\rho(600)$: Haverah Park particle density at 600 meters [58]
- $S_0(600)$: AGASA particle density at 600 meters [55]
- C_{120}: BLANCA photon density at 120 meters [33]
- $Q(100)$: Mt. Liang Wang Cherenkov light intensity at 100 meters [61]

Each experiment has its own formulae for extracting the primary energy or composition from its selected parameter. These formulae depend not only on the size and type of detector but also the altitude and location of the site, or zenith angle of the event. The energy resolution of the measurement can be checked against the various air shower models and Monte Carlo simulations.

In AMANDA, we will apply the same philosophy and introduce our own parameter for the deep muon component of the air shower:

- $K50$, the average AMANDA PMT amplitude measured at 50 meters from the reconstructed track axis, for bulk ice at a slant depth of 1750 meters,
  $= A\frac{1}{\sqrt{(50\text{ m})d_0}}e^{-(50\text{ m})/d_0}$.

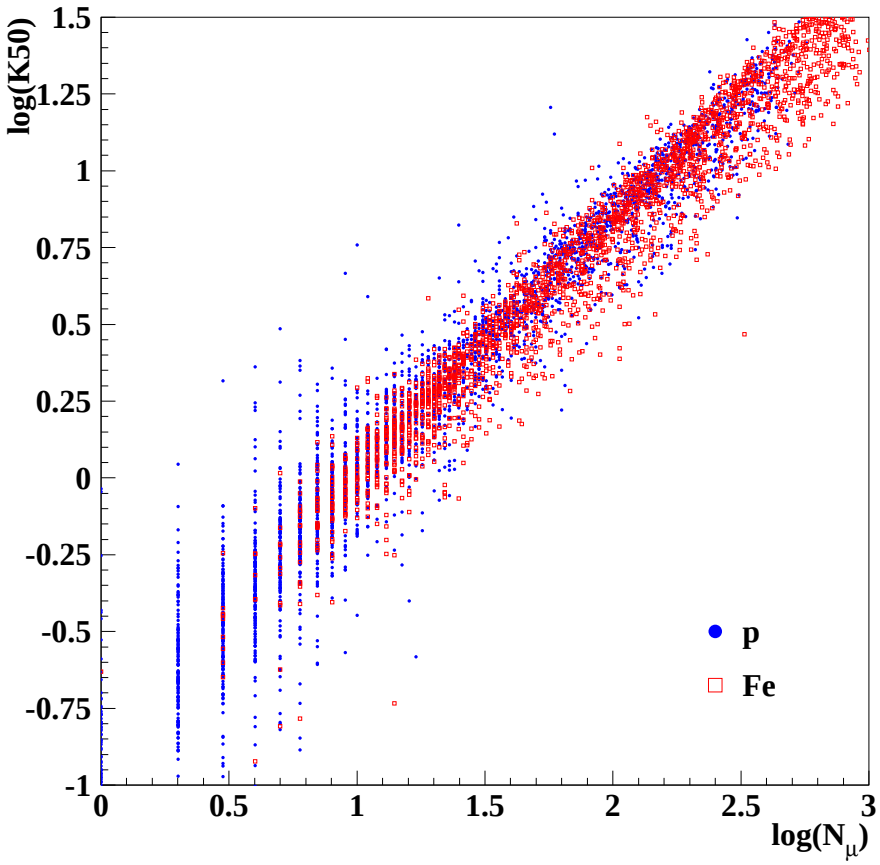

Figure 8.1: The reconstructed $K50$ vs. the true number of muons at 1750 meters into the ice, for protons and iron.

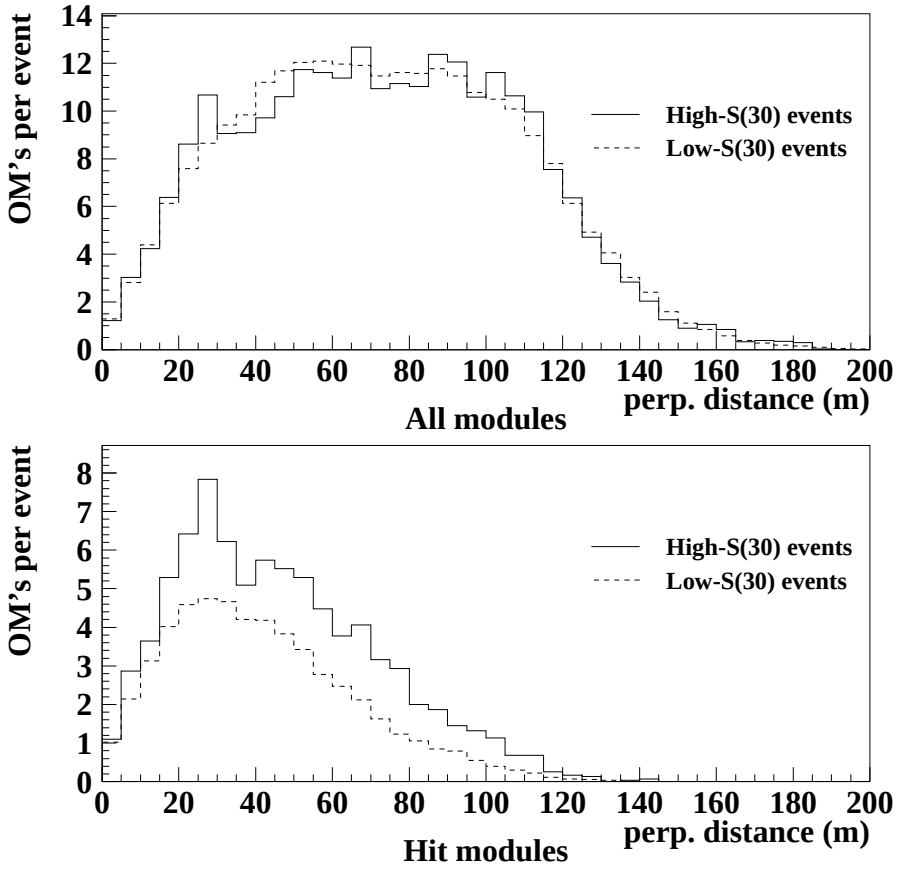

Figure 8.2: Distribution of distances from the track, per event, for all modules (above) and all hit modules (below).

Here, A and d_0 are the two free parameters of the ADC-based reconstruction, introduced in Chapter 5.

Figure 8.1 demonstrates the success of this parameter as an estimator of muon number. According to these simulations, the relationship between the two parameters is composition-independent (a fact which is crucial to the robustness of the measurement).

8.3 Why 50 meters?

8.3.1 The arguments for far distances

The ADC reconstruction is a global fit to all 302 OM's. But there are few (if any) OM's at 10 meters from the track, or at 150 meters. Most of them OM's participating in the fit lie in a

range of distances between 50 and 110 meters, as shown in Figure 8.2. The modules in this range of distances dominate the determination of the lateral distribution function which is extrapolated to all other distances.

Although our muon bundle track resolution is quite good (see Figures 5.11, 5.12, and 6.6 for instance), it is not perfect. If the track is off from the true track by an angle of a degree, this corresponds to a mislocation of the track by 30 meters at AMANDA depth. How does this affect the lateral distribution? To one side of the error, OM's will be assigned too small of a perpendicular distance, and their ADC's will be shifted into a smaller bin. On the other side of the error, OM's will be assigned too large of a perpendicular distance, and their ADC's will land in a larger bin. The end result is a "smearing" of ADC's across distance bins and a *flattening* of the ADC slope, especially at small distances on the order of the track error itself. The larger the distance, the more the shape of the ADC distribution becomes immune to changes in the central track.

8.3.2 The arguments for near distances

As we go out in distance, although many OM's participate in the fit, a greater percentage of them have zero hits. Not-hit modules at far distances will have a low probability of receiving a hit, and so their Poisson likelihood $P(0|small)$ is close to one. This doesn't provide very useful information about the hypothesis; the information is not very constraining of the fit. Hit modules, on the other hand, are very constraining; more effort must go into adjusting the hypothesis to bring it into agreement with the hits. Hit modules are most commonly found at a distance of around 30 meters (see again Figure 8.2).

Near OM's are also more likely to have linear ADC behavior. At OM's far from the track, photons will arrive scattered and delayed in time (see Figure 5.3). Pulses from the PMT are further smeared in time and integrated by both the electrical cable and the SWAMP amplifier at the surface, with a time constant of a few hundred nanoseconds. Although a "late" photon is just as good as an early one in this ADC analysis, if *multiple* late photons arrive at a faraway OM, separated by more than a few hundred nanoseconds, the peak-ADC will only measure the shaped charge of *one* of them and will underestimate the number of photons. If multiple photons arrive together, as they would for a nearby OM, then they are integrated together into a single shaped pulse that is correctly measured

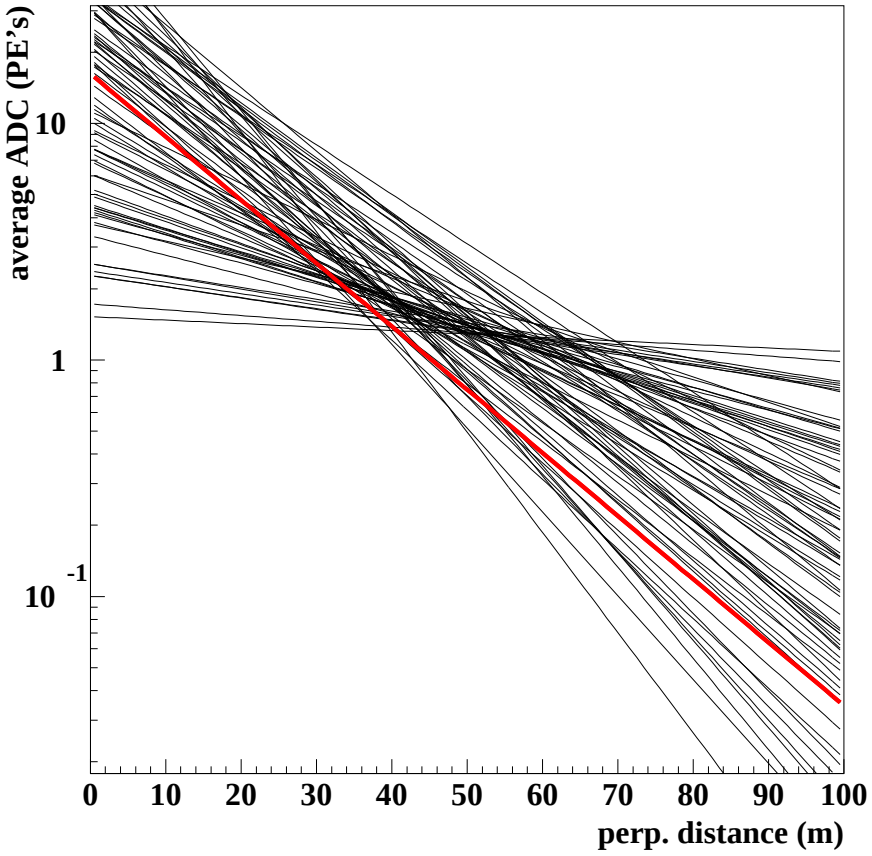

Figure 8.3: The fitted ADC lateral distribution functions relative to many different anchored tracks.

by the peak-ADC. (See Appendix D for more on the subject of ADC linearity.)

8.3.3 The most stable compromise

Figure 8.3 shows the fitted ADC lateral distribution functions for the "best" track fit to an individual event, and a collection of alternative tracks artificially moved in zenith and azimuth short distances (up to 1.5 degrees total) away from the best-fit track. The slope and intercept is re-reconstructed for each alternative track. At very large and very small distances, small changes in fitted slope produce large variations in amplitude. There is a region in the middle, however, between 40 and 60 meters, where the variation is the smallest. At these distances, the fit amplitude is the

most robust under errors in the track position. Thus, 50 meters offers the most stable measurement of this rather finicky quantity, the best compromise between modules contributing to the fit, modules hit, track resolution issues, and ADC linearity.

8.4 Interpreting the measurement: single muons vs. muon bundles

Light from a single muon of energy E comes from a superposition of continuous emission (Cherenkov light), and stochastic emission (intermittent showers). Two extremes of muon energy can be approximated: a minimum-ionizing muon can be described by Cherenkov light alone, and a very high-energy muon can be described by averaged "shower light" proportional to the muon's energy. This distinction is important when interpreting a measurement of the total amount of light emitted in an AMANDA event. If the event is a single high-energy muon, then the light is roughly proportional to the energy of the muon. If the event is a muon bundle dominated by minimum-ionizing muons, then the light is roughly proportional to the number of muons. Of course events in general are neither extreme, as muons (be they cosmic ray-induced or neutrino-induced) come in a spectrum of energies. So $K50$, which is really a measure of total energy loss, is sometimes compared to the "number of muons" in this work. But it is important to keep in mind that although the idea of "muon counting" may help us to visualize some of the physical processes at work, $K50$ measures something else unique.

Chapter 9

Systematics and model dependencies

$K50$, a measurement of light amplitude, is the culmination of many successive processes: hadronic interaction, propagation of particles in the atmosphere, propagation of muons in ice, emission of light, and reception of the light by AMANDA's photomultipliers. A simulation of these events has uncertainties at each step in the process, any of which could contribute or conspire to produce a discrepancy in $K50$ between Monte Carlo and experimental data. How, then, can we draw conclusions about cosmic ray composition from the measurement? Fortunately, the energy threshold of the SPASE/AMANDA coincidence detector is low enough that we can calibrate $K50$ against a known composition at low energies, a technique that will be described in the next chapter. In essence, we will anchor or *renormalize* $K50$ at low energies and watch whether its properties change as energy increases[1].

This philosophy is only sound if $K50$'s behavior as a function of energy does not itself change with different models. In other words, we can renormalize away the uncertainties only if models differ from each other by a *constant factor* in $K50$ over all energies such as the example in Figure 9.1. In this chapter we investigate whether this is true, whether variation between models is "renormalizable." In the following chapter, we will introduce the composition analysis itself and put each model independently through a renormalization procedure to measure systematic shifts in the answer after all is done.

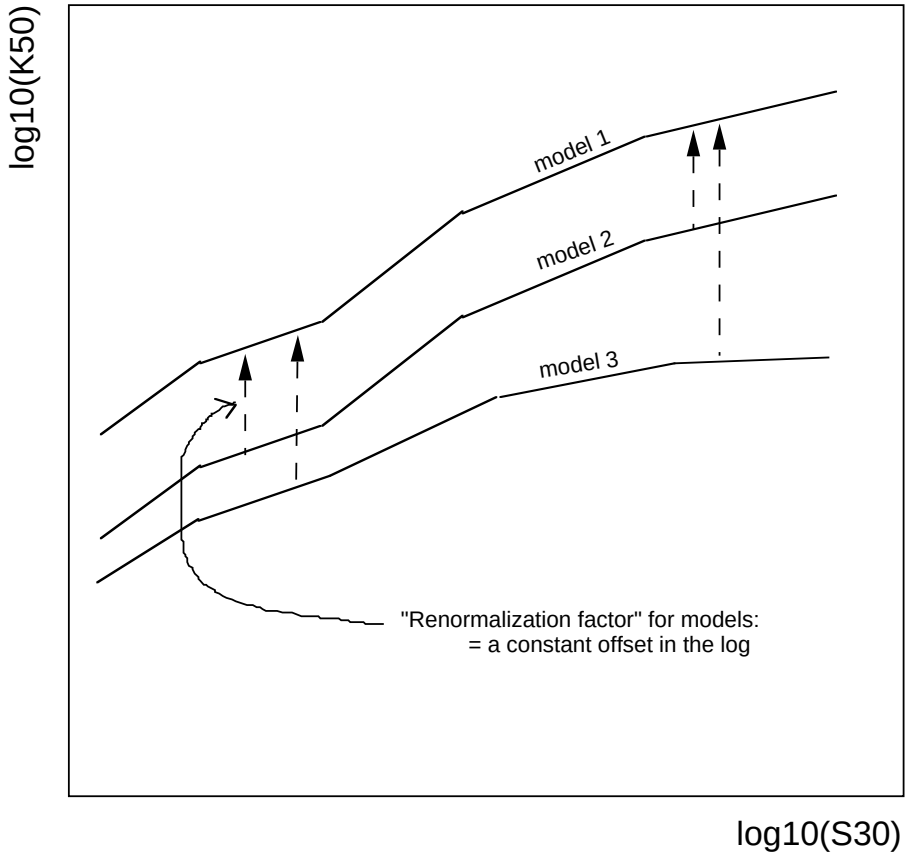

Figure 9.1: Toy model example of the principle of "renormalization:" models 1 and 2 differ from each other by a constant factor in $K50$ (a constant offset in $\log(K50)$). Model 3, on the other hand, is not "renormalizable" because its relative behavior changes with energy.

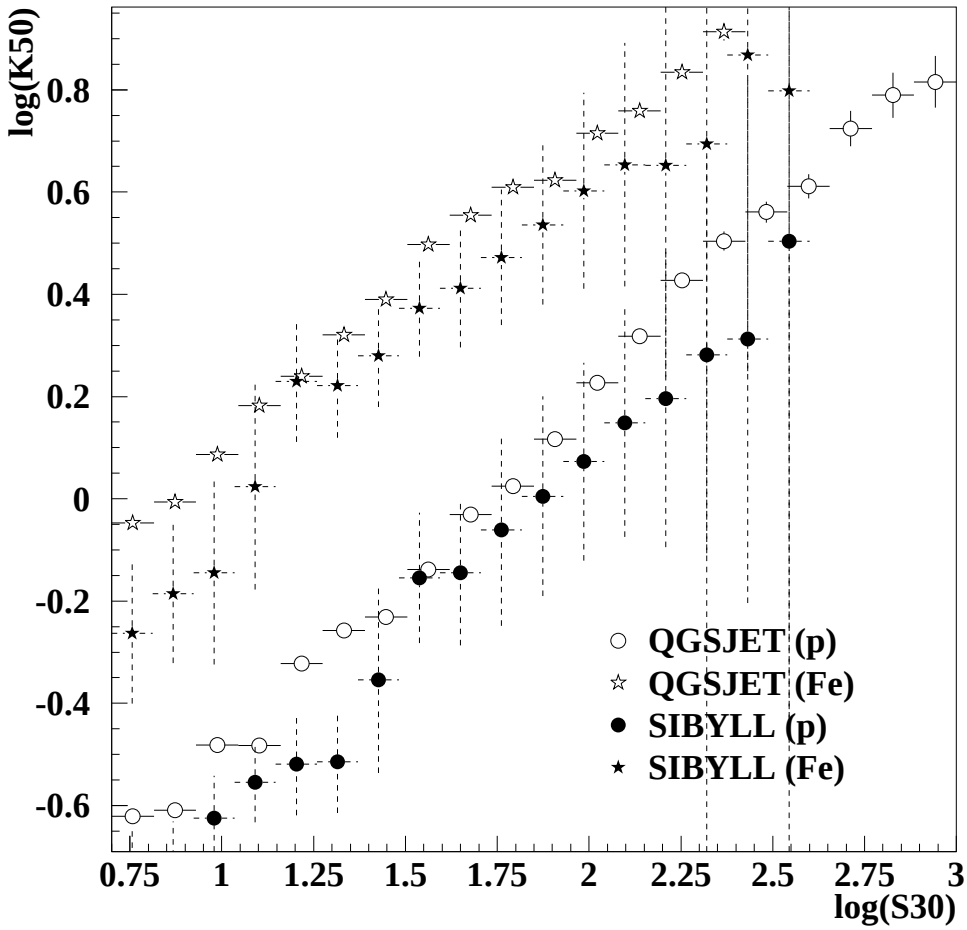

Figure 9.2: $S(30)$-$K50$ parameter space, for different hadronic interaction models. (The larger error bars for SIBYLL are due to much fewer showers generated with this model.)

9.1 Effect of hadronic interaction model

QGSJET is a favorite among hadronic interaction models, but we should not assume that it is the most correct at simulating the high-energy muons that reach AMANDA. In fact, the number of muons is one of the variables that varies between hadronic interaction models. SIBYLL, for instance, is known to produce fewer muons than other models [29]. So we will use SIBYLL to estimate the uncertainty due to interaction model. Figure 9.2 compares QGSJET and SIBYLL in their $K50$ reconstruction. With fewer muons, the SIBYLL model has lower average ADC's, as expected. In general, differences between models can produce uncertainties in electron number N_e or muon number N_μ of as much as 50% [28]. But the *relative* offset in the normalization of $K50$ between the two models *changes* by only about 5% between $S(30) = 10$ and $S(30) = 100$.

9.2 Effect of muon propagator

Different muon propagators produce different muon multiplicities, leading to differences in $K50$. A behavior comparison of two muon propagators (PROPMU and MMC) is shown in Figure 9.3. Although the curves look similar, there are systematic shifts at low energies. In fact, the normalization of the two models differs by up to 15-20% from $S(30) = 10$ to $S(30) = 100$.

9.3 Effect of light propagation models in AMANDA ice

Our model of the propagation of light in ice is crucial to the measurement of $K50$. In Chapter 5, we developed a simple model of ADC's as a function of distance and depth which matched well to experimental data. Monte Carlo simulations, however, match the expectation less well (see Figure 5.7).

By comparing the lateral distributions of amplitudes between data and Monte Carlo, as is shown in Figure 9.4, we see discrepancies in the amount of light as a function of distance. In other words, the *slope* of the lateral distribution of amplitudes is not being simulated correctly. By measuring amplitudes at one reference distance (in this case, 50 meters), we hope to render this slope discrepancy irrelevant, but to justify this choice we must show that the method is robust under

[1] We will deal primarily with the log of the quantities $K50$ and $S(30)$ from this point forward. Therefore I will occasionally describe a plot as "$S(30)$-$K50$ parameter space," even though it is really a log-log plot.

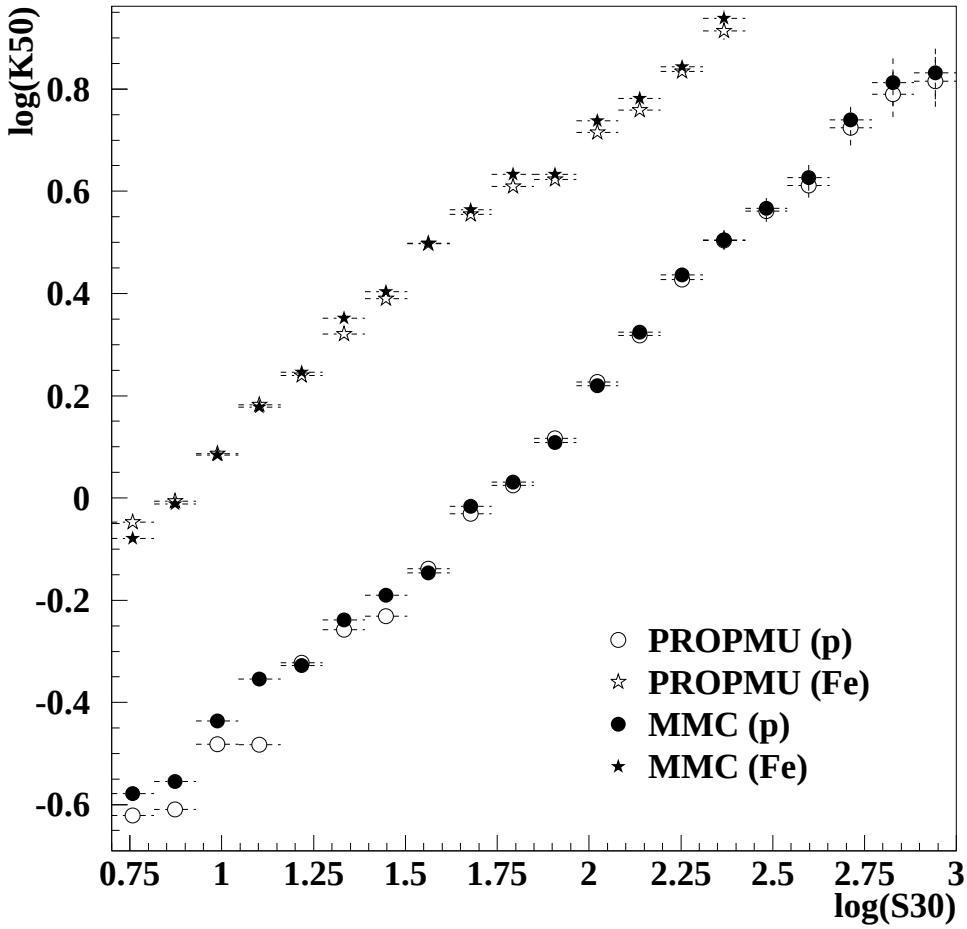

Figure 9.3: $S(30)$-$K50$ parameter space, for different muon propagators.

changes in ice properties and light propagation.

Three ice models are readily available. The default model is a "layered ice" model in which the instrumented region of ice is divided into 16 layers, each having its own set of photon tables defined by its absorption and scattering lengths. The photon density at each OM is computed from the tables of that OM's particular ice layer. Secondly, the "bulk ice" model treats the entire ice as homogeneous, with a single scattering and absorption length. In addition, there is a third ice model available by accident; a bug in the photon propagation code was discovered which altered the slope of the ADC lateral distribution, but not before a substantial number of air showers had been processed. Lateral distribution functions for this "buggy" ice are also included in Figure 9.4. An alternative light propagation code ("Photonics" [80]) will be available in the near future. This will provide another useful cross-check.

Changing the ice properties from layered to bulk makes little difference, as seen in Figure 9.5; the renormalization changes by on the order of 5% from $S(30) = 10$ to $S(30) = 100$. In the "buggy" ice, however, the renormalization wanders by as much as 30%. Although the bug itself has been fixed, this suggests that the analysis could be vulnerable to changes in the slope of the ADC lateral distribution. Carrying the buggy ice model to the final stages of the analysis will tell us more.

9.4 Effect of angular and absolute OM sensitivity

Recent measurements and analyses have cast doubt on previous measurements of the transmissivity of the OM's glass housing [91] and of the angular sensitivity of the OM's [92]. While these uncertainties greatly affect measurements of absolute flux or of zenith angle dependence, this analysis is relatively insensitive. We are not measuring absolute fluxes, and have an event sample confined to a narrow range of zenith angles around 12°. Changes in the absolute sensitivity affect all amplitudes equally. Changes in the angular sensitivity could be important for close distances (< 30 m) where hits are unscattered and directional, but these modules are few compared to farther-away modules for which light has been isotropized by scattering. Thus, I will claim without further proof that these uncertainties have a negligible effect on this analysis.

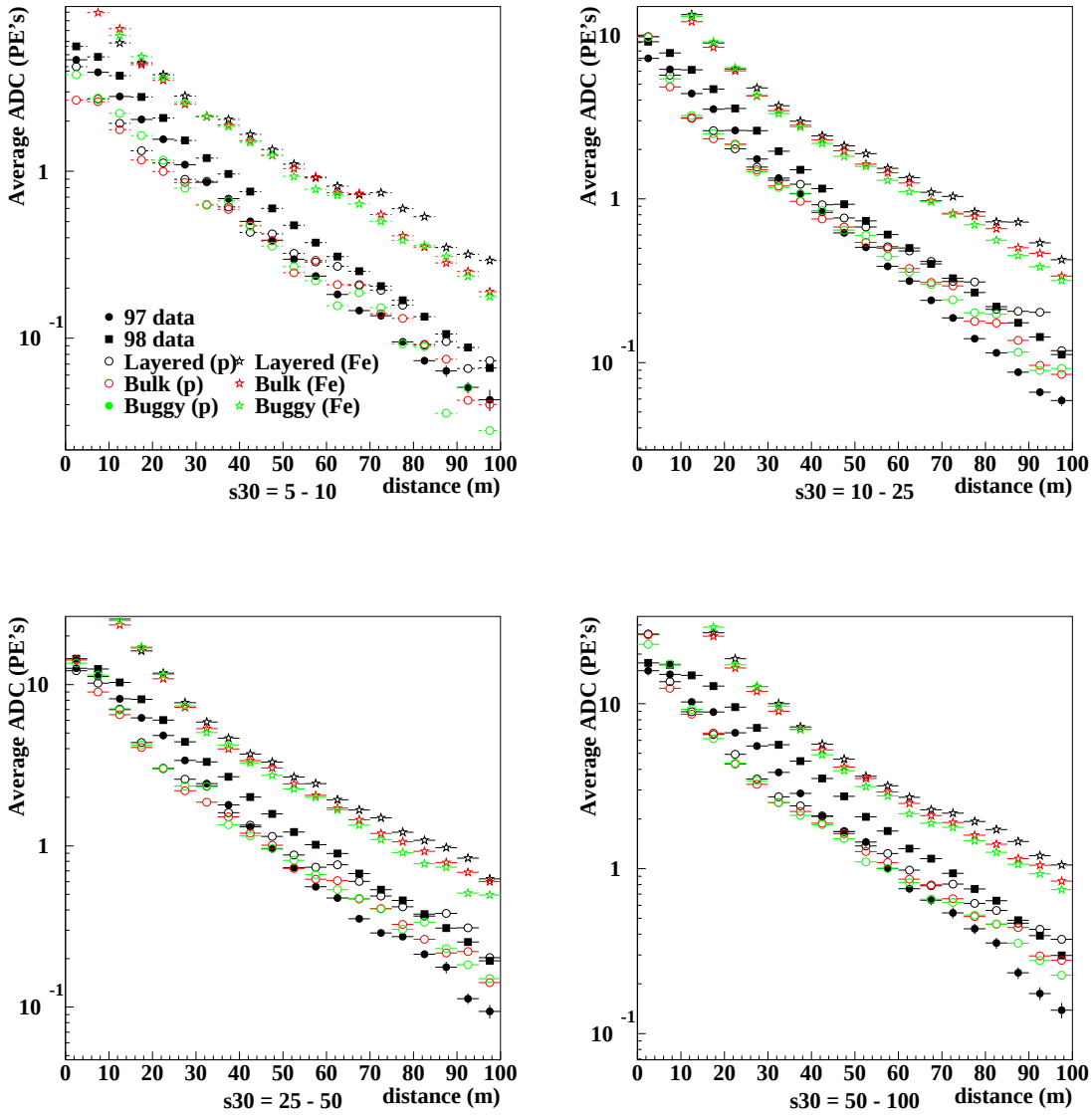

Figure 9.4: ADC lateral distribution functions, for different energies.

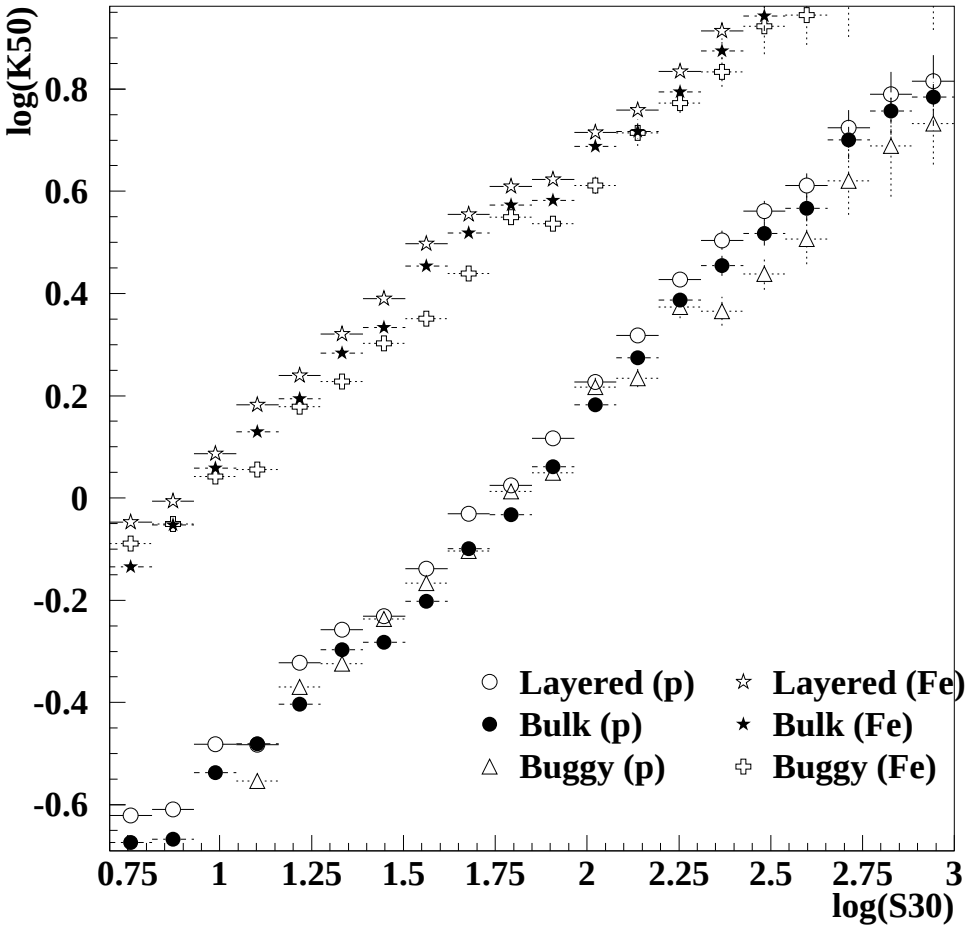

Figure 9.5: $S(30)$-$K50$ parameter space, for different ice models.

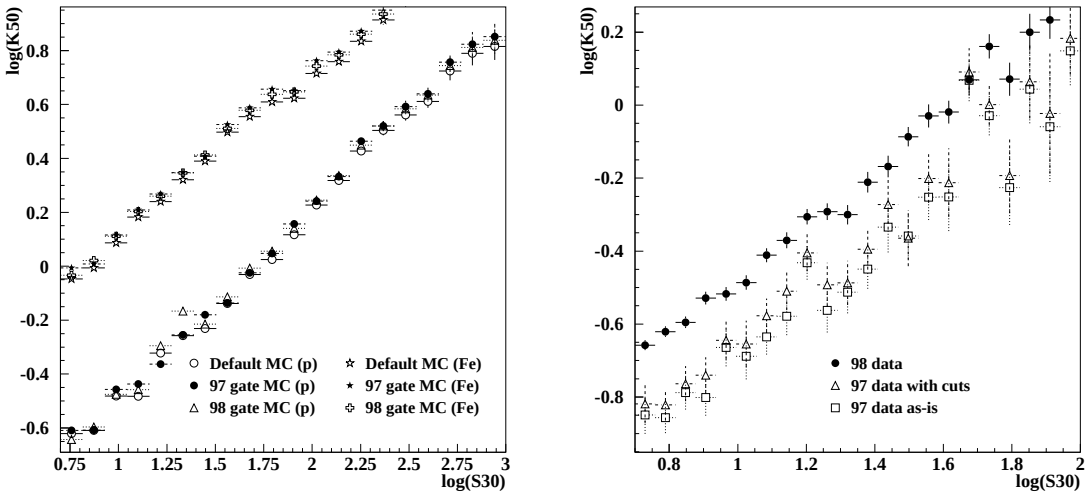

(a) Simulated ADC gates

(b) Data

Figure 9.6: $S(30)$-$K50$ parameter space, for different ADC gates and ADC treatment.

9.5 Effect of different ADC gates

Data from 1997 and 1998 had very different ADC gate settings. In 1997, the gate was narrow and ill-aligned; as a result many ADC's from the bottom modules in the detector arrived too late and were lost. In 1998, on the other hand, the ADC gate was wide enough to record all pulses, even from deep modules. Appendix C describes this issue in more detail, and the measures taken to account for this behavior. To summarize the situation: a variety of Monte Carlos were generated with different ADC gate settings: a "default" version, a "97-like" version, and a "98-like" version. In addition, a variety of data sets exist: 97 data analyzed as-is, 97 data with many bottom modules removed from the analysis (to account for the ADC problem), and 98 data which requires no special treatment. The effect of different ADC gates on the $K50$ reconstruction can be estimated by comparing *both* the different Monte Carlos and the different data treatments; this is shown in Figure 9.6. As one would expect, the removal of ADC's from the bottom of the detector is equivalent to a reduction in the absolute sensitivity of the detector, and its effect on renormalization is less than 5% over the $S(30)$

range of 10 to 100.

9.6 Systematics in the $S(30)$ measurement due to electronics saturation

In Chapter 6, we applied cuts to SPASE events in order to "fix" some strange features in the spectrum of $S(30)$. After the cuts were applied, the strange lobes of very large $S(30)$'s were removed from both data and Monte Carlo so that they agreed more closely (see Figure 6.3). However, even after the cut is applied, the data and Monte Carlo still do not agree in shape at $S(30)$ past about 100. While the Monte Carlo smoothly continues to high $S(30)$'s with a smooth power-law spectrum, the data cuts off rapidly. The cause of this cutoff has been traced to saturation behavior in the SPASE scintillators.

Each of the SPASE detector's thirty stations consists of four scintillator modules; three of them operate in normal "high-gain" mode, while the fourth runs in "low-gain" mode. The purpose of the low-gain module is to extend the dynamic range of the station when particle densities are so high that the high-gain modules saturate. The charge-ADC's which read out the signals from the modules saturate at 2048 mV. The reconstruction program SPV (which fits an $S(30)$ to each event) recognizes this effect; when it sees that the raw amplitude of a high-gain module in a station has hit this saturation point, it uses the low-gain module for that station instead.

However, a detailed examination of the raw ADC's from low-gain and high-gain modules [115] reveals that the true saturation point of modules is *less* than 2048; it is more like 1300. This is most likely due not to the ADC but to saturation of the signal splitter that precedes the ADC. As a result, SPV switches its attention to the low-gain modules too late. Without its knowledge, high-gain modules hitting only 1300 mV are saturating, the station amplitudes come out too low, and $S(30)$ is underestimated.

Tests on small sets of data have been performed [115] to see how changes in saturation treatment by SPV can affect the $S(30)$ spectrum. The "cutoff" behavior appears at close distances such as 30 meters, but disappears at farther distances where amplitudes are smaller. Removing any high-gain module exceeding 2048 does *not* change the cutoff behavior, indicating that saturation is occurring earlier. Using only low-gain modules in the analysis smoothes the spectrum at high energies; no cutoff behavior is observed. Measurements *in situ* by winter-overs support the theory as well, finding

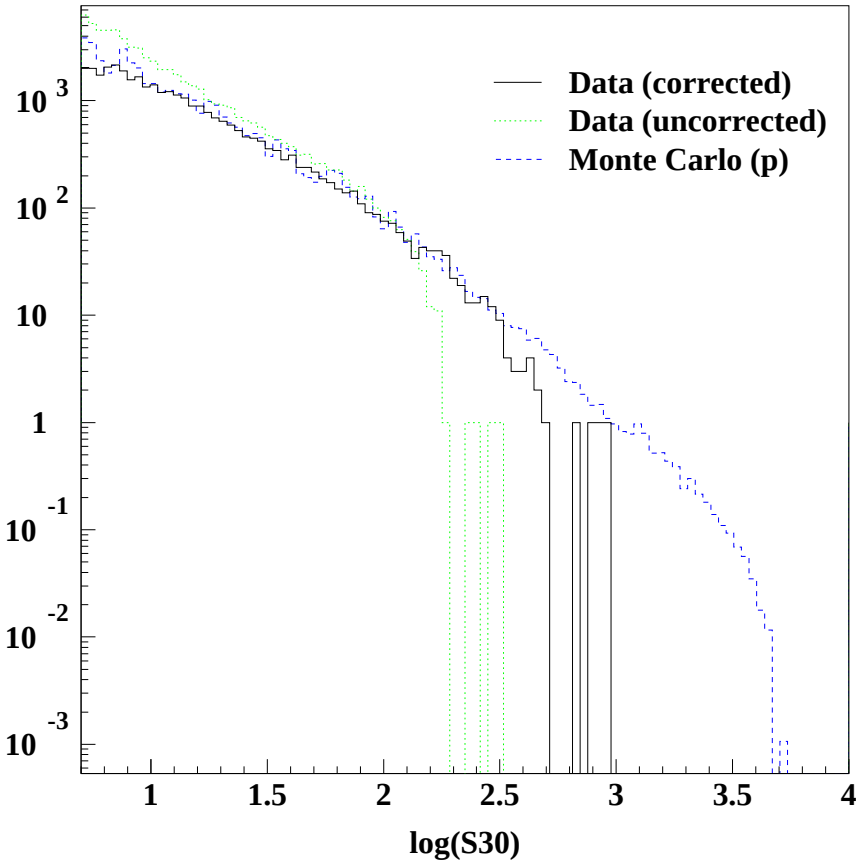

Figure 9.7: The effect of correcting the $S(30)$ measurement in experimental data, so that the spectrum of $S(30)$ better matches the Monte Carlo expectation.

a pileup of high-gain amplitudes at approximately 1.3 Volts.

The solution to the problem is to alter SPV so that it switches to low-gain modules earlier, at a saturation point of 1300 rather than 2048. This corrected reconstruction procedure has been performed on most of the 1998 data set. The correction recovers the $S(30)$ spectrum up to much higher energies, up to $\log S(30) = 2.4 - 2.5$, as shown in Figure 9.7. At this point, even the low-gain modules begin to saturate, and SPV has no recourse to extend the dynamic range further.

This effect is not really a "systematic error" in the same sense as the other effects presented in this chapter. Unlike the different hadronic models or muon propagators, there is no question as to which data set should be used for the analysis. The uncorrected data is wrong; the corrected

data is better. But a discussion of the effect helps us evaluate the vulnerability of this analysis to these kinds of pitfalls. Figure 9.8 compares the two 1998 data sets (corrected and uncorrected) in the now-familiar $S(30)$-$K50$ parameter space. The largest systematic effect occurs at high $S(30)$, where the uncorrected data are shifted and have depleted statistics.

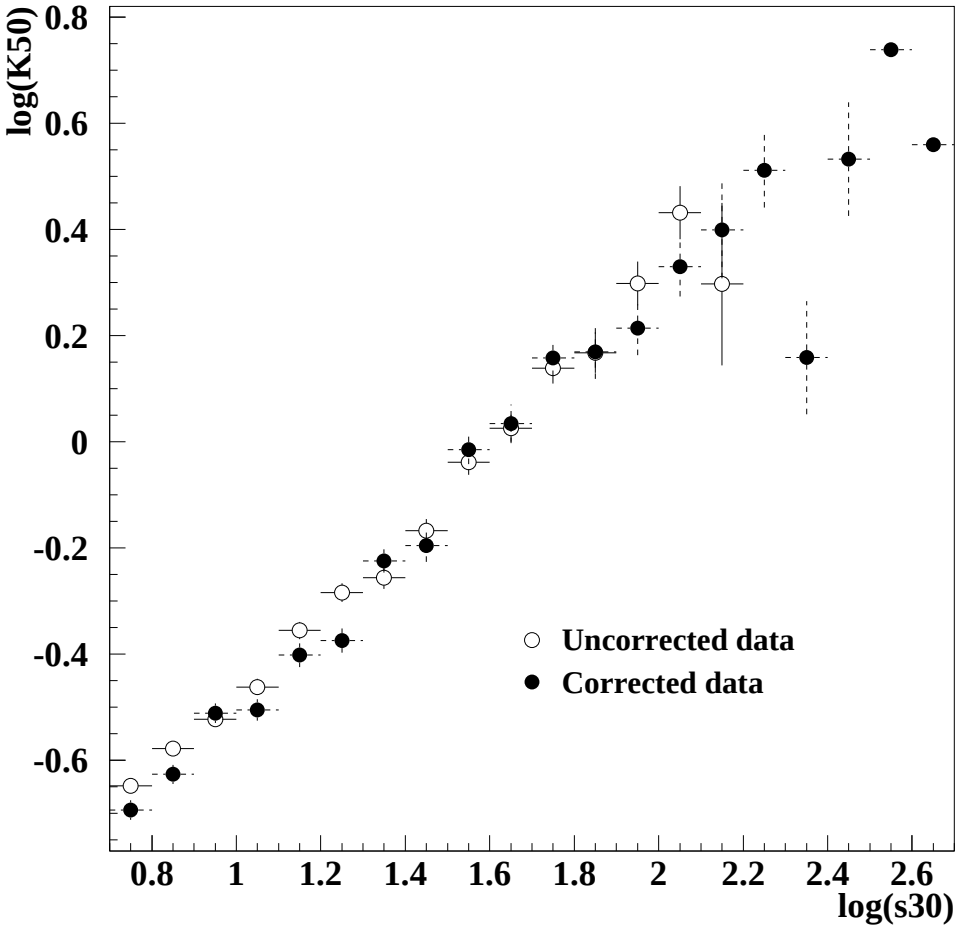

Figure 9.8: $S(30)$-$K50$ parameter space, for uncorrected and corrected experimental data.

Chapter 10

Composition

As shown in Chapter 3, protons and iron can be separated by plotting the muon component of a shower vs. the electron component. Here, $S(30)$ measured by SPASE is used for the electronic axis. $K50$ measured by AMANDA (described in Chapter 8) is used for the muonic axis. The two parameters plotted against each other on a log scale (for both Monte Carlo and data) is shown in Figure 10.1. This two-dimensional parameter space will be the focus of this chapter and the culmination of this work.

The absolute scale of $K50$ suffers from systematic uncertainties from a variety of sources. We know, for instance, that the Monte Carlo overestimates the amount of light at large distances from the track, resulting in $K50$ values which may be too high by a constant factor. In addition, the absolute number of muons could be over or underestimated by the hadronic interaction model or the muon propagation simulation, again by a constant factor. These uncertainties affect the absolute normalization of the $K50$ parameter, but not its properties or shape. Its behavior is always linear with the underlying muon physics.

The systematic shifts in the absolute scale of $K50$ preclude an absolute composition measurement from these data and Monte Carlo alone. However, cosmic ray composition is known at low energies from other experiments; if we renormalize our measurement at low energies to agree with the known composition, we can then investigate whether the composition *changes* as energy rises.[1]

[1]This philosophy has precedent, as problems with absolute normalization are not uncommon in cosmic ray physics. Using the parameter X_{max} for instance, has its systematics dangers. However, the rate of change of X_{max} with energy ($dX_{max}/d\ln E$, called the "elongation rate") is often used instead as a composition-sensitive parameter, because it is independent of absolute normalization.

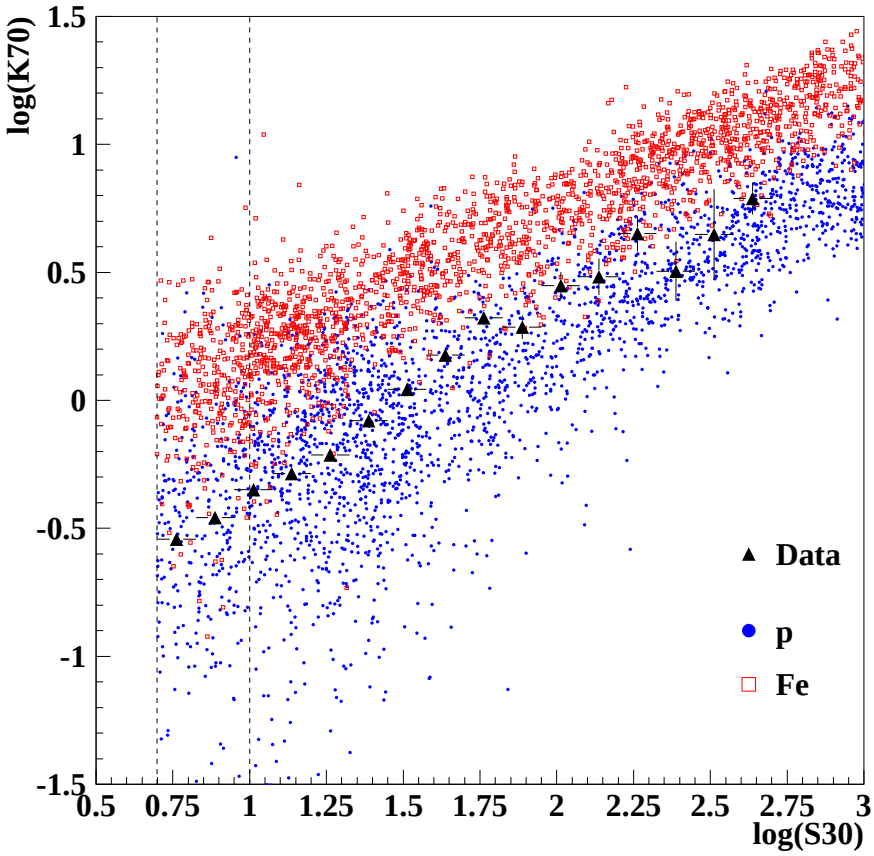

Figure 10.1: $S(30)$ vs. $K50$ for Monte Carlo (all events) and data (mean behavior). The "calibration bin" of $S(30) = 5 \rightarrow 10$ is shown.

So the analysis involves two distinct steps: 1) Calibrating the data to a known composition at low energies, and 2) Measuring the composition at higher energies.

10.1 Calibrating on low energies

To calibrate $K50$, we will use a vertical slice of Figure 10.1 with $S(30) = 5 \rightarrow 10$. This corresponds to energies of 200-350 TeV for protons and 400-650 TeV for iron. $S(30)$ of 5 is the threshold shower size at which SPASE reconstructions can be reliable, and $S(30)$ of 10 is where the energy *for iron* extends beyond where direct measurements are available.

At energies of hundreds of TeV, cosmic rays are neither pure protons nor pure iron, but rather a mixture of protons, iron, and intermediate nuclei (He, C, N, O, Si, Ne, etc.) which can be described together by a mean log mass $\langle \ln A \rangle$. The most recent results from direct measurements and the consensus for low-energy air shower experiments indicate that the composition at 500 TeV has a mean mass of $\langle \ln A \rangle \approx 2.0$ (see, for instance, Figure 1.4).

Since in this work we are comparing data only to the two extremes of protons and iron, we will describe composition in general as an admixture of the two with a mean log mass $\langle \ln A \rangle$. The fraction of iron f_{Fe} for a given $\langle \ln A \rangle$ is given by solving the equation:

$$\langle \ln A \rangle = (1 - f_{Fe}) \times \ln(1) + f_{Fe} \times \ln(56) = f_{Fe} \times \ln(56)$$

This way, our composition (derived from protons and iron only) can still be directly compared to other experiments which might measure four or more groups of nuclei. Our low-energy "calibration mixture", therefore, is the admixture of protons and iron which yields a mean log mass $\langle \ln A \rangle = 2$, or $f_{Fe} \approx 0.50$.

Figure 10.2(a) shows the distribution of $\log(K50)$ for data and for the known proton/iron mixture described above. Although the shapes of the distributions match well, the data is offset. To find the amount of the offset, we hypothesize potential offsets between -0.1 and 0.3 and perform a Kolmogorov-Smirnov test on each hypothesis. The K-S statistic for each hypothesis is shown in Figure 10.2(b), and the best fit offset is a $\log(K50)$ of 0.14. From this point onward in the analysis, therefore, the $\log(K50)$ of the *data* will be renormalized to the Monte Carlo by adding a constant factor of 0.14; this is equivalent to multiplying all $K50$'s by a uniform factor of 1.38.

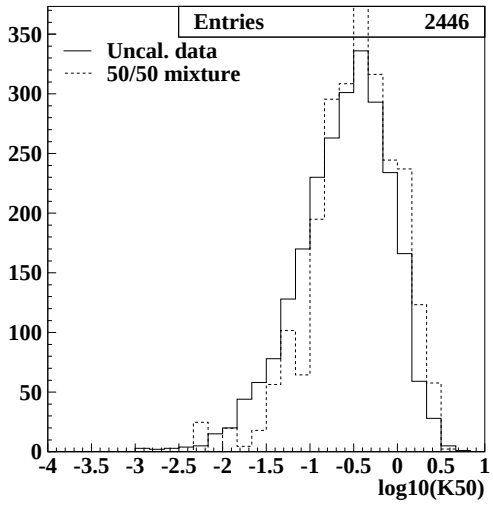

(a) The low-energy bin ($5 \leq S(30) < 10$) before calibration.

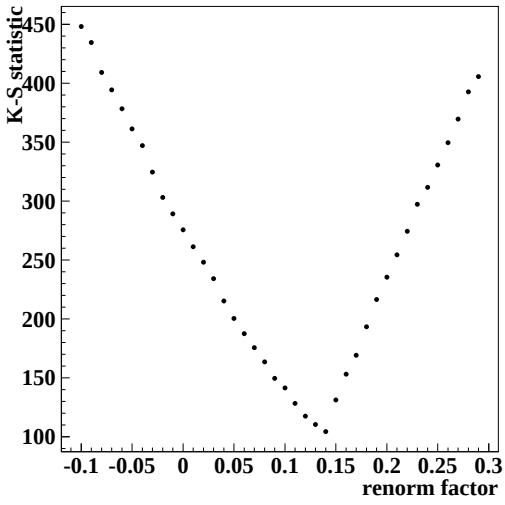

(b) K-S statistic as a function of renormalization factor (units of $\log(K50)$).

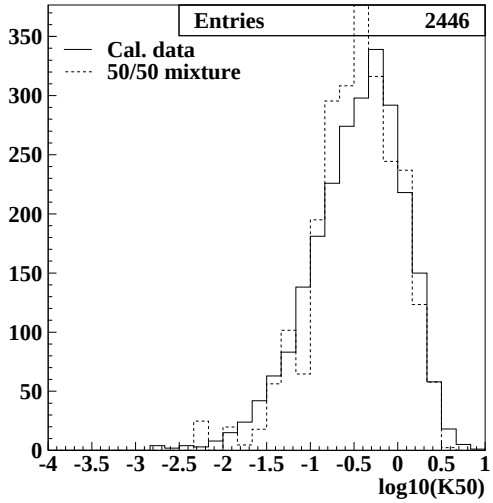

(c) The low-energy bin ($5 \leq S(30) < 10$) after calibration. (All data have been offset by 0.14.)

Figure 10.2: Procedure for calibrating the composition at low energy.

10.2 Two-dimensional calibration using fluctuations and shape

Within a slice of $S(30)$, the $K50$ curves of protons and iron differ not only in mean but also in *shape*; proton events have larger fluctuations and are more widely distributed in $K50$ than iron events. Thus, if the data and Monte Carlo are of high enough quality and statistics, it is possible to calibrate the data at low energy without having to declare a calibration mixture *a priori*, but rather by scanning through both normalization constant *and* calibration mixture and finding the best combination. The basic technique is the same as described above: compute the K-S statistic between data and hypothesis, and find the minimum. This time the minimum lies in a two-dimensional parameter space, and represents both the proton/iron mixture which best matches the data, *and* the renormalization factor necessary to get us there. Figure 10.3 shows a contour plot of the K-S statistic in this two-dimensional space and slices of the $K50$ distribution at some sample points in the space. The best-fitting mixture (of about 60% iron) matches reasonably to the mixture quoted in the literature for these energies, giving us confidence to proceed to the next step.

10.3 Higher energies: a change of coordinates

Once done, we turn our attention to composition. In Figure 10.1, we have created a two-dimensional parameter space described by $S(30)$ and $K50$. The placement of an event in this space depends on both the event's mass A and its energy E, giving rise to the two slanted "bands" of events in this plot. However, we can turn this statement around and measure an event's A and E from its $S(30)$ and $K50$; we merely execute a coordinate transformation between the $S(30)$ and $K50$ variables and a new set of axes which I will call A^* and E^*.

The new axes can be found by overlaying contours of *constant energy* over the Monte Carlo events plotted in $S(30)$-$K50$ space, as shown in Figure 10.4. Contours of constant energy are approximately parallel, and can be approximated by straight lines. The seven slanted straight lines drawn represent the constant energies of $\log(E/\mathrm{GeV}) = 5.6$, 5.8, 6.0, 6.2, 6.4, 6.6, and 6.8. They form six *bins* of constant energy, and they also define the angle of the A^* axis along which only composition changes. The E^* axis, along which only energy changes, is perpendicular to these lines.

Figure 10.5 shows the same Monte Carlo events plotted relative to the new transformed axes

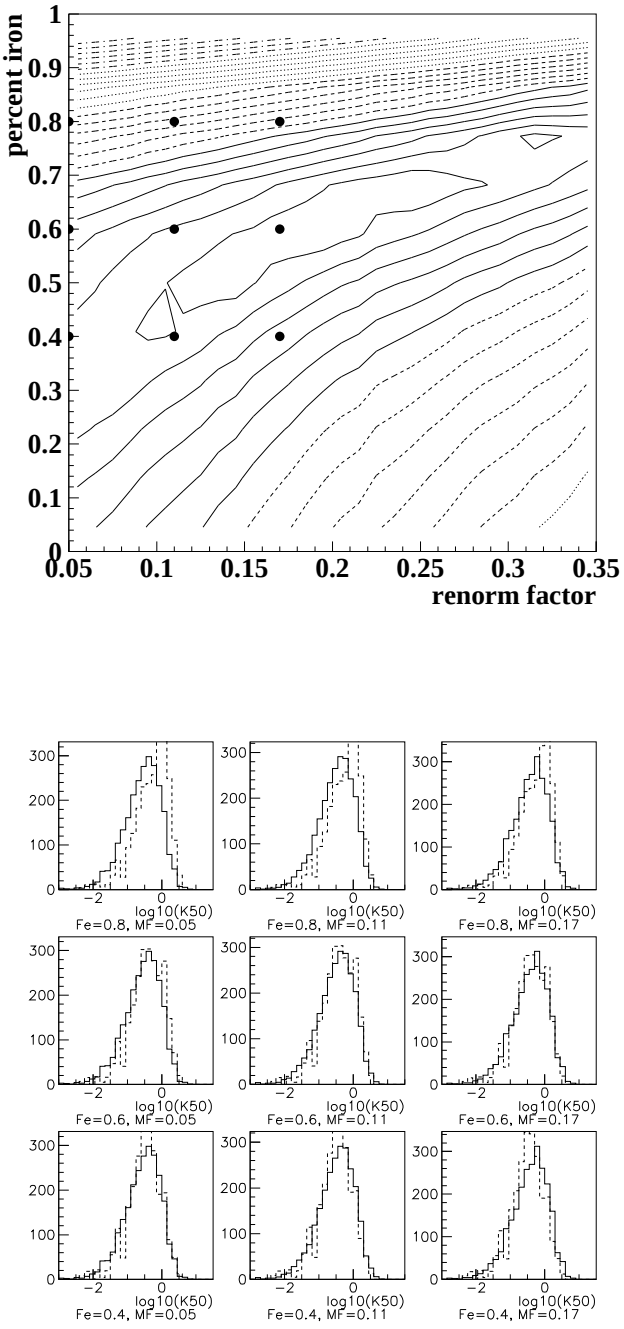

Figure 10.3: A two-dimensional calibration procedure. Upper: the two-dimensional version of Figure 10.2(b), where both renormalization constant and composition mixture are minimized. The nine dots are example points at which the $\log(K50)$ distribution is shown in the lower plot.

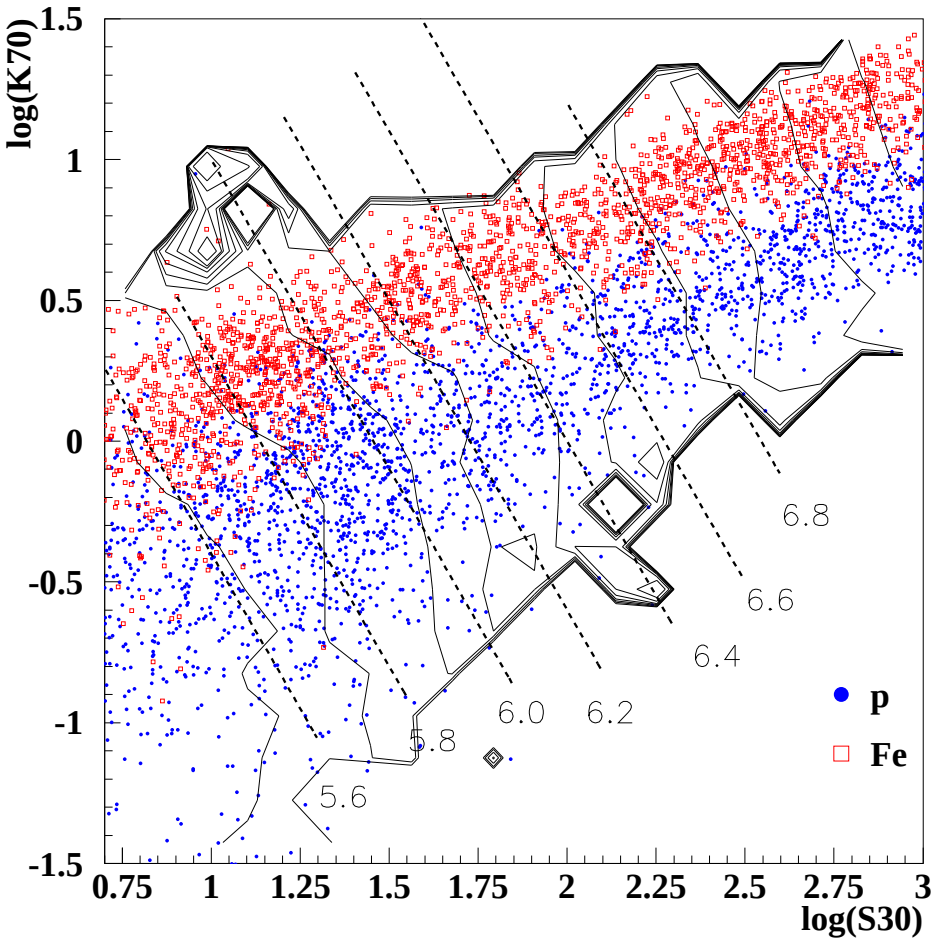

Figure 10.4: Contours of constant energy for proton and iron Monte Carlo, and the six constant-energy bins for composition analysis.

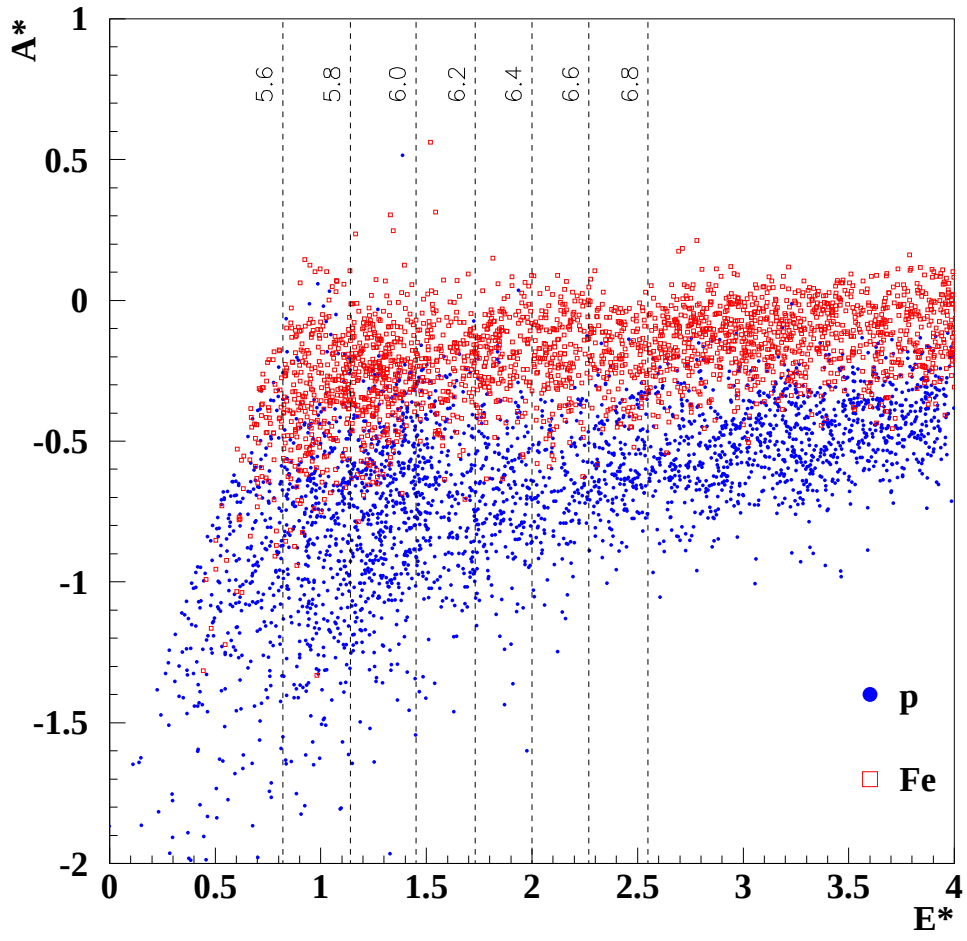

Figure 10.5: Proton and iron Monte Carlo (blue and red points) replotted relative to the transformed A^* and E^* axes. The six bins of constant energy are shown.

A^* and E^*. In this new parameter space, points of a constant composition (such as protons only) form a horizontal band of increasing energy[2], and the six bins of constant energy are vertical. We have succeeded in disentangling the two variables.

10.4 Measuring energy

The E^* axis is constructed in order to be linear with the log of the true primary energy. Figure 10.6 shows whether this is actually true using Monte Carlo. E^* is an excellent estimator of $\log(E)$, and is composition-independent.

A simple linefit yields this relationship:

$$\log(E_{primary}/\mathrm{GeV}) = 4.944 + 0.7168 \times E^*$$

The value of E^* for each event, converted by this formula, gives the reconstructed primary energy. In Monte Carlo, the resolution of this energy measurement is easily measured. A scatterplot of reconstructed and true primary energy is shown in Figure 10.6. The distribution and measured width of the reconstructed primary energy is shown in Figure 10.7 for six different energy ranges. $\Delta \log E = 0.12$ at energies just above 100 TeV, and improves to 0.057 at the highest simulated energies of 100 PeV.

One can see in Figure 10.6 that although $E_{primary}$ and E^* are proportional at most energies, the proton and iron curves do diverge from the ideal line at high and low energies. This indicates that the true "energy axis" is not a perfect straight line, as the E^* axis is. This slight divergence is the reason for the offset in the curves of Figure 10.7. A more sophisticated set of transformed axes (which are oblique and curved) could improve performance. Since protons and iron also begin to diverge from each other, the Gaussian resolution measured in this figure is the most conservative measurement (a possible 50/50 mixture).

---

[2]The astute reader will notice that the proton and iron bands are not precisely flat. This indicates that the best energy and mass axes are not truly perpendicular in the $S(30)$-$K50$ parameter space, but rather they are slightly oblique. A more advanced analysis should perform a coordinate transformation to these oblique axes, but since each energy bin will be considered independently, it does not much matter in this analysis.

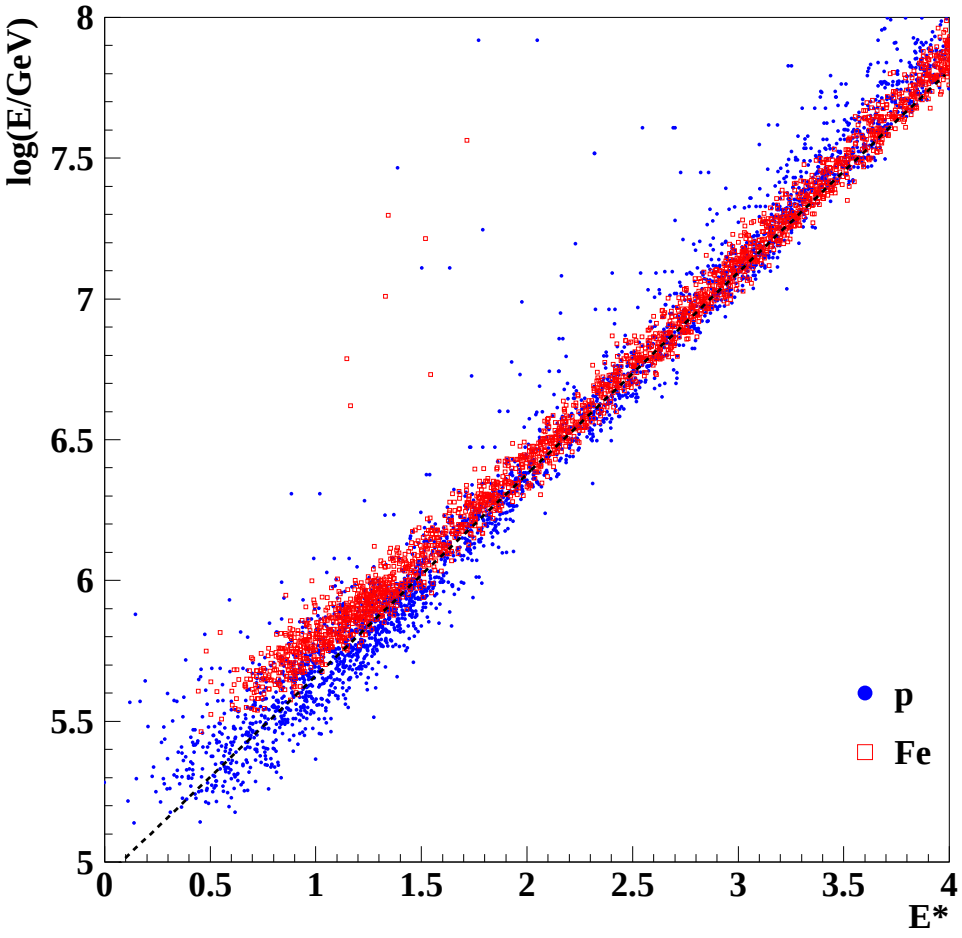

Figure 10.6: Reconstructed energy parameter E^* vs. log true primary energy for proton and iron Monte Carlo. The functional relation $\log(E_{primary}/\mathrm{GeV}) = 4.944 + 0.7168 \times E^*$ is drawn.

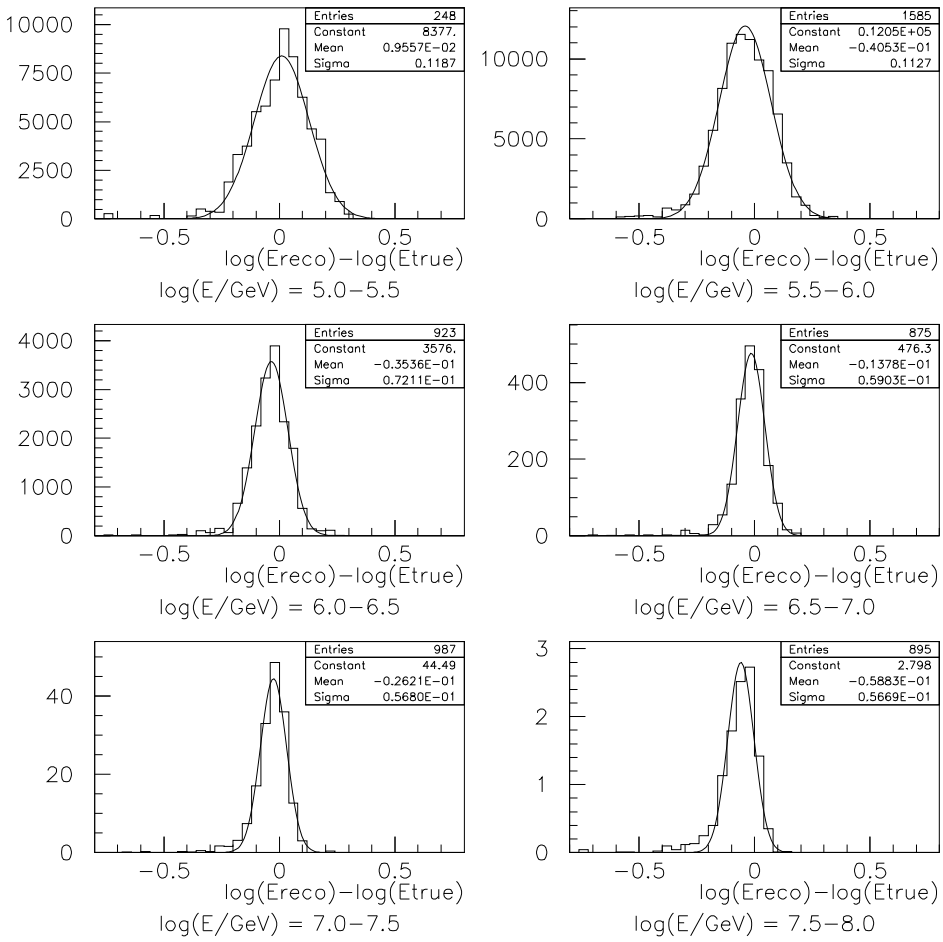

Figure 10.7: Distributions of reconstructed energy minus true energy, for six slices of true energy. The width of the distribution measures the energy resolution.

10.5 Measuring composition

In each bin of constant energy (constant E^*), the A^* of an event is a composition estimator. So to measure composition at a certain energy, we merely compare the A^* distributions of the data and the Monte Carlo. The proton and iron Monte Carlo events can be *mixed* with a certain relative proportion to produce a certain average cosmic ray mass. Some example mixtures (light, medium, and heavy) are shown for all six energy bins in Figure 10.8. The *best* mixture is found by testing hypothesis mixtures and measuring the probability of the data matching each hypothesis mixture.

This probability can be found in many different ways; two techniques have been used here: the K-S test (which computes the probability that two distributions, in this case data and Monte Carlo, were both drawn from the same underlying distribution [68]), and a maximum-likelihood test (which takes the Monte Carlo as the underlying distribution and computes the likelihood that the data events were drawn from it). The advantages of the K-S test are that it takes unbinned events as input, and that it correctly treats the fluctuations in the Monte Carlo events. The maximum-likelihood test assumes that the Monte Carlo is a perfectly smooth distribution (and thus our choice of binning can affect the outcome), but has the advantage that error bars are easily computed from it.

Hypothesis compositions every 5% between 0% and 100% iron were tested using both techniques (K-S and maximum-likelihood) for each of the six constant-energy bins, and the results are shown in Figure 10.9. The two techniques give the same most likely composition mixture, increasing our confidence in the method and the result.

The A^* parameter is sensitive enough to cosmic ray mass that the data do not fit perfectly to mixtures of protons and iron only. In Figure 10.8, for instance, one can see that at high energies a 50/50 mixture of the two extremes produces a flat (or even double-peaked) distribution of A^*, while the data is single-peaked between the extremes. Real cosmic rays also contain intermediate nuclei (such as He and CNO). Although this technique finds the *mean* mass well, by simulating and including these intermediate masses in this analysis we could improve the fits between Monte Carlo and data, and explore finer structure in cosmic ray mass.

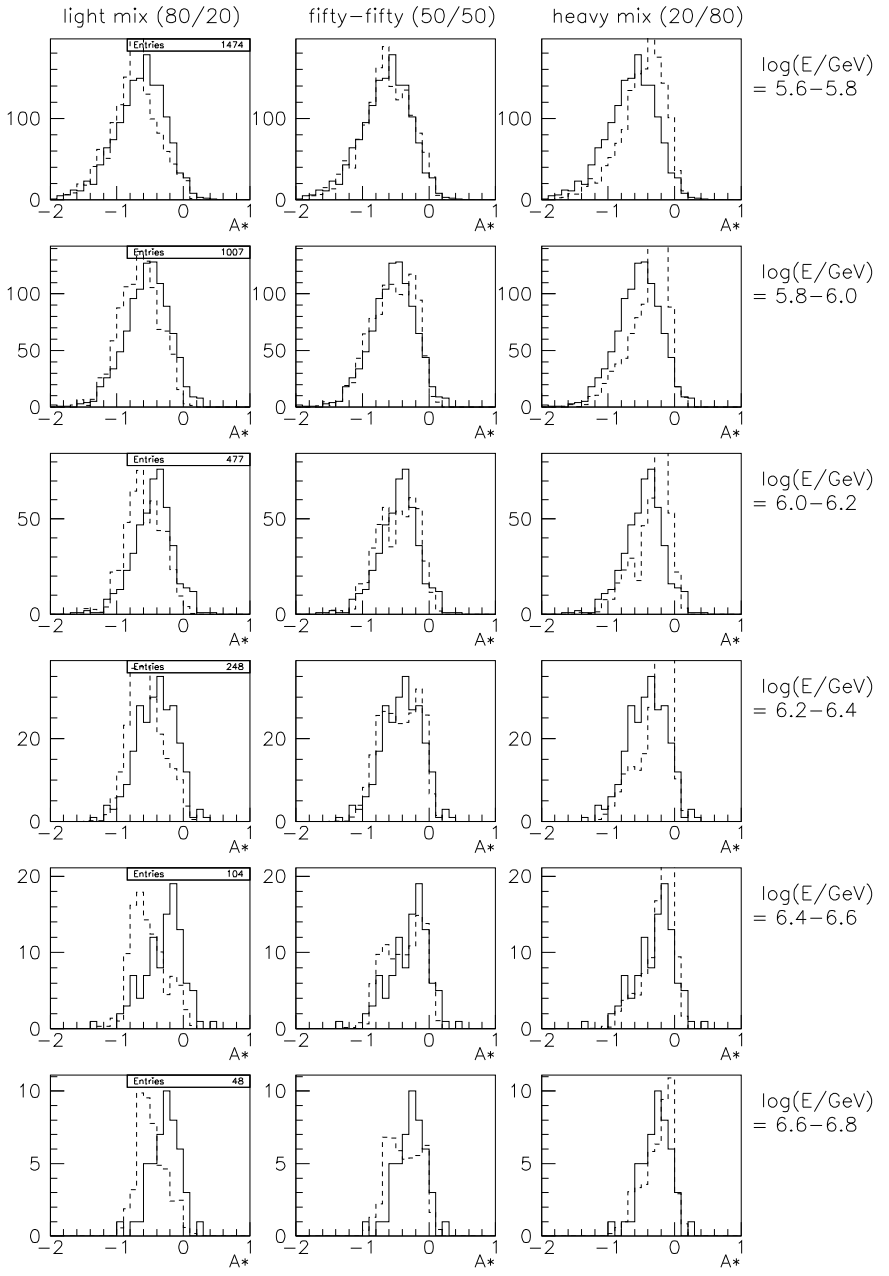

Figure 10.8: For the six constant-energy bins: Data (solid) compared to example hypothesis mixtures "light" (80% protons, 20% iron; left), "fifty-fifty" (50% protons, 50% iron; middle), and "heavy" (20% protons, 80% iron; right).

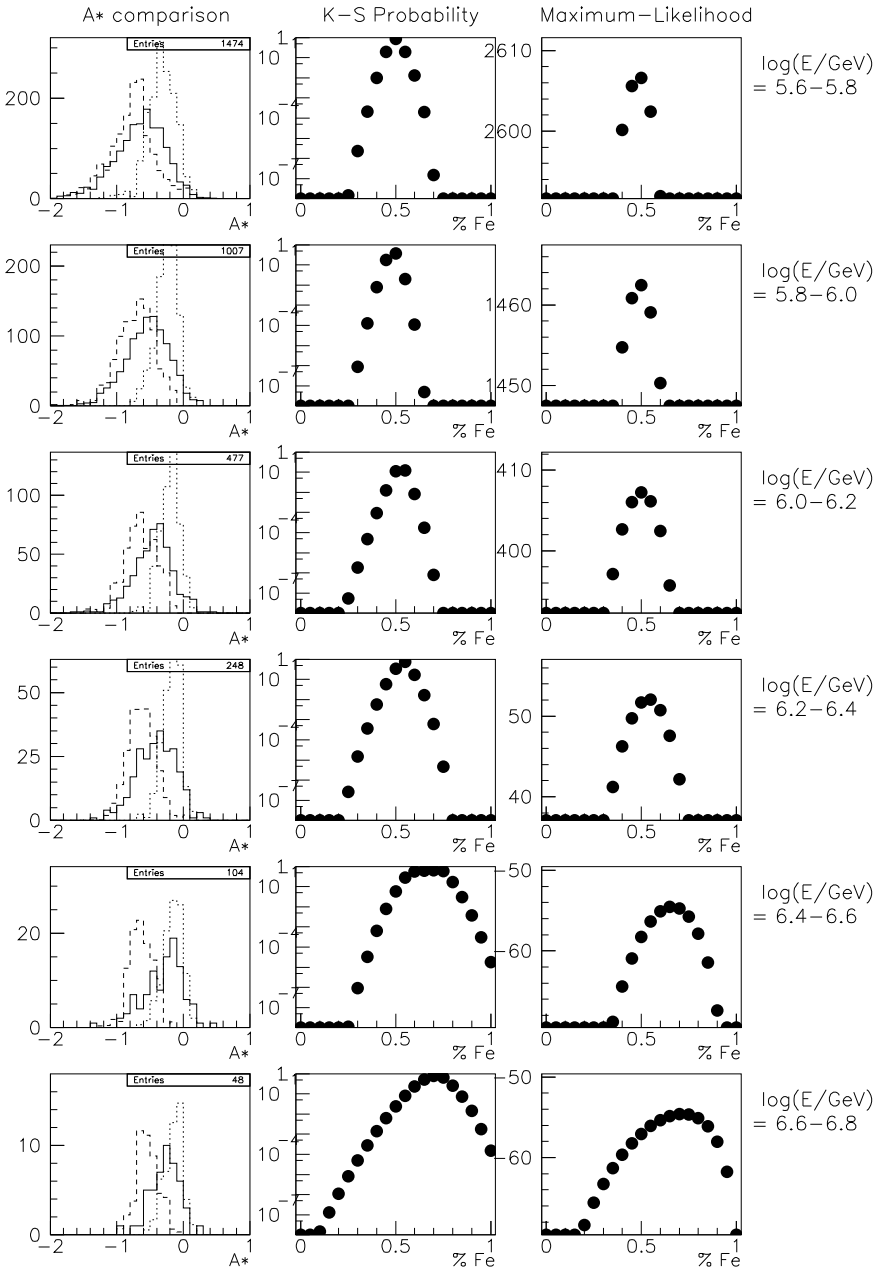

Figure 10.9: For the six constant-energy bins: Left: Distributions of A^* for pure protons (dashed), pure iron (dotted) and renormalized data (solid). Middle: K-S statistic as a function of iron percentage. Right: Likelihood as a function of iron percentage.

10.5.1 Error bars

The most likely mixture is the peak of the likelihood curve; error bars can be computed from the shape of the likelihood curve. We have mapped out the likelihood space $\ln \mathcal{L}$ as a function of a parameter x (in this case, the percent iron in the mixture). If $\mathcal{L}$ is Gaussian in this space, then 1σ is the distance from the mean within which 68% of the the likelihood curve is contained. In other words, given:

$$\mathcal{L}(x) = \mathcal{L}(\overline{x}) \exp\left(-\frac{(x-\overline{x})^2}{2\sigma^2}\right)$$

the 1σ error bar is the x at which:

$$\mathcal{L}(x_{1\sigma)}) = \mathcal{L}_{max} \exp\left(-\frac{(1\sigma)^2}{2\sigma^2}\right) = \mathcal{L}_{max} e^{-1/2}$$

$$\ln \mathcal{L}(x_{1\sigma}) = \ln \mathcal{L}_{max} - 0.5$$

The 2σ error bars can be computed using the same procedure:

$$\ln \mathcal{L}(x_{2\sigma}) = \ln \mathcal{L}_{max} - 2.0$$

Using our plot of $\ln \mathcal{L}$ as a function of iron fraction, the end of the error bar is the iron fraction at which $\ln \mathcal{L}$ has dropped 0.5 (or 2.0) from its maximum [65].

With a large number of data points, the best mixture is more tightly constrained (the probability distribution has a narrow peak) while with few data points, different mixtures all have a higher chance of being consistent with the data, resulting in a flatter and more uncertain distribution of probabilities.

10.6 Systematics

We are faced with a choice of different models (hadronic interaction models, muon propagators, etc.) each with a different absolute normalization. However, renormalizing data to Monte Carlo in a low-energy calibration bin is a technique adaptable to any model. By treating each model as an independent test of normalization and composition, we can gauge the stability of this technique under changing models, and measure the systematic error on the final measurement.

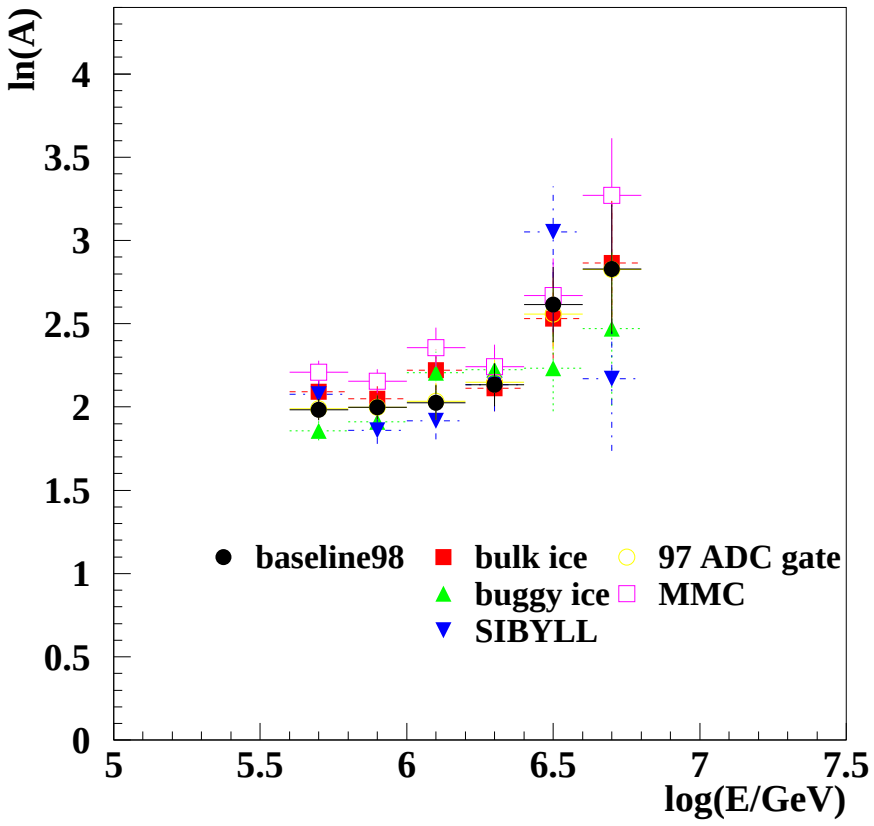

Figure 10.10: Composition as a function of energy, for different Monte Carlo assumptions.

Model	baseline	bulk	buggy	SIBYLL	98 gate	MMC
Mult.factor	1.38	1.15	1.02	1.02	1.38	1.45
Const.offset	0.14	0.06	0.01	0.01	0.14	0.16
log (E/GeV)	$\ln A \pm 1\sigma(2\sigma)$	$\ln A$				
5.6-5.8	1.98 $\pm$ 0.06 (0.13)	2.09	1.86	2.08	1.99	2.21
5.8-6.0	2.00 $\pm$ 0.07 (0.14)	2.05	1.91	1.86	2.00	2.15
6.0-6.2	2.03 $\pm$ 0.10 (0.21)	2.22	2.21	1.92	2.03	2.36
6.2-6.4	2.13 $\pm$ 0.13 (0.26)	2.11	2.22	2.13	2.15	2.24
6.4-6.6	2.62 $\pm$ 0.22 (0.45)	2.53	2.23	3.05	2.56	2.67
6.6-6.8	2.83 $\pm$ 0.39 (0.78)	2.87	2.47	2.17	2.83	3.2

Table 10.1: Summary of composition results from different Monte Carlo models.

For each of six independent models, a renormalization constant was computed using a 50/50 calibration mixture in the calibration bin $S(30) = 5 \rightarrow 10$. Then an identical analysis was performed; the experimental data was compared to the model in A^*, and the mean log mass and error bars were computed from the likelihood curve. Figure 10.10 shows the composition results for all six models; while there are systematic shifts in the *absolute* $\langle \ln A \rangle$, all of the composition measurements follow a similar *trend.* The numerical results from the six models are summarized in Table 10.1.

10.7 Conclusions

Figure 10.11 summarizes the findings of this work: the mean log mass as a function of energy. Data points indicate the best mixtures from the baseline model, with 1σ and 2σ statistical error bars computed from the likelihood curve. The band indicates the range of results from the use of different models, a measure of the systematic error.

The data show a robust trend of an unchanging composition between 500 TeV and 1.2 PeV of $\langle \ln A \rangle = 2.0$, after which it starts to become heavier. In the knee region (3 PeV), the composition continues to get heavier, up to $\langle \ln A \rangle = 2.8$ at 6 PeV, although the size of the error bars in these last bins allow our data to be consistent with a range of masses. The data are *not* consistent, however, with mass becoming lighter through the knee.

10.7.1 Comparison with other experiments

Figure 10.12 superimposes our results over a collection of results from other experiments of various types (including Cherenkov telescopes, scintillators, and coincidence experiments). Our

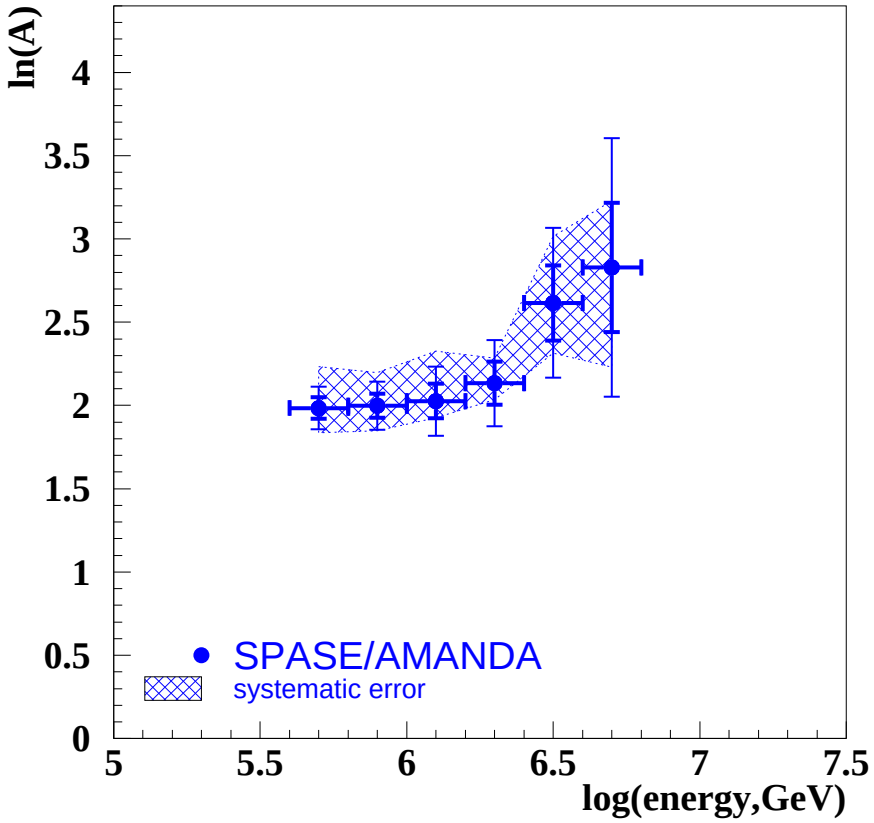

Figure 10.11: Final results: mass composition as a function of energy. Thick and thin error bars represent 1σ and 2σ statistical errors, respectively. Shaded region indicates systematic errors.

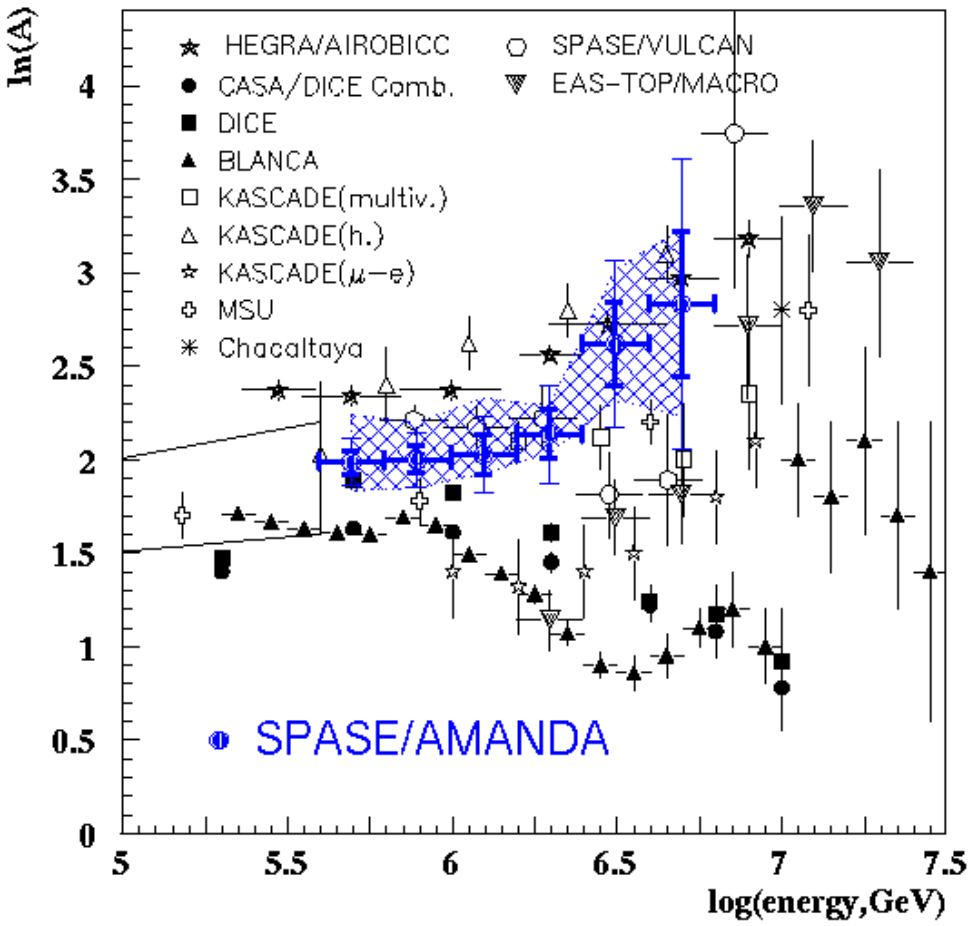

Figure 10.12: SPASE/AMANDA composition results compared to other experiments. Other experiments' data taken from [1]. HEGRA/AIROBICC data adapted from [48], SPASE/VULCAN data adapted from [114], and EAS-TOP/MACRO data adapted from [41]. Error bars for other experiments are statistical only.

results are consistent with those of some other experiments, but not others. In particular, the results of BLANCA and DICE (both Cherenkov telescopes which show the mass becoming lighter in this energy region) are in conflict with those of SPASE/AMANDA.

Of particular interest are SPASE/VULCAN (with which we have a detector in common) and EAS-TOP/MACRO (another deep underground muon coincidence experiment). SPASE/VULCAN's results are similar to ours, but share the "dip-and-then-rise" shape of the BLANCA results. EAS-TOP/MACRO has a high energy threshold and large error bars; it is difficult to say at this stage whether their results are comparable to ours.

Although each experiment alone has small statistical error bars (as can be seen in Figure 10.12), systematic errors are large and are not shown in this plot (except for ours). Each experiment suffers from different sources of systematics, and the ability of an experiment to understand and control its systematic effects determines the reliability of its result. It's a crowded room with a lot of shouting. But SPASE/AMANDA's technique was developed to be adaptable to any model and stable under systematics; we believe our results are a competitive voice.

Bibliography

Cosmic ray physics, theory, and reviews

[1] A. Castellina, "Cosmic ray composition and energy spectrum above 1 TeV: direct and EAS measurements." *Nucl. Phys. Proc. Suppl.* **97** (2001) 35-47.

[2] T. Gaisser, *Cosmic Rays and Particle Physics*. Cambridge (1990)

[3] M. S. Longhair, *High Energy Astrophysics, Volume 2*. Cambridge (1994)

[4] A.M. Hillas, "The Origin of Ultra-High-Energy Cosmic Rays." *Ann. Rev. Astron. Astroph.* **22** (1984) 425-444.

[5] M. Nagano and A.A. Watson, "Observations and implications of the ultrahigh-energy cosmic rays." *Rev. Mod. Phys.* **72** (2000) 689-732.

[6] G. Sigl, "Ultrahigh-Energy Cosmic Rays: Physics and Astrophysics at Extreme Energies." *Science* **5501** (2001) 73-79.

[7] P. Bhattacharjee and G. Sigl, "Origin and Propagation of Extremely High Energy Cosmic Rays." *Phys. Rep.* **327** (2000) 109-247.

[8] HiRes Collaboration, http://www.cosmic-ray.org/

[9] NGDC (NOAA), http://www.ngdc.noaa.gov/stp/SOLAR/COSMIC_RAYS/cosmic.html

[10] K-H. Kampert, "Methods of Determination of the Energy and Mass of Primary Cosmic ray Particles at Extensive Air Shower Energies." astro-ph/0101283 (2001)

[11] L. O'C. Drury, "Acceleration of Cosmic Rays." *Contemp. Phys.* **35** (1994) 231-242.

[12] M. Shapiro *et al.* (editors), *New Vistas in Astrophysics*. World Scientific (2000)

[13] J. J. Beatty, "Galactic Cosmic Rays With Energy Less Than 1 TeV/amu." in *26th ICRC Invited, Rapporteur, and Highlight Papers*, AIP Conference Proceedings (1999)

[14] K. Greisen, *Phys. Rev. Lett.* **16** (1966) 748, and G.T. Zatespin and V.A. Kuz'min, *Sov. Phys. JETP Lett.* **4** (1966) 78.

[15] E. Fermi, "On the Origin of the Cosmic Radiation." *Phys. Rev.* **75** (1949) 1169-1174.

[16] R. Blandford and D. Eichler, "Particle Acceleration at Astrophysical Shocks: a Theory of Cosmic Ray Origin." *Phys. Rep.* **154** (1987) 1-75.

[17] R.D. Blandford and J.P. Ostriker, "Particle Acceleration by Astrophysical Shocks." *Ap.J.* **221** (1978) L29-L32.

[18] A.R. Bell, "The acceleration of cosmic rays in shock fronts." *MNRAS* **182** (1978) 147-156.

[19] K. Greisen, "The extensive air showers." *Progress in Cosmic Ray Physics* **3** (1956) 1.

[20] P. Biermann, "Cosmic Rays I: The cosmic ray spectrum between 10^4 GeV and 310^9 GeV." *A&A* **271** (1993) 649-661.

[21] P. Biermann and J. Cassinelli, "Cosmic Rays II: Evidence for a magnetic rotator Wolf-Rayet star origin." *A&A* **277** (1993) 691-706.

[22] T. Stanev, P.Biermann, and T. Gaisser, "Cosmic Rays IV: The spectrum and chemical composition above 10^4 GeV." *A&A* **274** (1993) 902-908.

[23] R.J. Protheroe and A.P. Szabo, "High Energy Cosmic Rays from Active Galactic Nuclei." *Phys. Rev. Lett.* **69** (1992) 2885-2888.

[24] A.M. Hillas, "The knee of the cosmic ray spectrum: not a magnetic trapping effect?" *Proc. of the 16th ICRC (Kyoto)* **8** (1979) 7.

[25] J.R. Jokipii and G. Morfill, "Ultra-high-energy cosmic rays in a galactic wind and its termination shock." *Ap J* **312** (1987) 170-177.

[26] D. Fargion *et al.*, "Ultra High Energy Neutrino-Relic Neutrino Interactions in Dark Halos to Solve Infrared-TeV and GZK Cut-Off." *Proc. of the 27th ICRC (Hamburg)* (2001) 1578.

[27] M. Kachelriess, "Ultrahigh energy cosmic rays and new particle physics." astro-ph/0011231 (2000)

[28] J. Knapp, "Hadronic Interaction Models and Air Shower Simulations." *Nucl. Phys. B Proc. Suppl.* **75A** (1999) 89-98.

[29] J. Knapp, D. Heck, and G. Schatz, "Comparison of Hadronic Interaction Models Used in Air Shower Simulations and of Their Influence on Shower Development and Observables." Forschungszentrum Karlsruhe Report FZKA 5828 (1996)

Cosmic ray experiments and data

[30] A.V. Apanasenko *et al.*, "All particle spectrum observed by RUNJOB." *Proc. of the 27th ICRC (Hamburg)* (2001) 1622.

[31] D.J. Bird, *et al.* "Detection of a cosmic ray with a measured energy well beyond the expected spectral cutoff due to cosmic microwave radiation." *Astrophys. J.* **441** (1995) 144-150.

[32] K. Bernlöhr *et al.*, "The KASCADE view of cosmic rays." *Nucl. Phys. B Proc. Suppl.* **85** (2000) 311-317.

[33] J.W. Fowler *et al.*, "A Measurement of the Cosmic Ray Spectrum and Composition at the Knee." *Astropart. Phys.* **15** (2001) 49-64.

[34] J. Fowler, "Composition and Spectrum of Cosmic Rays at the Knee Measured by the CASA-BLANCA Experiment." Ph.D. dissertation, University of Chicago (2000)

[35] M.A.K. Glasmacher *et al.*, "The cosmic ray energy spectrum between 10^{14} and 10^{16} eV." *Astropart. Phys.* **10** (1999) 291-302.

[36] M. Aglietta *et al.*, "Study of the cosmic ray primary spectrum at $10^{15} < E_0 < 10^{16}$ eV with the EAS-TOP array." *Nucl. Phys. B Proc. Suppl.* **85** (2000) 318-323.

[37] G. Navarra *et al.* (for the EAS-TOP and LVD Collaborations), "Identification of light and very heavy cosmic ray primaries at $E_0 \approx 10^{15}$ eV from surface and deep underground measurements at the Gran Sasso Laboratories." *Nucl. Phys. B. Proc. Suppl.* **70** (1999) 512-514.

[38] M. Aglietta *et al.* (the EAS-TOP and LVD Collaborations), "The high energy muon spectrum in Extensive Air Showers: first data from LVD and EAS-TOP at Gran Sasso." *Astropart. Phys.* **9** (1998) 185-192.

[39] M. Aglietta *et al.* (the EAS-TOP and LVD Collaborations), "Study of the c.r. composition and interaction at $E_0 = 10 - 100$ TeV from observation of H.E. muons and atmospheric Cherenkov Light in EAS." *Nucl. Phys. B Proc. Suppl.* **75A** (1999) 259-261.

[40] M. Aglietta *et al.* (the EAS-TOP and MACRO Collaborations), "Study of the primary cosmic ray composition around the knee of the energy spectrum." *Phys. Lett. B* **337** (1994) 376.

[41] G. Navarra *et al.*, "Cosmic Ray composition around the knee from EAS electromagnetic and muon data." *Proc. of the 27th ICRC (Hamburg)* (2001) 120.

[42] T. Abu-Zayyad *et al.*, "Measurement of the Cosmic Ray Energy Spectrum and Composition from 10^{17} to $10^{18.3}$ eV Using a Hybrid Flourescence Technique." *Astrophys. J.* **557** (2001) 686-699.

[43] M. Nagano *et al.*, "Comparison of AGASA data with CORSIKA simulation." astro-ph/9912222 (1999)

[44] M. Ambrosio *et al.*, "High Energy cosmic ray physics with underground muons in MACRO. I. Analysis methods and experimental results." *Phys. Rev. D* **56** (1997) 1407-1417.

[45] M. Ambrosio *et al.*, "High Energy cosmic ray physics with underground muons in MACRO. II. Primary spectra and composition." *Phys. Rev. D* **56** (1997) 1418-1436.

[46] S.M. Kasahara *et al.*, "Study of cosmic ray composition in the knee region using multiple muon events in the Soudan 2 detector." *Phys. Rev. D* **55** (1997) 5282-5294.

[47] S.P. Wakely *et al.*, "Towards a New Cosmic Ray Composition Measurement in the Knee Using a Dual Air Cherenkov Array." *Proc. of the 26th ICRC (Salt Lake City)* **3** (1999) 148.

[48] F. Arqueros *et al.*, "Energy specrum and chemical composition of cosmic rays between 0.3 and 10 PeV determined from the Cherenkov-light and charged-particle distributions in air showers." *A&A* **359** (2000) 682-694.

[49] A. Röhring *et al.*, "Estimation of the Chemical Composition of Charged Cosmic Rays between 10^{14} eV and 10^{16} eV with the HEGRA Arrays." *Proc. of the 26th ICRC (Salt Lake City)* **3** (1999) 152.

[50] S.P. Swordy and D.B. Kieda, "The Composition near the 'Knee' from Multiparameter Measurements of Air Showers." *Proc. of the 26th ICRC (Salt Lake City)* **3** (1999) 144.

[51] D.B. Kieda and S.P. Swordy, "The Energy Spectrum in the Knee Region from DICE." *Proc. of the 26th ICRC (Salt Lake City)* **3** (1999) 191.

[52] C/C.H. Jui, for the HiRes Collaboration, "Measurement of the ultrahigh energy cosmic ray spectrum using monocular data from the High-Resolution Fly's Eye Experiment." Talk given at the 27th ICRC (Hamburg) (2001) 354.

[53] J. Bellido *et al.*, for the HiRes Collaboration, "Anisotropy studies of ultra-high energy cosmic rays as observed by the High-Resolution Fly's Eye (HiRes)." Talk given at the 27th ICRC (Hamburg) (2001) 364.

[54] K.A. Reil and R.W. Springer, for the HiRes Collaboration, "Preliminary stereo results from the High Resolution Fly's Eye cosmic ray observatory." Talk given at the 27th ICRC (Hamburg) (2001) 367.

[55] N. Sakaki *et al.*, "Cosmic Ray Energy spectrum above 3×10^{18} eV observed with AGASA." *Proc. of the 27th ICRC (Hamburg)* (2001) 333.

[56] M. Teshima *et al.*, "Anisotropy of cosmic-ray arrival directions at 10^{18} eV observed by AGASA." *Proc. of the 27th ICRC (Hamburg)* (2001) 337.

[57] M. Takeda *et al.*, "Clusters of cosmic rays above 10^{19} eV observed with AGASA." *Proc. of the 27th ICRC (Hamburg)* (2001) 341.

[58] M. Ave *et al.*, "Cosmic ray energy spectrum above 3×10^{17} eV measured with the Haverah Park Array." *Proc. of the 27th ICRC (Hamburg)* (2001) 381.

[59] C.G. Larsen, D.B. Kieda, and S.P. Swordy, "Reanalysis of energy spectrum and composition in the DICE experiment." *Proc. of the 27th ICRC (Hamburg)* (2001) 134.

[60] B. Allessandro *et al.*, "Study of the composition around the knee through the electromagnetic and muon detectors data at EAS-TOP." *Proc. of the 27th ICRC (Hamburg)* (2001) 124.

[61] M. Cha *et al.*, "Study of UHE primary cosmic ray composition with atmospheric Cherenkov light observations." *Proc. of the 27th ICRC (Hamburg)* (2001) 132.

[62] K.-H. Kampert *et al.*, "The KASCADE Air Shower Experiment: Composition Analyses and Energy Spectrum." *Proc. of the 26th ICRC (Salt Lake City)* **3** (1999) 159.

[63] M. Roth *et al.*, "Nonparametric determination of energy spectra and mass composition of primary cosmic rays for slant depth." *Proc. of the 27th ICRC (Hamburg)* (2001) 88.

[64] M. Boratav for the Auger Collaboration, "The Pierre Auger Observatory Project: An Overview." *Proc. of the 25th. ICRC (Durban)* **5** (1997) 205.

More physics

[65] P.R. Bevington and D.K. Robinson, *Data Reduction and Error Analysis for the Physical Sciences.* McGraw-Hill (1969)

[66] R.M. Barnett *et al.* (Particle Data Group), "Review of Particle Physics." *Phys. Rev. D* **45** (1996) 1.

[67] O.C. Allkofer and D.P. Bhattacharyya, "Depth-intensity relation for large depths in sea water derived from the primary-cosmic-ray energy spectrum." *Phys. Rev. D* **34** (1986) 1368-1371.

[68] W.H. Press *et al.*, *Numerical Recipes.* Cambridge (1989)

[69] P. Askebjer *et al.*, "Optical properties of deep ice at the South Pole: absorption." *Applied Optics* **36** (1997) 4168-4180.

[70] P.B. Price and L. Bergström, "Optical properties of deep ice at the South Pole: scattering." *Applied Optics* **36** (1997) 4181-4194.

[71] Y.D. He and P.B. Price, "Remote sensing of dust in deep ice at the South Pole." *J. of Geophys. Res.* **103** (1998) 17041-17056.

[72] D. Pandel, "Determination of water and detector parameters and reconstruction of muons up to 100 TeV with the Baikal neutrino telescope NT-72." Diploma thesis, Humboldt University, Berlin (1996)

[73] C. Wiebusch, "The Detection of Faint Light in Deep Underwater Neutrino Telescopes." Ph.D. dissertation, RWTH, Aachen (1995)

[74] P. Lipari and T. Stanev, "Propagation of multi-TeV muons." *Phys. Rev. D* **44** (1991) 3543-3554.

[75] G. Bossard *et al.*, "Cosmic Ray Air Shower Characteristics in the Framework of the Parton-Based Gribov-Regge Model NEXUS." *Phys.Rev. D* **63** (2001) 54030.

AMANDA references

[76] E. Andres *et al.*, "The AMANDA neutrino telescope: principle of operation and first results." *Astropart. Phys.* **13** (2000) 1.

[77] E. Andres *et al.*, "Observation of high-energy neutrinos using Cherenkov detectors embedded deep in Antarctic ice." *Nature* **410** (2001) 441-443.

[78] X. Bai *et al.*, "Calibration and Survey of AMANDA with the SPASE Detectors." in preparation.

[79] T. DeYoung, "Observation of Atmospheric Muon Neutrinos with AMANDA." Ph.D. dissertation, University of Wisconsin-Madison (2001)

[80] P. Miočinović, Ph.D. dissertation, University of California-Berkeley, in preparation.

[81] S. Young, "A Search for Point Sources of High Energy Neutrinos with the AMANDA-B10 Neutrino Telescope." Ph.D. dissertation, University of California-Irvine (2001)

[82] G. Hill *et al.* (The AMANDA Collaboration), "Performance of the AMANDA-B10 String Array." *Proc. of the 26th ICRC (Salt Lake City)* **2** (1999) 432.

[83] K. Woschnagg *et al.* (The AMANDA Collaboration), "Optical Properties of South Pole Ice at Depths from 140 to 2300 Meters." *Proc. of the 26th ICRC (Salt Lake City)* **2** (1999) 200.

[84] K. Woschnagg, http://amanda.berkeley.edu/kurt/ice2000/hq.html

[85] K. Woschnagg, presentation at AMANDA collaboration meeting, Madison WI, June 2001.

[86] D. Lowder and K. Woschnagg, "Determination of optical parameters in AMANDA-B ice." DESY-PROC-1999-1 (1999) 145.

[87] A. Karle, "Monte Carlo simulation of photon transport and detection in deep ice: muons and cascades." DESY-PROC-1999-1 (1999) 174.

[88] C. Wiebusch, "Muon reconstruction with AMANDA." DESY-PROC-1999-1 (1999) 302.

[89] S. Hundertmark, "AMASIM Neutrino Detector Simulation Program." DESY-PROC-1999-1 (1999) 276.

[90] S. Hundertmark, "Vertical Ice Properties for the AMANDA-Simulation." AMANDA internal report #20001001 (2000)

[91] P. Sudhoff, "Transmission measurements with Amanda Glass and Evaluation for IceCube." AMANDA internal report #20010701 (2001)

[92] P. Olbrechts and C. Wiebusch, "On the Angular Sensitivity of Optical Modules in Ice." AMANDA internal report #20010102 (2001)

[93] G. Hill, "Bayesian event reconstruction and background rejection in neutrino detectors." *Proc. of the 27th ICRC (Hamburg).* (2001) 1279.

[94] G. Hill, M. Leuthold and the AMANDA Collaboration, "Search for a Diffuse Flux from Sources of High Energy Neutrinos with AMANDA B-10." *Proc. of the 27th ICRC (Hamburg)* (2001) 1113.

[95] X. Bai *et al.* and the AMANDA Collaboration, "Calibration and Survey of AMANDA with Spase." *Proc. of the 27th ICRC (Hamburg)* (2001) 977.

[96] R. Hardtke, G. Barouch and the AMANDA Collaboration, "The AMANDA Search for High Energy Neutrinos from Gamma Ray Bursts." *Proc. of the 27th ICRC (Hamburg)* (2001) 1121.

[97] P. Niessen and the AMANDA Collaboration, "Search for Relativistic Monopoles with the AMANDA Detector." *Proc. of the 27th ICRC (Hamburg)* (2001) 1496.

[98] D. Chirkin and W. Rhode, "Muon Monte Carlo: a new high-precision tool for muon propagation through matter." *Proc. of the 27th ICRC (Hamburg)* (2001) 1017.

[99] J. Ahrens *et al.*, "Limits to the muon flux from WIMP annihilation in the center of the Earth with the AMANDA detector." in preparation.

[100] K. Rawlins, http://alizarin.physics.wisc.edu/kath/waveforms/ (2001)

[101] R. Stokstad, A. Smith, *et al.*, presentation at AMANDA collaboration meeting, Berkeley CA, April 1999.

[102] A. Karle, private communication.

[103] P. Desiati, private communication.

[104] P. Steffen, private communication.

SPASE, VULCAN, and GASP references

[105] T. Miller *et al.* (The AMANDA Collaboration), "Calibration of AMANDA with Coincidence Events from SPASE-2." *Proc. of the 26th ICRC (Salt Lake City)* **2** (1999) 465.

[106] J.E. Dickinson *et al.*, "Studies of the mass composition of cosmic rays with the SPASE-2/VULCAN instrument at the South Pole." *Proc. of the 26th ICRC (Salt Lake City)* **3** (1999) 136.

[107] N.J.T. Smith *et al.*, "An experiment to search for ultra high energy γ-sources from the South Pole." *Nucl. Instr. and Meth. A* **276** (1989) 622.

[108] J. Beaman *et al.*, "Performance of the South Pole Air Shower Experiment during 1987 to 1992." *Phys. Rev. D* **48** (1993) 4495-4503.

[109] J. van Stekelenborg, *et al.*, "Search for point sources of ultrahigh energy gamma rays in the southern hemisphere with the South Pole Air Shower Experiment." *Phys. Rev. D* **48** (1993) 4504.

[110] J.E. Dickinson *et al.*, "The new South Pole air shower experiment - SPASE-2." *Nucl. Instr. and Meth. A* **440** (2000) 95-113.

[111] J.E. Dickinson *et al.*, "A new air-Cerenkov array at the South Pole." *Nucl. Instr. and Meth. A* **440** (2000) 114-123.

[112] P. Romenesko, A. Karle, and R. Morse, "Analysis of coincident detection of high energy cosmic ray showers in the GASP air Cherenkov telescope and the AMANDA neutrino detector at the South Pole." AMANDA internal report #20000905 (2000)

[113] K. Rochester, "Measurements of the Mass Composition of Cosmic Rays near 10^{15} eV made at the South Pole." Ph.D. dissertation, University of Leeds. (2000)

[114] J. Hinton, "The Electron, Muon and Cerenkov Components of Extensive Air Showers Studied at the South Pole." Ph.D. dissertation, University of Leeds. (1998)

[115] X. Bai, private communication.

FFT References

[116] M.Abramowitz and I.A.Stegun, *Handbook of Mathematical Functions.* (1965) 940.

[117] A. Bouchta *et al.*, "Supernova Neutrino-Burst Detection with the AMANDA-B10 Neutrino Telescope.", AMANDA Internal Report #20000901 (2000)

[118] S. Geer, "Neutrino beams from muon storage rings: Characteristics and physics potential." *Phys. Rev. D* **57** (1998) 6989.

[119] E.J.Groth, "Probability distributions related to power spectra." *Ap. J. Suppl.* **29** (1975) 285.

[120] F. Halzen, private communication.

[121] J. Jacobsen "Simulating the detection of muons and neutrinos in deep Antarctic ice." Ph.D. Thesis, University of Wisconsin-Madison (1996)

[122] D.A.Leahy *et al.*, "On searches for pulsed emission with application to four globular cluster X-ray sources: NGC 1851, 6441, 6624, and 6712." *Ap. J.* **266** (1983) 160.

[123] B.A.Vaughan *et al.*, "Searches for millisecond pulsations in Low-Mass X-ray Binaries II." *Ap. J.* **435** (1994) 362.

Appendix A

Derivation: Cylindrical proximity cut

First we must define the physical size and placement of AMANDA-B10. On the surface, the strings are arranged in concentric rings, and the outer edge of B10 lies at a radius of approximately 60 meters (see Fig. 4.1(b)). The height and position of the cylinder is determined by the distribution of depths of the optical modules in B10 (see Fig. A.1). From this figure, we see that the actual center of the array is not at zero but at about +45 meters in the AMANDA coordinate system, and that most of the modules lie within ±175 meters from this central depth.

For every SPASE track with coordinates $(x_0, y_0, z_0, \theta, \phi)$, there is exactly one smallest cylinder of a fixed height/radius ratio and fixed center position which the track intersects. There are two possible ways that the track could intersect the cylinder: by clipping the rim of the top or bottom circle, or by grazing the side of the cylinder (see in Figure A.2). We discuss the two possibilities separately.

A.1 Top/bottom-clippers

The cylinder is defined by its fixed radius-to-height ratio R/H. So all the possible points that could lie on the *edge* of the top or bottom of the cylinder are defined by a *cone* of aspect ratio R/H (see Figure A.2(a)) A track which nicks the top or bottom must intersect the cone at some point (x, y, z). We solve for the size of the cone by finding this point.

We describe the cone with the equation: $\sqrt{x^2 + y^2} = kz'$ where $k = R/H$ is a fixed number and $z' = z - z_{center}$ is a coordinate relative to the center of the array (rather than of the coordinate

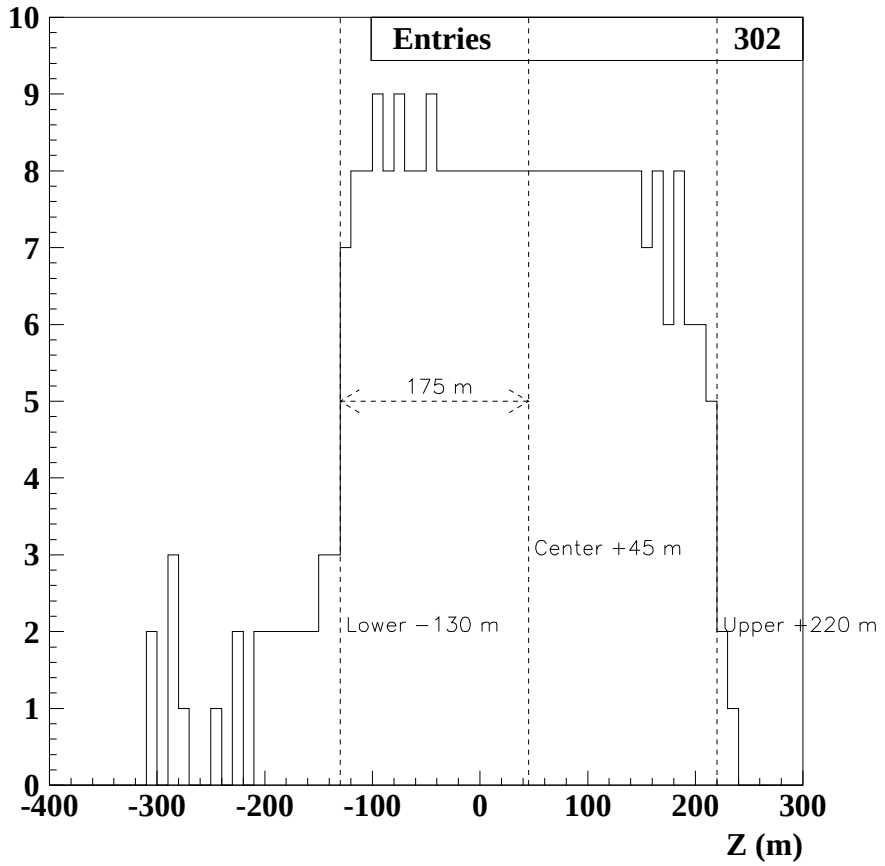

Figure A.1: Distribution of depth of all OM's in AMANDA-B10, in the AMANDA coordinate system. The dotted "boundary" indicates the depth range which contains most of the 302 modules (strings 1-4 are a bit deeper, but contain fewer modules, than strings 5-10). The center of this range is at a depth of +45 meters.

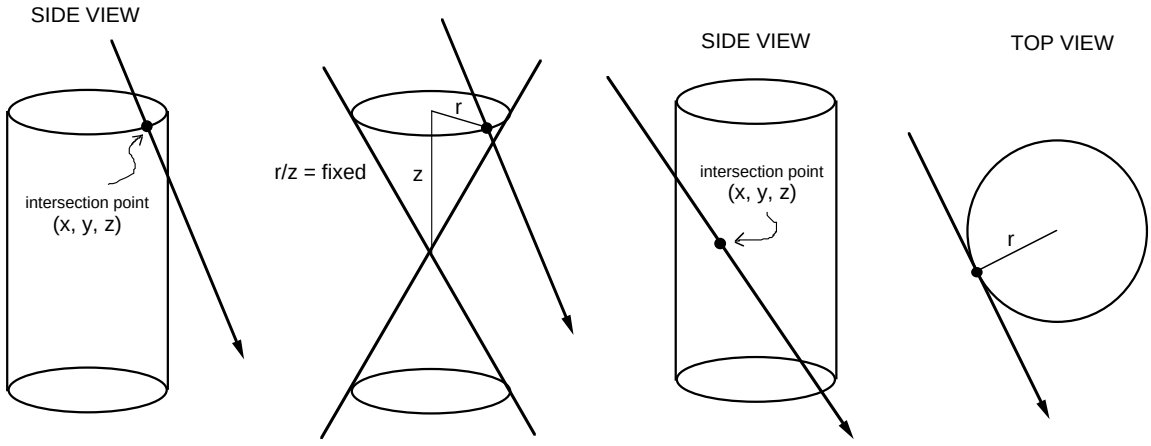

(a) Top- and bottom-clippers

(b) Cylinder side-clippers

Figure A.2: Two possible cylinder-of-closest-approach algorithms

system). The track can be described by the equations

$$\begin{cases} x = x_0 + d\cos\phi\sin\theta = x_0 + dp_x \\ y = y_0 + d\sin\phi\sin\theta = y_0 + dp_y \\ z = z_0 + d\cos\theta = z_0 + dp_z \end{cases}$$

By combining these sets of equations one can solve for the distance d:

$$\begin{aligned} x^2 + y^2 &= k^2 z'^2 \\ (x_0 + dp_x)^2 + (y_0 + dp_y)^2 &= k^2(z_0 + dp_z - z_{center})^2 \\ x_0^2 + 2x_0p_xd + d^2p_x^2 + y_0^2 + 2y_0p_yd + d^2p_y^2 &= k^2((z_0 - z_{center})^2 + 2(z_0 - z_{center})p_zd + d^2p_z^2) \end{aligned}$$

$$d^2(p_x^2 + p_y^2 - k^2p_z^2) + 2d(x_0p_x + y_0p_y - k^2(z_0 - z_{center})p_z + x_0^2 + y_0^2 - k^2(z_0 - z_{center})^2 = 0$$

The equation to be solved is quadratic in d. Therefore there can be one, two, or zero solutions. If there are two solutions than the one which yields the smallest size is chosen. If there are no solutions, then the track must intersect the side of the cylinder rather than the top or bottom.

If a solution for d exists, then it can be used to find the intersection point (x, y, z). The size of the cylinder is then: $C = z'/H = (z_0 + dp_z - z_{center})/H$.

A.2 Cylinder side-clippers

Similarly to above, again we find the intersection point (x, y, z), this time between the track (described by the same equations as above) and a cylinder (see Figure A.2(b)), described by the equation $x^2 + y^2 = r^2$.

$$\begin{aligned}(x_0 + dp_x)^2 + (y_0 + dp_y)^2 &= r^2 \\ x_0^2 + 2x_0p_xd + d^2p_x^2 + y_0^2 + 2y_0p_yd + d^2p_y^2 &= r^2 \\ d^2(p_x^2 + p_y^2) + 2d(x_0p_x + y_0p_y) + x_0^2 + y_0^2 - r^2 &= 0\end{aligned}$$

Again, combining these two equations leads to a quadratic formula for d. However, the *smallest* cylinder which has an intersection point is the one where this quadratic formula has *exactly one* root, requiring:

$$4(x_0p_x + y_0p_y)^2 - 4(p_x^2 + p_y^2)(x_0^2 + y_0^2 - r^2) = 0$$

$$(x_0p_x + y_0p_y)^2 = (p_x^2 + p_y^2)(x_0^2 + y_0^2 - r^2)$$

$$r^2 = (x_0^2 + y_0^2) - \frac{(x_0p_x + y_0p_y)^2}{(p_x^2 + p_y^2)}$$

This condition imposed, the resulting size is: $C = r/R$, but only if the corresponding z' to this intersection point

$$z' = z_0 + dp_z - z_{center} = z_0 - z_{center} - p_z(x_0p_x + y_0p_y)/(p_x^2 + p_y^2)$$

is less than $C \times H$.

Both the top/bottom-clipping and side-clipping solutions are computed, and whichever computation gives the smallest size C is the final result.

Appendix B

A muon bundle likelihood function for `recoos`

B.1 Motivation and general theory

At the heart of `recoos` is the "likelihood function." Given a hypothesis, this function returns the probability that that hypothesis could have given rise to the observed hit pattern in the detector. The hypothesis is passed to the function as a "track," a set of parameters describing the position, direction (and sometimes length or energy) of either an infinite muon from a ν_μ, or a cascade from a ν_e. To find the best track, `recoos` calls this function repeatedly with different hypothesis tracks until it finds the most likely one.

The AMANDA collaboration has written many likelihood functions. Most of them perform a of loop through all optical modules, for each one computing the probability that the hit on the module (or lack of a hit) could have come from the current track hypothesis. Hit and not-hit modules must be treated differently; if a module is not hit, the likelihood is P_{nohit}. If it is hit, the likelihood is $P_{hit}(time, ADC, etc.)$, which is often more complicated. The total likelihood for the event as a whole is then the product of the individual OM likelihoods, as discussed in Chapter 5.

What if, however, we want to hypothesize a more complicated phenomenon (such as a stopping or starting muon) or two phenomena at once in the detector (for instance, two coincident muons or a muon plus a burst of bremsstrahlung light)? This necessitates a "multiple hypothesis." Let's consider first a simple double-hypothesis case. For the modules which are not hit, the probability is:

$$P_{nohit} = P_{nohit_{hyp1}} \quad \text{AND} \quad P_{nohit_{hyp2}}$$

$$= P_{nohit_{hyp1}} \times P_{nohit_{hyp2}}$$

For modules which are hit, the probability is:

$$P_{hit}(time, ADC) = P_{hit_{hyp1}}(time, ADC) \quad \text{OR} \quad P_{hit_{hyp2}}(time, ADC)$$

$$= 1 - \{(\text{NOT} \quad P_{hit_{hyp1}}(time, ADC)) \quad \text{AND} \quad (\text{NOT} \quad P_{hit_{hyp2}}(time, ADC))\}$$

$$= 1 - \{(1 - P_{hit_{hyp1}}(time, ADC)) \times (1 - P_{hit_{hyp2}}(time, ADC))\}$$

This philosophy can be extended to any number of hypotheses; for instance, a bundle of N muons, or a muon with N bremsstrahlung bursts.

B.2 The Muon-Bundle Hypothesis

The infrastructure of `recoos` is not yet capable of handling multiple hypotheses, although work on this is in progress. However, with some mathematical inventiveness, one particular application can be carried out within the existing infrastructure: muon bundles.

Depending on the energy and composition of the cosmic ray primary, bundles of from a few to hundreds of muons trigger AMANDA as downgoing events. These events currently are analyzed and reconstructed as though they were single muons, despite the fact that their bundle nature disturbs the delicate timing of hits that is of crucial importance to the reconstruction.

The *bundle hypothesis* does not attempt to treat tens or hundreds of muons as individual tracks; this would be far to involved. Rather, we treat the bundle as a mathematical distribution of muons with certain assumed properties. Specifically, we assume:

- The center of the muon bundle is the "primary track," or the incidence direction of the cosmic ray primary particle. At AMANDA depth, all muons are approximately parallel to the primary track at distances R away from it.

- Muons are distributed spatially around the center of the bundle according to a radially-symmetric density function $\rho_\mu(R)$ where R is the distance from the bundle center and ρ_μ

has units of number of muons per square meter. The integral of $\rho_\mu(R)$ over the whole plane is the total number of muons N_μ at some reference slant depth (such as 1750 meters).

- The energy per muon is also described by a radially-symmetric function $E(R)$. In general, muons closer to the center of the bundle have higher energy than outliers.

Given these basic assumptions, we now compute a likelihood function. As has been done before, the total likelihood of an event given a hypothesis is the product of the likelihoods from all individual OM's:

$$-\log(\mathcal{L}) = \sum_{OM's} -\log(\mathcal{L}_{OM})$$

So now we must ask what the bundle hypothesis "looks like" from the point of view of an optical module.

The OM is a distance D from the center of the bundle, and so there is a distribution of muons at a variety of distances. The probability of the OM being hit (or not) from a *particular* muon depends on the distance r from that muon to the OM and its energy E. For a module which is not hit, the likelihood is $P_{nohit}(r, E)$. For a module which is hit, the likelihood is $P_{hit}(r, E)\mathcal{L}_{upandel}(r, t)$ where $\mathcal{L}_{upandel}(r, t)$ is the "U-pandel" probability of observing the hit at the expected time. These functions are already available in `recoos`for single muons, and we will adapt them to muon bundles.

Each muon in the bundle hypothesis has its own probability for the OM. From the OM's point of view, the probability of being hit by a muon with certain properties must be weighted by the number of muons in the bundle that have those properties. For instance, if an OM has a hit which arrives early in time, it may be 100 times more likely that it came from an "outlier" muon close to the OM but far from the center of the bundle. However, there may be 100 times as many muons in the center of the bundle than outlying; each probability must be weighted by the number of muons contributing.

To do this correctly, we divide the space around the OM into small bins of r and θ, shown in Figure B.1. Each bin contains a number of muons n_i equal to $\rho_\mu(r, \theta)rdrd\theta$, where ρ_μ is the muon density function, re-expressed in terms of the variables r and θ (relative to the OM) instead of R (relative to the bundle center).

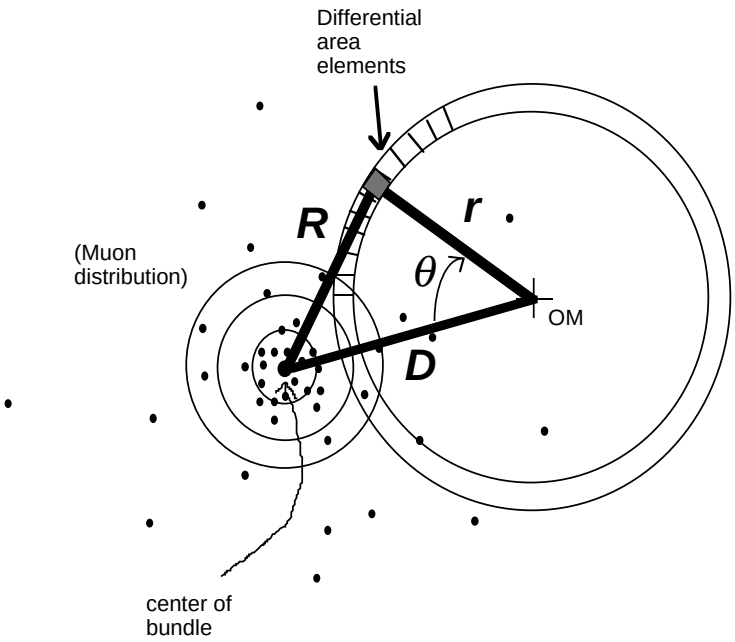

Figure B.1: Coordinates used in the bundle-likelihood reconstruction.

B.2.1 If the OM is not hit

Consider a single small bin i, which is at a radius r from the OM. If there is one muon in this bin with energy E, then:

$$\mathcal{L}_i = P_{nohit}(r, E)$$

If there are two muons in this bin with energy E, then:

$$\begin{aligned} \mathcal{L}_i &= P_{nohit}(r, E) \times P_{nohit}(r, E) \\ &= P_{nohit}(r, E)^2 \end{aligned}$$

In general, if there are n_i muons with energy E in this bin, then:

$$\mathcal{L}_i = P_{nohit}(r, E)^{n_i}$$

Now consider muons from different bins $i = 1, 2, 3....$ The OM has not been hit by any of the

muons in *any* of the bins. Therefore,

$$\begin{aligned}
\mathcal{L}_{OM} &= \mathcal{L}_1 \times \mathcal{L}_2 \times \mathcal{L}_3 \times ... \\
&= P_{nohit}(r_1, E_1)^{n_1} \times P_{nohit}(r_2, E_2)^{n_2} \times P_{nohit}(r_3, E_3)^{n_3} \times ... \\
\log(\mathcal{L}_{OM}) &= n_1 \log(P_{nohit}(r_1, E_1)) + n_2 \log(P_{nohit}(r_2, E_2)) + n_3 \log(P_{nohit}(r_3, E_3)) + ... \\
&= \sum_{bins,i} n_i \log(P_{nohit}(r_i, E_i)) \\
&= \sum_{bins,r,\theta} \rho_\mu(r,\theta) r dr d\theta \log(P_{nohit}(r_i, E_i)) \\
&= \int_0^\infty \int_0^{2\pi} \rho_\mu(r,\theta) \log(P_{nohit}(r, E(r,\theta))) r dr d\theta
\end{aligned}$$

This last step transforms a sum over all bins surrounding the OM into a two dimensional integral over r and θ.

B.2.2 If the OM is hit at time t

We follow the same general procedure as above: consider first a single bin i. If there is one muon in this bin with energy E, then:

$$\mathcal{L}_i = P_{hit}(r, E) \mathcal{L}_{upandel}(r, \theta, t)$$

If there are two muons in this bin with energy E, then:

$$\begin{aligned}
\mathcal{L}_i &= 1 - \{1 - P_{hit}(r, E) \mathcal{L}_{upandel}(r, \theta, t)\} \times \{1 - P_{hit}(r, E) \mathcal{L}_{upandel}(r, \theta, t)\} \\
&= 1 - \{1 - P_{hit}(r, E) \mathcal{L}_{upandel}(r, \theta, t)\}^2
\end{aligned}$$

In general, if there are n_i muons with energy E in this bin, then:

$$\mathcal{L}_i = 1 - \{1 - P_{hit}(r, E) \mathcal{L}_{upandel}(r, \theta, t)\}^{n_i}$$

Now consider muons from different bins $i = 1, 2, 3....$ The OM has could have been hit by any

of the muons in *any* of the bins. Therefore,

$$\begin{aligned}
\mathcal{L}_{OM} &= 1 - [(1-\mathcal{L}_1)\times(1-\mathcal{L}_2)\times(1-\mathcal{L}_3)\times ...] \\
&= 1 - [\{1 - P_{hit}(r_1,E_1)\mathcal{L}_{upandel}(r_1,\theta_1,t)\}^{n_1}\times \\
&\quad \{1 - P_{hit}(r_2,E_2)\mathcal{L}_{upandel}(r_2,\theta_2,t)\}^{n_2}\times \\
&\quad \{1 - P_{hit}(r_3,E_3)\mathcal{L}_{upandel}(r_3,\theta_3,t)\}^{n_3}\times ...] \\
\log(1-\mathcal{L}_{OM}) &= n_1 \log\{1 - P_{hit}(r_1,E_1)\mathcal{L}_{upandel}(r_1,\theta_1,t)\} + \\
&\quad n_2 \log\{1 - P_{hit}(r_2,E_2)\mathcal{L}_{upandel}(r_2,\theta_2,t)\} + \\
&\quad n_3 \log\{1 - P_{hit}(r_3,E_3)\mathcal{L}_{upandel}(r_3,\theta_3,t)\} + ... \\
&= \sum_{bins,i} n_i \log\{1 - P_{hit}(r_i,E_i)\mathcal{L}_{upandel}(r_i,\theta_i,t)\} \\
&= \sum_{bins,r,\theta} \rho_\mu(r,\theta) r dr d\theta \log\{1 - P_{hit}(r,E(r,\theta))\mathcal{L}_{upandel}(r,\theta,t)\} \\
&= \int_0^\infty \int_0^{2\pi} \rho_\mu(r,\theta) \log\{1 - P_{hit}(r,E(r,\theta))\mathcal{L}_{upandel}(r,\theta,t)\} r dr d\theta
\end{aligned}$$

B.3 Functions

Both functions ρ_μ and E depend on the physical model we assume for the muon bundles, but each one is radially symmetric in R and can be reexpressed as a function of r and θ through this relationship:

$$R = \sqrt{r^2 + D^2 - 2rDcos\theta}$$

The energy function has not been well-studied, and so for now is assumed to be flat:

$$E = 200 \text{ GeV}$$

but this can be easily modified as long as it remains radially symmetric with respect to R. For the lateral distribution of the muons ρ_μ, we choose a functional form from [2]:

$$\rho_\mu(r) = N_\mu C \frac{1}{(r+r_0)^\alpha} \quad \text{where} \quad C = (\alpha-1)(\alpha-2)/r_0^{(2-\alpha)}$$

From examination of MOCCA-QGSJET Monte Carlo, this form fits quite well (see, for instance, Figure 3.6) The parameter α is always close to five, while the characteristic radius r_0 depends on the composition; for protons, $r_0 \approx 8$ m, while for iron it is double that. This means that r_0 alone, if measured well, could measure cosmic ray composition.

B.4 Computation

For the single muon hypothesis, the likelihood function had to make a single function call for each OM. Now, for the muon bundle hypothesis, for each OM the function must perform a two-dimensional integral! The computationally-expensive U-pandel function must be called for each bin in the numerical integral.

Thus, we must make use of as many approximations and timesavers as we can in the execution of this two-dimensional integral. For instance, for small numbers using the approximation $log(1+x) \approx x$ can improve computation speed.

What improves the speed the most, however, is reducing the number of function calls to the functions P_{nohit}, P_{hit}, and $\mathcal{L}_{upandel}$. This can be done first of all by removing the θ-dependence from these functions, integrating with respect to θ first, and reducing the two-dimensional integral to a one-dimensional integral in r only. θ-dependence in these functions in generally embedded in a dependence on the orientation angle η of the PMT.

Although the U-Pandel function strictly addresses timing only, and one might not expect that it would depend on the PMT orientation at all, it does depend on this variable. But the orientation is used only in the parametrization of the variables τ and λ, through the computation of the "effective distance" [88]:

$$d_{eff} = 3.1 - 3.9\cos(\eta) + 4.6\cos^2(\eta) + 0.84 d_\mu$$

For most regions of our integration space, d_μ will be the dominant part of this expression, and small changes to η will not greatly affect the outcome. Therefore, we will assume that the value of the U-Pandel function is nearly constant in η (and therefore also θ), and depends only on r:

$$\mathcal{L}_{upandel}(r,\theta,t) \approx \mathcal{L}_{upandel}(r,t) \quad \text{where} \quad \eta = \eta_{primary}$$

The P_{hit} and P_{nohit} functions, however, will depend strongly on θ because of the changing sensitivity of the PMT to different incidence angles. However, the η-dependence can be separated out.

$$\begin{aligned} P_{nohit} &= (1 - P^0_{hit}(r,E))^{\epsilon} \\ &= (1 - P^0_{hit}(r,E))^{\epsilon_{PMT}\epsilon_E(E)\epsilon_{ori}(E,\eta)} \\ \log(P_{nohit}) &= [\epsilon_{PMT}\epsilon_E(E)\epsilon_{ori}(E,\eta)]\log(1 - P^0_{hit}(r,E)) \end{aligned}$$

Here, ϵ_{PMT} is a constant (the sensitivity of the PMT), $\epsilon_E(E)$ scales the efficiency by the amount of muon light, and $\epsilon_{ori}(E,\eta)$ corrects the efficiency according to the PMT's orientation relative to the light.

The quantity $P^0_{hit}(r,E)$ does not depend strongly on the energy E, but rather a dependence on E is buried deeply into the calculation of the "effective distance" d_{eff}. This distance is computed differently for the P_{nohit} and $\mathcal{L}_{upandel}$ functions, but as above, we will assume that varying E is only a higher-order correction, and approximate:

$$P^0_{hit}(r,E) \approx P^0_{hit}(r) \quad \text{where} \quad E = 200\ \text{GeV}$$

The next step is to translate a dependence on η into a dependence on r and θ:

$$\begin{aligned} \cos\eta &= -\cos\theta_c\cos\theta_{track} - \sin\theta_c\sin\theta_{track}[\cos\theta\cos\phi'_{track} - \sin\theta\sin\phi'_{track}] \\ &= \cos\eta_{primary}\cos\theta + \cos\theta_c\cos\theta_{track}(1-\cos\theta) + \sin\theta_c\sin\theta_{track}\sin\phi'_{track}\sin\theta \end{aligned}$$

where ϕ'_{track} is relative to a transformed z-axis.

Now to insert all these expressions into the integral likelihood: For modules *not hit*:

$$\log(\mathcal{L}_{OM}) = \int_0^{\infty}\int_0^{2\pi} \rho_\mu(r,\theta)\log(P_{nohit}(r,E(r,\theta)))rdrd\theta$$

$$= \int_0^{\infty}\int_0^{2\pi} \rho_\mu(r,\theta)\epsilon_{PMT}\epsilon_E(E)\epsilon_{ori}(E,\eta)\log(1 - P^0_{hit}(r))rdrd\theta$$

$$= \int_0^\infty \left(\int_0^{2\pi} \epsilon_{PMT} \rho_\mu(r,\theta) \epsilon_E(r,\theta) \epsilon_{ori}(r,\theta) d\theta \right) \log(1 - P^0_{hit}(r)) r dr$$

The integral in parentheses is relatively fast to compute, leaving only the one-dimensional integral with the time-consuming function calls.

For modules which *are hit*:

$$\log(1 - \mathcal{L}_{OM}) = \int_0^\infty \int_0^{2\pi} \rho_\mu(r,\theta) \log\{1 - P_{hit}(r, E(r,\theta)) \mathcal{L}_{upandel}\} r dr d\theta$$

$$\approx \int_0^\infty \int_0^{2\pi} \rho_\mu(r,\theta) \{-P_{hit}(r, E(r,\theta)) \mathcal{L}_{upandel}\} r dr d\theta$$

$$= \int_0^\infty \int_0^{2\pi} \rho_\mu(r,\theta) \{(P_{nohit}(r, E(r,\theta)) - 1) \mathcal{L}_{upandel}\} r dr d\theta$$

$$= \int_0^\infty \left(\int_0^{2\pi} \rho_\mu(r,\theta) (P_{nohit}(r, E(r,\theta)) - 1) d\theta \right) \mathcal{L}_{upandel} r dr$$

...which unfortunately doesn't reduce any further. Since the P_{hit} function must be called in both integrals, this computation is slower. But since there are fewer hit modules than not-hit modules in general, the routine as a whole does not suffer too much.

B.5 Implementation

The likelihood function is now written down completely in terms of existing functions and existing variables, with the addition of only two extra parameters: the number of muons N_μ and the characteristic radius of the bundle r_0. Fortunately, in addition to the free parameters (x, y, z, θ, ϕ), a track also has available the parameters energy E and length L, which are part of the software's existing infrastructure. So, we implement this function by assigning N_μ to the track's "energy" and r_0 to its "length" and asking `recoos` to *fit* them both as free parameters.

B.6 Results

I attempted to implement this function in `recoos`. The resulting reconstruction takes approximately two minutes per event, making debugging extremely difficult.

Although all the "parts" of the code seem to be in working order, the reconstruction does not perform well. There is almost no correlation between $N_{\mu_{reco}}$ and $N_{\mu_{true}}$ when run on Monte Carlo, nor is there any separation between protons and iron in the characteristic radius parameter r_0.

The problem could lie in the P_{hit} and P_{nohit} functions, since doubt has been cast on their validity by the recent discovery of a bug in the photon tracking package PTD. However, the reconstruction doesn't work even on Monte Carlo for which "model in" should yield "model out." Since AMANDA is a sparse array, it could simply be that there is not enough information contained in the hits to distinguish between different hypothesis bundle-shapes. After all, r_0 is typically less than the spacing between OM's. But even without resolution in r_0, N_μ should at least scale with the number of muons and this, too, fails. A coding problem could still be lurking undiscovered.

Despite the failures so far, it is this author's fervent hope that this technique might someday function correctly and fulfill its potential for mapping out muon bundles.

Appendix C

ADC gates in 1997 and 1998

Data from the AMANDA-B10 array in 1997 is the most closely scrutinized data set of the experiment to date. It has been the subject of low-level hardware and software checks, and the focus of published analyses [77].

In the 1997/98 Antarctic summer season, three new strings were deployed supplementing the existing ten. Strings 11-13 operate quite differently, running the PMT's current pulses through an LED inside the optical module and transmitting the signal to the surface via a fiberoptic cable. The optical pulses from these modules (which are much narrower than the B10 pulses) are read out by an optical receiver board and passed along through TDC's and ADC's similar to the rest of the array. But as a result of this upgrade, the 13-string array is a hybrid of electronic and fiberoptic transmission technology. To analyze data from the full array presents new challenges in calibration, reconstruction, and simulation. In particular, the three newer strings participate in the triggering of the detector and the multiplicity trigger threshold in 1998 was changed. The change in trigger behavior has not been simulated, and because of its unknown systematic effects, the entire year's data set has been left largely unexplored and unused.

SPASE coincidences, however, are different. To simplify data analysis and avoid unforeseen problems with the new strings, we can simply disregard Strings 11-13 and treat the 10-string "subarray" identically to 1997 data. Where a standard AMANDA analysis would suffer from trigger-related systematics in doing this, SPASE coincidence analysis remains immune because the trigger itself comes externally.

Although greater study has already been invested in 1997 data than in 1998 data, this appendix

attempts to justify the use of 1998 data preferentially. There is a compelling reason to do this: a difference in the relative settings of the SPASE trigger and ADC gate, causing hits deep in the detector to be lost in 1997.

C.1 Raw ADC vs. TDC in 1997

The TDC gates in AMANDA-B10 can record up to 16 edges (leading or trailing). Thus it can record the arrival time of up to 8 threshold-crossing pulses. The TDC gate width is large (32 microseconds) to ensure that all pulses are captured. The peak-sensing ADC, on the other hand, only records one value: the maximum pulse amplitude which arrives within its gate. The ADC recorded for a module in an event can not be identified to a particular hit, so to avoid recording spurious ADC's from noise, the ADC gate width is set as narrow as possible, and aligned in time with the expected arrival times of pulses from real muons. Ideally, the gate should open when the first muon-induced signals arrive at the surface electronics, and close when the last of them arrive.

It takes 2-3 microseconds for the muon to traverse the detector, but there are additional delay times introduced by the lengths of the cables. Signals from the deepest modules in the array must travel a farther distance and will take longer to arrive at the surface. Signals from an upgoing muon (in which the bottom modules are hit first and the top modules last) all arrive within about 4 microseconds. So the ADC gate was set to be 4 microseconds wide in 1997.

A downgoing muon, however will fire the top modules (with the shortest signal transit time) first, and the bottom modules (with the longer transit time) last. Depending on the geometry of the event, the last hits can come from up to 5 microseconds after the first hits; the 4-microsecond-wide ADC gate is not wide enough to catch them all. Although the gate catches the ADC's from the first hits well, the last hits from the bottom of the detector are recorded in TDC's only. SPASE events are especially prone to this problem, as they are not only steep in angle but also externally triggered. The relative time of the trigger and the opening of the ADC gate for SPASE coincidences was set in 1997 such that the first muon-induced pulses arrive one microsecond after the opening of the gate [110]. This wasted microsecond shrinks the effective width of the ADC gate from 4 microseconds down to 3.

This effect can be verified by looking at distributions of hits in individual modules. Figure C.1

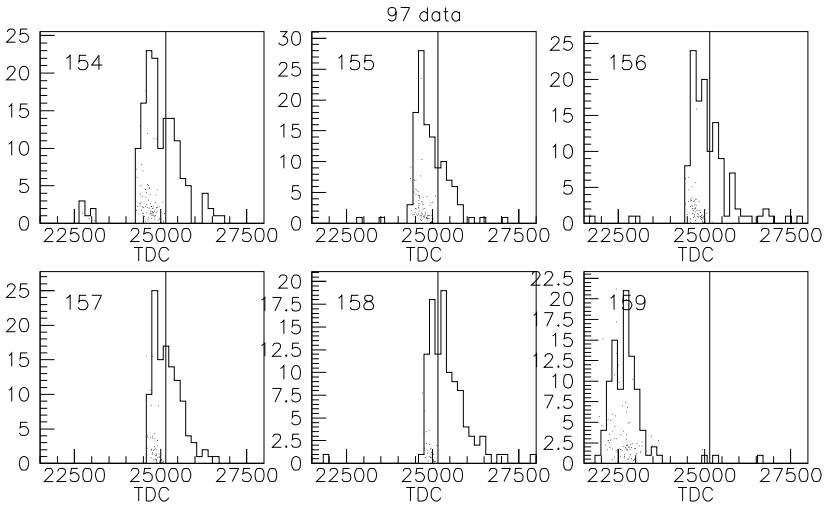

Figure C.1: Some sample raw TDC/ADC distributions for 97 data. The ADC gate is indicated by the vertical lines. No ADC's outside of this gate are recorded. Module 158 is the bottom of one string, and module 159 is the top of the next string.

shows the distribution of leading edge arrival times (uncalibrated) for some deep modules. The peak in each distribution represents real hits from real muons; these are the hits we want to measure. The ADC recorded for each module is assigned to the first hit, and only the first hit is included in this distribution. The small dots overlaid on the TDC distribution are the raw ADC vs. the raw TDC for this same set of hits; where there is a dot present a hit arrived successfully within the ADC gate. But for deep modules, one can clearly see a TDC time after which there are *no* ADC's recorded; these are hits which arrived after the ADC gate had closed. This gate cut-off time should be the same for all modules, since it is fixed in the DAQ. Sure enough, in the raw data the ADC information disappears at the same raw time (shown as a vertical line) for all modules. The deeper the module, the more seriously the closing gate cuts into the distribution of hits. Some modules such as OM 158 are almost cut out entirely.

C.2 Raw ADC vs. TDC in 1998

Strings 11-13 each contained some optical modules at very shallow (1200-1500 meters) and very deep (2000-2400 meters) depths (see Figure 4.1(a)). To capture signals from these far-flung

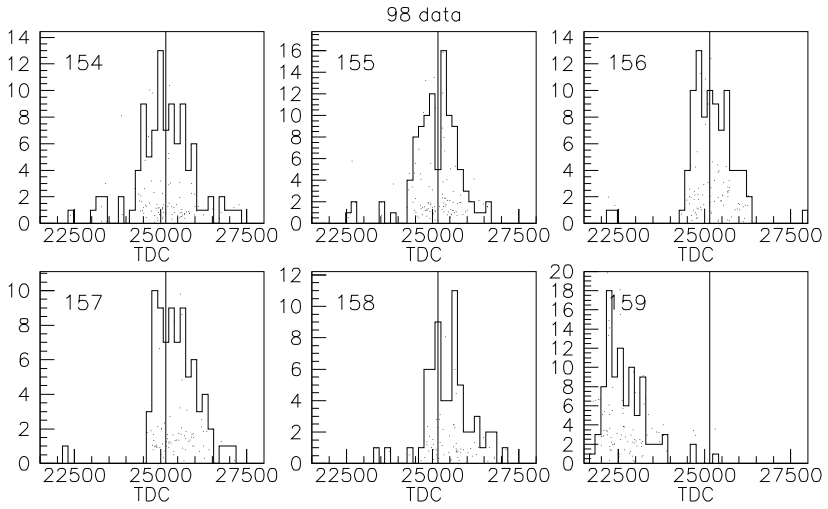

Figure C.2: Some sample raw TDC/ADC distributions for 98 data. The old 97 gate is indicated by the vertical lines. ADC's are successfully recorded for all real hits.

modules, the width of the ADC gate for the 1998 season was expanded from 4 microseconds to 9 microseconds [104]. As a result, 1998 data does not exhibit the same ADC problem as 1997. An examination of the raw TDC and ADC distributions for 1998 data (shown in Figure C.2) shows that ADC's are being successfully recorded for very late pulses.

C.3 The impact of the problem

Starting at a depth of around $z_{OM} = -40$, the outer six strings (which contain a greater density of modules and therefore contribute the most information) become systematically less sensitive.

This problem is unique to *downgoing* muons. The severity depends on the track geometry. Steeper downgoing tracks are in general worse than shallow downgoing tracks, but the details are complex. The outer six strings in AMANDA-B10 are connected to the surface electronics by longer cables (even though they are shallower in the ice overall), so the worst-affected tracks are those which enter the array at the top of the inner four strings and exit at the bottom of the outer six. The effect is especially exacerbated in SPASE data by the less-than-ideal choice of time delay between trigger and gate opening (the "wasted" microsecond). Regular AMANDA triggers, which are triggered by

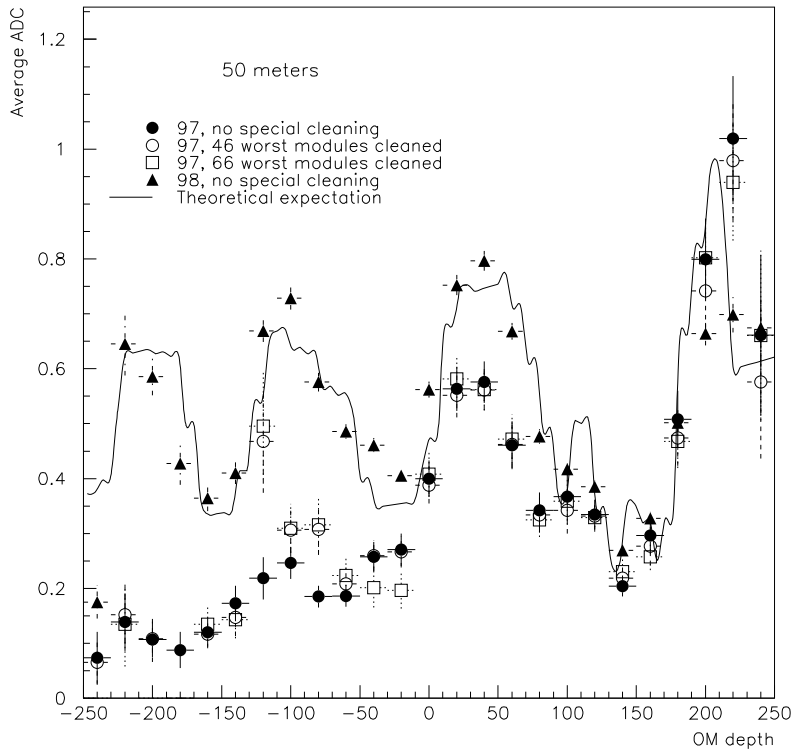

Figure C.3: Average ADC at 50 meters from the track, as a function of OM depth, comparing 97 and 98 data.

hit multiplicity at a relatively later time, are less affected but the effect can be found in downgoing muon data as well [103].

Any hit which does not contain an ADC is thrown out in the hit cleaning process, since leading edge time calibration requires amplitude information. Having "missing" hits in an analysis will have an effect that depends on the analysis. A Upandel timing reconstruction, for instance, uses only information from recorded hits, and so it will still work correctly but with reduced accuracy (as if only two-thirds of the detector were operating). The ADC reconstruction in this work, however, takes both hit and *not hit* modules into account; if the track hypothesis expects hits deep in the detector and finds none, it will adjust the hypothesis accordingly and get systematically the wrong answer. The only solution to the problem is to remove the worst deep modules from the analysis *a priori*, as if they were "dead" modules, and suffer the reduction in sensitivity.

Figure C.3 shows the average ADC (a fundamental observable in this work) as a function of OM depth, for a fixed perpendicular distance of 50 meters. Below $Z = -40$, there is a clear deficit of ADC's relative to the expectation for 1997 data. Hit cleaning of the deepest and most problematic modules alleviates the problem and brings the curve closer to the expectation, but does not solve the problem completely. 1998 data on the other hand behaves well without any special cleaning.

C.4 Differences in treatment of 97 and 98 data in this work

In this work, a composition analysis was performed for both 1997 and 1998 data (Strings 1-10 only). Although most features of the analysis are identical, there are a few important differences necessary because of the differing detector configurations of the two years.

C.4.1 Gate simulation

Simulated events output by PROPMU were put through two nearly-identical but distinct versions of the detector simulation package `amasim`. Both used the SPASE (external) trigger option in the package, but with different ADC gate start times and duration. For 97-like settings, the ADC gate was set to 4400 microseconds (which is standard for AMANDA-B10 mass production Monte Carlo) and the position of the gate was aligned as well as possible with the observed cutoff times in the 1997 data. A second set of Monte Carlo was run with 98-like settings: the length of the gate was set to 8 microseconds, more than enough to capture all the muon-induced hits. Both sets of simulated events were derived from the same air shower events, but were passed through `amasim` with different random number seeds; thus, events from the two Monte Carlo sets cannot be compared to each other directly. For the final analysis of composition, 97 data is compared only to 97-like Monte Carlo, and 98 data is compared only to 98-like Monte Carlo. A study of the systematic effects due to this problem is investigated in Chapter 9.

C.4.2 Hit cleaning

The details of event-by-event hit cleaning (such as event time window, isolation cleaning, crosstalk cleaning, etc.) was kept identical in the two analyses. However, the two data sets require different "bad-channel lists," both because different modules were dead or alive in the two years, and

Year	Bad Modules	ADC gate problems	Total removed
97	28, 32, 34, 39, 40, 47, 49, 50, 57, 62, 78, 81-86, 96, 102, 143, 167, 172, 181, 182, 184, 186, 190, 195, 197, 199, 215, 219, 227, 231-235, 252, 255, 257, 259, 260 261, 267, 289, 290, 291, 292, 299, 301	19, 20, 114, 116-122, 150-158, 187-194, 221-230, 263-266, 293, 295-302	51 + 46 = 97
98	3, 18, 28, 32, 34, 39, 40, 41, 42, 47, 50, 57, 61, 62, 74, 75, 78, 81-86, 94, 96, 117, 143, 167, 172, 186, 188, 189, 190, 194, 195, 197, 198, 199, 201, 215, 216, 224, 225, 227, 234, 235, 249, 258, 263, 264, 267, 280, 290		53

Table C.1: Bad module lists for 97 and 98 data

also because in 97 we are forced to remove deep modules which suffer from the ADC gate problem. A table of permanently-cleaned "bad channels" for the two years which was used in this analysis is given in Table C.1.

Appendix D

Linearity of peak-ADC's

D.1 Motivation

Amplitudes play a crucial role in this work, and in other developments in energy reconstruction in AMANDA. However, the hardware which reads out amplitudes for the AMANDA-B10 array suffers from some fundamental drawbacks. The inner 10 strings are read out with electrical cables rather than fiberoptics, so the signals must be amplified at the surface. In particular, the SWAMP amplifier creates a "fast" output for timing and a "delayed" output for measuring amplitude. The delayed signal is put through an additional amplifier and also an integrator. This means that the *peak* voltage of the delayed signal is proportional to the integrated charge carried by the signal, and this peak voltage is read out by a peak-sensing ADC (PADC).

This scheme works well for single photons or multiple photons are all arriving at once; the integrator in the SWAMP will respond correctly and produce an output pulse with a correspondingly large voltage. But if photons arrive staggered, the peak voltage output by the integrator will fall short of the correct value, and the number of photoelectrons will be underestimated. This becomes more of a risk at larger distances, where a greater proportion of photons arrive scattered and delayed. In any case, the linear response of the ADC's must be checked before an analysis based on them can continue.

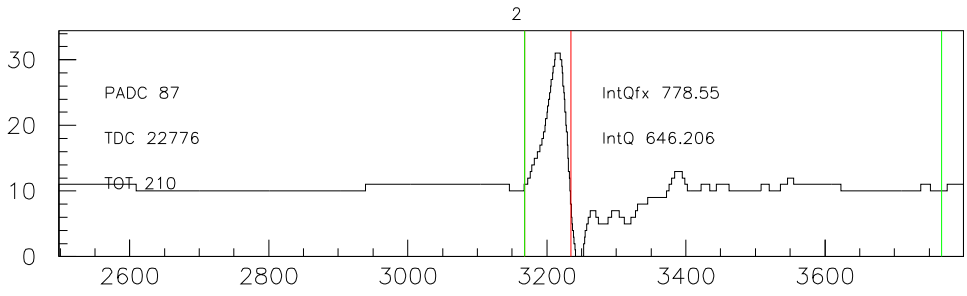

Figure D.1: A typical single-PE pulse waveform

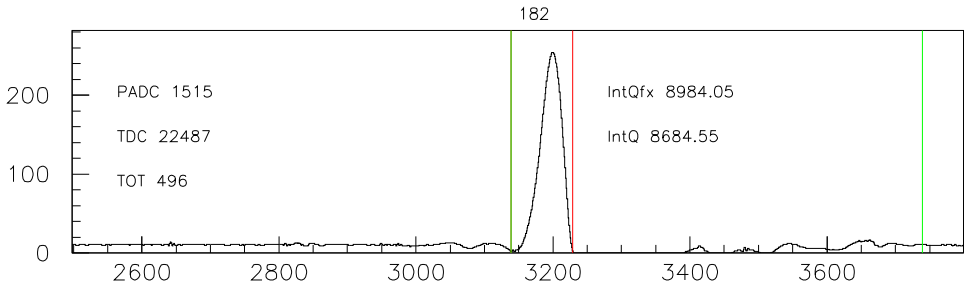

Figure D.2: A multi-PE waveform, where all the photoelectrons are arriving more or less simultaneously

D.2 Direct Measurement: Waveform Data from the Pole

In the Antarctic summer season of 2000/2001, one Flash-ADC (FADC) was installed at the South Pole, with its own DAQ which was kludged together with the AMANDA Main DAQ. A detailed description of the experimental setup and the data taken can be found in [100]. Using this waveform setup, one can directly measure the relationship between integrated charge (measured from the waveform) and the peak-ADC (measured by the DAQ). This allows us to evaluate how reliable PADC's are as a measure of the total number of photoelectrons.

There are different ways of measuring the integrated charge, because waveforms have structure. (Some examples of waveforms are shown in Figures D.1, D.2, and D.3.) Even a simple single-PE waveform has a positive pulse and a negative overshoot, making the concept of "integrated charge" not straightforward. To make sense of it, we will define not just one but two different types of integrated charge.

- IntQ ("Integrated Charge") is the integral under the curve of the waveform between the time

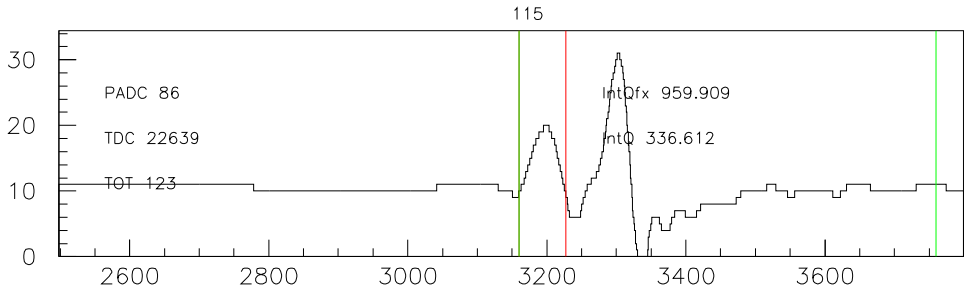

Figure D.3: A two-PE waveform, where the photoelectrons are staggered in time

when the waveform first crosses a small threshold (the first line in Figures D.1, D.2, and D.3) and the time when it drops below the threshold again (the second line). Thus, if several pulses arrive well-spaced in time, this integrates only the first pulse, as in Figure D.3.

- IntQfx ("Fixed Gate Integrated Charge") is the total integral of *positive* charge between the first threshold-crossing and a fixed time 6 microseconds later (the third line). We count only the positive charge because large negative overshoots can often bring the integral misleadingly close to zero.

The relationship between uncalibrated peak-ADC (PADC) vs. integrated charge (IntQ) is shown in Figure D.4. There is a clear difference between strings 1-4 and strings 5-10, due to different cables. The longer integration time of the coax cables on 1-4 causes pulses to be wider and integrated charges to be greater for the equivalent peak amplitude. But an important initial conclusion is that both sets of strings are remarkably linear up until saturation of the peak-ADC.

To study this in greater detail we must express the x and y axes in terms of *photoelectrons*, rather than voltages or charge. For peak-ADC's, this is trivial: simply divide by the ADC "β" from the Optical Module DataBase (OMDB) (this is the number used by the calibration program to translate peak-ADC voltage into photoelectrons, unique to each OM). Integrated charge from module to module should also scale by this number.

To put the x-axis in units of photoelectrons rather than charge, we assume that the PADC responds linearly to charge in the small-amplitude region surrounding 1 PE. We can then use 1-PE events to calibrate one axis to the other. Strings 1-4 and 5-10 must be calibrated separately because

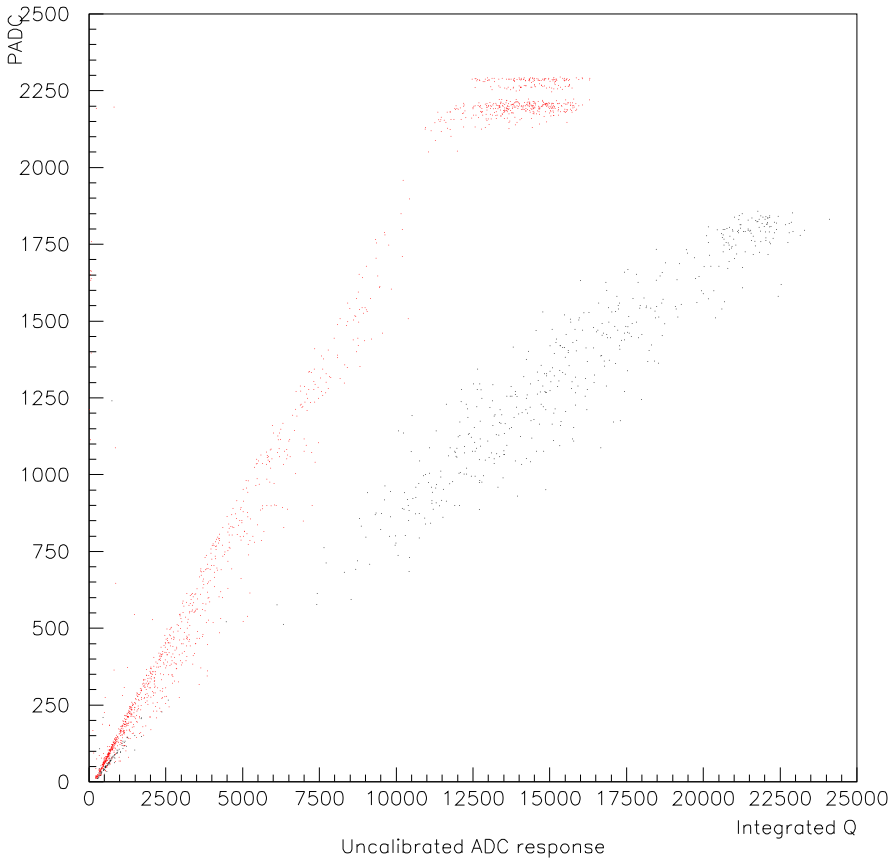

Figure D.4: Peak-ADC vs. integrated charge (uncalibrated, in "raw units"). Black: strings 1-4. Red: strings 5-10.

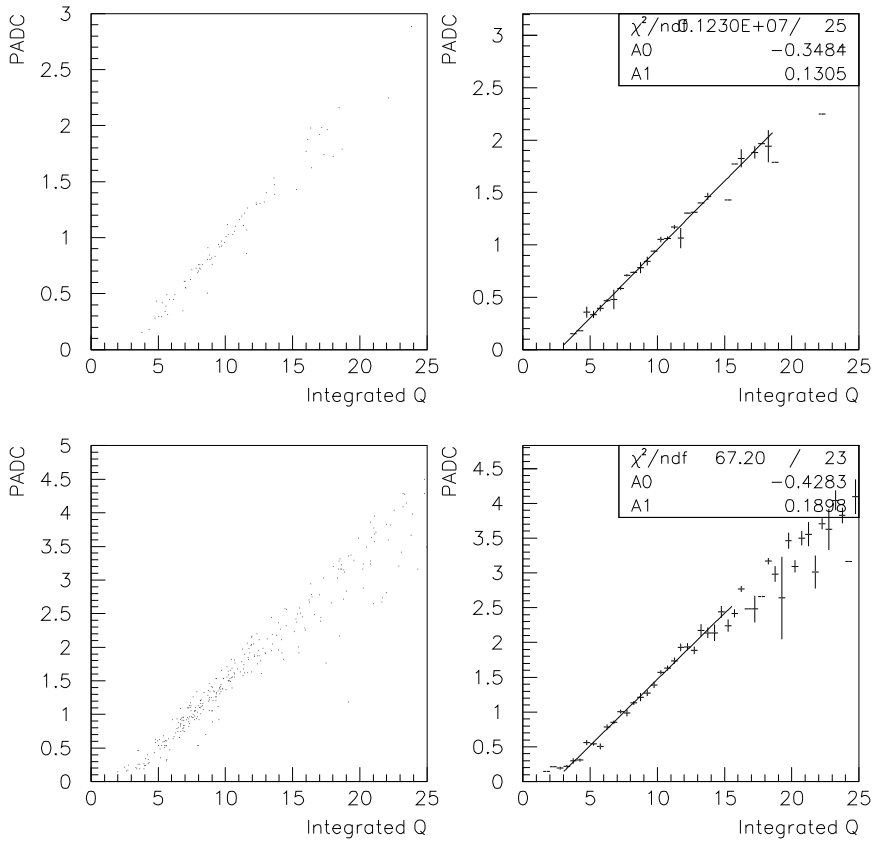

Figure D.5: Calibrating the x axis to the y-axis, using 1-PE events only. Top: strings 1-4. Bottom: strings 5-10.

of the difference in cable integration time discussed above. To ensure that the events we are looking at truly are one photoelectron, we can impose a cut that the number of hits seen by the DAQ is exactly one. Although a powerful cut, it does not get rid of all the strange-looking events. The remaining strange-looking things can be removed by demanding that the *fixed-gate* integrated charge (IntQfx) be within 1.5 of the first-hit-only integrated charge (IntQ); a discrepancy larger than that between the two numbers would mean that strange multi-PE things are going on.

After these 1-PE cuts are applied, the plot of PADC vs. IntQ looks nicely linear and undisturbed by outlying points, and can be fit to a linear function, as shown in Figure D.5. The slope of the linear fits (0.13048 for 1-4 and 0.18983 for 5-10) can then be used as a multiplicative factor to

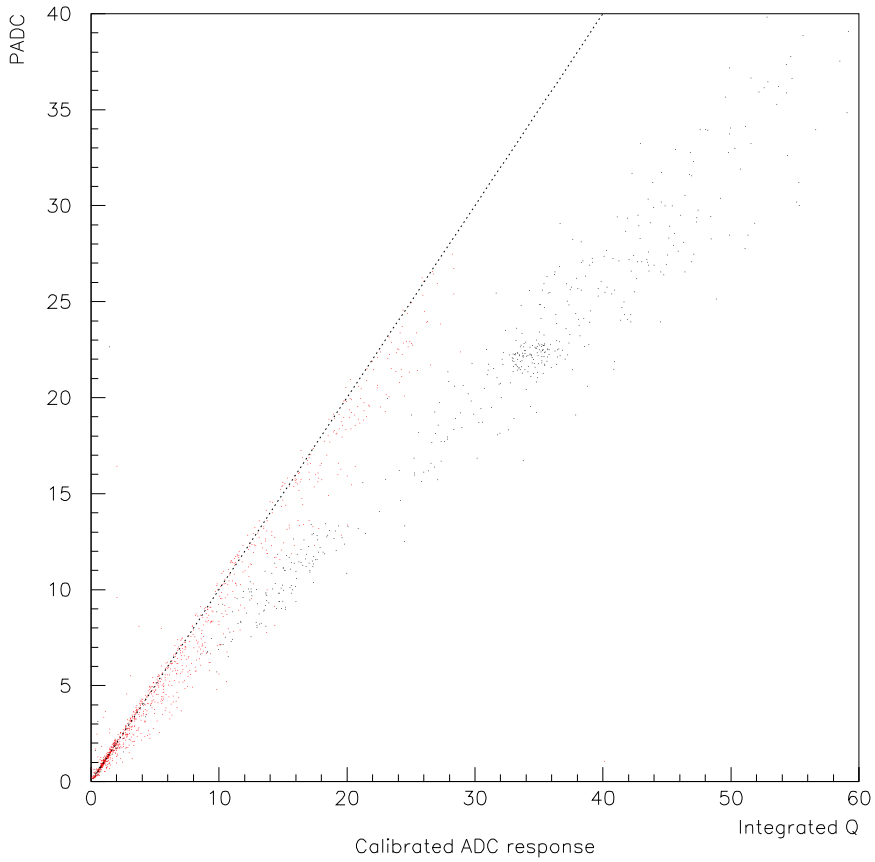

Figure D.6: Peak-ADC vs. integrated charge (calibrated, in photoelectrons). Black: strings 1-4. Red: strings 5-10. The line represents perfect one-to-one linearity

adjust IntQ so that it is in units of photoelectrons.

After making this calibration, the PADC vs. IntQ plot (in units of PE's) looks like Figure D.6. Again, the PMT response is remarkably linear, but with different slopes for 1-4 and 5-10. This supports the contention that $K50$ is a linear quantity as well.

D.2.1 A word about saturation

In this set of data, the peak-ADC itself saturates at 2.5 Volts before the PMT shows signs of saturation. This 2.5 Volt saturation point will translate into a different number of PE's for each OM, depending on its gain and its calibration. Therefore, there is no single calibrated amplitude at

which saturation occurs; any analysis which incorporates saturation effects must either account for it *before* calibration while the amplitude is still in Volts, or know the saturation point in PE's for each individual module.

Appendix E

Dark Noise in PMT's: Evidence for Glass Radioactivity

E.1 Motivation

There is a dramatic difference between the dark noise rates of optical modules in strings 1-4 of the AMANDA detector, strings 5-13, and strings 14-19. Modules in 1-4 measure rates of approximately 300 Hz in the ice, whereas modules in 5-13 measure rates of around 1100 Hz and 14-19 measure around 800 Hz. The presence of noise creates problems for identification of neutrino events; a single chance noise hit can throw off a computer's reconstruction of an event, and prevent the event from passing cuts. Thus, it is important to understand why the noise rates are so much higher in later strings, so that the problem can be reduced in the future[1].

The first task is to isolate the source of the noise: does it come from the cables, from the glass housing of the module, from the gel which couples the glass to the photomultiplier tube (PMT), or is it coming from within the PMT itself? Fortunately, our lab was equipped with several sample modules from the different batches, as well as some bare PMT's which were known to be low-noise (~300 Hz). Thus, by rearranging the various components of the modules (PMT, gel, glass, and cables), we could isolate the source of the high noise.

[1]This work was done and this chapter written in 1999. It was presented at a collaboration meeting but was never published. I include it here for reference and for posterity, even though the language is a bit archaic and the conclusions have been part of AMANDA collective knowledge for several years now.

E.2 Experimental setup and techniques

A PMT or module to be tested was placed in a light-tight freezer (capable of temperatures of -40°C). High voltage to the PMT was supplied into the freezer through an HV splitter box. The output signal (a negative pulse of typically 100-150 mV) was sent simultaneously to an oscilloscope and to a 30 mV discriminator. The discriminator's output was sent through a gate generator and then a scaler, which sent the count rate (counts per second) to a PC where it was histogrammed (see Figure E.1).

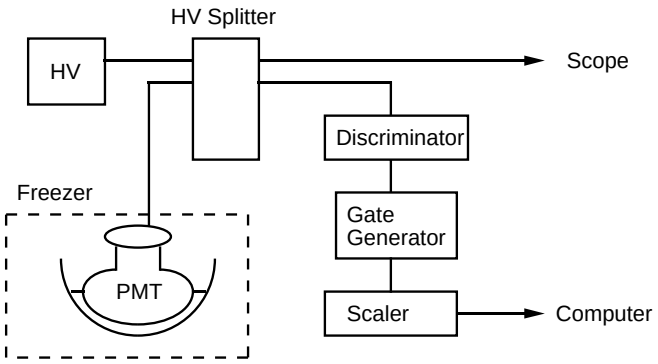

Figure E.1: Experimental setup of noise measurements.

E.2.1 Afterpulse Suppression

Occasionally, accelerated photoelectrons in the PMT will liberate a positively charged particle at the anode, which is accelerated back by the high voltage and will produce an extra photoelectron when it strikes a surface. This "after-pulse" can arrive up to a microsecond after the original photoelectron. When these experiments first began, our discriminator's gate was so short (tens of nanoseconds), that many of these after-pulses were being recorded as independent pulses. To circumvent this problem, we lengthened the gate to 8 microseconds. All the final results presented here use this longer gate, unless specified otherwise. Noise rates using the short gate are noticeably higher and should be considered with caution.

E.2.2 Solid and liquid gel

At first, PMT's and their gels could be swapped in and out of glass hemispheres simply using one's hands. The solidified gel could be kept in one piece and transported between spheres. But the quality of the gel dropped the more it was handled; bubbles formed, or the gel broke into pieces. So for later experiments we used uncured, or "liquid", gel for optical coupling. The PMT was suspended above an open glass hemisphere and held in place, and the liquid gel could be poured between it and the glass. This allowed us to swap PMT's in and out of different spheres without worrying about degrading the quality of the gel.

E.2.3 Simulating ice with an "absorber"

In the Antarctic ice, the lowest-noise spheres (Billings spheres, on strings 1-4) run at near 300 Hz. Although we measured bare PMT's with this noise rate, none of the modules we tested, including the Billings, had noise this low. The discrepancy between the deep ice measurements and lab measurements is partly due to the good optical coupling between the outside of the sphere and the ice; some of the photons created in the glass can easily escape into the ice through this interface. Whereas, in the lab, the outside of the sphere is open to air; more photons can reflect off this interface and can be seen by the PMT. We tested this theory by surrounding the outside of the sphere with something of similar refractive index to glass, or something that would absorb photons exiting the glass rather than reflect them back: an "absorber." For the absorber, first we tried resting the glass hemisphere in a "bed" of solid gel resting inside a black plastic bag. Then we tried covering the outside of the module with black electrical tape. Both gave similar results: a lower noise rate as expected, closer what is measured in the ice (but still not perfectly efficient).

E.3 All the numbers

The following is a table of all the noise measurements made, describing the type of glass, the PMT, and the conditions of the experiment. I list each PMT by its serial number. Since glass spheres do not have serial numbers themselves, I have labeled each sphere (or hemisphere) according to the type of glass ("Benth" for Benthos, "Bill" for Billings, etc) followed by the serial number of the PMT which was originally housed in that sphere. Test spheres sent to us by glass companies (such as

McLane) contained no PMT's originally, and so they are labeled by an arbitrary number (such as #1 and #2).

I have organized the table by glass sample, so that patterns of variation from glass to glass can be easily picked out.

All noise numbers rounded to the nearest ten, since there is enough variation in measurements from run to run to make that last digit useless. Experiments with an absorber on the outside are labeled either "gel outside" or "black tape."

Date	PMT#	Glass#	Gel	Temp.	Comments	Noise
1/11/99	bb6814	none	none	-40	short gate	350
1/12/99	bb6657	none	none	-40		230
1/13/99	bb6814	none	solid	-30	gel only	280
1/14/99	bb6814	none	solid	-40	gel only	310
1/16/99	bb6437	none	none	-30		210
1/21/99	bb6437	none	none	-40		240
1/27/99	bb6814	none	none	-30		350
1/28/99	bb6814	none	none	-30		330
2/2/99	bb6814	none	none	-30		300
2/4/99	bb6814	none	none	-30		310
2/8/99	bb6814	none	none	-30		310
2/22/99	bb6814	none	none	-30		280
3/2/99	bb6814	none	none	-30		320
3/8/99	bb6814	none	none	-30		250
4/21/99	bb6657	none	none	-30		310
4/22/99	bb6657	none	none	-30		290
1/11/99	bb6657	Benth6657	solid	-40	short gate	3320
1/12/99	bb6814	Benth6657	solid	-40		1620
1/13/99	bb6657	Benth6657	none	-30	glass only	740
1/14/99	bb6657	Benth6657	none	-40	glass only	900
1/16/99	bb6657	Benth6657	solid	-30		1790
1/21/99	bb6657	Benth6657	solid	-40		1970
1/27/99	bb6657	Benth6657	liquid	-30		2130
2/2/99	bb6657	Benth6657	liquid	-30	gel outside	1880
1/11/99	bb6771	Benth6771	solid	-40	short gate	3260
1/16/99	bb6717	Benth6717	solid	-30		2080
1/21/99	bb6717	Benth6717	solid	-40		2390
1/12/99	bb6314	Bill6314	solid	-40		740
2/22/99	bb6314	Bill6314	solid	-30	black tape	510
1/13/99	bb6330	Bill6330	solid	-30		580
1/14/99	bb6330	Bill6330	solid	-40		680

1/13/99	bb6437	Bill6437	solid	-30		690
1/14/99	bb6437	Bill6437	solid	-40		790
1/16/99	bb6814	Bill6437	solid	-30		810
1/21/99	bb6814	Bill6437	solid	-40		830
1/27/99	bb6437	Bill6437	liquid	-30		670
1/28/99	bb6437	Bill6437	liquid	-30	gel outside	540
4/21/99	bb6437	Bill6347	liquid	-30		660
2/4/99	bb6437	McLane1	liquid	-30		940
2/8/99	bb6437	McLane2	liquid	-30		960
4/22/99	bb6437	McLane2	liquid	-30	black tape	660
2/22/99	bb6657	17"Benth	liquid	-30		2360
3/2/99	bb6657	17"Benth	liquid	-30	black tape	1400
2/22/99	bb6437	17"Nautilus	liquid	-30		1450
3/2/99	bb6437	17"Nautilus	liquid	-30	black tape	780
4/21/99	bb6814	Benth302	liquid	-30		1860
4/22/99	bb6814	Benth301	liquid	-30	black tape	1160

E.4 Easy conclusions

1) As all measurements were done using the same sets of cables, the cables are not the source of the noise.

2) All PMT's *alone* measures low noise (200-400 Hz). Cosmic rays may be the source of some of this noise, and the rest we assume is due to thermal liberation of photoelectrons from the PMT.

3) Any PMT when placed in a '96 Benthos sphere becomes high-noise (1600-2400 Hz). The only exception to this result occurred when there was no gel between the glass and the PMT; we believe that the lack of good optical coupling caused many of the noise photons from the glass to never reach the PMT.

4) Any PMT when placed in a Billings sphere becomes low- noise (600-850 Hz).

5) A low-noise PMT in *only* gel (no glass) measures noise as low as if it were bare. Therefore, the gel does not contribute to the noise.

6) Putting gel or black tape on the *outside* of a sphere of any type reduces its noise, as expected. However, our techniques are not totally efficient at doing this.

7) After-pulses contribute significantly to the apparent count rate, if long-gate precautions are not taken.

8) McLane spheres, although quiet relative to Benthos (~950 Hz), are not as quiet as their predecessors.

9) 17" spheres in general have much higher noise rates, because of their greater thickness and volume. Conclusions about these samples require some more in-depth analysis (see below).

10) Liquid gel will "go bad" if left exposed to the air for a long time. All the liquid gel measurements above used the same sample of gel, which was simply poured from sphere to sphere. But after a long break in time between measurements, I found that the gel suddenly was producing almost 1000 Hz of excess noise in all measurements. It had been exposed to air for several months. On close inspection, I found small filamentary-looking reddish particles floating in the gel, and it had turned a slightly orange color. The "bad" gel was replaced with a sample from the same year, but which had been sitting on the shelf, not exposed to air or used. This solved the problem and previous measurements could be repeated.

E.5 Radioactivity

If the excess noise is coming from the glass, the most likely cause is radioactive material in the glass. Samples of all the glass types were sent to LBL for further testing. They measured the rates of beta decay from potassium (40K), uranium, and thorium using a high-purity germanium gamma-ray spectrometer. LBL's results clearly suggest that radioactive potassium is responsible for most of the noise, with uranium and thorium contributing small amounts as well. In addition, they were able to measure the percentage of potassium in each sample. [101]

Alerted about the potassium levels in their glass, Benthos agreed to do a self-test for potassium for their old glass (strings 5-13) and their new glass (strings 14-19) for comparison. The found 1.0% in the 5-13 sample and 0.5% in the 14-19 sample.

E.6 Geometric Effects

For a better analysis, one must take into account the differing sizes and thicknesses of the samples in these tests.

Dimensions:

17" diameter Benthos: thickness 1.6 cm

17" diameter Nautilus: thickness 1.4 cm

13" diameter Benthos: thickness 1.2 cm

12" diameter Billings: thickness 0.9 cm

We must also understand the mechanism for the noise. Assume that 300 Hz is inherent within the PMT itself and cannot be avoided, even if the sphere is low in potassium. The remainder of the noise which is due to radioactivity will scale either by volume or by thickness (or a combination of the two) depending on how photons behave in glass. If most photons reflect off the glass/air interface, then photons generated anywhere inside the volume of the hemisphere will arrive eventually at the PMT, and the count rate should scale by the volume. However, if most photons escape the glass when they hit the glass/air interface, then any photons reaching the PMT must have come from a fixed solid angle "below" it, and the count rate should scale by thickness. (See Figure E.2.)

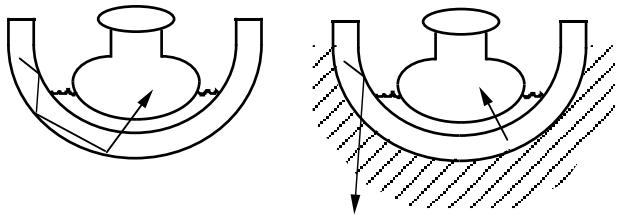

Figure E.2: Photon behavior a) with reflections b) with absorption.

It is difficult to actually do the scaling, since we are probably dealing with a combination of both effects. However, gel or black tape on the outside of a sphere should reduce the importance of volume and give us primarily a thickness dependence. We can make a very simple assumption that only the photons immediately "below" the PMT are seen by the PMT, and that all other photons escape through the absorber.

E.7 Putting it all together

Here is a table showing the noise rates for all kinds and sizes of spheres. (If multiple measurements were made, the most reliable one was chosen.) The first column is measured noise rate. The second is after subtracting 300 Hz of noise inherent to the PMT, unrelated to radioactivity. The third column is the second column scaled by thickness to the thickness of 13" Benthos. (This is done only for "absorber" measurements, for which our simple assumption may be valid). I have also included for comparison the percentage potassium as measured by LBL, and as measured by Benthos's self-test.

Type of glass	Noise Rate	-300 PMT	Thickness Scaled	40K LBL	40K Benthos
13" old Benthos	2100	1800			
with absorber	1800	1500	1500	0.75-1.2	1.0
in ice	1100				
13" new Benthos	1860	1560			
with abs.	1160	860	860	0.32	0.5
in ice	800				
17" new Benthos	2360	2060			
with abs.	1400	1100	825	0.23	
12" old Billings	700	400			
with abs.	540	240	320	0.04	
in ice	300				
12" new McLane	950	650			
with abs.	660	360	480	0.08	
17" Nautilus	1500	1200			
with abs.	780	480	410	0.01	

As the "absorber" technique is obviously not as efficient as real Antarctic ice, as the noise rates of modules in the ice are consistently lower in the ice than in the lab. There is consistency in the behavior of the three batches of glass; this aspect of the noise appears to be well-understood.

Appendix F

A Fourier Analysis of Supernova Data from 1997

F.1 The Supernova Data Acquisition System

The AMANDA detector has two separate data acquisition systems: the "muon" DAQ, which records muon- or shower-induced events which trigger the detector, and the "supernova" DAQ, which monitors the count rates of all the detector's optical modules and operates continuously. The purpose of the supernova DAQ is to detect the low-energy electron-neutrinos from events such as supernovae. A flooding of such low-energy particles may not produce any triggered events in AMANDA, but would instead raise the ambient light level in the ice, and raise the singles count rate of all optical modules.

Data from this specialized DAQ can also be used to search for weak periodic signals. Performing a Fast Fourier Transform on this time series data allows us to search frequency space for periodicities. This technique is sensitive to very weak signals which would not cause AMANDA to trigger or be detectable in the muon data, and allow us to search for low-energy neutrinos from soft gamma repeaters, pulsars, or x-ray binaries.

Like muon data, supernova data is organized into runs. Each run contains a continuous recording of all optical modules' count rate binned every 0.5 seconds. This report will address a study of all such data from 1997: 65 runs varying in length from 1300 seconds to 7 days, covering 176.2 total days of live time[1].

[1]This work was published as an AMANDA internal report, #20010401 (not an April Fool!). I have reproduced it here basically unmodified.

F.2 Fast Fourier Transforms: A Review

We take the average count rate for all modules as a continuous time series x_k which is sampled every Δt seconds, thus, $t_k = \Delta t \times k$. The series has a total number of bins N and total duration T. First the mean value of x_k is calculated and subtracted from every time bin, giving the time series a zero mean. Then a Fourier transform of the time series is calculated, yielding coefficients a_j for each bin of frequency $f_j = j/T$:

$$a_j = \sum_{k=1}^{N} (x_k - \overline{x}) \exp(2\pi i f_j t_k)$$

Such a transform can be easily calculated with an FFT algorithm if N is a power of two. This means that some data at the end of a run was simply neglected and left out of the analysis.

The a_j coefficients are complex numbers, and cover both positive and negative frequencies up to the Nyquist frequency $f_{Ny} = 1/2(\Delta t)$. A physically meaningful quantity is the power contained in each frequency bin:

$$P_j = 2 \times |a_j|^2 / N\sigma^2.$$

The factor of 2 comes from the fact that positive and negative frequencies are symmetric and redundant; this also implies that the number of bins in our power spectrum is half the number of bins in the original time series. The normalization factor $N\sigma^2$ is different from what one finds in most literature (N_γ, or the total number of photons, equal to $N\overline{C}$ where $\overline{C}$ is the mean number of total counts per time bin). The reason for this difference has to do with the Gaussian behavior of the distribution of noise rates. In a purely Poissonian process with many photons, the distribution of noise rates approximates a Gaussian, where the variance σ^2 is equal to the mean $\overline{C}$. Although the noise in this data is Gaussian, its variance is larger than what one would expect for a purely Poissonian process. The reason for this is not understood yet, but the effect has been observed before, for instance in [117]. For this analysis, then, $N\sigma^2$, computed for each series as:

$$N\sigma^2 = \sum_{k=1}^{N} (x_k - \overline{x})^2$$

gives the correct normalization for each resulting power spectrum. The total normalized power over all bins is 2.

The maximum frequency that this analysis is sensitive to (the Nyquist frequency) is determined by the minimum time binning of the data ($\Delta t = 0.5$ seconds $\rightarrow f_{Ny} = 1$ Hz). The longer in total duration the series, the finer the binning of frequencies. But in a search for weak signals, signal to noise is more important than fine frequency binning. Chopping a set of data into M smaller segments and adding together the power spectra of all the separate segments will enhance any real feature in the power spectrum relative to the random fluctuations.

F.3 Removing problematic modules

Removing bad modules from the analysis is very important; individual bad modules can in fact produce significant spikes in a Fourier power spectrum. The raw (0.5-second time series) data from all 302 AMANDA-B10 optical modules were Fourier transformed individually, for three runs (one at the beginning of the year's data, one in the middle, and one at the end). Modules were rejected from the entire 1997 analysis if they were suspicious in any of the three inspected runs, in any of the following respects:

- High noise rate
- Low or zero noise rate (dead modules)
- "Glitchy" noise rate
- Strange features in Fourier spectrum (see below)

Examples of some cases are shown in Figure F.1. The top module is a normal one, with no strange features either in time-series or frequency-space. The middle module (module 5) appears normal in all respects looking at the time series. It does not appear on any "bad module" list in AMANDA. And yet it produces a strange 23-second feature and harmonics in frequency-space. Modules 5, 6, 17, and 18 have this property which is not understood and not found in any other modules. The bottom module in Figure F.1 (module 186) is on several "bad module" lists for obvious reasons; it is high noise and glitchy, sometimes saturating the supernova DAQ. Three bad modules of this type produce a 1.3-second feature in the Fourier transform. A list of all removed modules can be found in Table F.1.

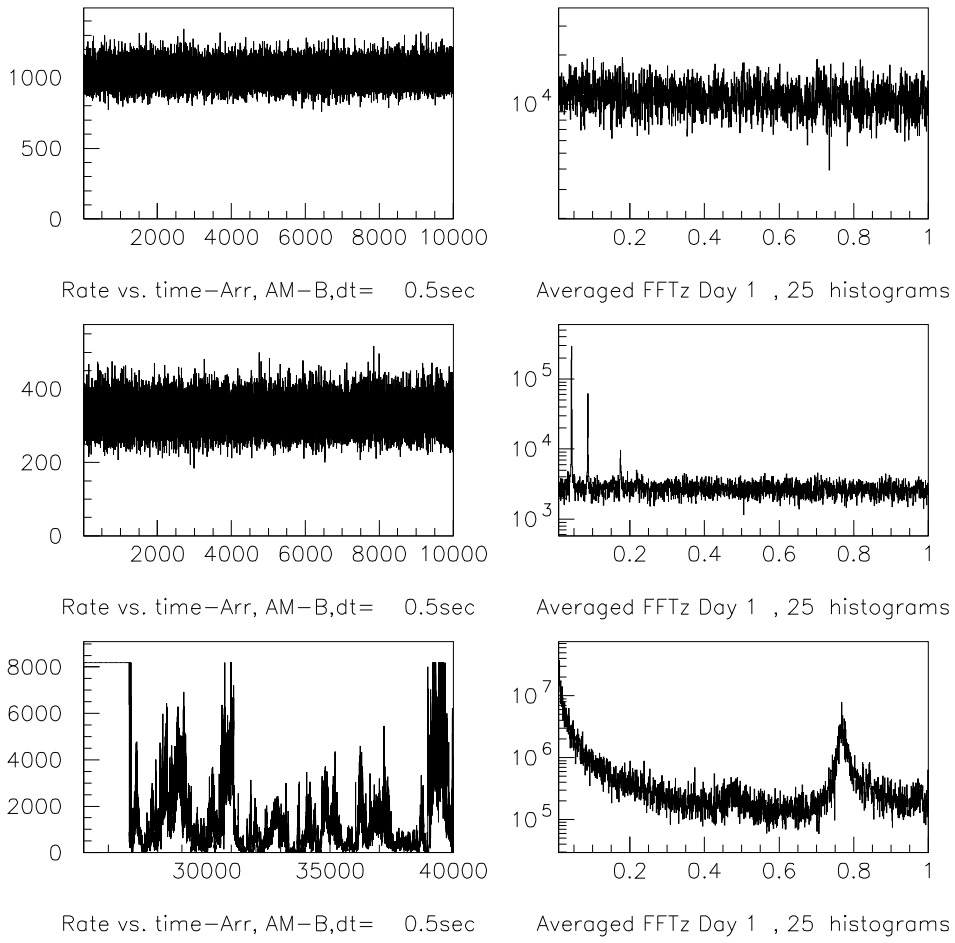

Figure F.1: Top: module 100 and its Fourier spectrum (normal). Middle: module 5 and its spectrum (23-second Fourier feature; removed). Bottom: module 186 and its spectrum (1.3-second Fourier feature; removed).

Module	Reason
5	Produces 23-second Fourier feature
6	Produces 23-second Fourier feature
17	Produces 23-second Fourier feature
18	Produces 23-second Fourier feature
28	Dead
32	Dead
34	Dead
39	Dead
40	Dead
47	Dead
50	Dead
57	Dead
62	Dead
78	Dead
81-86	Not in use
96	Very low noise rate
106	Low oscillating noise rate
143	Dead
167	Very low noise rate
172	Dead
186	High noise, glitchy, produces 1.3-second Fourier feature
190	Very low noise rate
195	Very low noise rate
197	Very low noise rate
199	Very low noise rate
215	Very low noise rate
227	Dead
229	High noise, “screwy”
231	Dead
232	Dead
233	High noise, glitchy, produces 1.3-second Fourier feature
234	High noise, saturating
235	Very low noise rate
255	High noise, saturating
257	Glitchy
259	High noise, saturating
260	High noise, glitchy, produces 1.3-second Fourier feature
261	Somewhat high noise
262	Somewhat high noise
263	Glitchy
264	Dead
267	Dead

Table F.1: Removed optical modules from B10 for FFT analysis

F.4 Slicing each run into 34-minute "segments"

For a first search for very weak signals, there are advantages to dividing a long series of data into many shorter segments, transforming each segment separately, and then summing the transforms of each segment together into one total power spectrum.

There are some logistical advantages to this technique. For one thing, it allows us to combine data from runs of various sizes (some are as short as 1300 seconds and others as long as 7 days) by chopping all runs into segments each of equal duration and equal importance. Secondly, as the duration of each segment is arbitrary, we are free to choose one which conveniently contains a number of bins which is a power of two (making the Fourier transform algorithm easy to implement). Thirdly, if a glitch or spike or other undesirable event occurs in a segment, that segment can be discarded without affecting the other segments or having to throw out the entire run.

But most importantly, if the Fourier transform is dominated by white noise (as we believe it is), then by summing together many independent spectra of independent segments of time, we can smooth out the fluctuations in the noise while enhancing any existing signal. In effect, we sacrifice frequency resolution for sensitivity.

The segment duration was arbitrarily chosen to be 2^{12} bins, or 2^{11} seconds, which is about 34 minutes. The resulting power spectra then contain 2^{11} bins of frequency from 0 Hz to the Nyquist frequency of 1 Hz. The frequency bin size is then 4.9×10^{-4} Hz.

F.5 Rejecting spikes and glitches

As mentioned above, one of the advantages of splitting the data into segments is that one misbehaving segment can be thrown out without throwing away the entire run of data.

A segment is identified as containing a spike or a glitch if it meets either of the following criteria:

- Spike: The highest or lowest count rate lies outside 10σ from the average count rate (where σ is computed as in the discussion of normalization above)
- Glitch: The maximum or minimum "sliding mean" (that is, mean count rate in a sliding window of 100 time bins) lies outside $\pm 2\%$ of the overall average count rate.

Run 46, File 1 contains examples of problematic spikes. Run 43, File 1 contains an example of a glitch in the noise rate down and then back up again (see Fig. F.2). These discontinuities cause problems in the Fourier spectrum. Notice, however, that we do not throw out the data in between the two glitches, where the noise rate is lower than normal. This is because we are sensitive only to changes in noise rate and not the absolute noise rate.

The causes of spikes and glitches is not well-studied. Many of them are believed to be attributable to hardware-related events at the South Pole (such as laser runs, loss of high voltage to modules, crashing or re-starting of the DAQ, etc., see [117] for a more in-depth discussion). In the meantime, these untrustworthy events are simply thrown out of the analysis and we proceed.

F.6 The Distribution of Powers

Performing this segmentation of the data and summing of the transforms affects the statistical properties of the resulting power spectrum. If M is the number of independently-transformed Fourier power spectra from independent time-series segments, then distribution of powers in the summed power spectrum is expected to follow a χ^2 distribution with $2M$ degrees of freedom [122, 123].

Data from a sample run agree with this expectation. Figure F.3 shows the output Fourier spectrum of one segment ($M = 1$) and its χ^2 distribution of powers. For $M = 1$, the distribution reduces to an exponential. Figure F.4 shows the same thing but for $M = 25$ summed spectra. The shape of the curve is now more complicated, but for very high values of M it will approach a Gaussian. A theoretical χ^2_{2M} curve (computed with no free parameters) matches very well to the data.

With confidence that the method is working as expected, we can now proceed with a search for very weak signals, using the combined data from all of 1997.

F.7 Sensitivity and Upper Limit Statistics

F.7.1 Theoretical detection threshold

For a χ^2 distribution with a large number of degrees of freedom, approximations exist [116] for computing not only the probability curve itself but also the power P_0 such that:

$$probability(P_{\chi^2_{2M}} > P_0) = Q(P_0) = C$$

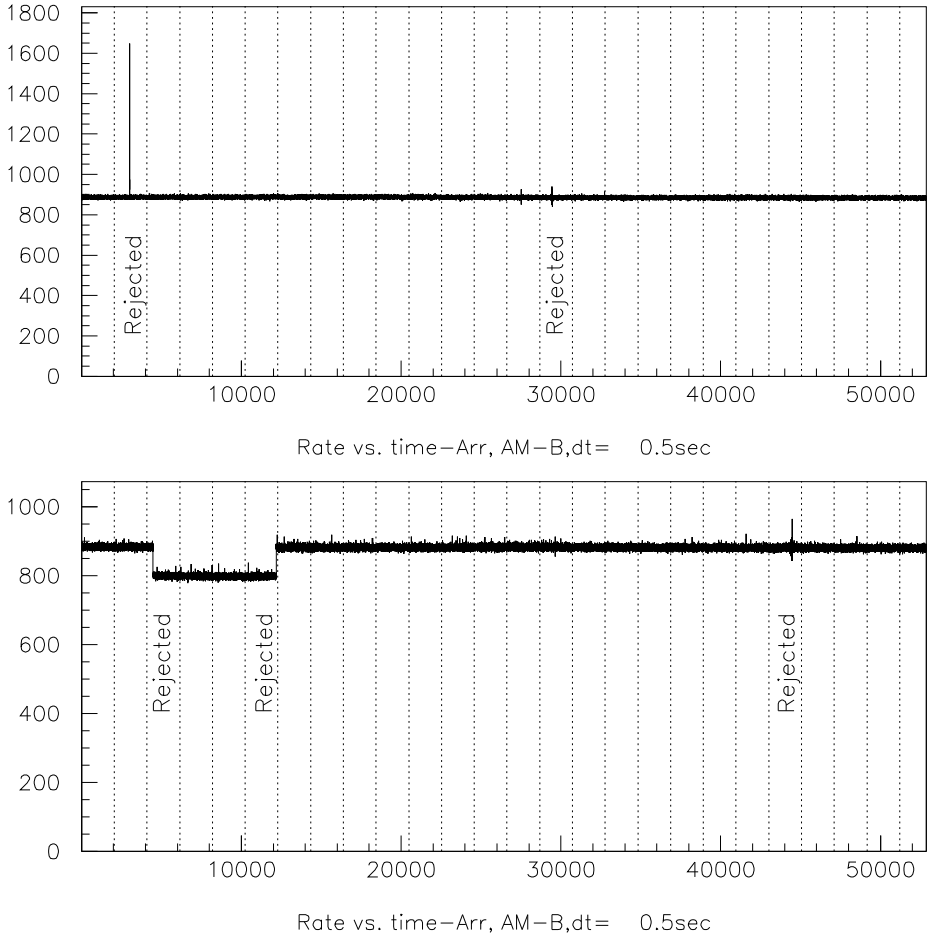

Figure F.2: Above: Run 46, File 1 and its separation into segments. Two segments are rejected due to spikes. Below: Run 43, File 1 and its separation into segments. Two segments are rejected because of glitches, and a third segment is rejected due to a spike.

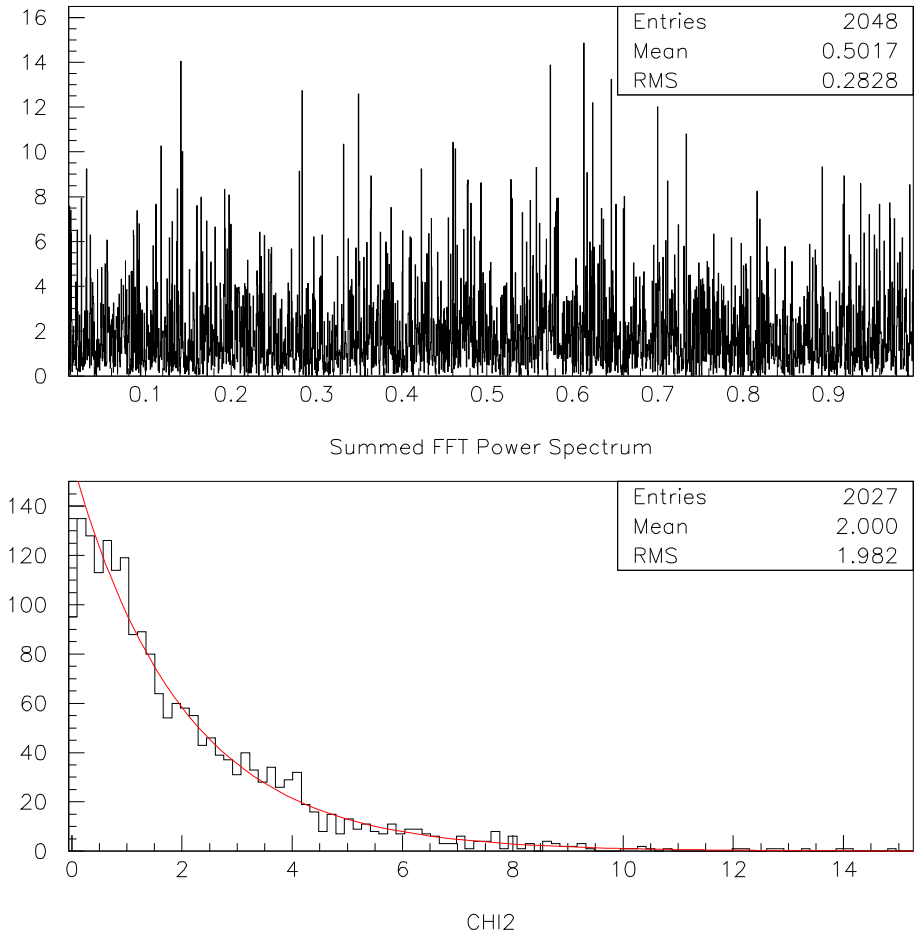

Figure F.3: Summed power spectrum of M=1 segment (top), and its distribution of powers (bottom). The smooth curve is the χ^2_{2M} expectation.

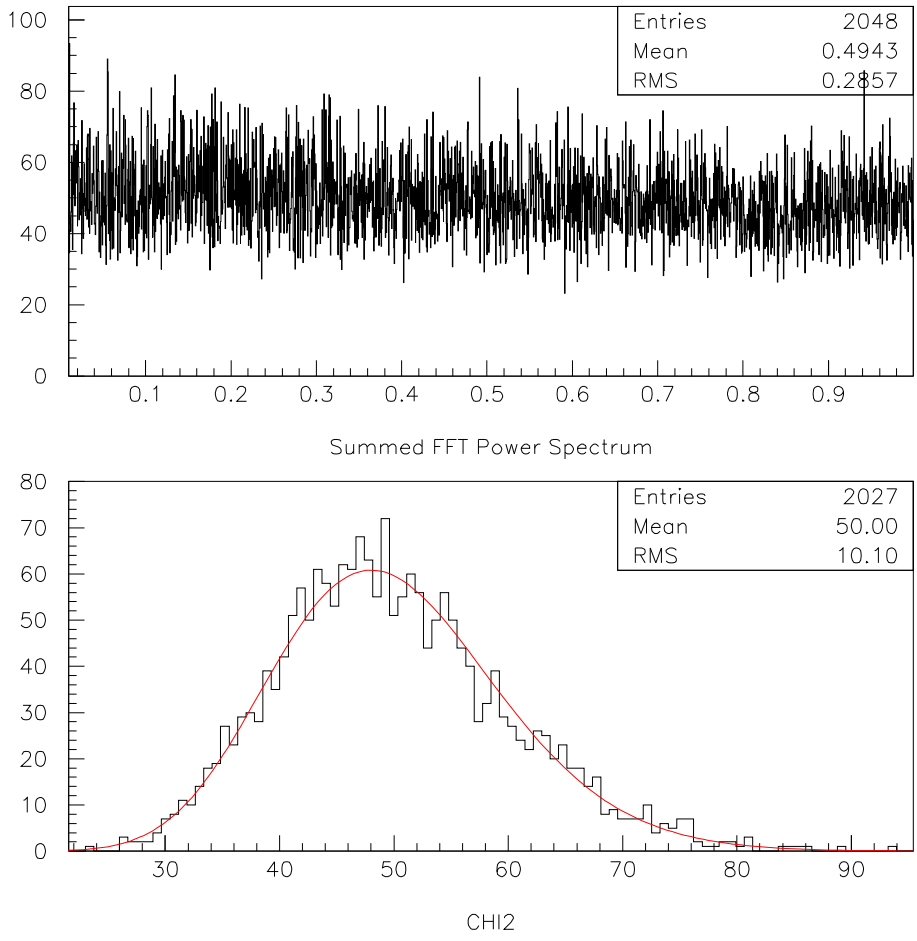

Figure F.4: Summed power spectrum of M=25 segments (top), and its distribution of powers (bottom). The smooth curve is the χ^2_{2M} expectation.

where C is a confidence level for power exceeding P_0.

Without looking at the data, but theorizing a χ^2_{2M} distribution of noise powers and the absence of any signal, one can compute a detection threshold power for a confidence level C (say, 90%, or $C = 0.90$). This is defined (following the terminology of [123]) as the power which will be randomly exceeded by noise in only $(1-C)$ of experiments. For just one bin of frequency, the detection threshold is merely the solution to:

$$probability(P_{\chi^2_{2M}} > P_{det}) = Q(P_{det}) = 1 - C$$

A power spectrum, however, has N_f independent bins of frequency, any of which could by chance have a high power. A detection threshold for a power spectrum, therefore, must be computed from the probability that *any* of the bins exceed the threshold:

$$probability(P_{\chi^2_{2M}} > P_{det}) = 1 - (1 - Q(P_{det}))^{N_f} = 1 - C$$

If the confidence level is high and $Q(P_{det})$ is small, we can apply a binomial expansion here and get:

$$1 - C = 1 - (1 - Q(P_{det}))^{N_f} = 1 - (1 - N_f Q(P_{det}) + O(Q(P_{det})^2)...$$

$$C = (1 - N_f Q(P_{det}))$$

$$Q(P_{det}) = \frac{1 - C}{N_f}$$

F.7.2 Signal power upper limit from data

What if a signal is present? Although it is tempting to treat the background and signal simply as additive, [123] warns that this is not correct. In the presence of both signal P_{sig} and a white noise background, which together add up to a total power P_{tot}, the probability distribution of P_{tot} in any single bin is derived in [119] and given by:

$$p_M(P_{tot}; P_{sig}) = (P_{tot}/P_{sig})^{(M-1)/2} \exp(-(P_{tot} + P_{sig})/2) I_{M-1}(\sqrt{P_{tot} P_{sig}})$$

where I_{M-1} is a modified Bessel function. Although a complicated expression, at high values of M this can be approximated by a Gaussian with mean $2M + P_{sig}$ and a variance $4M + 4P_{sig}$. This can

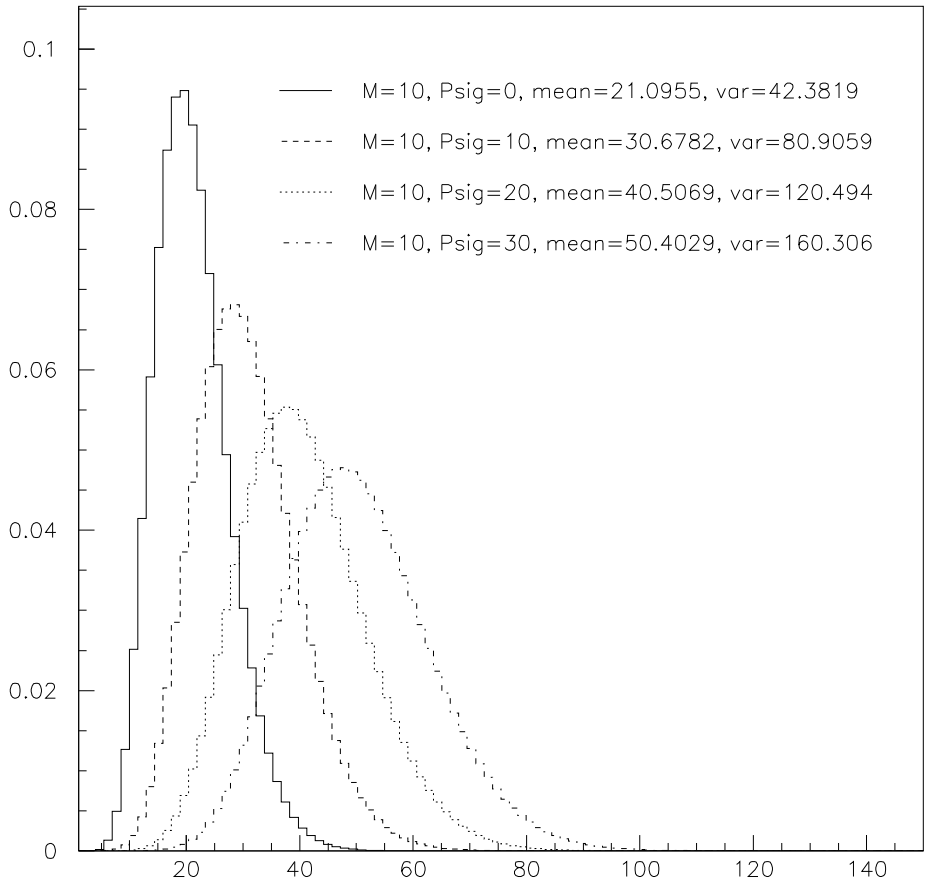

Figure F.5: Shapes of the distribution functions $p_M(P_{tot}; P_{sig})$ for noise and signal, for $M = 10$ and for four different values of P_{sig}.

be seen in Figure F.5, in which this complicated function is computed for $M = 10$ and a variety of different P_{sig}.

Notice that even at high M, the result is still not simply additive; if it were, the variance would be $4M + 2P_{sig}$.

Now that we know how the probability distribution depends on P_{sig}, we can compute an upper limit on P_{sig} for all independent bins of frequency. Assuming that the signal will produce a power excess in only one frequency bin, we strive to ensure that our upper limit power is very likely (with confidence C of, say, 90%) to be visible above even the highest power level present in the noise P_{max}. Thus, the upper limit signal power is the solution P_{sig} to:

$$probability(P_{tot} > P_{max}) = C$$

where P_{max} is the largest observed power of all frequency bins in the data. In this equation, C is given, as is P_{max}. The unknown in the equation, P_{sig}, is embedded in the shape of the probability function in a complex way, making it difficult to solve for. Fortunately, if we can approximate the function by a Gaussian (with mean μ and variance σ^2 that depend on P_{sig} as described above), it is possible to disentangle P_{sig} in the following way:

$$probability(P_{tot} > P_{max}) = C$$

$$Q_{G_{\mu,\sigma^2}}(P_{max}) = C$$

$$Q^{-1}_{G_{\mu,\sigma^2}}(C) = P_{max}$$

$$\sqrt{\sigma^2} Q^{-1}_{G_{1,1}}(C) + \mu = P_{max}$$

$$\sqrt{4M + 4P_{sig}} Q^{-1}_{G_{1,1}}(C) + 2M + P_{sig} = P_{max}$$

which is quadratic in $\sqrt{P_{sig}}$ and can be solved as a function of C, M, and $Q^{-1}_{G_{1,1}}(C)$. This last quantity is the inverse of $Q(P)$, the power which will be exceeded $(C)\%$ of the time, for a Gaussian distribution with unit mean and unit variance, which is easily computed from the tables in [116]

M	Threshold P_{det}	Sensitivity P_{sig}	P_{sig}/M
1	19.83		
25	98.87	74.43	2.98
100	287.57	126.12	1.26
1000	2255.80	349.98	0.350
7435	15550.99	915.23	0.123

Table F.2: Sensitivities for different M's

F.7.3 Theoretical signal sensitivity

To compute an expected signal sensitivity from theory only (rather than an upper limit from data), apply the same method only use the detection threshold P_{det} instead of P_{max} [123]. Computing the theoretical sensitivities for different values of M (Table F.2), it becomes evident why there is an advantage to summing the power spectra of many independent segments: the signal power sensitivity per segment becomes much more constraining.

F.8 Signal power and amplitude

To convert a Fourier power upper limit into upper limit on a signal *amplitude*, it is necessary first to make some assumptions about what the signal would look like. In the case of pulsed or oscillating neutrino emission from astrophysical sources, no good model for pulse shape exists, so we shall assume for simplicity (following [122]) a sinusoidal pulse shape:

$$r(t) = r_0 + A\sin(\omega t + \delta)$$

where r_0 is the mean count rate of the noise (in units of PE's/OM/sec), and A is the amplitude (also in units of PE's/OM/sec) of a sinusoidal modulation. A real pulsing source would not produce positive and negative photoelectrons, of course, but rather would oscillate between 0 and $2A$. This differs from the above formula only by the addition of A, which for weak signals is very small compared to r_0 and can be ignored. The average number of PE's contained in the pulsations, therefore, is also A.

Leahy et al. ([122]) go through the derivation of how this signal is manifested in a Fourier transform; it is not as simple as one might expect. The sinusoidal shape is contorted by binning effects, a "diffraction term" appears in the Fourier power in the signal's frequency bin j, and the final answer (re-derived for our definitions and normalization) is frequency-dependent:

$$< P_j >= 0.773M\frac{(AT)^2}{2N\sigma^2}\frac{\sin^2(\pi f_j/2f_{Nyq})}{(\pi f_j/2f_{Nyq})^2}$$

So when we find an upper limit power P, which is valid for all frequency bins, we can transform this into an amplitude upper limit by inverting this equation:

$$A = 1.61\sqrt{\frac{PN\sigma^2}{M}}\frac{1}{T}\frac{(\pi f_j/2f_{Nyq})}{\sin(\pi f_j/2f_{Nyq})}$$

Figure F.6 demonstrates these equations for "fake" data: an artificial sinusoidal signal is introduced into otherwise normal data, and the Fourier peak appears at the correct place with the correct amplitude.

F.9 Results and Discussion

All available data from 1997, excluding segments containing glitches and spikes, and "leftover" sections of data at the end of a run not fitting nicely into 2^{12} bins, consists of 7435 segments of 2^{11} seconds each, a total of 176.2 days. Each segment was Fourier-transformed, and all transforms summed together. The resulting power spectrum is shown in Figure F.7. It is not ideal white noise: there is both a steep delta-function-type structure at very low frequencies (due to non-zero mean effects) and a gentle exponential component, the cause of which is not known.

To search for periodic signals (appearing as spikes in the Fourier spectrum), we must first remove the delta-function and gentle-exponential components of the spectrum, even though their origins may not be fully understood yet. A constant plus two exponentials (one gentle, one steep) are fit to the total power spectrum (the smooth curve in Figure F.7). The two exponential fits can then be subtracted to give the white noise component only. The distribution of powers of this white-noise-only power spectrum (adjusted for the change in overall normalization when subtracting the exponentials) is compared in Figure F.8 to the expectation of a χ^2 distribution with 2×7435 degrees of freedom.

A periodic signal, if it existed, would produce a spike in Fourier space, and a frequency bin with an unusually high power. In the data, the highest power appearing in any bin is 14652.5 (renormalized slightly to 15421.0 in the removal of the exponential component). So, a 90% confidence level signal power upper limit P_{UL} is the power that (when combined with the noise) would produce a total power greater than P_{max} in 90% of experiments. For this data, P_{UL} is computed to be 783.415 (un-renormalized to 744.37).

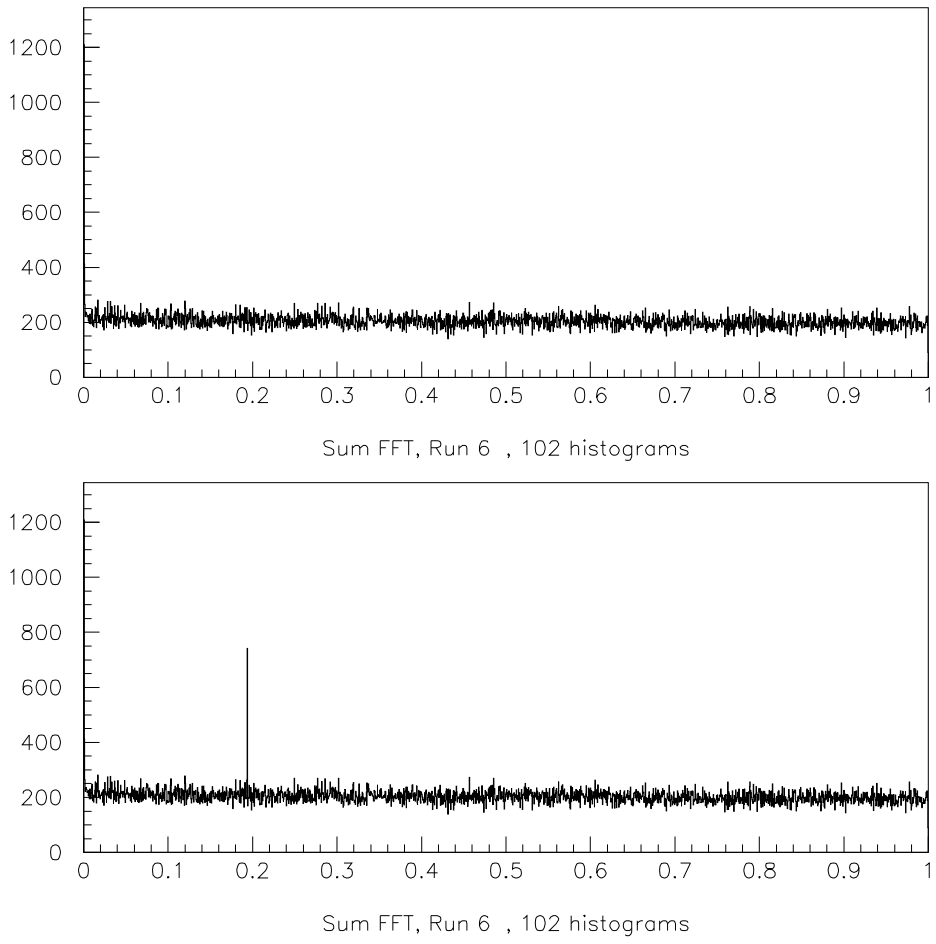

Figure F.6: Upper plot: Fourier spectrum of a normal run. (102 summed segments: average count rate 896.7 Hz, $T = 2048$ seconds, and normalization $N\sigma^2 = 92000$ for each segment.) Lower plot: the identical run, but with an artificial sinusoidal signal added, with amplitude $A = 0.5$ at a frequency of 0.1938 Hz. The resulting signal amplitude is as predicted by the equations.

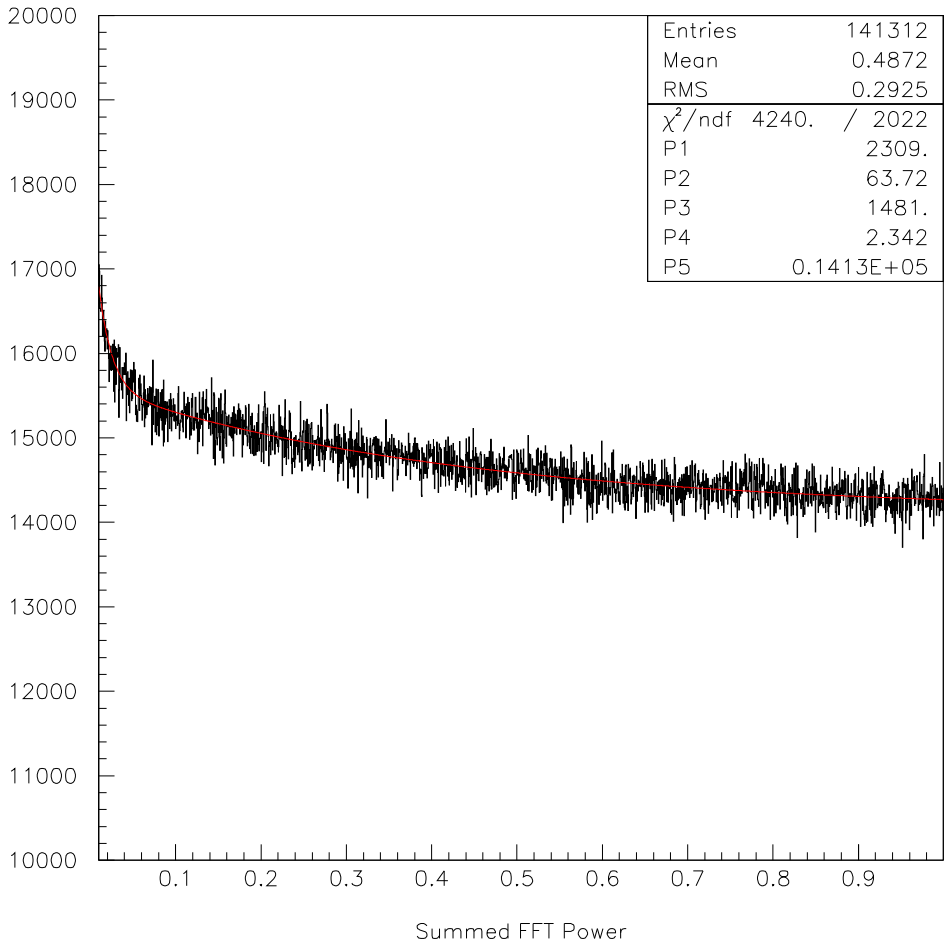

Figure F.7: Summed power spectrum of all 1997 data

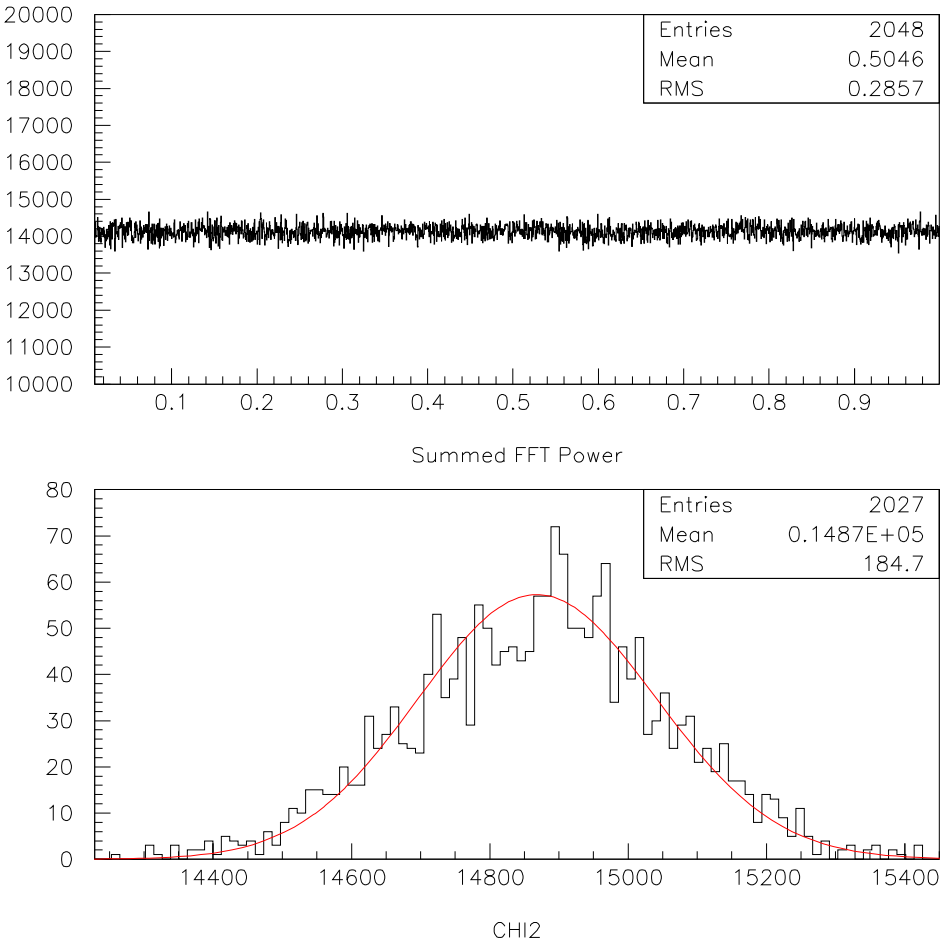

Figure F.8: White noise component only of the 1997 power spectrum for M=7435 segments (top), and its distribution of powers (bottom). The smooth curve is the χ^2_{2M} expectation

To translate this power upper limit into a sinusoidal signal amplitude upper limit, we apply the equations in Section 8 to each bin of frequency. At the Nyquist frequency, the diffraction term approaches $\pi/2$, and at low frequencies it approaches 1. Therefore, the amplitude upper limit for all of 1997 ($P_{UL} = 744.37$, $r_0 = 880.5$, $N\sigma^2 = 91220$) is:

	Amplitude (PE/OM/s)
low frequencies	0.0751
high frequencies	0.118

This limit, of course, assumes that the neutrino signal is a purely sinusoidal one, and is constant in amplitude over all of 1997.

The next step is to convert photoelectrons per module per second into a limit on the flux of low-energy neutrinos from a pulsing source in the sky. This is difficult, however, since there are no models for neutrino pulsations and no known neutrino point sources. However, just to put the limit in perspective, we can take a few guesses.

F.9.1 Supernova-like source

A single supernova explosion at the center of the galaxy, emitting neutrinos with energy of a few MeV, is expected to produce 100 PE's/OM/10 seconds in AMANDA [121]. Though no such objects exist, consider a hypothetical pulsing source with the same supernova-like neutrino spectrum. Further suppose that the total neutrinos produced by the source (which produce 100 PE's/OM total) are spread uniformly over 170 days (1.5E7 seconds) instead of 10 seconds. Such a source would produce 0.0000067 PE's/OM/sec in pulsations. This is four orders of magnitude below our upper limit.

F.9.2 Gamma-ray signal from a pulsar-like source

Pulsations have been found in some objects in x-rays and even gamma-rays. This analysis could be sensitive not only to excess photons from neutrinos, but also from high energy gamma-ray showers. The Vela Pulsar, for instance, is expected to produce 100000 muons from gamma rays which penetrate to AMANDA depth per year in a km^3-size detector.[120] Rescaling this to AMANDA-B10 size, this is approximately 1000 muons per year. Assuming each muon produces an 25-hit event (0.1 PE's/OM), this causes a net excess over all modules of 100 PE's/OM/year, a number similar to

the expectation for the "supernova-like" source above. Again, this is four orders of magnitude below the upper limit.

F.9.3 Weird Stuff (cosmic strings, extraterrestrial communications, etc.)

In this regime, of course, there are very few rules and absolutely no data. So consider, just for fun, an alien civilization capable of producing a beam of neutrinos with a flux such as we can achieve in the present day from a muon collider. [118] predicts a charged-current event rate of 10^5 events/kton/year for a detector 10000 km downstream of a 200-GeV muon collider. The neutrinos would have energies of tens of GeV. Rescaled to AMANDA-B10, this is about 20 events/sec, each of which causes 0.01 PE's/OM, resulting in a signal of 0.2 PE/OM/sec. Further suppose that this beam was expectantly aimed at Earth, from a distance away D; we need to correct for the distance by a factor of $(10000\text{ km})^2/D^2$. A neutrino signal from the nearest star would need 20 orders of magnitude greater intensity to reach our upper limit.

If, however, we disregard the dispersion of the neutrinos across the vastness of space and consider a perfectly-collimated neutrino beam of similar amplitude, then the signal is on the same order as our upper limit. Perhaps with further refinement in the analysis, this model can be ruled out.